



**UNIVERSITAT POLITÈCNICA
DE CATALUNYA
BARCELONATECH**

**Structural Performance of Continuous Composite
Bridges with Partial Shear Connection and Double
Composite Action**

Name: Su Hang
Doctoral program: Construction Engineering
Discipline: Engineering
Supervisor: Prof. Dr. Joan Ramon Casas
Prof. Dr. Su Qingtian

September, 2023



**UNIVERSITAT POLITÈCNICA DE CATALUNYA
BARCELONATECH**

Departamento de Ingeniería Civil y Ambiental

Acknowledgments

The author thanks the support of the China Scholarship Council for the funding provided through the research projects 202106260050.

First and foremost, I would like to thank my supervisors, Prof. Joan Ramon Casas, and Prof. Qingtian Su for their patient guidance, continuous support, and motivation during my Ph.D. study. Their hard-working and rigorous academic attitude towards research is worth learning and is what I always admire. They have spent so much time on inspiring me, discussing with me and cultivating my academic critical thinking, and training me with strict requirements. Their roles are deeply imprinted in my heart as models not only in the field of research but also in daily life. It is my honour to work with them during my Ph.D. stage, and all of my Ph.D. time will be the most memorable life experience.

I want to thank all the professors and members of UPC, who are being helpful and supportive all the time. And I want to thank Sizhe Wang for his help in my research and Guandong Zhou, Xieli Zhang for the research method proposed. And thanks to my colleagues and friends in UPC, Jinglong Liu, Guanzhi Liu. And also, to my roommates in Barcelona, Subiao Bian, Haofu Zheng, thanks for your companionship.

Thanks to my mother, Lifang Ao and my father Wei Su. Thanks for your support, encouragement and accompany. Last, my profound gratitude goes to my wife, Yuemei Wu. Your countless contributions and support are always my driving force. Thank you for supporting and understanding my decision to study abroad.

ABSTRACT

The steel-concrete composite structural solution has been widely applied in the execution of simply supported bridges since the merits of concrete compressive strength and steel tensile strength can be efficiently utilized. However, there is an inverse stress situation in the hogging moment region of a continuous composite girder, where the concrete tensile cracks and steel buckling are both likely to happen. Normal composite bridges adopt Full Shear Connection (FSC) due to convenient construction and clear mechanical properties. However, large tensile stress in concrete is generated in hogging moment regions in continuous girders. In response to this issue, Partial Shear Connection (PSC) achieved by reducing shear connection efficiency in hogging moment region of continuous composite bridge can help to decrease the interaction extent between concrete slab and steel girder, thus reducing the concrete cracking and simultaneously maintaining the ultimate bearing capacity and overall stiffness of the structure. Meanwhile, casting an extra concrete bottom layer to a steel-concrete composite box girder (double composite action) in a hogging moment region can also prevent steel buckling and improve the mechanical performance of the continuous composite bridge. In order to study the structural performance of composite girder with PSC and double composite action, this thesis presents an in-depth study through the combination of experimental, numerical and analytical studies as follows:

(1) To study the mechanical properties of the rubber sleeved stud connector, five groups of 15 push-out specimens were fabricated and tested. Numerical models were established. The results of the test and numerical analysis show that the rubber sleeved stud (RSS) connector effectively reduces the shear stiffness of the push-out specimen without changing the load carrying capacity.

(2) To study the structural performance of composite girders with partial shear connection, four simply supported composite girder specimens and two continuous composite girder specimens were fabricated and tested by static loading tests. The mechanical behaviour of the hogging moment regions of each specimen was compared and based on them, the theoretical background was settled for the practical application of partial shear connection in composite bridges.

(3) A case study of Qiwu bridge in Jiangxi Province (China) using partial shear connection action was introduced. A nonlinear finite element model of Qiwu Bridge

was established through ABAQUS to simulate and predict the mechanical properties and structural performance. Based on the FEM results, the influence of partial shear connection on various parameters were analysed by performing a parametric analysis. Monitoring of the bridge during the construction and in service stages is also carried out in order to check the design rules derived in this thesis in a real bridge

(4) A static loading test on a large-scaled two-span continuous girder specimen with the double composite action in hogging moment region was conducted for mechanical investigation. In parallel, a parametric analysis was carried out as well for a rational design scheme of the double composite section.

According to the experimental, numerical and analytical studies, several conclusions can be listed:

(1) Wrapping rubber sleeve around the stud shank near stud root could enhance the slip capacity and reduce the stiffness of the connector in the push-out tests, while it could hardly affect the shear strength of the connector. The rational rubber sleeve thickness and height were 4mm and 50mm for a 22mm-diameter and 220mm-high stud. The parametric analysis on a continuous composite girder with RSS connectors configured in the hogging moment region showed a maximum of 39% concrete slab stress reduction and a 13% increase of steel stress on the top flange.

(2) Configuring the RSS connectors with a shear stiffness of only 8.1% of the corresponding ordinary stud (OHS) connectors or setting a 2000 mm OHS spacing caused a reduction in load-carrying capacity of 17% and 11%, respectively. In contrast, the RSS connector decreased the bending stiffness by 12% and reduced concrete crack development, whereas increasing the stud spacing hardly changed the bending stiffness or improved the cracking resistance. The RSS connector contributed to increase the efficiency of the prestressing (if present), by increasing the prestressing action in the concrete slab by a maximum of 19.4% and by declining it in the steel girder by 92.6%, while the figures were only 8% and 26.9%, respectively, for increasing the stud distance.

(3) Partial connection and additional prestressing can effectively improve the cracking resistance of continuous composite girders. The simulation results showed that compared to conventional composite girders, the cracking load increased by 11.8% and 157.0 % when applying RSS and prestress alone, respectively, and by 234.3% when applying RSS and prestressing at the same time. In the case of full connection, the shear stiffness of the stud connectors does not have an important influence on the amount of prestressing transferred to the concrete slab. It keeps constant at around 75 % for

relative stiffness between 1 and 100.

(4) Arranging PSC can effectively reduce the crack region. While the crack region tends to be wider and continuous with the increase of the load, PSC action helps to spread the concentrated stress in the zone. Meanwhile, the shear stiffness mutation can magnificently increase the stress level at the edge of PSC region in concrete slab and made it easier to crack. Actions of increasing the reinforcement ratio or adopting high-performance concrete at this position is essential for crack control.

(5) Double composite action helps to restrain lateral deformation of steel web and steel bottom flange. It can effectively improve the anti-buckling ability of the continuous girder. Based on the parametric analysis, the additional concrete slab helps to increase the cracking load and ultimate strength by 12% and 4%, and the optimal concrete slab thickness was found around 15 % of the height of the steel girder. In addition, the steel web thickness can be saved by 16.7%, while the steel bottom flange thickness only needs to meet the constructing requirement after using the double composite action. The box section could contribute to a 24.4% and 3.2% stress decline respectively in steel top flange and concrete slab compared with tub section.

Keywords: Steel-concrete composite structure, Partial shear connection, Double composite, Hogging moment regions, Rubber Sleeved Stud Connector

RESUMEN

La solución mixta acero-hormigón se ha utilizado ampliamente en la construcción de puentes simplemente apoyados, ya que en esta configuración longitudinal es como mejor se aprovecha la alta resistencia a compresión del hormigón junto con la alta resistencia a tracción del acero. Sin embargo, la solución se vuelve contraproducente en la zona de flexión negativa de puentes continuos, donde la fisuración a tracción del hormigón y la abolladura del acero son fenómenos probables. Los puentes mixtos adoptan una solución de conexión completa (CC) debido a la facilidad constructiva y respuesta estructural. Para reducir las tensiones de tracción en la zona de flexión negativa, una solución alternativa es la conexión parcial (CP), que ayuda a reducir la interacción entre la losa de hormigón y la viga de acero, reduciendo la fisuración en el hormigón aunque manteniendo la resistencia y la rigidez global de la estructura. Por otro lado, colocar un recrecido de hormigón en la zona inferior de la zona de apoyos (doble acción mixta) puede prevenir la abolladura de las chapas metálicas y mejorar la respuesta de los puentes mixtos continuos. Con el objetivo de estudiar el comportamiento estructural de puentes mixtos continuos con conexión parcial y doble acción mixta, en esta tesis se desarrolla un estudio completo combinando experimentación con soluciones numérica y analíticas con el siguiente contenido:

(1) Estudiar las propiedades mecánicas del conector enfundado en neopreno (CEN), mediante el ensayo push-out en laboratorio de 5 grupos de 15 muestras y establecer modelos numéricos de su comportamiento estructural. Los resultados experimentales y estudios numéricos han puesto de manifiesto que este tipo de conector reduce de manera efectiva la rigidez transversal sin variar la capacidad de carga.

(2) Estudiar el desempeño de vigas mixtas con conexión parcial, mediante el ensayo en laboratorio de 4 vigas simplemente apoyadas y dos vigas continuas mixtas, cargadas estáticamente hasta rotura. Mediante la comparación de la respuesta estructural en la zona de flexión negativa de cada viga se han obtenido conclusiones en relación a la aplicación práctica de la conexión parcial en puentes mixtos continuos.

(3) Analizar la posibilidad de la solución de puentes mixtos semi-continuos y conexión parcial a través de la construcción del puente Qiwu en la provincia de Jiangxi (China). Mediante un modelo de elementos finitos (ABAQUS) del puente se ha simulado la respuesta estructural, analizando los efectos de la conexión parcial en varios

parámetros de diseño. Al mismo tiempo, se ha llevado a cabo la monitorización durante las fases de construcción y servicio para verificar los resultados del estudio.

(4) Se ha hecho un estudio experimental y teórico de la doble acción mixta, lo cual ha permitido obtener unos criterios de diseño para puentes continuos con este tipo de solución.

En base a los resultados experimentales, numéricos y teóricos llevados a cabo se han obtenido las siguientes conclusiones:

(1) Enfundar con neopreno los conectores cerca de la raíz aumenta la capacidad de desplazamiento relativo y reduce la rigidez de la conexión, a la vez que no afecta la resistencia a cortante del conector. El espesor y altura de neopreno óptimos son 4 mm y 50 mm para un conector de 22 mm de diámetro y altura de 220 mm. Su aplicación da lugar a una reducción de las tensiones de tracción en el hormigón de un 39 % y un aumento de la tensión de tracción del 13 % del acero en la zona superior.

(2) Utilizando conectores enfundados en neopreno con una rigidez transversal de sólo un 8.1 % del correspondiente a un conector normal, o una separación de 2000 mm en conectores normales da lugar a una reducción de la carga última del 17 % y 11 % respectivamente. Por otro lado, el conector con neopreno disminuye la rigidez a flexión un 12 %, limitando la fisuración, mientras que aumentar la separación entre conectores prácticamente no varía la rigidez a flexión ni mejora la fisuración. En el caso de que la losa superior se pretense, el conector con neopreno aumenta la eficacia del pretensado en la losa en un máximo de un 19.4 % y disminuye el pretensado que se filtra a la viga de acero en un 92.6 %. Estos valores caen a un 8 % y 26.9% respectivamente si la solución adoptada es la de aumentar el espacio entre conectores.

(3) La conexión parcial combinada con el pretensado de la losa aumenta favorablemente el comportamiento frente a fisuración de la misma. Los resultados muestran que, comparado con la solución convencional, la carga de fisuración aumentó en un 18 % y un 157 % cuando se utiliza el conector con neopreno o el pretensado solos, respectivamente. Cuando se aplican conjuntamente, el incremento fue del 234.3 %. En el caso de conexión total, la rigidez transversal del conector no tiene una influencia importante en la cantidad de pretensado transferido a la losa de hormigón, manteniéndose constante alrededor de un 75 % para una rigidez relativa entre 1 y 100.

(4) La conexión parcial reduce notablemente la zona fisurada. Mientras que la zona fisurada tiende a crecer con el aumento de la carga, la conexión parcial ayuda a

distribuir la concentración de tensiones en la zona. Al mismo tiempo, la zona de cambio de conexión parcial a total es la crítica, aumentando las tracciones en la misma y facilitando la fisuración en dicha zona. Para controlar la fisuración, es imprescindible aumentar la cuantía de armadura o bien utilizar hormigón de altas prestaciones en dicha zona de cambio de rigidez en la conexión.

(5) La doble acción mixta ayuda a coaccionar la deformación lateral del alma y fondo de la sección de acero, limitando las posibilidades de abolladura en puentes mixtos continuos. El estudio paramétrico llevado a cabo pone de manifiesto que el recrecido de hormigón aumenta las cargas de fisuración y última en un 12 y 4 % respectivamente. El espesor óptimo de recrecido es del 15 % del canto de la viga de acero. Además, se puede reducir el espesor del alma en un 16.7 %, mientras que el espesor de la chapa inferior se puede reducir a un mínimo constructivo. La solución de sección de acero en cajón puede contribuir a un descenso del 24.4 % y 3.2 % de las tensiones en la chapa superior y losa de hormigón, respectivamente, si la comparamos con la solución de viga en U.

Palabras clave: estructura mixta acero-hormigón, conexión parcial, doble acción mixta, zona de flexión negativa, conector enfundado en neopreno.

TABLE OF CONTENTS

Chapter 1 Introduction	1
1.1 Motivation.....	1
1.2 State of the art	2
1.2.1 Development Process of Steel-concrete Composite Girders	2
1.2.2 Research progress in mechanical behavior of composite members.....	5
1.2.3 Research progress in shear connectors	9
1.2.4 State of partial shear connection	11
1.3 Objectives	12
1.4 Structure of the thesis.....	14
Chapter 2 Shear Performance and Dimension Rationalization Study on the Rubber Sleeved Stud Connector	16
Chapter 3 Structural performance of Composite Girder with Partial Shear Connection	18
3.1 Structural performance of partial shear connection	18
3.2 Prestressed Continuous Composite I-Girder Bridges with Partial connection	19
Chapter 4 Mechanical Performance Based Rationalization Research on Steel-concrete Double Composite Action.....	22
Chapter 5 Application of Partial Shear Connection in Steel-concrete Semi-continuous Composite Girder Bridge	24
Chapter 6 Published papers.....	26
6.1 Engineering Structures 2021	26
6.2 Structures 2022	46
6.3 Journal of Bridge Engineering 2023	76
6.4 Journal of Constructional Steel Research 2022	105
6.5 Structural Engineering International 2022	133
6.6 Structure and Infrastructure Engineering 2023	148
Chapter 7 Conclusions and Future Research	171

7.1 Conclusions.....	171
7.2 Future Research	174
References.....	175

Chapter 1 Introduction

1.1 Motivation

The steel-concrete composite structure has been widely applied in the simply supported bridges since the merits of concrete compressive strength and steel tensile strength can be efficiently utilized. However, there is an inverse stress situation in the hogging moment region of a continuous composite girder, where the concrete tensile cracks and steel buckling are both likely to happen. Increasing reinforcement ratio ^[1], introducing pre-stress effect ^{[2]-[5]}, configuring a double composite section ^{[6]-[8]} help to restrain the tensile concrete cracks and prevent the steel from buckling. Moreover, the high performance concrete with good tensile performance ^{[9]-[11]} and Fiber Reinforced Plastic (FRP) bonding material ^{[12][13]} can be good choices as well for the concrete crack resistance and reinforcement.

Meanwhile, a low level of composite action achieved by reducing connector number or adopting connector with an initial lower stiffness could also make a reduction of tensile stresses on the concrete slab, which will effectively relieve the cracking problem in the hogging moment region and is convenient to construct. Besides, the bending capacity, global stiffness and deflection of the girder can be possibly maintained with small reductions ^{[14]-[17]}.

The partial shear connection was initially achieved by reducing the number of connectors. Researchers have found that few connectors in the negative bending moment regions contributes to reduce the stress in concrete slab and maintain an unchanged load-carrying capacity of composite girders ^{[18][19]}. Although some composite bridges have applied this solution during designing, a normative design criteria to reduce the number of connectors is not yet available and, therefore, the subject needs to be further studied.

To improve the efficiency of shear connection stiffness decrease, connector with an initial lower stiffness was also introduced. The Rubber-Sleeved Stud (RSS) connector was a kind of newly developed connector consisting of an Ordinary Headed Stud (OHS) connector simply wrapped by rubber sleeve at the root. It is featured by its fast construction advantage. Though adopting RSS could be one of the most convenient

ways to make a low level of composite action, a rational design criteria of RSS connector, summarizing the existing state of the knowledge has not been developed yet. Again, this becomes a problem that hinders the application of RSS connector in the bridge design practice.

Recently, there was a much radical attempt on partial shear connection which canceled all the shear connectors near the mid support of the steel-concrete composite bridge. This solution may cause the problem of sudden stress change at the stiffness mutation region and the separation of the steel and concrete parts at the mid support, so, again, further research should be conducted to study the mechanical behavior of non-composite action at the intermediate supports.

1.2 State of the art

1.2.1 Development Process of Steel-concrete Composite Girders

1.2.1.1 Stage of embryonic (1920 to 1940)

Steel-concrete composite beams firstly appeared in the 1920s. At that time, the main consideration was to wrap concrete outside the steel girders for fire protection, without considering the mechanical advantage. In 1922, H. M. MacKay and P. Ginespie of The Dominion Bridge Company of Canada conducted experimental research on two steel girders wrapping with concrete, and put forward the concept of composite beam for the first time ^[20]. Almost at the same time, the British National Physics Laboratory also conducted experiments on composite beams. In 1923, R.A. Caughen conducted tests of 6 T-shaped composite beams. According to the test results, it is suggested that the design can be carried out according to the method of material mechanics. In the above-mentioned tests, all the specimens were not equipped with mechanical connectors on the steel-concrete interface. In 1933, R.C. Maning first studied composite beams with shear connectors. In the same year, M.Ros first designed and conducted push-out tests to study shear connectors. This method is effective and is still used today. In 1936, the Swiss Voellmy conducted a test of the composite beam specimen with spiral reinforcement shear connectors ^{[21][22]}. In 1939, Batho, Lash, Kirkham and others conducted a comprehensive study of composite beams without shear connectors. The results showed that the steel-concrete contact surface without mechanical connectors

began to fail when slippage occurred. It is pointed out that the shear connectors can enhance the overall working performance of the composite beam and significantly increase the ultimate bearing capacity ^[23]. It can be seen that the research on composite beams in the embryonic stage mainly focuses on the research on the steel girders wrapping with concrete and its function of fire protection. The concept of shear connection is also introduced. Researches at this stage have laid the basis for the development of steel-concrete composite bridges in the next future.

1.2.1.2 Stage of initial development (1940 to 1966)

In this stage, a more in-depth and comprehensive experimental and theoretical research was carried out on the composite beam, especially for the shear connectors. Many technologically advanced countries have formulated design standards related to composite beams, so that the application of composite beams was gradually popularized under scientific guidance. In 1943, Lehigh University reported a test report on channel steel connection composite beams ^[24]. In 1954, L.M. Viest conducted research on stud connectors for the first time, and proposed to use the shear strength when the residual slip is 0.07mm as the permissible shear capacity of the stud ^[21]. In 1964, Chapman and Balakrishnan conducted the first research on stud connectors considering the sliding and lifting effects between the steel and concrete layer ^{[25][26]}.

In 1936, the American Institute of Steel Construction (AISC) formally revised the 1923 Code and added standards for the design and construction of outsourcing concrete composite beams. In 1944, the American AASHTO standards added the design provisions for composite beams for the first time. After 1945, the former Federal Republic of Germany urgently needed to rebuild a large number of houses and bridges destroyed in the war. Due to the shortage of steel, a large number of composite structures were adopted. In 1954, the "Composite Beam Bridge Standard" (DIN-1078) was formulated. The United Kingdom formulated the "Steel and Concrete Composite Structure " (CP117: Part1) in 1965, and the "Steel and Concrete Composite Structure · Bridge" (CP117: Part2) standard in 1967. The first highway composite bridge in the Soviet Union was built in 1944. The "Technical Code for the Design of Bridges and Culverts in the Soviet Union for Railways, Highways, and Urban Roads" (CH200-62) promulgated in 1962 has a special chapter, which systematically introduces the design of "steel-concrete composite structure". In 1959, Japan formulated the "Guidelines for the Design and Construction of Composite Bridges".

Since then, 80% of highway steel bridges have been converted into composite girder bridges. Besides, the Indian Standards Association formulated the "Combined Structure Design Code" (IS:3955-1966) in 1966.

1.2.1.3 Stage of overall development (1966 to 1985)

At this stage, based on the previous research and application, the relevant design standards of composite bridges were further improved. The application and development of composite beams gradually matured, almost catching up with the development of steel structures, and received extensive attention ^[26]. The focus of research on composite bridges also changed. In-depth research was conducted on the characteristics of continuous composite beams. Representative theoretical research results are: RG Slutter proposed the calculation method of the ultimate flexural strength of composite beams in 1965 ^[27], the calculation method of the shear strength for shear connectors was formulated by J. G. Ollgaard in 1971 ^[28] and the calculation method of the strength and deformation for shear connectors proposed by RP Johnson in 1975 ^[29].

The Architectural Society of Japan formulated the "Design and Construction Regulations and Instructions for Profiled Steel Plate Structures" in 1970. In the "Code for Design, Manufacturing and Installation of Steel Structures for Houses" revised in 1978, the United States added design clauses for welding connectors. In 1981, the European International Concrete Association (CEB), the European Steel Structure Association (ECCS), the International Association of Prestressing (FIP) and the International Association for Bridge and Structural Engineering (IABSE) jointly promulgated the "Composite Structure" Standard ^[30]. Revised and supplemented on the basis of the "Composite Structure" standard, the Commission of the European Communities (CEC) officially promulgated the design code for steel-concrete composite structures "Eurocode 4 (EC4)" in 1985 ^{[31][32]}. This is currently the most complete composite structure design standard in the world. It has made a comprehensive summary of the research and application of composite structure and pointed out the direction for future development. By now, the Eurocode 4 is in the process of up-dating and a new version is expected to appear in the coming years.

1.2.1.4 Stage of popularization and application (1985 to 2023)

During this period, with the development of new materials and technologies, a variety of new structural forms such as prefabricated composite beams, superposed

beams, prestressed composite beams, steel sandwich composite beams, double-composite beams and corrugated web composite beams emerged one after another. At the same time, more detailed and comprehensive studies were carried out on the stiffness, ultimate bearing capacity, stability performance, and fatigue performance of composite beams. The development of finite element technology made the research on composite beams more convenient, and the numerical models have gradually developed in the direction of non-linearity, three-dimensionality, and refinement in the modelling of local details. It has solved a large number of practical problems in real constructions and promoted the rapid development of composite beams [33]-[35].

1.2.2 Research progress in mechanical behavior of composite members

Andrews E.S. first proposed the conversion section method based on elasticity theory [36]. This method assumes that both steel and concrete are ideal elastic objects that are connected reliably and completely deformed. The two materials are converted into one material through the ratio of their elastic modulus, and then the cross-section calculation and design are carried out according to the elementary bending theory. This method has clear physical meaning and simple calculation. It has been adopted by various design codes as the basic method of elastic analysis. However, there are two shortcomings in the analysis of composite beams using the converted section method: one is that the actual material is not an ideal elastic object; the other is that the concrete slab and the steel girder are connected by the shear connectors. The relative slippage occurs at the interface of the composite beam. Due to the deformation of the stud, the two materials cannot be completely deformed together. There is a certain gap between the theoretical analysis and the actual situation, and the bearing capacity and deformation calculation results will be biased.

Newmark proposed the differential equation of the longitudinal shear force at the interface of composite beams [37]. For the first time, the influence of the relative slip of the steel girder and concrete interface on the bearing capacity and deformation of composite beams was considered, and the "incomplete interaction theory" was established. In the differential equation, the unknown quantity is the axial force generated by the shear connector on the interface. For simply supported composite beams subjected to concentrated loads, the differential equations can be used to solve the axial force, the shear force distribution, the slip and the deflection. The theoretical

formula is relatively complicated and not convenient for practical application. However, it has great theoretical significance because it considers the influence of relative slip on the interface of composite beams.

Viest summarized the test results of 185 steel-concrete composite beams and 249 push-out specimens, and compared the calculation methods of elastic bearing capacity, ultimate bearing capacity and deflection of simply supported composite beams proposed by different scholars^{[38][39]}.

Barnard studied the factors affecting the ultimate bending strength of composite beams^[40]. Since the shear connector will deform after being subjected to shear force, there is a slippage effect between the steel girder and the concrete slab. Because of the difference in bending rigidity between the concrete slab and the steel girder, there is a tendency of pull-out. Therefore, the theoretical ultimate bearing capacity of composite beams is always larger than the measured ultimate bearing capacity.

Mallick and Chattopadhyay carried out loading tests on 8 2-span and 10 3-span continuous composite beams with different loading methods^{[41][42]}. The rotation angle of the plastic hinge is derived from the curvature distribution of the sagging and hogging moment region, and a simplified design method is proposed. Tests show that the test beam can always reach the plastic design flexural bearing capacity as long as secondary failures such as shear connector failure, concrete longitudinal splitting and steel girder buckling are avoided.

Hamada and Longworth carried out a test of three continuous composite beams with two equal spans^[43]. The test plan was concentrated loading in the middle of the span. The main conclusions from the experimental analysis are: the crushing of concrete in the sagging moment region or the local buckling of the steel flange in the hogging moment region can be used as the failure mode to accurately calculate the ultimate load of the continuous composite beam; the amount of longitudinal steel reinforcement is the main factor for the failure mode of the hogging moment region.

Ansourian conducted 6 continuous composite beam tests^[44]. The specimen used thick plate steel girders, two of which were single-span loaded, which required high rotation capacity in the sagging moment region. The remaining 4 are 2-span symmetrical single-point loading, which are affected by the local buckling of the steel girder when they fail. The test shows that the simplified plastic theory can be used for design in the early loading process, regardless of the loading method, span and other factors.

Bradford et al. analyzed the long-term performance of steel-concrete simply supported composite beams and compiled corresponding calculation programs ^{[45][46]}. The program considers the shrinkage and creep of the concrete slab by introducing the method of age adjustment, and also considers the influence of the slip effect. The calculation results of the ultimate bearing capacity obtained according to this method are in good agreement with the test results. The calculation shows that the slip increases with the increase of the concrete shrinkage and creep, but the absolute value is very small under normal operational conditions. Based on calculation and analysis, Bradford proposed a simplified design method to calculate the long-term effects of steel-concrete composite beams.

Richard et al. summarized the test results of 44 steel-concrete simply supported composite beams under static and fatigue loads ^[47]. The variable parameters of the 44 composite beam specimens mainly included the degree of shear connection, the transverse reinforcement of the concrete slab, the stress amplitude and the stress ratio. The test shows that the concrete slab begins to crack under the action of fatigue load, and the cracks gradually propagate and eventually lead to the failure of the specimen. In part of the fatigue test, the concrete near the shear connector appeared to be crushed. In the fatigue test, the flexural rigidity of the composite beam gradually decreased. There is not much difference in the fatigue test between the composite beam with complete shear connection and the composite beam with 80% shear connection.

Brain summarized the response of composite beams under combined actions ^[48]. Load combinations of bending moment and shear force, bending moment and axial force, bending moment and torque are summarized. Based on the theoretical analysis and experimental research, calculation methods of bending-shear and bending-torsion were summarized.

Q. H. Zhang conducted research on the calculation method of deflection of steel-concrete composite beams ^[49]. The study showed that the deflection calculation needs to consider the effect of inter-layer slip. Since the stiffness of the beam decreases with the increase of the slip, the deflection of the beam tends to be larger. When the shear stiffness of the shear connector is greater than 1200MPa, the slip effect can be ignored, otherwise it needs to be considered.

Z. W. Guo studied the coupling effect of bending and torsion of steel-concrete composite beam ^[50]. Results show that the coupling effect of bending and torsion increases the shear lag effect of steel-concrete composite beam under live load. At the

same time, when the local effect of shear lag is not considered, the eccentric load coefficient of the control section can be controlled. It can be inferred that the coupling effect of bending and torsion will increase the shear lag coefficient of the mid-span section and the fulcrum section of the steel-concrete composite beam.

Z. M. Hou's research shows that the flexible stud connectors of the composite beam will affect the dynamic response of the structure^[51]. The interface slip caused by the flexible studs can reduce the stiffness of the beam and reduce the natural frequency. At the same time, the stiffness of the stud connector also has a greater impact on the beam's mid-span deflection response.

L. Jin's research^[52] shows that for steel-concrete composite segment beams, the stress changes in the joint section are smooth. The stress level is low, which can effectively transmit the internal force. However, there are stress concentrations in some parts, such as the end of the stiffened T rib and the corner of the steel bottom flange. Besides, the shear connector is not uniformly stressed. The farther away from the pressure-bearing plate, the greater the shear force is.

J. Luo tested 40 steel UHPC composite panels and 8 steel UHPC composite beams^[53] and respectively studied their cracking characteristics in the transverse and longitudinal directions. The research results show that the reinforcement ratio and the thickness of the protective layer have a great impact on the cracking stress. When the thickness of the protective layer is small, the cracking stress can be maximized by increasing the reinforcement ratio, while the cracking stress can also be increased by reducing the stud spacing. It can be inferred that for the generally thinner UHPC layer, improving the reinforcement ratio is an effective way for crack prevention.

Q. H. Zhang proposed a new type of composite beam named fabricated UHPC waffle-type composite beam^[54]. The study took a typical 3-span continuous beam bridge as the research object. The research results show that the UHPC waffle plate can effectively reduce the weight of the bridge deck and increase strength. The application can be extended to the hogging moment region of the general steel-concrete composite structure.

Y. M. Liu studied the lateral fatigue behavior of the steel-UHPC bridge decks^[55]. The research results show that the degradation of the mechanical properties of the composite structure accelerates the accumulation of the fatigue details of the orthotropic steel decks (OSD). The degradation of the mechanical properties must be considered in the fatigue strength evaluation.

1.2.3 Research progress in shear connectors

Newmark et al. ^[56] first carried out research on stud connectors, and proved through experiments that stud connector is a kind of reliable composite structure connector. The research also made a conclusion that the shear strength of the shear connector should be taken from the nonlinearity stage.

Viest ^[57] carried out push-out tests of stud connectors and studied the stress performance of stud connectors with different dimension. The results show that there are three failure modes for the push-out test: failure of the stud connector at the root, concrete cracking, and simultaneous destruction of stud connector and concrete. In addition, it is considered that the load corresponding to a residual slip of 0.76 mm is a critical load for the stud connector. The calculation formula of the stud connector's shear strength is also derived.

Ollgaard et al. ^[58] conducted 48 push-out tests of stud connectors and studied the influence of ordinary concrete and lightweight concrete on their shear resistance and proposed a simplified calculation formula for the shear strength of the stud connector. The main variables considered are the stud diameter, the strength of the concrete and the modulus of elasticity. Based on the test data, the shear-slip curves under continuous loading and repeated loading are obtained.

Oehlers ^{[14][15]} studied the results of 116 stud connector by push-out tests. The research proposed that the elastoplastic boundary of the stud connector is near half of the shear strength. The research derives the calculation formula for the shear stiffness, the ultimate slip of the elastoplastic boundary point, and the slip corresponding to the shear strength of the stud connector.

An et al. ^[59] focused their research on the mechanical properties of stud connector embedded in ordinary concrete or high-strength concrete, and obtained the mechanical properties of stud connectors by conducting experimental studies. The results show that the compressive strength of the concrete is the main factor affecting the shear strength of stud connectors, and the stud connectors show good ductility in ordinary concrete. When ordinary concrete is used, the ordinary steel bars near the stud connector have influence on the shear resistance of the stud connectors, while this effect becomes smaller when high-strength concrete is used.

Wang ^[60] proposed that the design stiffness of the stud connector should take the secant stiffness corresponding to the slip of 0.8 mm when studying the deflection of

composite beams with partial shear connection

Kim et al. ^[61] fabricated different push-out specimens by placing the stud connector horizontally and vertically, and studied their stress performance in different pouring methods. The research also proposed the formula for calculating the shear strength of the stud connector.

Shim et al. ^[62] used large-diameter stud connector connectors with diameters of 25mm, 27mm, and 30mm as the research object, and carried out a push-out test study. The ultimate slip of the stud connector is greater than 6mm, which meets the requirements of European standard. Based on the experimental data, a three-fold load-slip curve was recommended for large-diameter stud connector. The research also proposed that the calculation formula for shear stiffness proposed by Oehlers et al. is too conservative for large-diameter stud connector.

Pallares et al. ^[63] collected 391 test data of stud connectors under different loading methods through extensive literature research. The calculation formula of the shear strength of stud connectors proposed in the papers were compared and analyzed.

Xue et al. ^[64] studied the mechanical behavior of stud connector when group studs are arranged. The research shows that the bearing capacity of single stud is 10% higher than that of group stud, and the ultimate slip of single stud is 19% larger than that of group stud. In addition, the initial shear stiffness of a stud group is smaller than that of single stud. Based on the test results, a load-slip curve suitable for group stud is proposed.

Zhai et al. ^[65] studied the failure mode, shear stiffness, ductility and energy dissipation capacity of stud connector under monotonic and hysteretic loading. The test results show that as the stud diameter increases, the shear resistance, stiffness and slip of the stud connector increase significantly. Compared with monotonic load, the stud connector under repeated load exhibits lower shear resistance and smaller slip. In addition, empirical formulas for the shear strength and stiffness of stud connector under cyclic loading were put forward.

Wang et al. ^[66] conducted 6 single studs and 18 group studs push-out specimens. The research studied the influence of casting method and material strength on different parameters. The test results show that the group stud effect of ultra-high performance concrete (UHPC) specimens is not obvious. The ultimate strength of precast UHPC slab with group stud is 10% higher than that of ordinary strength concrete precast slabs. The interface slip of UHPC specimens is 17% lower than that of ordinary strength concrete

precast slabs.

Kumar et al. [67] studied the influence of steel bars on the mechanical properties of stud connectors by changing the number and position of steel bars in concrete. The results showed that with the increase of the reinforcement ratio in the concrete block, the shear stiffness, strength and ductility of the stud connector all increase. The distance between the root of the stud connector and the first layer of rebar is inversely proportional to the strength and stiffness, while is directly proportional to the ductility.

1.2.4 State of partial shear connection

Compared with steel structures and prestressed reinforced concrete structures, steel-concrete composite structure has merits in concrete compression and steel tension in sagging moment regions. However, steel compression and concrete tension occurs in the hogging moment regions of a continuous composite girder resulting steel buckling and concrete cracks. In order to improve the mechanical properties of hogging moment regions in steel-concrete composite structure, different methods have been proposed by scholars. From a structural view, applying prestress [68]-[71] or increasing reinforcement ratio [72][73] can effectively reduce tensile stress in concrete slab. From the aspect of materials, carbon nanotube concrete [74][75], reactive powder concrete [76] or minor expansion fiber concrete [77] contributes to improve the mechanical properties of concrete in hogging moment regions. In terms of construction methods, post-combined technology [78] or attaching ultra-high-performance fiber reinforced concrete (UHPFRC) [79] and Fiber Reinforced Plastic (FRP) layer [80][81] can improve the crack resistance of the structure. In this research, technology of partial shear connection and double composite action will be the focus.

Meanwhile, a low level of composite action achieved by reducing connector number or adopting connector with an initial lower stiffness could also make a reduction of stresses on the concrete slab, which will effectively relieve the cracking problem in the hogging moment region and is convenient to construct. Besides, the bending capacity, global stiffness and deflection of the girder can be possibly maintained with small reductions [82]. In fact, RSS configuration could be one of the most efficient and economical ways of ameliorating the cracking situation in the hogging moment region.

For the method of reducing connector number, Wright showed a nonlinear

connection behavior through full-scale composite girders ^[83]. Molenstra presented the steel-concrete interlayer slip could be remarkably influenced by the partial shear connection ^[84]. Loh revealed an unchanged load-carrying capacity of composite girders with lower connector stiffness ^{[18][19]}.

1.3 Objectives

Based on the current state of the knowledge as presented in the previous sub-chapter, we have identified the following problems and knowledge gaps in the structural performance on continuous composite bridges with partial shear connection:

(1) According to current experimental research, it is known that using RSS connector can effectively reduce the shear stiffness of the stud connector. However, there is no quantitative indication of the effect of RSS connector in the overall structural performance of the bridge, and, in addition, there is a lack of calculation and design criteria for this type of connector.

(2) The practical methodology of partial shear connection mainly includes changing the longitudinal spacing of connectors and using RSS connectors in the negative bending moment region. At present, the research on the composite bridges with partial shear connection mainly focuses on changing the longitudinal spacing of connectors. The research on using RSS connectors is mostly limited to the shear performance characterization by push-out tests. The experimental and theoretical research on composite girders using RSS connectors has not yet matured.

(3) Both changing the longitudinal spacing of connectors in the negative bending moment region and using RSS connectors can reduce the degree of connection between the steel-concrete interlayer in the composite beam. However, there is no research comparing the effectiveness of the two partial shear connection methods, while the parameters used in the implementation of the two methods lack a structural performance-based optimization.

(4) Most of the existing experimental studies on partial shear connection use small scale ratios, which can comprehensively study the overall mechanical properties, but cannot deeply study the local mechanical response. Large scale ratio testing can more accurately reflect the stress conditions of actual bridges, and is more instructive for determining reliable design criteria of composite bridges with partial shear connection.

(5) Though applications of double composite actions have been reported in particular bridge practices, few particular design criteria are introduced in the design codes so far. The global mechanical behavior of composite girder with double composite action was concerned by some previous researches. However, large-scaled experimental study focused on its detailed mechanical behavior is rare.

Based on the current research status and identified knowledge gaps, this thesis aims to address the following technical issues by achieving the following objectives:

(1) To explore the shear performance and influencing factors of RSS connectors through push-out tests and to develop a non-linear finite element model to analyze the effects of rubber, material properties, and stud dimensions on the mechanical response of the RSS connectors. The obtained result will be later on used in the numerical analysis of composite bridges

(2) To investigate the effect of RSS connectors on the overall mechanical performance of steel-concrete composite girders To this end four simply supported specimens without prestressing and two large-scale continuous specimens with additional post-tensioning in the concrete slab in the hogging moment zone are designed and tested under monotonic static load. The research also compares the differences between composite girder with and without partial shear connection.

(3) To compare the effectiveness of the two most popular partial shear connection methods (less density of connectors and RSS). This study conducts model tests on four composite beams with different partial shear connection methods. Nonlinear finite element models and parameter analysis are conducted to compare the effectiveness of changing the longitudinal spacing of connectors and using RSS connectors. The key parameters in the design process of partial shear connection are also optimized.

(4) To develop rational design criteria of the additional concrete slab thickness in the bottom flange of the hogging moment zone in a double composite section. An experimental study on a large scaled composite girder was conducted for detailed mechanical investigation on double composite action, and a parametric study was executed as well for.

(5) To analyze the performance of semi-continuous composite bridges as a solution to solve the problems appearing in the intermediate supports of continuous composite bridges

1.4 Structure of the thesis

The present thesis is sub-divided in 7 chapters and submitted as a compendium of papers. In this sense, each chapter is only describing a brief summary of the main results and conclusions that are fully developed in the corresponding annexed papers.

The list of papers are as follows:

[1] Su H , Su Q , Xu C , et al. Shear performance and dimension rationalization study on the rubber sleeved stud connector in continuous composite girder. *Engineering Structures*, 2021, 240(OCT.30):112371. DOI: 10.1016/j.engstruct.2021.112371

[2] Su H , Su Q , Casas JR , et al. Influence mechanism of Steel-concrete interlayer partial shear connections on mechanical properties of composite girders. *Structures*, 2022, 46: 503–520. DOI: 10.1016/j.istruc.2022.10.082

[3] Tang J , Su Q , Su H , Casas JR ,et al. Experimental and Numerical Study on the Mechanical Behavior of Prestressed Continuous Composite I-Girder Bridges with Partial Connection. *Journal of Bridge Engineering*, 2023, 28: 1084-0702. DOI: 10.1061/JBENF2.BEENG-5955

[4] Su H , Su Q , Xu C , Casas JR , et al. Mechanical performance based rationalization research on steel-concrete double composite action. *Journal of Constructional Steel Research*, 2022, 197:107492. DOI: 10.1016/j.jcsr.2022.107492

[5] Su H , Su Q , Casas JR, et al. Application of Partial Shear Connection in Steel–Concrete Semi-Continuous Composite Girder Bridges. *Structural Engineering International*, 2022, 32: 411-420. DOI: 10.1080/10168664.2022.2048436

[6] Su H, Su Q, Casas JR, et al. Structural performance and on-site monitoring of steel-concrete composite bridge with link slab. *Structure and Infrastructure Engineering*. Submitted.

In the first chapter, the present research's work frame is presented in order to inform the reader of its significance and importance in the present-day research environment. Following up, the main problematic that this thesis tackles is explained and the methodologies to perform such are summarized in concise research objectives. Finally, the structure of the thesis is elucidated.

The second chapter presents the work developed in the characterization of RSS connectors (objective 1) and introduces paper number 1.

The third chapter presents the work developed to study the effect of RSS connectors on the overall mechanical performance of steel-concrete composite girders

(objectives 2 and 3) and introduces papers number 2 and 3.

In chapter 4 the double composite action is analyzed (objective 4), introducing paper number 4.

In chapter 5, the solution of semi-continuous composite bridges with simply-supported spans connected by a link slab and removing the connectors in a large area close to the support is proposed and the performance monitored during the construction stage (objective 5). This is fully developed in papers number 5 and 6.

Chapter 6 contains the full version of the published papers listed above and, finally, in chapter 7 the conclusions and future research are outlined.

Chapter 2 Shear Performance and Dimension Rationalization

Study on the Rubber Sleeved Stud Connector

A low level of composite action achieved by reducing connector number or adopting connector with an initial lower stiffness could make a reduction of stresses on the concrete slab, which will effectively relieve the cracking problem in the hogging moment region and is convenient to construct. Besides, the bending capacity, global stiffness and deflection of the girder can be possibly maintained with small reductions [14][15]. In fact, RSS configuration could be one of the most efficient and economical ways of ameliorating the cracking situation in the hogging moment region.

However, the specific mechanical effects of the rubber dimension and modulus on the connector performance have not been understood, which hinders the application in practice. To this end, 15 push-out tests on studs wrapped with rubber sleeves were conducted for the investigation. And a push-out parametric analysis with damage plasticity models was executed for dimension rationalization.

The detailed study is presented in Chapter 6.1. The following conclusions could be drawn from the study:

(1) The ultimate fracture at the stud root could be observed in every push-out test. And the shank bending deformation of RSS was obvious at the ultimate status. Meanwhile, the local concrete crush around stud root was observed in common, of which the difference between the OHS and RSS was not significant.

(2) Wrapping rubber sleeve around the stud shank near stud root could enhance the slip capacity and reduce the stiffness of the connector in the push-out tests, while it could hardly affect the shear strength of the connector.

(3) In terms of the effect on stud stiffness reduction, the rational rubber sleeve thickness and height were 4mm and 50mm for a 22mm-diameter and 220mm-high stud.

(4) The parametric analysis results showed that the RSS stiffness began to decrease obviously when the elastic modulus of the wrapped material was 10% lower than that of concrete.

(5) The parametric analysis on a continuous composite girder with RSS

connectors configured in the hogging moment region showed a maximum of 39% concrete slab stress reduction and a 13% increase of steel stress on the top flange.

The complete results are presented in Chapter 6.1.

Chapter 3 Structural performance of Composite Girder with Partial Shear Connection

This part of the research work is divided in 2 main parts: the study of simply supported composite girders with partial shear connection achieved either by increasing the separation between connectors or using RSS modelling the hogging zone of a continuous composite beam, and the structural performance of Prestressed Continuous Composite I-Girder Bridges with partial shear connection

3.1 Structural performance of partial shear connection

Decline of composite action in hogging moment region could decrease the concrete slab tensile stress at this region in a girder. Normal continuous composite bridges adopt Full Shear Connection (FSC) due to convenient construction and clear mechanical properties. However, large tensile stress in concrete will be generated in hogging moment regions in continuous girders. In response to this issue, Partial Shear Connection (PSC) helps to decrease the interaction extent between concrete slab and steel girder in hogging moment regions, simultaneously maintaining the ultimate bearing capacity and overall stiffness of the structure ^{[86][87]}.

Although many push-out tests revealing the low stiffness of RSS connector have been conducted, few studies concern its detailed influence on girder specimens. In addition, effectiveness of the two PSC methods has not been fully compared in the existing literature. Therefore, this subchapter studies the detailed influence of RSS connector and enlarging connector distance on steel-composite girder in hogging moment regions by experiments and analysis works. 4 simply supported composite girders were tested simulating the hogging zone of a continuous beam for detailed mechanical investigation on PSC action. 6 push-out specimens were tested to present the mechanical properties of RSS connector in girder tests as well as to determine the shear stiffness for finite element modeling. A parametric study was executed as well for rational design criteria of PSC action. The study could help to establish design methods and evaluation for PSC action.

The detailed experimental set up and numerical simulations are presented in

Chapter 6.2. The following conclusions could be drawn from the study:

(1) According to the girder tests under negative bending, the failure modes were similar. But configuring the RSS connectors with a shear stiffness only 8.1% of corresponding OHS connectors or setting a 2000mm OHS spacing could respectively cause 17% and 11% reductions of the load-carrying capacity. On the other hand, the RSS connector could also lead to a 12% decrease of bending stiffness and relieve the concrete crack development, while increasing stud spacing could hardly change the bending stiffness or improve the cracking resistance.

(2) Based on the parametric analysis on the effect of prestressing the concrete slab, RSS connector had a larger influence on the prestress distribution between concrete slab and steel girder than increasing the stud distance. RSS connector could contribute to a maximum pre-stress increase in concrete slab by 19.4% and decline in steel girder by 92.6%, while the figures were only 8% and 26.9% for increasing the stud distance.

(3) Based on the parametric analysis on girder under negative bending, RSS connector with shear stiffness lower than 20% of the OHS connector could efficiently decrease the concrete tensile stress, while the load-carrying capacity could have a maximum decline of only 12.3%. On the other hand, when setting OHS connectors with a 2000mm spacing, the concrete and steel stress could increase by 145.2% and 584.8%. Besides, avoiding stud position at region with large bending moment could decrease the concrete stress by 14.4%.

(4) According to the analytical analysis, the stress variation in composite girder became larger when the stud stiffness was less than 20% of the origin stiffness. The concrete stress was exponentially related to the stud stiffness, while the exponential was supposed to be $5/3$.

The complete results are presented in Chapter 6.2.

3.2 Prestressed Continuous Composite I-Girder Bridges with Partial connection

In the negative moment region of medium and long-span continuous composite girders, concrete cracking may facilitate corrosion of connectors and reinforcing steel and have an adverse impact on structures' service and durability performance. Prestressing the concrete slab is the most commonly used and effective method to avoid

cracking.

However, the prestressing efficiency in the conventional prestressed continuous composite girder could be relatively low due to the prestress transmission from the concrete slab to the steel girder. Reducing the steel-concrete interaction can decrease the transmission. To date, most of the studies regarding the partial shear interaction of composite structures considering this problem are based on beams used in building structures. To elucidate the effect of RSS on the overall stiffness and capacity of composite girder bridges, experimental evidences and numerical simulations are needed.

In this section, Partial Connection-Prestressing (PCP) method was adopted. The mechanical behavior of prestressed continuous composite I-girder with RSSs in the negative moment region were studied through the static test of two two-span specimens with large scale ratio of 1:3. A numerical model is also developed and calibrated with the results from the tests.

The tests and numerical analysis are fully presented in Chapter 6.3. The following conclusions could be drawn from the study:

(1) PCP (Partial connecting and prestressing) method can effectively improve the cracking resistance of continuous composite girders. Compared to the normal composite girder specimen (GCN), the cracking load of the partial connection-prestressing girder specimen (GCRP) was 3.1 times higher. The crack width of specimen GCRP was no more than 81.3 % of that of specimen GCN at same load level.

(2) Specimen GCRP produced greater interfacial slip (more than 10 times) compared to the specimen GCN, but the overall stiffness of the two specimens were similar, which means that RSS has little effect on the deflection of the composite girders.

(3) The instability of steel girders occurred in both specimen when they reached limit state and the ultimate load capacity of them were close. The partial shear connection provides a clear increase in the cracking moment without affecting the load capacity.

(4) The numerical results showed that compared to conventional composite girders, the cracking load increased by 11.8% and 157.0 % when applying RSS and prestress alone, respectively, and by 234.3% when applying RSS and prestressing at the same time.

(5) In the case of full connection, the shear stiffness of the stud connectors does not have an important influence on the amount of prestressing transferred to the

concrete slab. It keeps constant at around 75 % for relative stiffness between 1 and 100.

The complete results are presented in Chapter 6.3.

Chapter 4 Mechanical Performance Based Rationalization

Research on Steel-concrete Double Composite Action

Casting an extra concrete bottom layer to a steel-concrete composite box girder in a hogging moment region can increase sectional stiffness and prevent steel buckling. However, a lower sectional neutral axis may not be favorable to concrete slab cracking and steel flange stress control. To this end, a double composite girder segment was proposed and investigated. Particularly, a static loading test on a large-scaled two-span continuous girder specimen with the double composite action in hogging moment region was conducted for mechanical investigation. Meanwhile, parametric analysis was carried out as well for a rational design scheme of the double composite section.

The detailed experimental set-up and parametric analysis are presented in Chapter 6.4. The following conclusions could be drawn from the study:

(1) According to the test observations, the concrete bottom slab helps to restrain lateral deformation of steel web and steel bottom flange. It can effectively improve the anti-buckling ability of the continuous girder.

(2) Based on the parametric analysis, the additional concrete slab helps to increase the cracking load and ultimate strength by 12% and 4%. However, the additional gravity load can accelerate the crack development. Besides, the optimal concrete slab thickness was found around 15 % of the height of the steel girder. The ultimate strength decreases afterwards mainly due to a continuing downward translation of the sectional neutral axis. In addition, the concrete bottom slab can also replace the function of the lower longitudinal stiffening ribs.

(3) Based on the parametric analysis, the steel web thickness can be saved 16.7%, while the steel bottom flange thickness only needs to meet the constructing requirement after using the double composite action. Besides, the box section could contribute to a 24.4% and 3.2% stress decline respectively in steel top flange and concrete slab compared with tub section.

(4) According to the concrete bottom slab optimization, the cracking moment was increasing to a maximum and after that decreasing with the increase of the concrete bottom slab thickness, while the steel bottom flange stress can be decreased up to 20%.

Taking into account both the cracking moment and stress state at the service stage, the optimal concrete bottom slab thickness was 15% of steel girder height. This is also in agreement with the optimal thickness obtained according to conclusion 2.

(5) Due to its advantage of steel flange stress reduction and buckling prevention, the novel double composite system is particular economical for long-span continuous composite bridge which bears high stress level in the hogging moment region. Furthermore, the double composite action can be applied together with high strength steel. Since the local buckling is prevented, the high strength of the steel material can be better utilized.

The complete results are presented in Chapter 6.4.

Chapter 5 Application of Partial Shear Connection in Steel-concrete Semi-continuous Composite Girder Bridge

In the hogging moment regions of steel-concrete composite continuous girder bridges, detrimental condition appears that concrete slab bears tensile stress and steel girder bears compressive stress. Decreasing the shear connection in the hogging moment regions helps to improve the mechanical performance for steel-concrete continuous composite girder bridges. The connection of the spans by only the upper concrete slab (link slab), resulting in the so-called semi-continuous solution can also help to release the tensile stresses in the concrete due to the composite action, but, in the other hand may increase the internal forces in the link slab. In this section, analytical models for the calculation of composite girder considering PSC action and link-slab are discussed. A project case of Qiwu bridge in Jiangxi Province using partial shear connection action was introduced. Nonlinear finite element model of Qiwu Bridge was established through ABAQUS to simulate and predict the mechanical properties and structural performance. Qiwu Bridge is also monitored by vibrating strain meters to experimentally check the results from the numerical model to study the mechanical behavior of this structural solution both during the construction and operating stages. The study supplements the numerical data of PSC component and to shed further light into practical application of PSC in bridge engineering.

The detailed study is presented in Chapters 6.5 and 6.6. The following conclusions could be drawn from the study:

(1) The midspan deflection of composite girder drops linearly with the increase of the interaction degree, and the deflection increase rate decreases with the span-length. The numerical result matches up with the Nie's model, which is recommended for simply-supported and semi-continuous bridge design.

(2) Arranging PSC region can effectively reduce the crack region. Compared with bridge without PSC region, crack region decreases from 1.6m (when the length of the PSC region is 0m) to 0.5m (when the length of the PSC region is 5.6m) and 0.3m (when the length of the PSC region is 10m) under dead load. The decline becomes even larger under load combination of dead load and vehicle load. In addition, while the crack region tends to be wider and continuous with the increase of the load, PSC action helps

to disperse the concentrated stress in the zone.

(3) The shear stiffness mutation can magnificently increase the stress level at the edge of PSC region in concrete slab and made it easier to crack. Actions of increasing the reinforcement ratio or adopting high-performance concrete at this position is essential for crack control.

(4) Except for the hogging moment region, PSC action had limit influence on the whole structure. With the length of PSC region increasing from 0 to 10m, the growth rate of deflection and steel bottom flange stress at midspan was respectively below 4% and 2%. Meanwhile, the steel top flange stress at mid-support declined rapidly with the increase of the length of PSC region, which also hints the stress reduction in concrete slab around the mid-support.

(5) Integral temperature reduction and shrinkage can obviously increase the tensile stress in concrete slab with or without PSC region, and gradient cooling has a larger impact on structures without PSC region. The influence of concrete creep is subtle in both kinds of structures.

(6) Influence of the link slab on the stress variation of the whole structure is within 15%, which infers that the link slab can improve the driving comfort with limited influence on the mechanical behaviour.

(7) From the monitoring results, it is observed that during construction, the strain of the steel beam at the mid-span section was obviously larger than at the shear stiffness mutation section and the support section as will be during service. There is a daily strain fluctuation both in the concrete slab and the steel beam because of the temperature variation. The fluctuation in the concrete slab is relatively larger than that in the steel beam.

The complete results are presented in Chapters 6.5 and 6.6

Chapter 6 Published papers

6.1 Engineering Structures 2021

Su H, Su Q, Xu C, et al. Shear performance and dimension rationalization study on the rubber sleeved stud connector in continuous composite girder. Engineering Structures, 2021, 240(OCT.30):112371. DOI: 10.1016/j.engstruct.2021.112371

Shear performance and dimension rationalization study on the rubber sleeved stud connector in continuous composite girder

Hang Su ^a, Qingtian Su ^{a,b}, Chen Xu ^{a*}, Xieli Zhang ^a, Dongyang Lei ^a

^a*Department of Bridge Engineering, Tongji University, Shanghai, China 200092*

^b*Shanghai Engineering Research Center of High Performance Composite Bridge, Shanghai, China 200092*

Abstract

Wrapping rubber sleeve around a stud shank near the root makes a low level of shear connection between the steel girder and concrete slab in a composite girder. It helps to reduce the concrete tensile stress and steel compressive stress in the hogging moment region. However, the specific mechanical effects of the rubber dimension and modulus on the connector performance have not been understood, which hinders the application in practice. To this end, 15 push-out tests on studs wrapped with rubber sleeves were conducted for the investigation. And a push-out parametric analysis with damage plasticity models was executed for dimension rationalization. The test results showed an obviously lower stiffness and larger bending deformation of rubber-sleeved stud as compared with a normal stud, while the strength varied little. The analysis results showed that the efficient rubber thickness and length for a 22mm-diameter and 220mm-high stud could be 4mm and 50mm in terms of the stiffness reduction extent. It also showed an obvious stiffness reduction occurred when the wrapping material modulus was 10% lower than concrete. Furthermore, the connector stiffness effect on the stress distribution along with a continuous composite girder was analyzed and quantified, showing a 39% reduction of concrete slab stress in the hogging moment region and a 13% increase of steel stress on the top flange.

Keywords: Steel-concrete composite structure; Push-out test; Numerical study; Stud connector; Rubber sleeve; Composite mechanism

Nomenclature

OHS: Ordinary Headed Stud

RSS: Rubber-Sleeved Stud

LVDT: Linear Variable Differential Transformer

H_r: Rubber sleeve height

T_r : Rubber sleeve thickness
 d_s : Stud diameter
 V_u : Shear strength of the push-out test specimen
 K_{s1}, K_{s2} : shear stiffness corresponding to 30%, 50% shear strength
 S_p : slip response corresponded to the maximum shear force
 E_c : Elasticity modulus of concrete
 α_t, α_c : Regulation coefficient of the descending part of the concrete
 d_c, d_t : Compressive and tensile damage factor of the concrete
 $f_{t,r}, f_{c,r}$: Ultimate tensile and compressive strength of the concrete
 $\varepsilon_{t,r}, \varepsilon_{c,r}$: Strain corresponding to the ultimate tensile and compressive strength of the concrete
 E_0 : Initial elasticity modulus of concrete
 W : Strain energy density
 C_{10}, C_{01} : Parameter describe the shear behaviour of the rubber sleeve
 I_1, I_2 : The first and second invariant of the strain tensor
 σ_1 : Principal stress of the rubber sleeve
 λ_1 : Principal elongation ratio of the rubber sleeve
 ε_1 : Strain of the rubber sleeve in tensile direction
 δ : Slip between the concrete beam and the steel beam
 P : Force between the concrete beam and the steel beam
 l : Length of the rigid arm
 E_{ra} : Elasticity modulus of the rigid arm
 I_{ra} : Inertia moment of the rigid arm

Introduction

The steel-concrete composite structure has been widely applied in the simply supported bridges since the merits of concrete compressive strength and steel tensile strength can be efficiently utilized. However, there is an inverse stress situation in the hogging moment region of a continuous composite girder, where the concrete tensile cracks and steel buckling are both likely to happen. Increasing reinforcement ratio [1], introducing pre-stress effect [2-5], configuring a double composite section [6-8] help to restrain the tensile concrete cracks and prevent the steel from buckling. Moreover, the high performance concrete with good tensile performance [9-11] and FRP bonding material [12-13] can be good choices as well for the concrete crack resistance and reinforcement.

Meanwhile, a low level of composite action achieved by reducing connector number or adopting connector with an initial lower stiffness could also make a reduction of stresses on the concrete slab, which will effectively relieve the cracking problem in the hogging moment region and is convenient to construct. Besides, the bending capacity, global stiffness and deflection of the girder can be possibly maintained with small reductions [14-16]. In fact, RSS configuration could be one of the most efficient and economical ways of ameliorating the cracking situation in the hogging moment region.

For the method of reducing connector number, Wright showed a nonlinear connection behavior through full-scale composite girders [17]. Molenstra presented the steel-concrete interlayer slip could be remarkably influenced by the partial shear connection [18]. Loh revealed an unchanged load-carrying capacity of composite girders with lower connector stiffness [19-20].

As for adopting connector with an initial lower stiffness, Hiragi showed a more flexible Ordinary Headed Stud (OHS) wrapped with urethane at the root in the conducted tests [21]. Kitagawa proposed a kind of stud wrapping with high-intensity resin and revealed its stiffness hysteresis character [22]. Nie showed a study on the uplift-restricted and slip-permitted connection, which included screw-type, sliding-type and T-shape connectors [23]. Abe [24] verified the safety of T-shaped and H-shaped shear connectors wrapped with flexible foams through fatigue tests, and applied them to the hogging moment regions in continuous composite girder bridges. Xu conducted 18 push-out tests on the Rubber-Sleeved Stud (RSS) connectors and showed the shear strength of RSS was similar to the OHS, whereas the RSS stiffness decreased remarkably [25].

The RSS is a kind of screw-type connectors consisting of an OHS connector simply wrapped by rubber sleeve at the root. It is featured by its fast construction advantage. Zhuang presented that

RSS shear strength kept almost unchanged, while stiffness reduced by 36.5%. And deformation ability enhanced because of the wrapped rubber sleeves [26-27].

Though adopting RSS could be one of the most convenient ways to make a low level of composite action, the rational design of RSS connector has not been summarized in literatures. This becomes a problem that hinders the application of RSS connector in the bridge design practice. This paper aimed to study the detail stiffness and strength variations of RSS connector in bridges by push-out tests and parametric analysis. Meanwhile, the rationalization study on the dimensional size of connector was also conducted. An analysis example on a composite girder with RSS connectors in the hogging moment region was also provided, which showed the effect of RSS on the stress and deflection distributions along with the girder. In general, the research outcome would be helpful for establishing reliable evaluation and design methods of RSS connector. And this is an important step for the rational practical application.

Experimental method

Specimen design

Five groups of push-out test specimens were fabricated as listed in Table 1, and each group contained three identical specimens. The specimen groups were differentiated by the height and thickness of the rubber sleeved at stud root. In particular, the rubber sleeve height included 50mm and 100mm, and the thickness included 2mm, 4mm and 6mm. The rubber sleeves were manually bounded around the stud shanks near stud roots by the steel wire circles.

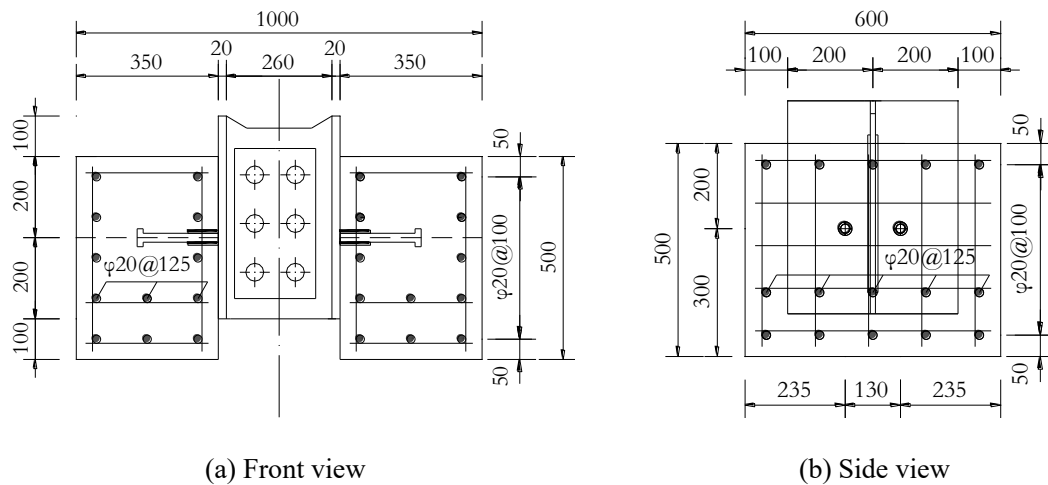
Fig.1 shows the specimen and the reinforcement layout. The steel beam was assembled by two T-shape steel components, of which the flange and web thicknesses were 20mm and 12mm. Two studs were welded on each of the steel flanges and embedded in the reinforced concrete slab, which means each push-out test included four studs in all. The stud spacing was 130 mm, and the stud diameter and height were 22mm and 220mm respectively. Reinforcement in the concrete blocks adopted HRB400, of which the diameter was 20mm. Thickness of the protective layer of reinforcement was 50mm.

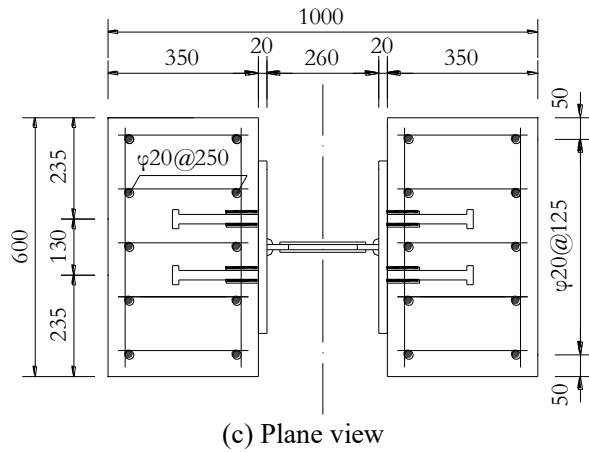
The concrete was cast in beam direction, before which the oil was brushed on the steel flange surfaces to prevent binding between steel and concrete. The fabrication process is shown in Fig.2.

Table 1

Groups of test specimens.

Specimen group	Stud diameter /mm	Rubber height /mm	Rubber thickness /mm	Specimen amount
OHS-0-0	22	0	0	3
RSS-4-50	22	50	4	3
RSS-2-100	22	100	2	3
RSS-4-100	22	100	4	3
RSS-6-100	22	100	6	3

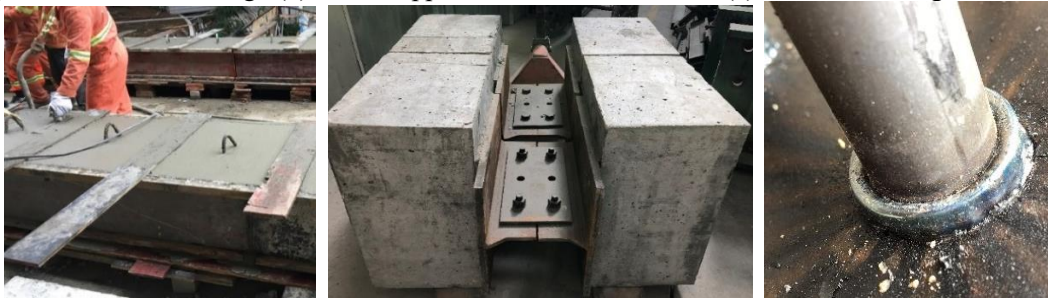




(c) Plane view
Fig.1 Configurations of test specimen (mm)



(a) steel beam assemblage (b) stud wrapped with rubber sleeves (c) rebar assemblage



(d) Casting concrete (e) Fabricated specimen (e) Welded collar

Fig.2 Fabrication process of test specimen

Material properties

The concrete cubic specimens with a 150mm edge length were fabricated and tested at the 28th day after casting. The averaged cubic compressive strength was 52.0 MPa. Three ordinary stud connectors were reserved and fabricated (as shown in Fig.3) for tensile tests. The averaged yield strength and the ultimate tensile strength were 457 MPa and 493 MPa respectively. In addition, Table 2 lists the material property of NR45 natural rubber for wrapping around the stud roots.

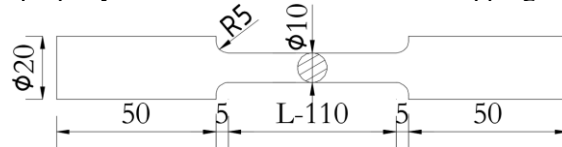


Fig.3 Configurations of stud material test specimen (mm)

Table 2
 Material property of NR45 natural rubber

Hardness	Tensile strength (MPa)	Elongation (%)	Brittleness temperature (°C)
45	≥ 18	≥ 400	-40

Test setup and loading programs

Fig. 4 shows the push-out test setup, in which an electrohydraulic servo loading machine was utilized. A spherical bearing was set on the specimen top, and the sand pieces were arranged on the bottom of the concrete to ensure the uniform force distributions on both sides of specimen. All the specimens were monotonically loaded at a rate of 2kN/s until 60% of the estimated bearing capacity. Afterwards, the load was controlled by displacement. The loading speed was 0.01mm/s.

Fig. 5 shows the measurement setup. Four linear variable differential transformers (LVDTs) were mounted near the position of studs to measure the interlayer slip between the concrete and steel.

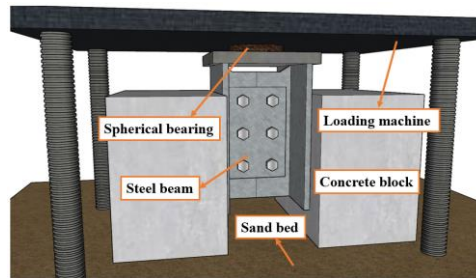


Fig. 4 Test setup

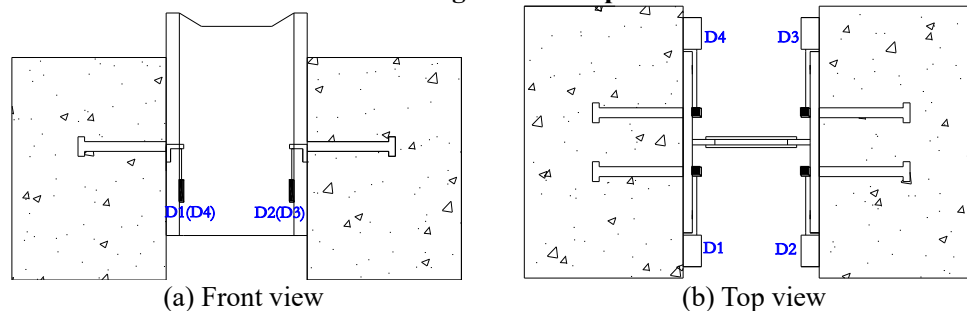


Fig. 5 measuring setup

Experimental results

Failure modes

Fig. 6 shows sectional fracture surfaces of stud root at steel and concrete sides in specimens with OHS and RSS. The local concrete crushes around the stud roots could be generally observed as well.

Fig. 7 shows the typical ultimate deformations of OHS and RSS connectors. The rubber sleeve on the compression side of the stud was greatly deformed, while that on the tension side was separated from the stud. Moreover, the deformed length along the RSS shank was much longer than OHS connector. In this sense, the failure mode of OHS was dominated by shear failure at the stud root, while the RSS had an extra integral bending deformation.

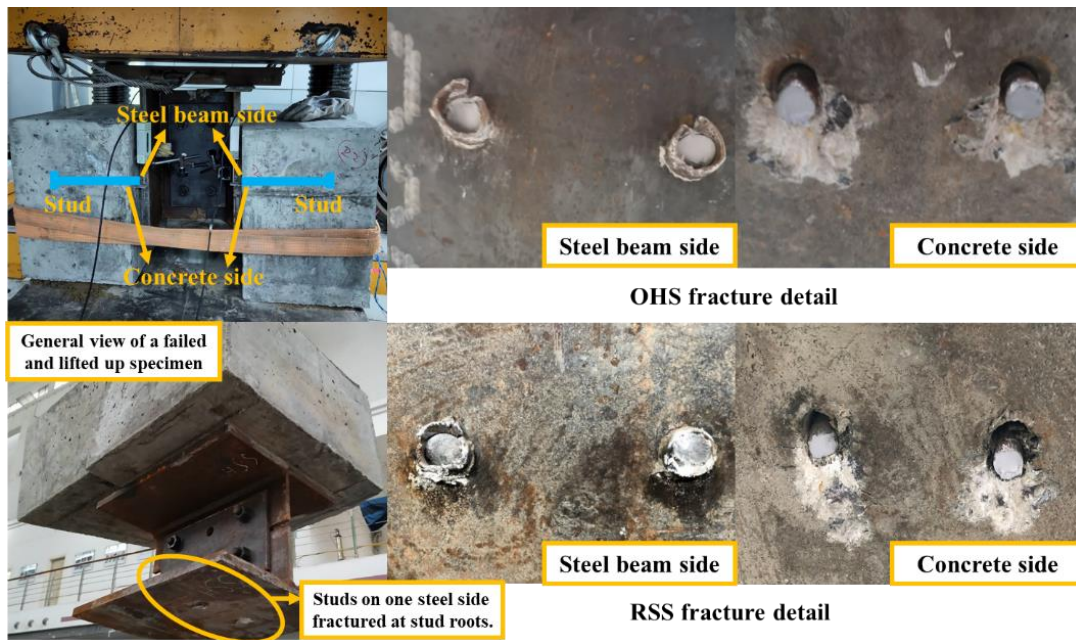


Fig. 6 Failure modes

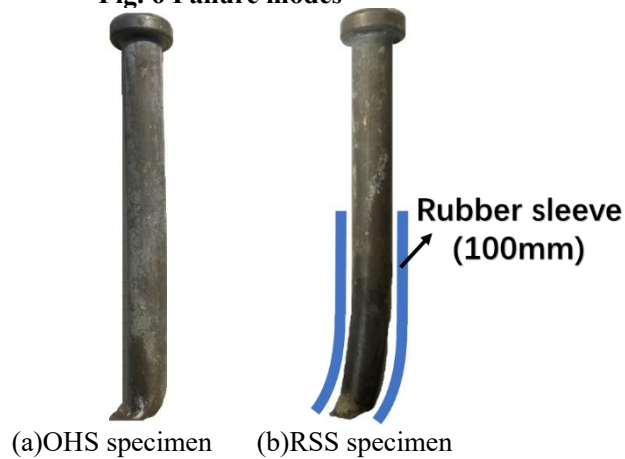


Fig. 7 Failure modes of studs

Load-slip curves and discussion

Fig. 8 shows the load-slip curves of each specimen group. The horizontal axis refers to the average slip of the four LVDTs and the vertical axis represents the averaged shear force on a single stud. The measured load-slip curves of specimens in the same group were consistent with each other in general. The observed individual shear strength deviation was mainly due to the concrete material property deviation, boundary condition error and initial geometrical imperfections in the push-out tests undertaken on specimens. Besides, wrapping the rubber sleeve around stud shank by manual hand works could be another factor to influence the shear stiffness, for example the stiffness deviation of RSS-4-100 appeared obvious. In other words, a standard rubber-wrapping method was preferred for the RSS configuration in application, or the discrepancy of stiffness should be taken into consideration.

In addition, Fig. 9 showed the average curves of all the specimen groups. The sleeve size had obvious impacts on respectively reducing the stiffness and increasing the slip capacity.

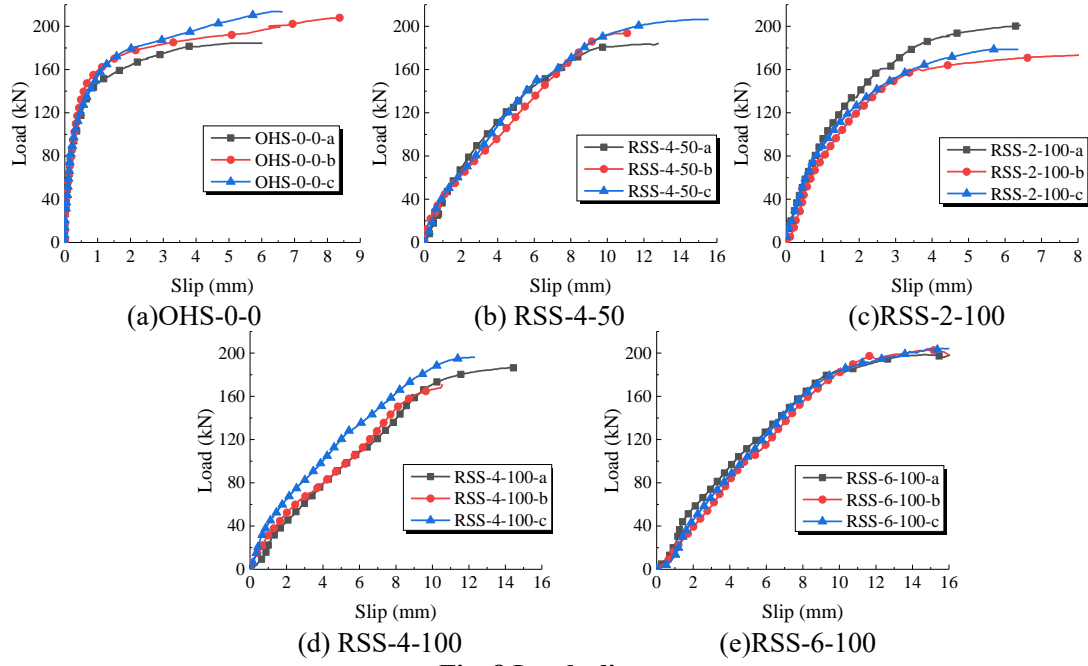


Fig. 8 Load-slip curves

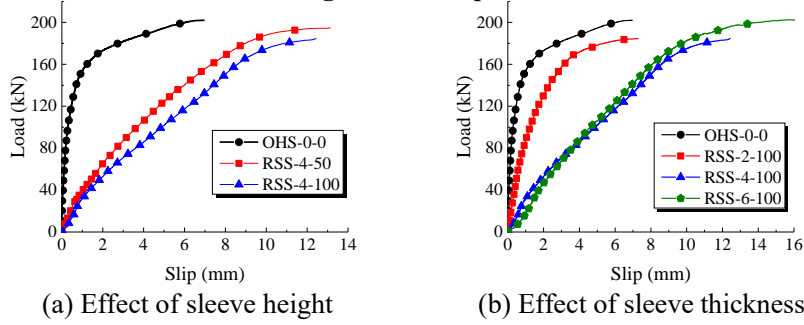


Fig. 9 Effect of RSS size on load-slip curves

Table 3 summarizes the stud shear strength V_u , shear stiffness (K_{s1} and K_{s2}), and slip capacity S_p based on Fig. 8. V_u was defined by the maximum shear force on the load-slip curve, and S_p was a slip response corresponded to the maximum shear force. K_{s1} and K_{s2} was defined as the secant modulus corresponding to 30% V_u [28] and 50% V_u [29][30].

As shown in Table 3, a lower than 10% difference of V_u among the specimens indicated that wrapping rubber sleeve could hardly affect the shear strength of the stud. However, the S_p increased with a larger thickness or height of rubber sleeve. Particularly, the S_p of RSS-2-100, RSS-4-100 and RSS-6-100 were 7.3mm, 12.5mm, and 15.3mm respectively, which were 4%, 78%, and 117% larger than that of specimen OHS-0-0. And the S_p of RSS-4-50 and RSS-4-100 were 13.2mm, 12.5mm respectively, which were 88%, 78% larger than that of specimen OHS-0-0.

Table 3
Test results and comparison

Specimen		V_u (kN)	S_p (mm)	K_{s1} (kN/mm)		K_{s2} (kN/mm)			
Group	Number								
OHS-0-0 (I)	a	184.4	6.02	417.3		343.8			
	b	208.3	Avg:202	8.45	Avg:7.03	404.2	Avg:403	337.7	Avg:332.3
	c	213.2	6.63	387.6		315.4			
RSS-4-50 (II)	a	184.3	12.81	35.4		30.6			
	b	194.1	Avg:194.9	11.27	Avg:13.21	29.5	Avg:31.8	24.2	Avg:27.3
	c	206.3	15.55	30.6		27.2			

	a	201		6.43		106.3		91.1	
RSS-2-100 (III)	b	174.6	Avg:184.7	9.14	Avg:7.31	94	Avg:102.8	74.2	Avg:85
	c	178.6		6.36		109		89.6	
	a	186.8		14.59		23.0		19.3	
RSS-4-100 (IV)	b	171.3	Avg:184.7	10.55	Avg:12.49	24.7	Avg:25.8	19.4	Avg:21.2
	c	196.1		12.33		29.8		24.8	
	a	202.6		16.75		25.9		23.4	
RSS-6-100 (V)	b	202.2	Avg:202.7	14.34	Avg:15.27	20.1	Avg:22.8	20.7	Avg:21.7
	c	203.2		14.72		22.5		21.1	
(II)/(I)			0.96		1.88		0.08		0.08
(III)/(I)			0.91		1.04		0.26		0.26
(IV)/(I)			0.91		1.78		0.06		0.06
(V)/(I)			1		2.17		0.06		0.07

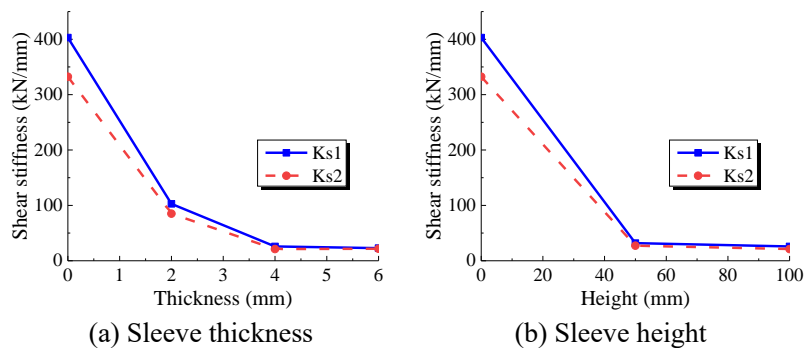


Fig. 10 Influence of sleeve size on shear stiffness

Fig. 10 shows the rubber sleeve size effect on the stud shear stiffness. The stiffness reduction resulted by the wrapped rubber sleeve was significant when the rubber thickness or height was below 2mm or 50mm. As shown in Fig.10(a), K_{s1} and K_{s2} of RSS-2-100 respectively decreased by 74.5% and 74.4% in comparison with OHS-0-0. As shown in Fig. 10(b), the K_{s1} and K_{s2} of RSS-4-50 decreased by 92.1% and 91.8% in comparison with OHS-0-0.

Fig. 11 presents the stiffness variation of specimens with RSS. $V_{0.2mm}$ refers to the stiffness at the load level corresponding to the slip of 0.2mm. It can be observed that the shear stiffness was more sensitive to sleeve thickness when T_r was less than 4mm, while the influence of sleeve height on shear stiffness was relatively smaller.

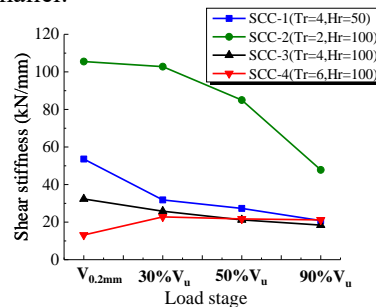


Fig. 11 Stiffness variation tendency of RSS specimens

Simulation and parametric analysis

General

Besides the tests, the push-out simulation and parametric analysis were conducted for the further mechanism understanding and rational design of RSS. Fig. 12 shows the FEM model and the boundary conditions. Only a quarter part of the push-out specimen was established according to

the symmetry condition. In particular, the model included a concrete block, a steel beam, reinforcement bars, a stud and a rubber sleeve.

Two rigid bases coupling to a reference point was established and coupled with the upper surface of the steel beam and the lower surface of the concrete block respectively. A displacement controlled load action was applied to the reference point at the upper rigid base.

The general contact algorithm was introduced to simulate the steel-concrete and stud-concrete interlayer interactions. The penalty frictional formulation was used to simulate the interaction along the tangential direction. The 'Hard' contact was used to simulate the interaction along the normal direction. Moreover, the general contact interactions were also used to constrain the concrete block with the rubber-sleeved stud, and the friction coefficient was set as 0.1^[31]. Embedded region was set to constrain the reinforcement bar with the concrete block.

Fig. 13 shows the meshed components for analysis. The concrete block, steel beam and rubber sleeve were meshed with solid element C3D8R, while the reinforcement bar was meshed with T3D2. The overall mesh size of the model was 12mm. Instance of concrete block and steel beam surrounding the stud was locally encrypted with a size of 2.5 mm to ensure the calculation accuracy.

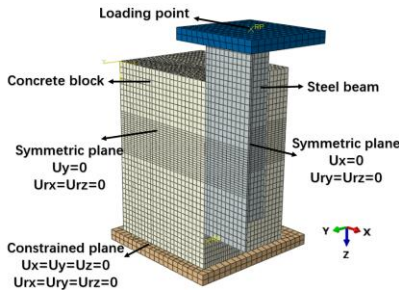


Fig. 12 The push-out model

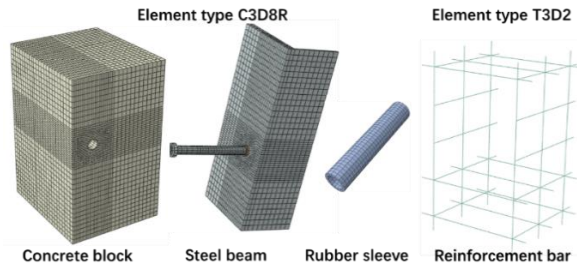


Fig. 13 Element type and mesh of the model

Material constitutions

Concrete material constitutions

The uniaxial compressive and tensile stress-strain relationships of concrete material, as shown in Fig. 14, could be determined by Eq.1~Eq.6^[32], where α_t and α_c was the regulation coefficient of the descending part. Moreover, the concrete damage plasticity model was also introduced in the analysis. The damage factor d was calculated by Eq. 7 derived from principle of energy equivalence that proposed by Sidoroff^[33].

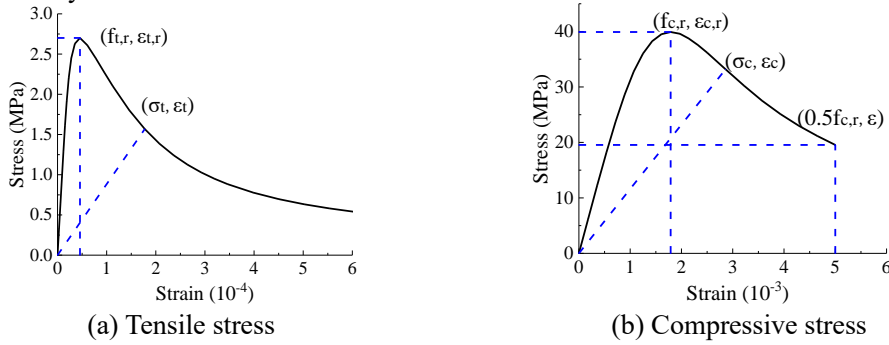


Fig. 14 The stress-strain curve of concrete

$$\sigma = (1 - d_t) E_c \varepsilon \quad \text{Eq. 1}$$

$$d_t = \begin{cases} 1 - \rho_t [1.2 - 0.2x^5] & x \leq 1 \\ 1 - \frac{\rho_t}{\alpha_t (x-1)^{1.7} + x} & x > 1 \end{cases} \quad \text{Eq. 2}$$

$$x = \frac{\varepsilon}{\varepsilon_{t,r}} \quad \rho_t = \frac{f_{t,r}}{E_c \varepsilon_{t,r}} \quad \text{Eq. 3}$$

Where

$$\sigma = (1 - d_c) E_c \varepsilon \quad \text{Eq. 4}$$

$$d_c = \begin{cases} 1 - \frac{\rho_c n}{n-1+x^n} & x \leq 1 \\ 1 - \frac{\rho_c}{\alpha_c (x-1)^2 + x} & x > 1 \end{cases} \quad \text{Eq. 5}$$

Where

$$x = \frac{\varepsilon}{\varepsilon_{c,r}}, \quad \rho_c = \frac{f_{c,r}}{E_c \varepsilon_{c,r}}, \quad n = \frac{E_c \varepsilon_{c,r}}{E_c \varepsilon_{c,r} - f_{c,r}} \quad \text{Eq. 6}$$

$$d = 1 - \sqrt{\frac{\sigma}{E_0 \varepsilon}} \quad \text{Eq. 7}$$

Steel material constitution

Fig. 15(a) shows a trilinear stress–strain curve for the stud material constitution based on the material test results. The yielding and ultimate stresses were 457MPa and 493MPa, respectively. The ultimate strain ε_{us} was 0.6%. The Young's modulus was 207GPa.

Fig. 15(b) shows a bilinear stress–strain model for the steel and reinforcement. The yield stresses of the steel and reinforcement were 400MPa and 345MPa, respectively. And the Young's modulus was 200GPa.

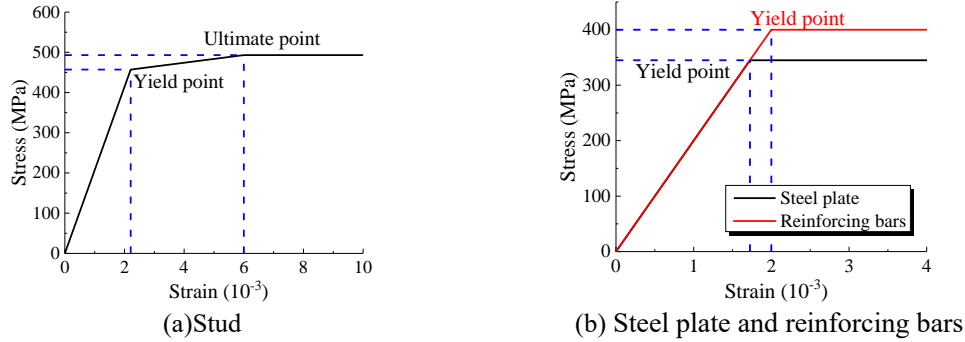


Fig. 15 Stress-strain model for steel material

Rubber material modeling

The phenomenological theory was often used to describe the constitutive relation of rubber, which assumed that rubber was a kind of incompressible material and was homogeneous in undeformed state. According to the assumptions, constitutive relation of rubber materials could be expressed by strain energy density function^[34]. The model of Mooney-Rivlin could properly describe the hyper-elastic properties of rubber materials at small strain, whose strain energy density function was expressed as Eq. 8. In the equation, W was the strain energy density, I_1 , I_2 were the first and second invariant of the strain tensor. The C_{10} and C_{01} described the shear behaviour of the rubber sleeve.

$$W = C_{10}(I_1 - 3) + C_{01}(I_2 - 3) \quad \text{Eq. 8}$$

According to the relationship between Kirchoff stress tensor and Green strain tensor, the relationship between the principal stress σ_1 and the principal elongation ratio λ_1 under uniaxial force could be obtained as Eq.9. Parameter ε_1 represented strain in tensile direction.

$$\sigma_1 = 2\left(\lambda_1 - \frac{1}{\lambda_1^2}\right)\left(\frac{\partial W}{\partial I_1} + \frac{1}{\lambda_1} \frac{\partial W}{\partial I_2}\right) \quad \text{Eq.9}$$

Where

$$\lambda_1 = 1 + \varepsilon_1 \quad \text{Eq.10}$$

Eq.11 could be deduced by substituting Eq. 8 into Eq.9. Stress value and corresponding elongation could be measured by material test. After drawing the curve with $1/\lambda_1$ as abscissa and $\sigma_1/2(\lambda_1 - \frac{1}{\lambda_1^2})$ as ordinate, intercept and slope of the curve could be obtained as C_{10} and C_{01} , which were taken as 0.0064 MPa and 0.21 according to rubber properties and trial calculations^[35-37].

$$\frac{\sigma_1}{2(\lambda_1 - \frac{1}{\lambda_1^2})} = C_{10} + \frac{1}{\lambda_1} C_{01} \quad \text{Eq.11}$$

Simulation verification

Load–slip curves

Fig. 16 presents the simulated and measured load-slip curves. And the detail simulated stiffness and strength were summarized and compared with test results in Table 4. The shear strength difference between the test and analysis results was lower than 10%, while that of shear stiffness was lower than 15% except the K_{s1} of RSS-2-100. These could be explained by the material constitution accuracies and the welding quality. Generally, the load-slip curves from the simulation matched with the curves measured in tests.

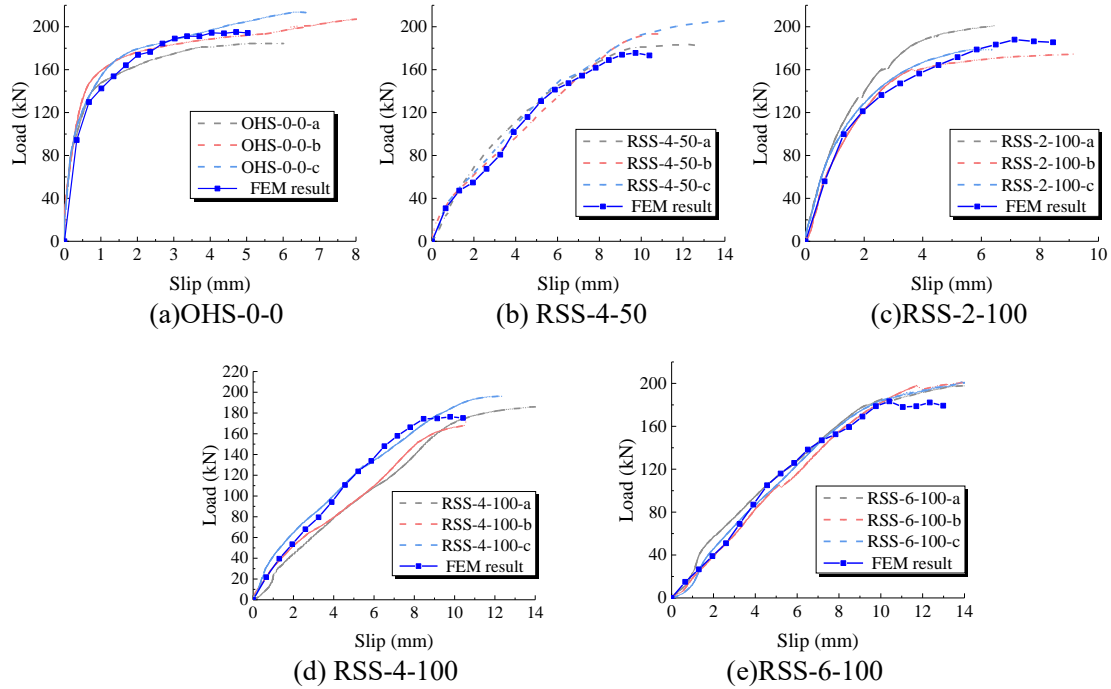


Fig. 16 Verification of load-slip curves between test result and FEM result

Table 4

Comparison between FEM result and test result

		OHS-0-0	RSS-4-50	RSS-2-100	RSS-4-100	RSS-6-100
V_u (kN)	FEM (a)	195.1	175.6	188.0	176.4	183.3
	Test (b)	202.0	194.9	184.7	184.7	202.7
	(a)/(b)	96.6%	90.1%	101.8%	95.5%	90.4%
K_{s1} (kN/mm)	FEM (a)	386.3	28.0	69.0	27.5	19.6
	Test (b)	403.0	31.8	102.8	25.8	22.8
	(a)/(b)	95.9%	88.1%	67.1%	106.6%	86.0%
K_{s2} (kN/mm)	FEM (a)	279.7	26.1	76.4	24.1	23.0
	Test (b)	332.3	27.3	85.0	21.2	21.7
	(a)/(b)	84.2%	95.6%	89.9%	113.7%	106.0%

Failure modes

Fig. 17a and Fig. 17b present the simulated and tested failure modes of RSS-4-100 and OHS-0-0. The simulated failure modes were consistent with the test results reflecting that a shank bending was resulted by wrapped rubber sleeve in addition to the stud shear fracture, and the concrete damage area was near the stud root.

Fig. 18 demonstrates the compressive concrete damage distribution details in OHS-0-0-FEM and RSS-4-100-FEM. The damage distribution zone of RSS-4-100-FEM were larger than that of OHS-0-0-FEM but the damage extent became lower. In particular, the concrete damage zone of OHS-0-0-FEM under the load of V_u were $1.4d_s$ in depth and $3d_s$ in height, while those of RSS-4-100-FEM were $4.1d_s$ and $2d_s$. d_s is the stud diameter. The rubber sleeve helped to ameliorate the damage concentration and extent.

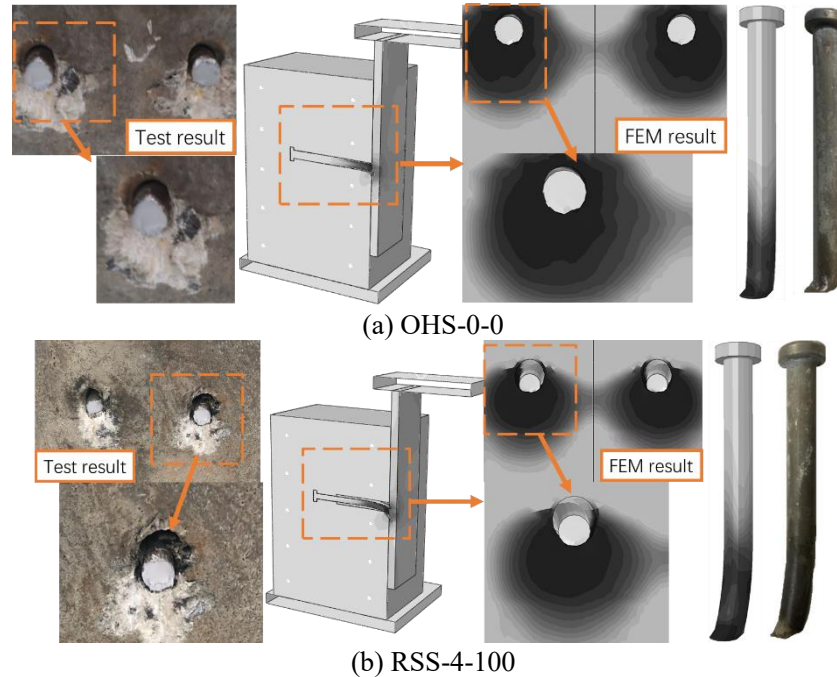


Fig. 17 Failure mode comparison (The dark area represented the damage level)

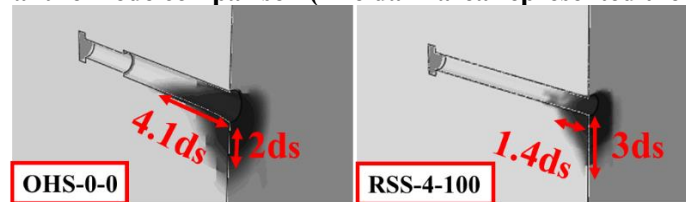


Fig. 18 Compressive damaging zone comparison
(The dark area represented the damage level)

Stress distribution on the stud shank

Fig. 18 provides the simulated stress distributions at load levels of $0.5V_u$ and $0.9V_u$ on the upper and bottom edges of stud shanks in the push load direction. The rubber height and thickness were 100mm and 4mm in the simulated RSS.

As shown in Fig. 19a and Fig. 19b which shows the axial stress distributions on the upper and bottom edges of stud shanks, the stress distribution pattern was somewhat similar to a uniformly loaded beam with one end fixed and the other simply supported. The simulated compressive and tensile stresses on the upper and bottom edges near the stud root reduced to zero at about 20mm distance away. Afterwards, the stress status sequentially increased and decreased inversely in a certain distance. And the stress level and non-zero distribution length were larger in RSS than in OHS. It was attributed to the wrapped rubber sleeve in RSS.

Fig. 20 shows the shear stress distribution along center line of the stud. The maximum shear stress was 250MPa at $50\% V_u$ and 300MPa at $90\% V_u$. The maximum shear stress appeared near the

root of the stud. With the increase of the distance from the stud root, the shear stress decreased rapidly to zero and then kept at a low stress level. It can be seen that the variation curve of OHS and RSS connector was approximately the same, while large shear stress was more widely distributed in RSS connector.

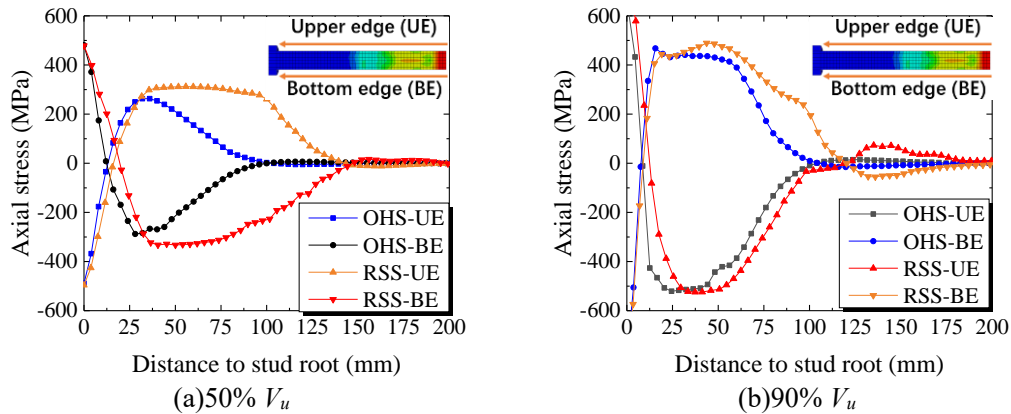


Fig. 19 Axial stress distribution

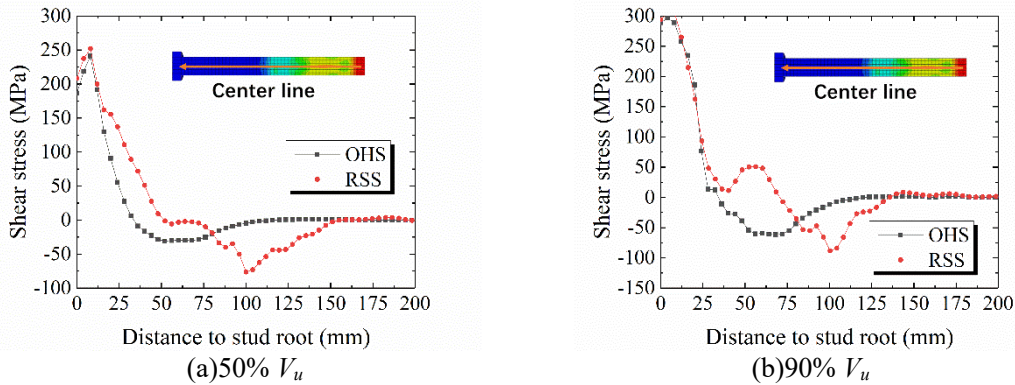


Fig. 20 Shear stress distribution

Fig. 21 shows the deflection distribution of OHS and RSS along the center line of stud in the push load direction. The rubber height and thickness were 100mm and 4mm in the simulated RSS. It can be seen that a large deformation appeared at the stud root. However, the deformation was small at position with distance to the root beyond 75mm, which can explain why the stiffness couldn't keep going down with the increase of the sleeve height.

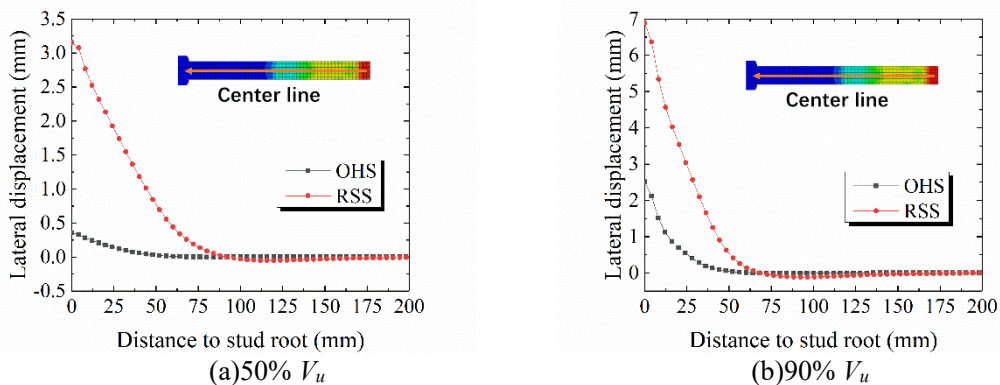


Fig. 21 Vertical displacement distribution of studs

Parametric analysis

Size effect of rubber sleeves

In addition to the push-out tests and simulations on OHS and RSS connectors, additional FEM models were established for the analysis on the rational dimension size of rubber sleeve of RSS

connector with 22mm stud diameter.

Table 5 summarized the analyzed shear strength and stiffness of RSS with different size of rubber sleeves. The RSS had an obvious lower stiffness than OHS when the thickness or height of rubber sleeve were lower than 4mm or 40mm. Compared with OHS, K_{s1} and K_{s2} of RSS with 1mm thick rubber sleeve decreased by 71.0% and 71.3% respectively. When the thickness or height went beyond 4mm or 40mm, the shear stiffness hardly changed.

Table 5
Comprision between specimens with different T_r (H_r was fixed at 100mm)

Specimen	T_r (mm)	V_u (kN)	K_{s1} (kN/mm)	K_{s2} (kN/mm)
Tr-0 (a)	0	195.1	386.3	279.7
Tr-1 (b)	1	194.1	112.2	80.2
Tr-2 (c)	2	188.0	69.0	76.7
Tr-3 (d)	3	203.1	27.8	30.6
Tr-4 (e)	4	176.4	27.5	24.1
Tr-5 (f)	5	175.9	20.1	20.0
Tr-6 (g)	6	183.3	19.6	23.0
Hr-0 (h)	0	195.1	386.3	279.7
Hr-20 (i)	20	171.3	91.0	37.1
Hr-40 (j)	40	173.7	29.8	25.0
Hr-50 (k)	50	175.6	28.0	26.1
Hr-60 (l)	60	201.6	25.0	26.1
Hr-80 (m)	80	187.6	26.9	26.1
Hr-100 (n)	100	176.4	27.5	24.1
Hr-150 (o)	150	191.4	26.2	23.7
(b)/(a)	/	99.5%	29.0%	28.7%
(c)/(a)	/	96.4%	17.9%	27.4%
(d)/(a)	/	104.1%	7.2%	10.9%
(e)/(a)	/	90.4%	7.1%	8.6%
(f)/(a)	/	90.2%	5.2%	7.2%
(g)/(a)	/	94.0%	5.1%	8.2%
(i)/(h)	/	87.8%	23.6%	13.3%
(j)/(h)	/	89.0%	7.7%	8.9%
(k)/(h)	/	90.0%	7.2%	9.3%
(l)/(h)	/	103.3%	6.5%	9.3%
(m)/(h)	/	96.2%	7.0%	9.3%
(n)/(h)	/	90.4%	7.1%	8.6%
(o)/(h)	/	98.1%	6.8%	8.5%

Fig. 22 presents the load-slip curve of RSS connectors with different T_r , while the sleeve height H_r was kept to be 50mm. A stiffness lagging feature could be observed when the sleeve thickness was larger than 6mm. The slip increased rapidly with small applied loads after 40kN, and the load-slip curve was almost unchanged when T_r was up to 8mm because of insufficient deformation. There wasn't a sharp decline for initial stiffness, which could be attribute to the concrete at the edge of the rubber sleeve bears the initial load before its destruction.

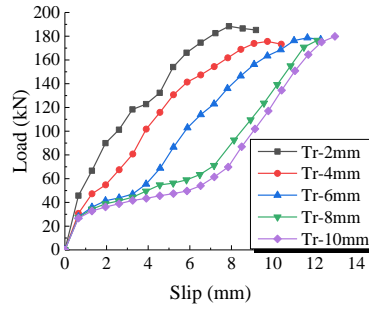


Fig. 22 Load-slip curve of RSS connectors with different T_r

Effect of stud diameter

Fig. 23 shows the analyzed RSS strength variation with stud diameter and rubber sleeve thickness. 19mm, 22mm and 25mm shank diameter stud were respectively investigated in the analysis. The shear strength increased obviously with diameter, while the effect of rubber sleeve dimension was not remarkable. Although there were some strength variations in the analysis due to the distortion of elements simulating the thin rubbers, it would not change the tendency that the strength varied little by the rubber dimension.

Table 6 compares the shear strength V_u between the FEM result and the design code result (JTG D64-2015^[38], Eurocode 4^[39] and AASHTO^[40] were calculated). It can be inferred that the design code result is generally a little larger than the FEM result for redundancy in designing, while the result of AASHTO is the closest to the FEM result. And it is noteworthy that the rubbers were not considered in all the evaluations according to codes.

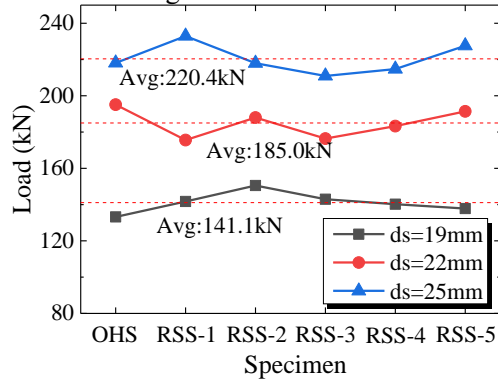


Fig. 23 Shear strength of studs with different diameters

Table 6

Comparison of V_u between the FE model and the design code

Specimen	$V_u(\text{FEM})/\text{kN}$	$V_u(\text{Design code})/\text{kN}$			$V_u(\text{FEM})/V_u(\text{Design code})$		
		JTG	Eurocode 4	AASHTO	JTG	Eurocode 4	AASHTO
R19-OHS	133.2				1.68	1.84	1.38
R19-RSS-1	141.7				1.79	1.95	1.47
R19-RSS-2	150.5	79.4	72.6	96.4	1.9	2.07	1.56
R19-RSS-3	142.9				1.8	1.97	1.48
R19-RSS-4	140.2				1.77	1.93	1.45
R19-RSS-5	137.8				1.74	1.90	1.43
R22-OHS	195.1				1.83	2.01	1.51
R22-RSS-1	175.6				1.65	1.80	1.36
R22-RSS-2	188.0	106.4	97.3	129.2	1.77	1.93	1.46
R22-RSS-3	176.4				1.66	1.81	1.37
R22-RSS-4	183.3				1.72	1.88	1.42

R22-RSS-5	191.4				1.80	1.97	1.48
R25-OHS	218.1				1.59	1.74	1.31
R25-RSS-1	232.9				1.69	1.85	1.40
R25-RSS-2	217.9	137.4	125.6	166.9	1.59	1.73	1.31
R25-RSS-3	210.9				1.53	1.68	1.26
R25-RSS-4	214.7				1.56	1.71	1.29
R25-RSS-5	227.6				1.66	1.81	1.36

Fig. 24 shows the shear stiffness K_{s1} variation of RSS with different stud shank diameter. The stiffness became lower in RSS with different stud shank diameter. Such feature was obvious when the sleeve thickness or height was lower than 4mm or 50mm. It was consistent with the discussion of the sleeve size effect on the stud stiffness. The influence on K_{s2} was similar.

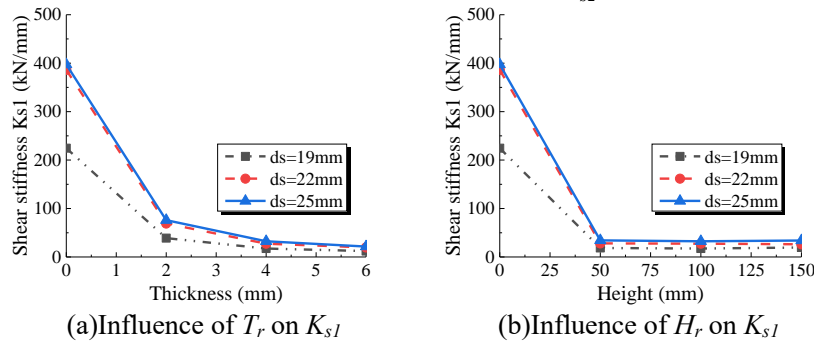


Fig. 24 Shear stiffness K_{s1} variation of RSS with different stud shank diameter

The material modulus effect

Additional modulus values were configured in the parametric models to investigate the RSS performance variation. The results were listed in Table 7. The material thickness and height were respectively 4mm and 100mm. It can be seen the stiffness degradation occurred when the modulus of wrapped material was lower than 10% of 34500MPa which was a normal value of elastic concrete modulus.

Table 7

Elastic modulus variation with the change of wrapping material

$E(\times 10^4 \text{MPa})$	3.45	3	2	1	0.5	0.3	0.1	0.05	0.01
	(a)	(b)	(c)	(d)	(e)	(f)	(g)	(h)	(I)
K_{s2}	148.1	147.2	146.8	143.8	138.6	132.0	116.7	94.3	62.3
(n)/(a)	1.00	0.99	0.99	0.97	0.94	0.89	0.79	0.64	0.42

Stress variation in the hogging moment region with RSS

The stress variation feature of concrete and steel flanges in the hogging moment region with RSS connectors in a 3-span continuous composite girder was parametrically investigated. The span length was 40m. Fig. 25 shows a typical cross section of the girder. Table 8 lists a series of design parameters of the girder.

As illustrated in Fig. 26, the steel girder and concrete slab were separately simulated by beam elements, and the RSS connectors were simulated by a series of vertical rigid arm element with horizontal stiffness. Since the rigid arms were coupled with the concrete beam and the steel beam, the slip δ under the force P (as shown in Fig. 26(a)) can be derived by Eq.12, where l represented the length of the rigid arm, E_{ra} and I_{ra} was the elasticity modulus and inertia moment of the rigid arm. As the shear stiffness K_{s1} could be defined as $K_{s1} = P / \delta$, the moment of bending inertia I could be calculated by Eq.13. Thus, influence of different RSS on the concrete slab stress can be calculated by substituting different shear stiffness K_{s1} obtained by the experiments to Eq13.

Particularly, connectors of OHS-0-0, RSS-2-100 and RSS-4-100 were respectively introduced in the parametric models. The dead load was applied during the analysis.

$$\delta = 2P \left(\frac{l_{ra}}{2} \right)^3 / (3E_{ra} I_{ra}) \quad \text{Eq.12}$$

$$I = K_{sl} l_{ra}^3 / 12E_{ra} \quad \text{Eq.13}$$

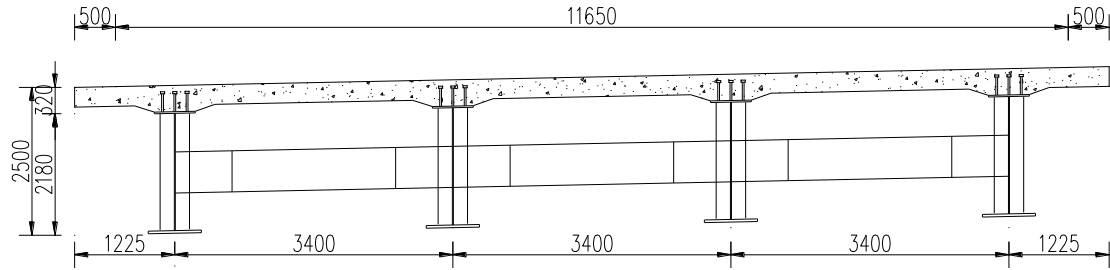
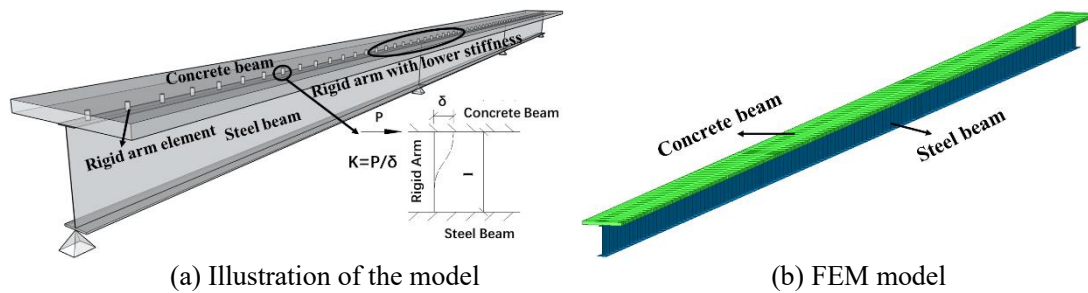


Fig. 25 Configuration of a 3x40m continuous composite girder (mm)

Table 8

Section detail of the 3x40m continuous composite girder

Steel top flange		Steel bottom flange		Web		Stud distance	
Width	Thickness	Width	Thickness	Height	Thickness	Transverse	Longitudinal
400	30	600	40	2110	16	100	200

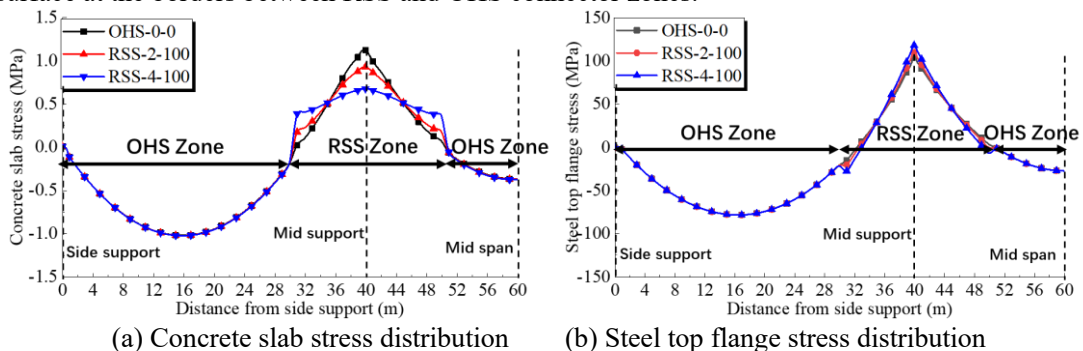


(a) Illustration of the model

(b) FEM model

Fig. 26 The double-beam model

Fig. 27(a) and Fig. 27(b) respectively shows the stress distributions on the concrete slab surface and top steel flanges in accordance with the beam analysis results. The concrete tensile stress at the internal support reduced significantly due to the lower shear stiffness of RSS. Meanwhile, the tensile stress on steel top flange increased. It is noteworthy that there was a stress increase on the concrete surface at the borders between RSS and OHS connector zones.



(a) Concrete slab stress distribution

(b) Steel top flange stress distribution

Fig. 27 Influence of the connector shear stiffness change on stress distribution variation

Fig. 28 quantified the concrete and steel stress variations at several critical positions(A-A, B-B, and C-C). The stress in sagging moment region varied little with the RSS configuration in terms of the stress variations at B-B and C-C. Regarding A-A at the hogging moment region, concrete tensile stresses with OHS and RSS (type of RSS-4-100) were respectively 1.12MPa and 0.68MPa,

and the stresses on steel top flanges were 123.7MPa and 140.2MPa. This shows that RSS in hogging moment region contributed to a 39% reduction of concrete tensile stress and a 13% increase of stress on steel top flange. Meanwhile, the effect of RSS on the girder deflection was not significant. The deflection growth was below 8.9% in the midspan and 1% in the side span when using RSS-4-100 (as shown in Figure 29).

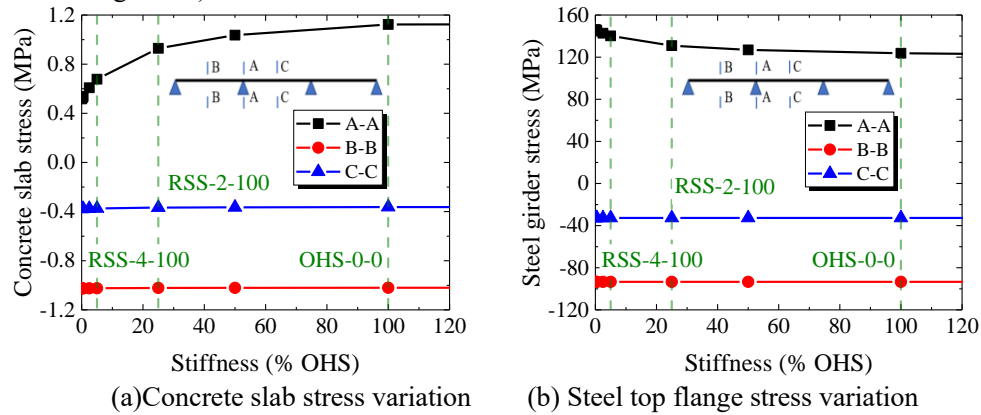


Fig. 28 Stress variation in key sections

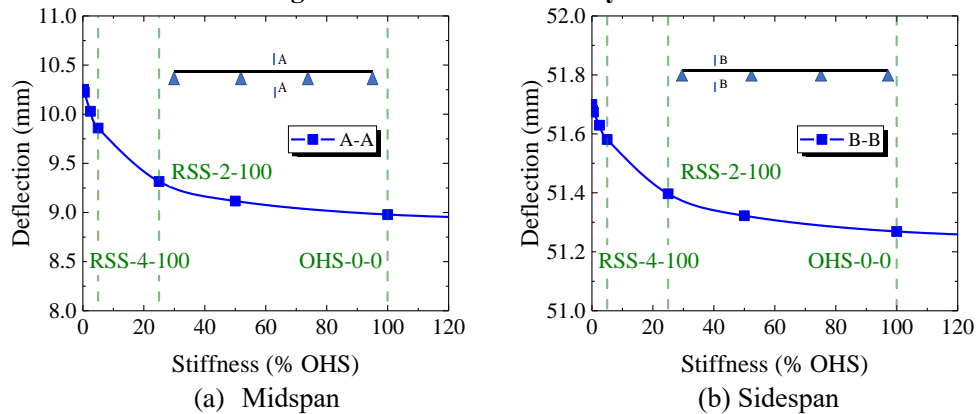


Fig. 29 Deflection variation in key sections

Conclusion

Applying RSS to the hogging moment region in steel-concrete composite bridges helps to achieve a low level of composite action, which can efficiently reduce the tensile stress on the concrete slab and thus the cracking risk. The mechanical performance of Rubber Sleeved Stud (RSS) was investigated through 15 push-out tests and analysis works. The following conclusions could be drawn.

- (1) The ultimate fracture at the stud root could be observed in every push-out test. And the shank bending deformation of RSS was obvious at the ultimate status. Meanwhile, the local concrete crush around stud root was observed in common, of which the difference between the OHS and RSS was not significant.
- (2) Wrapping rubber sleeve around the stud shank near stud root could enhance the slip capacity and reduce the stiffness of the connector in the push-out tests, while it could hardly affect the shear strength of the connector.
- (3) In terms of the effect on stud stiffness reduction, the rational rubber sleeve thickness and height were 4mm and 50mm for a 22mm-diameter and 220mm-high stud.
- (4) The parametric analysis results showed that the RSS stiffness began to decrease obviously when the elastic modulus of the wrapped material was 10% lower than that of concrete.
- (5) The parametric analysis on a continuous composite girder with RSS connectors configured in the hogging moment region showed a maximum of 39% concrete slab stress reduction and a 13% increase of steel stress on the top flange.

Acknowledgement

This research is sponsored by the National Natural Science Foundation of China (No.

51978501), Tongji Civil Engineering Peak Discipline Plan. The supports were greatly appreciated.

References

- [1] El-Gendy M , El-Salakawy E . Effect of flexural reinforcement type and ratio on the punching behavior of RC slab-column edge connections subjected to reversed-cyclic lateral loads[J]. *Engineering Structures*, 2019, 200:109703-.
- [2] Chin C L , Khun M C , Awang A Z , et al. Confining stress path dependent stress-strain model for pre-tensioned steel-confined concrete[J]. *Engineering Structures*, 2019, 201:109769-.
- [3] Massaro F M , Malo K A . Stress-laminated timber decks in bridges: Friction between lamellas, butt joints and pre-stressing system[J]. *Engineering Structures*, 2020, 213:110592.
- [4] Steensels R , Vandoren B , Vandewalle L , et al. Evaluation of end-zone detailing of pre-tensioned concrete girders[J]. *Engineering Structures*, 2019, 187(MAY 15):372-383.
- [5] Jiang C , Wu C , Jiang X . Experimental study on fatigue performance of corroded high-strength steel wires used in bridges[J]. *Construction and Building Materials*, 2018, 187(OCT.30):681-690.
- [6] Kim H H , Shim C S . Experimental investigation of double composite twin-girder railway bridges[J]. *Journal of Constructional Steel Research*, 2009, 65(6):1355-1365.
- [7] Kim, Choong-Eon, Yun. Structural behavior of a continuous composite truss with a composite bottom chord[J]. *Journal of Constructional Steel Research*, 2015.
- [8] Chen Xu, Qingtian Su, Chong Wu, Kunitomo Sugiura. Experimental study on double composite action in the negative flexural region of two-span continuous composite box girder[J]. *Journal of Constructional Steel Research*, 2011, 67(10):1636-1648.
- [9] Meszoely T , Randl N . Shear behavior of fiber-reinforced ultra-high performance concrete beams[J]. *Engineering Structures*, 2018, 168(AUG.1):119-127.
- [10] Wan-Wendner L , Wan-Wendner R , Cusatis G . Age-dependent size effect and fracture characteristics of ultra-high performance concrete[J]. *Cement and Concrete Composites*, 2018:S0958946516305297.
- [11] Poon C S , Kou S C , Lam L . Compressive strength, chloride diffusivity and pore structure of high performance metakaolin and silica fume concrete[J]. *Construction and Building Materials*, 2006, 20(10):858-865.
- [12] Ribeiro F , Sena-Cruz J , Branco F G , et al. 3D finite element model for hybrid FRP-confined concrete in compression using modified CDPM[J]. *Engineering Structures*, 2019, 190(JUL.1):459-479.
- [13] Abdullah A , Bailey C G . Punching behaviour of column-slab connection strengthened with non-prestressed or prestressed FRP plates[J]. *Engineering Structures*, 2018, 160:229-242.
- [14] Oehlers D J , Coughlan C G . The shear stiffness of stud shear connections in composite beams[J]. 1986, 6(4):273-284.
- [15] Uddin M A , Sheikh A H , Bennett T , et al. Large deformation analysis of two layered composite beams with partial shear interaction using a higher order beam theory[J]. *International Journal of Mechanical Sciences*, 2017, 122:331-340.
- [16] Keo P , Nguyen Q H , Somja H , et al. Exact finite element formulation for an elastic hybrid beam-column in partial interaction with shear-deformable encasing component[J]. *Engineering Structures*, 2016, 125(oct.15):494-503.
- [17] Wright H D . The deformation of composite beams with discrete flexible connection[J]. *Journal of Constructional Steel Research*, 1990, 15(1-2):49-64.
- [18] Molenstra N , Johnson R P . Partial shear connection in composite beams for buildings[J]. *Proceedings of the Institution of Civil Engineers Part Research & Theory*, 1991.
- [19] Loh H Y , Uy B , Bradford M A . The effects of partial shear connection in the hogging moment regions of composite beams: Part I—Experimental study[J]. *Journal of Constructional Steel Research*, 2004, 60(6):897-919
- [20] Loh H Y , Uy B , Bradford M A . The effects of partial shear connection in the hogging moment regions of composite beams Part II—Analytical study[J]. *Journal of Constructional Steel Research*, 2004, 60(6):921-962
- [21] Hiragi H , Matsui S , Muto K . Development of favorable stud shear connectors to flexible composite actions[J]. *Struct Eng JSCE* 1998;44A(3):1485–96.

- [22] Kitagawa, K. et al. Development of Innovative Composite System-Between Steel and Concrete Members. International Symposium on connections between Steel and Concrete, 2001.
- [23] NIE Jianguo, TAO Muxuan, NIE Xin, et al. New technique and application of uplift-restricted and slip-permitted connection[J]. China Civil Engineering Journal, 2015,48(4):7-15.
- [24] H. Abe, T. Hosaka. Flexible shear connectors for railway composite girder bridges. Composite Construction in Steel and Concrete IV Conference, 2002, pp. 71–80.
- [25] Xu X , Liu Y . Analytical and numerical study of the shear stiffness of rubber-sleeved stud[J]. Journal of Constructional Steel Research, 2016, 123(aug.):68-78.
- [26] Zhuang B , Liu Y , Yang F . Experimental and numerical study on deformation performance of Rubber-Sleeved Stud connector under cyclic load[J]. Construction and Building Materials, 2018, 192:179-193.
- [27] Zhuang B , Liu Y . Study on the composite mechanism of large Rubber-Sleeved Stud connector[J]. Construction and Building Materials, 2019, 211:869-884.
- [28] Japanese Society of Steel Construction. Standard on push-out test for headed stud [S]. Japanese Society of Steel Construction, 1996.
- [29] Oehlers DJ, Coughlan CG. The shear stiffness of stud shear connections in composite beams. Journal of Constructional Steel Research 1986; 6:273–84.
- [30] Oehlers DJ, Bradford MA. Elementary behaviour of composite steel & concrete structural members. Butterworth-Heinemann; 1999.
- [31] Rabbat B G , Russell H G . Friction Coefficient of Steel on Concrete or Grout[J]. Journal of Structural Engineering, 1985, 111(3):505-515.
- [32] Chinese Standard GB50010-2010 Code for design of concrete structures, China, 2010
- [33] Mander J A B , Priestley M J N . Theoretical Stress-Strain Model for Confined Concrete[J]. Journal of Structural Engineering, 1988, 114(8):1804-1826.
- [34] Kan C , Jing-Feng S , Guan-Ren Y U , et al. Parameter Determination of Mooney-Rivlin Model and Finite Element Simulation of the Compression Deformation of Rubber Rail Fastener[J]. Materials for Mechanical Engineering, 2016.
- [35] Marcin Kamiński, Lauke B . Probabilistic and stochastic aspects of rubber hyperelasticity[J]. Meccanica, 2018, 53.
- [36] Yuan Y , Wei W , Tan P , et al. A rate-dependent constitutive model of high damping rubber bearings: modeling and experimental verification[J]. Earthquake Engineering & Structural Dynamics, 2016, 45(11):1875-1892.
- [37] Liang Z , Zhonghua L I , Xinqiang M A . Study on Parameter Characteristics of Rubber Mooney-rivlin model[J]. Noise and Vibration Control, 2018.
- [38] JTG D64-2015, Specifications for design of highway steel bridge [S]. Beijing: China Communication Press, 2015.
- [39] BS EN 1994-2. Eurocode 4: Design of composite steel and concrete structures [S]. Brussels: European Committee for Standardization, 2004.
- [40] AASHTO LRFD. Bridge design specifications [S]. Washington D C: American Association of State Highway and Transportation Officials,2007

6.2 Structures 2022

Su H, Su Q, Casas JR, et al. Influence mechanism of Steel-concrete interlayer partial shear connections on mechanical properties of composite girders. Structures, 2022, 46: 503–520. DOI: 10.1016/j.istruc.2022.10.082

Influence Mechanism of Steel-concrete Interlayer Partial Shear Connections on Mechanical Properties of Composite Girders

Hang Su ^{a,b}, Qingtian Su ^{a,c}, Joan R. Casas ^b, Chen Xu ^{a*}, Jian Tang ^a, Chao Jiang ^a

^a *Department of Bridge Engineering, Tongji University, 1239 Siping Road, Shanghai, China 200092*

^b *School of Civil Engineering. Department of Civil and Environmental Engineering, Technical University of Catalunya, c/Jordi Girona 1-3. Campus Nord. Modulo C-1, Barcelona (Spain) 08034*

^c *Shanghai Engineering Research Center of High Performance Composite Bridge, 901 Zhongshanbeier Road, Shanghai, China 200092*

Abstract

A reduction in composite action using a partial shear connection (PSC) in the hogging moment region of a steel–concrete bridge can mitigate the concrete tensile cracking risk while maintaining the structural ultimate bearing capacity. To date, specific mechanical effects, important for the establishment of evaluation theory, have not been studied. To this end, four girders and six push-out specimens were tested for the effect investigation. Numerical analysis with material damage plasticity models and an analytical study were conducted for parametric and mechanistic investigations. The push-out test results showed that a wrapping rubber sleeve reduced the shear stiffness of the stud by 91.9%, whereas its strength varied slightly. The girder test results showed that arranging rubber sleeved stud (RSS) connectors in the composite girders reduced the girder load-carrying capacity and bending stiffness by 17% and 12%, respectively. Moreover, the concrete tensile cracking performance was improved. The analysis results showed that, for reducing the concrete tensile stress, the RSS connector in the girder had a more favourable effect on prestress distribution than increasing the ordinary stud spacing. In addition, an evident stress concentration appeared when the stud distance was increased. According to the analytical analysis of the girder under negative bending, the concrete tensile stress is exponentially related to the interlayer stud stiffness, and the exponential is expected to be 5/3. The research revealed the detailed mechanical behaviour of the girder with a PSC and simultaneously compared the effects of the two PSC methods. This research will help establish design and evaluation methods for PSC action.

Keywords: Steel–concrete composite structure; Partial shear connection; Rubber-sleeved stud

connector; Numerical study; Experimental study; Hogging moment regions

Nomenclature

FSC: Full shear connection
PSC: Partial shear connection
OHS: Ordinary headed stud
RSS: rubber-sleeved stud
 V_u : Stud shear strength
 K_{s1} and K_{s2} : Secant moduli corresponding to $1/3 V_u$ and $1/2 V_u$, respectively
 s_u : Slip response corresponded to the maximum shear force
 f_y : Yielding strength
 f_t : Ultimate tensile strength
LVDTs: Variable differential transducers
D: Deflection sensor
S: Steel–concrete interlayer slip sensor
 k_{200} and k_{300} : Stiffnesses at load levels of 200 kN and 300 kN, respectively
 E_c : Elasticity modulus of concrete
 α_t and α_c : Regulation coefficients of the descending part of concrete
 d_c and d_t : Compressive and tensile damage factor of the concrete
 $f_{t,r}$ and $f_{c,r}$: Ultimate tensile and compressive strengths, respectively, of concrete
 $\varepsilon_{t,r}$ and $\varepsilon_{c,r}$: Strains corresponding to the ultimate tensile and compressive strengths of concrete, respectively
 E_0 : Initial elasticity modulus of concrete
 σ_{ys} : Stress at yield point
 σ_{us} : Stress at ultimate point
 ε_{ys} : Strain at yield point
 ε_{us} : Strain at ultimate point
PS: Specimen with prestress
NPS: Specimen without prestress
DC: Distance change
 L : Span of the simply supported girder
 w_c and t_c : Width and thickness of the concrete slab, respectively
 h_s : Steel girder height
 n_s and k_s : Stud number and stiffness, respectively
 K_s : Shear stiffness per unit along the girder
 P : Concentrated load on the midspan
 $N_s(x)$ and $N_c(x)$: Axial forces in steel girder and concrete slab, respectively
 $M_s(x)$ and $M_c(x)$: Bending moments in steel girder and concrete slab, respectively
 h_0 : Distance between the centroid axis of the steel girder and the concrete slab
 $q(x)$: Shear stress per unit length between the steel girder and concrete slab
 \mathcal{E}_{slip} : Slip strain between the steel girder and concrete slab
 y_c : Distance between the concrete centroid axis and the concrete bottom edge
 y_s : Distance between the steel centroid axis and the steel top edge
 σ_{ct} and σ_{sb} : Stresses at the concrete top edge and steel bottom edge, respectively.

Introduction

Compared to steel or prestressed concrete structures, steel–concrete composite structures have the advantages of steel tension and concrete compression in the sagging moment regions of continuous beams. However, concrete tension in the hogging moment regions of a continuous composite girder may result in cracks. Several methods have been proposed to decrease tensile stresses in concrete slabs and reduce cracks. Adopting an initial prestress ^{[1]-[4]} on a concrete slab, increasing the reinforcement ratio ^{[5][6]} and attaching fibre-reinforced plastic (FRP) layers ^{[7][8]} to the concrete slab can limit crack development. Casting an extra concrete bottom layer to a steel–concrete composite box girder in a hogging moment region can increase the cracking moment and prevent steel buckling ^{[9][10]}. In addition, steel fibre-reinforced concrete ^{[11]-[13]}, carbon nanotube concrete ^{[14][15]} and ultra-high performance concrete ^{[16][17]} have been applied to improve material performance.

Meanwhile, the decline of composite action in the hogging moment region in a girder can also decrease the concrete slab tensile stress in this region. Normal composite bridges adopt a full shear connection (FSC) for construction convenience and to obtain clear mechanical properties. However, large tensile stresses in concrete occur in the hogging moment regions. In response to this issue, a partial shear connection (PSC) can help decrease the extent of interaction between the concrete slab and steel girder in hogging moment regions and simultaneously maintain the ultimate bearing capacity and overall structural stiffness^{[18][19]}.

PSC action is typically achieved by adopting a low-stiffness connector or by enlarging the connector distance. To increase the connector distance, Wright ^[20] conducted full-scale tests on composite girders with enlarged stud spacings and revealed a nonlinear connection behaviour. Molenstra ^[21] showed that PSC action had a significant impact on the steel–concrete interlayer slip. Loh ^{[22][23]} conducted an experimental and analytical study and demonstrated that the effect of PSC action on the load-carrying capacities of composite girders was not significant. Mirambell ^[24] studied the higher deflections of composite beams with PSC through numerical method. Bradford ^[25] presented the derivation of a theoretical model for the time-dependent response of composite beams with PSC. El-Sisi ^[26] conducted numerical and experimental studies on externally post-tensioned composite beams with PSC. Hassanin ^[27] presented the fatigue behaviour of steel-concrete composite beams with PSC by nonlinear finite element analysis. Nicoletti ^[28] studied the influence of PSC on the effective width of steel-concrete composite box girder through numerical analysis. Regarding low-stiffness connectors, Hiragi ^[29] wrapped urethane at the root of an ordinary headed stud (OHS), achieving lower stiffness features. Kitagawa ^[30] proposed a type of resin-stud connector and revealed its stiffness hysteresis characteristics. Xu ^{[31][32]} revealed the constant shear strength and low stiffness of rubber-sleeved stud (RSS) connectors through push-out tests. Zhuang and Su used push-out tests to demonstrate that RSS connectors could help resist deformation ^{[33][34]}. Qureshi ^[35] presented a numerical study on the behaviour of headed shear stud in composite beams with profiled metal decking.

Although many push-out tests revealing the low stiffness of RSS connectors have been conducted, few studies have focused on their detailed influence on girder specimens. In addition, the effectiveness of these two PSC methods has not been compared in literature. This study aims to experimentally and analytically investigate the detailed influence of RSS connectors and enlarging

connector distances on steel-composite girders in hogging moment regions. Four simply supported composite girders were tested for a detailed mechanical investigation of PSC action. Six push-out specimens were tested to determine the mechanical properties of the RSS connector in girder tests and to determine the shear stiffness for finite element modelling. A parametric study was also conducted for the rational design criteria of PSC action. This study could help establish design methods and evaluate PSC action.

Experimental method

Specimen design

Four simply supported composite girders were manufactured and tested in this study. Fig. 1 shows the dimensional details of the specimens, which were 1:3 scale models of the hogging moment region of an actual 5 m × 40 m continuous composite bridge. Table 1 lists the specimen groups; the specimens were divided into two groups based on the composite section. Compared with GSN-1, GSN-2 also had prestressed reinforcements, while GSP-1 and GSP-2 used RSS connectors and fewer OHS connectors, respectively, for PSC action.

As shown in Fig. 1(a), the full girder length was 10 m, including a 1.3 m free extension at each end. The thicknesses of the steel top flange, bottom flange, and web are shown in Fig. 1 (a). The thicknesses of the horizontal and vertical steel stiffeners were 4 mm and 5 mm, respectively, and 8 mm thick supporting stiffeners were installed on the steel bottom flange around the supports and loading area. As shown in Fig. 1 (b), the composite girder height was 731 mm, including an 85 mm thick concrete slab with a 20 mm thick haunch and a 626 mm high steel tub girder. The width of the concrete deck slab was 1100 mm.

Two layers of longitudinal reinforcements were included (12 mm in diameter in the hogging moment region and 8 mm in diameter in the sagging moment region). The stirrup spacing (diameter: 10 mm) was 75 mm. Specimens GSN-2, GSP-1, and GSP-2 were prestressed. Details of the prestressed reinforcement consisting of four tendons (composed of two steel strands with a diameter of 15.2 mm for each tendon) are also presented in Fig. 1 (b). The prestressed reinforcements were fixed on one side and tensioned on the other after the concrete material had cured sufficiently and reached the design strength.

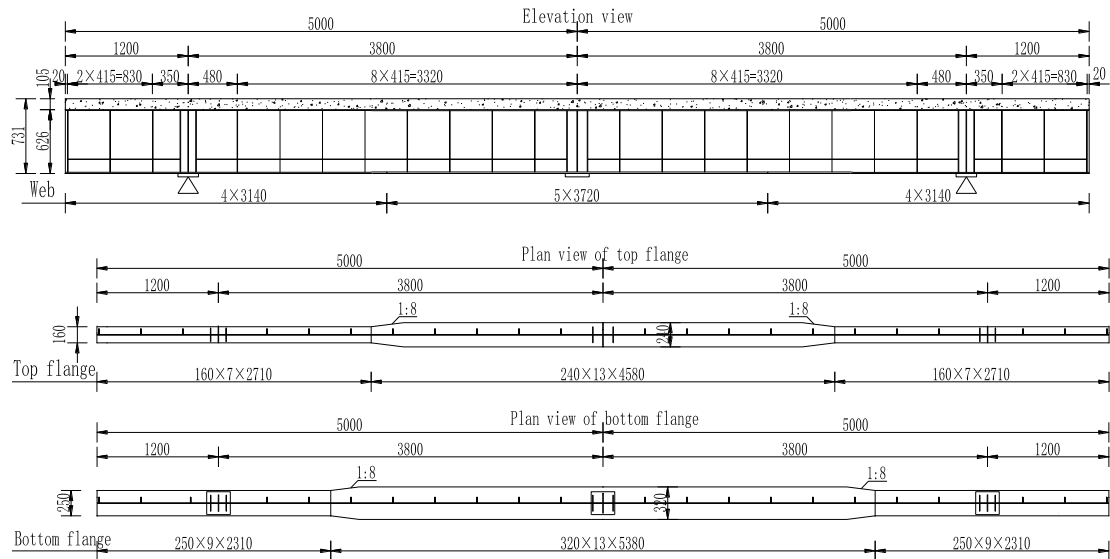
Fig. 1 (c) shows the arrangement of the shear studs. The stud height and shank diameter were 13 mm and 60 mm, respectively. The studs were uniformly welded on the steel top flanges, and the longitudinal and transverse spacings were 120 mm and 80 mm, respectively. The transverse stud spacing was 60 mm, while the longitudinal spacings were 100 mm for GSN-1, GSN-2, and GSP-1 and 200 mm for GSP-2. In addition, rubber sleeves (3 mm thick and 45 mm high) were bound around the stud shanks in specimen GSP-1.

Fig. 2 presents photographs of the specimens. Fig. 2 (a) shows the RSS connectors in GSP-1. Fig. 2 (b) shows the formwork and reinforcement of the concrete slab. Fig. 2 (c) shows the casting procedure for the concrete slab.

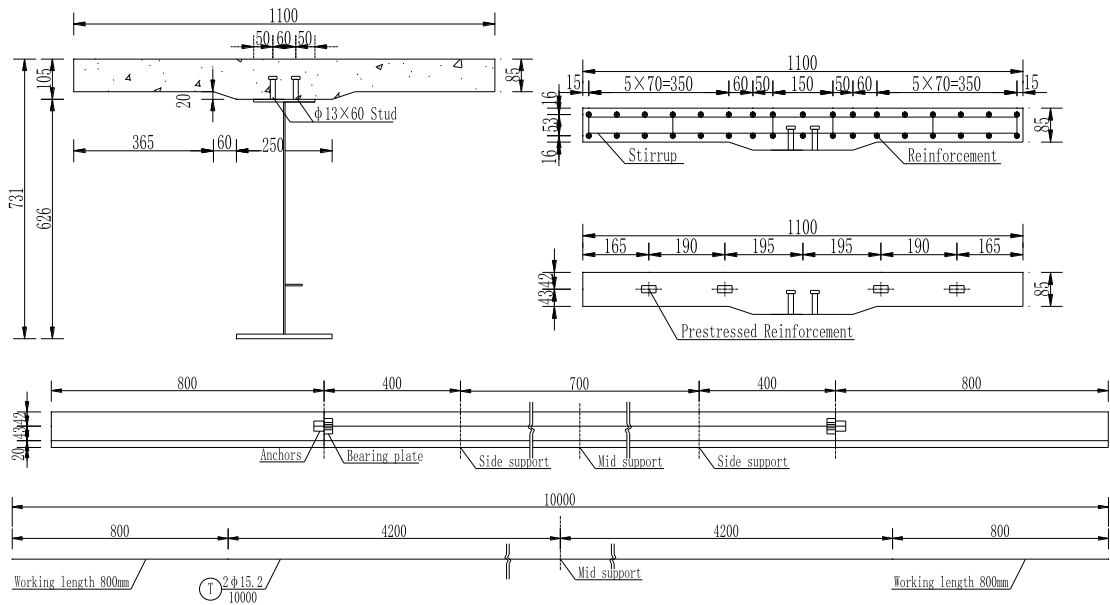
Table 1

Specimen configurations

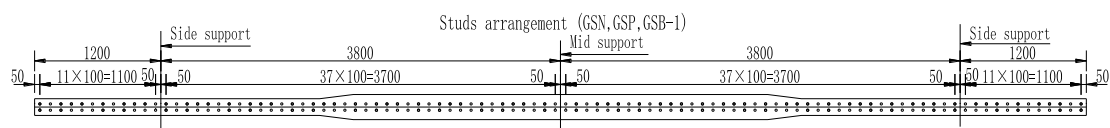
Specimens	Composite action	Prestressed reinforcement stress (MPa)	Longitudinal spacing of studs (mm)	Rubber dimension Thickness × height (mm)
GSN-1	FSC	0	100	0
GSN-2	FSC	758	100	0
GSP-1	PSC	758	100	3×45
GSP-2	PSC	758	200	0

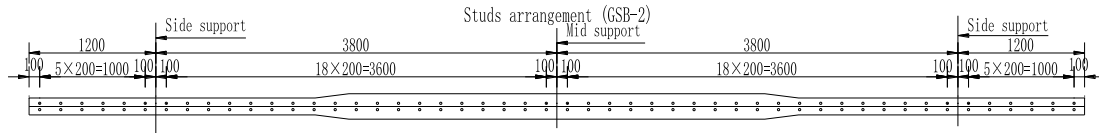


(a) Specimen layout



(b) Composite sections and reinforcement layout





(c) Stud arrangement

Fig. 1 Description of test specimen (mm)



(a) RSS connectors

(b) Formwork and reinforcement

(c) Casting concrete

Fig. 2 Specimen photos

Material properties

The concrete properties were tested on the 28th day after casting. For the uniaxial compressive strength test, 150 mm cubic test specimens were used. For the Young's modulus tests, 150 mm × 150 mm × 300 mm specimens were used. The compressive strength and elastic modulus results were 51.9 MPa and 36500 MPa, respectively.

Table 2 summarises the tensile yielding and ultimate strengths of the steel plates. The tensile properties of the reinforcing bars are also listed in Table 2, where rebars with diameters of 10 mm exhibited no evident yielding point.

Table 2

Steel and reinforcing bar properties (MPa)

Plate thickness or rebar diameter (mm)	4	5	7	9	13	R10	R12
f_y	489.3	460.6	381.5	403.6	459.4	-	400.9
f_u	550.4	537.3	499.5	546.6	585.9	645.4	581.1

* f_y is the yielding strength, and f_u is the ultimate tensile strength.

Three stud connector specimens were fabricated (as shown in Fig.3) for tensile tests. The average yield strength and the ultimate tensile strength were 457 MPa and 493 MPa respectively.

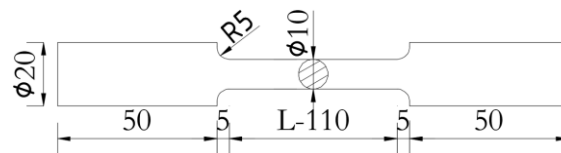


Fig. 3 Configurations of stud material test specimen (mm)

Shear connector properties

Two groups of push-out tests (as listed in Table 3) were conducted to derive the mechanical properties of the RSS connector for the subsequent girder tests and finite element modelling. The OHS and RSS specimen groups were labelled NSS and RSS, respectively. The specimen layout is

illustrated in Fig. 4. The details of the stud connectors are presented in Fig. 5. To measure the interlayer slip, four linear variable differential transformers (LVDTs) were arranged according to the positions of the studs.

Table 3

Groups of test specimens.

Specimen group	Stud dimension	Rubber dimension	Number of specimens
	Diameter × height	Thickness × height	
NSS	φ13 mm × 60 mm	/	3
RSS	φ13 mm × 60 mm	3 mm × 45 mm	3

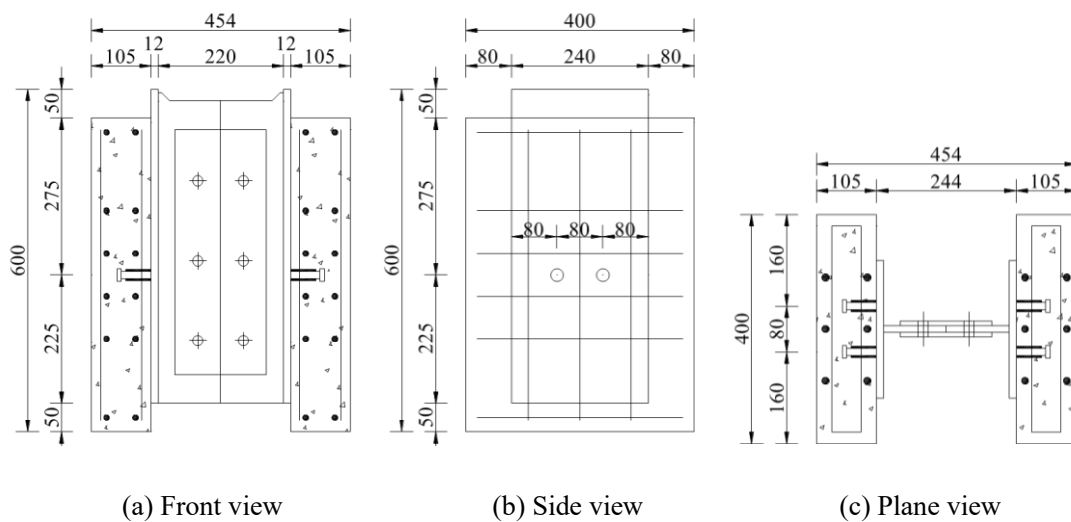


Fig. 4 Configurations of test specimens (mm)

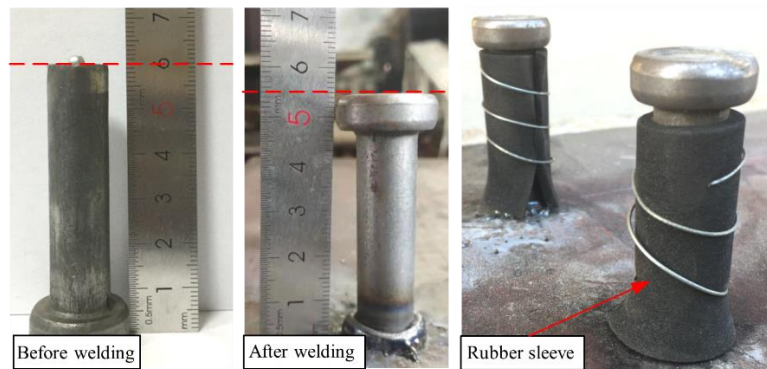
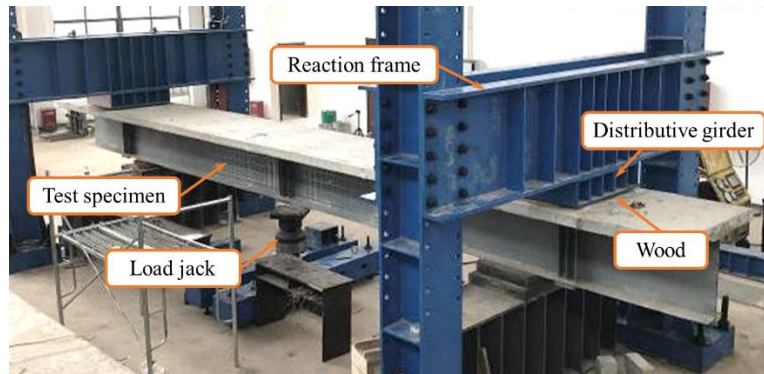


Fig. 5 Stud details

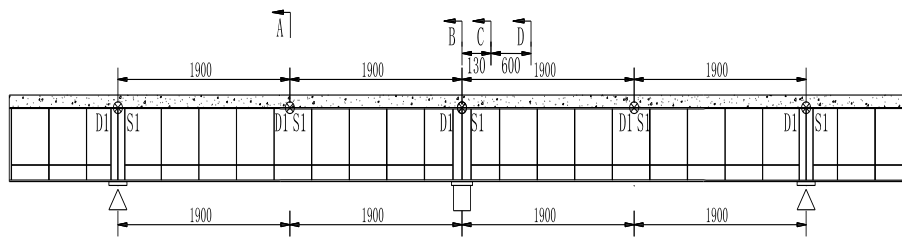
Loading and monitoring setup

Fig. 6 shows the bending test set-up of a typical girder specimen. The specimen was loaded using a 2000 kN capacity hydraulic jack. The test adopted reverse loading, and the supports at both ends were restrained using distributive girders. A wooden board between the distributive girder and the concrete slab simulated the hinge support. The loading program included a 50 kN preload and monotonic loading up to the ultimate states. Fig. 7 shows the positions of the sections under

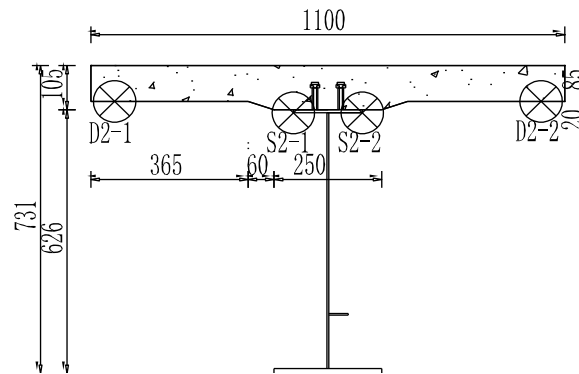
investigation in the test. The deflections and steel–concrete interlayer slips of each specimen were measured using 10 linear variable differential transducers (LVDTs) and 10 dial indicators installed at midspans, quarter spans, and side spans. In particular, two transducers were symmetrically mounted in the transverse direction to check load eccentricity. Fig. 8 shows a typical strain gauge distribution on the cross section of each specimen, including the steel girder, concrete slab, and rebars. The same gauge configuration was repeated at sections B-B, C-C, and D-D. Additionally, the crack widths and patterns in the concrete were measured and recorded.



(1) Fig. 6 Loading setup



(a) Identification of sections of interest



(b) Detailed sensor positions in section A-A

D: deflection sensor; S: steel–concrete interlayer slip sensor

Fig. 7 Sensor positions (mm)

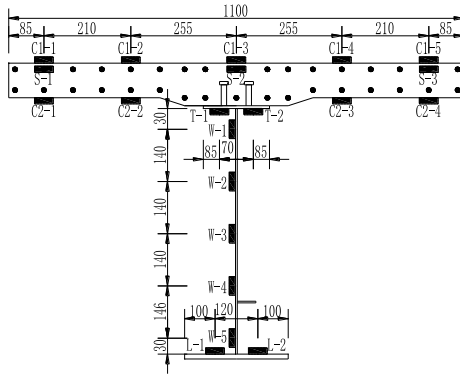


Fig. 8 Strain gauge arrangement (mm)

Experimental results

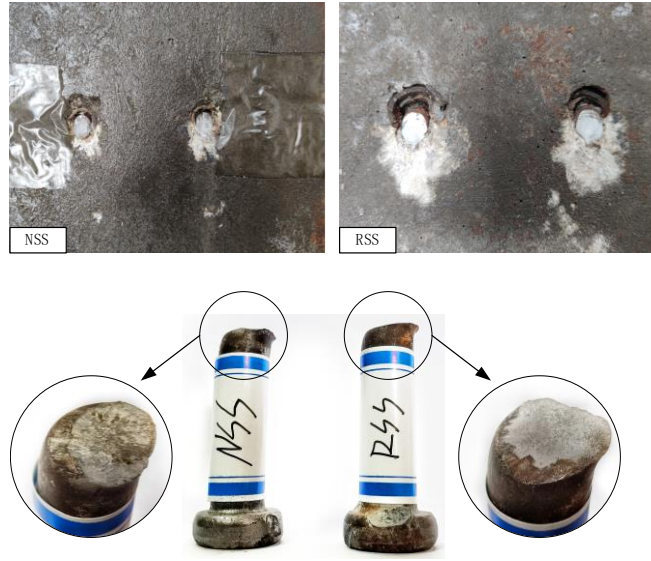
Shear performance of connectors

Fig. 9 summarises the observed failure modes of the OHS and RSS connectors in the push-out tests. It can be inferred that the stud roots exhibited evident plastic deformation, and the failure sections were smooth and flat. Moreover, the deformation of the RSS connector was greater than that of the OHS connector. The load–slip curves of each specimen are presented in Fig. 10. An evident stiffness hysteresis phenomenon was observed in the RSS specimens when the slip was in the range of 1–2 mm.

In general, the load–slip curves of the specimens in each group were similar. Deviations could be attributed to boundary condition errors, variability in the material properties of the concrete, and initial geometrical imperfections. As summarised in Table 4, the difference in V_u between the specimens was lower than 2%, while K_{s1} and K_{s2} of the RSS decreased by 91.9% and 89.0 %, respectively, compared with those of the OHS.

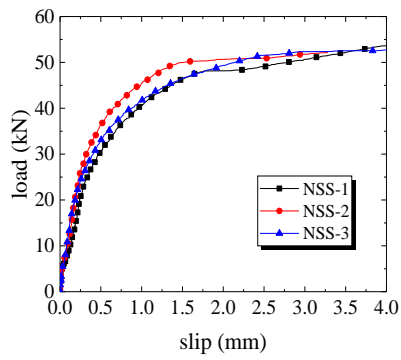


(a) General failure mode

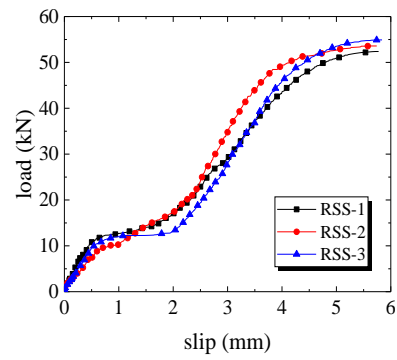


(b) Fracture surfaces

Fig. 9 Failure modes



(a) NSS specimens



(b) RSS specimens

Fig. 10 Load-slip curves from push-out tests

Table 4

Test specimen groups.

Specimen	V_u (kN)	K_{S1} (kN/mm)	K_{S2} (kN/mm)
1	53.7	91.4	81.1
NSS(I) 2	52.1 53.0	109.6 102.4	102.8 89.1
3	53.3	106.1	83.5
1	52.4	8.6	9.7
RSS(II) 2	53.6 53.6	8.7 8.3	10.4 9.8
3	54.9	7.5	9.2

V_u : Stud shear strength

K_{s1} and K_{s2} : Secant moduli corresponding to $1/3 V_u^{[36]}$ and $1/2 V_u^{[37][38]}$, respectively.

Load–deflection relationship and failure mode of girder specimens

Fig. 11 presents the load–deflection curves at midspans in the girder tests. The deflection values depicted are the averages of the twin LVDTs. In general, the curves included elastic and plastic hardening stages.

The elastic girder stiffness defined by the slopes of the secant lines between the origin and the points on the curves at specific loads of 200 kN and 300 kN are listed in Table 5. The two load values corresponded to the stages of observed crack initiation, and the maximum crack width was 0.2 mm. According to Table 5, the PSC action caused a lower load-carrying capacity (17% and 11% for GSP-1 and GSP-2, respectively) compared with those of the two specimens without PSC. The load-carrying capacity difference between the specimens without PSC was not large. Specimen GSN-1 had the lowest bending stiffness because the early concrete cracking resulted in an overall stiffness reduction. In addition, GSP-1 showed a lower bending stiffness than GSN-2 (decreased by 12% and 11% for k_{200} and k_{300} , respectively). However, the PSC action in GSP-2 showed no evident effect on the bending stiffness compared with GSN-2.

The failure mode differences among the specimens were not evident. The main cause of destruction was buckling of the bottom steel flange, along with local web instability and concrete slab deformation (Fig. 12).

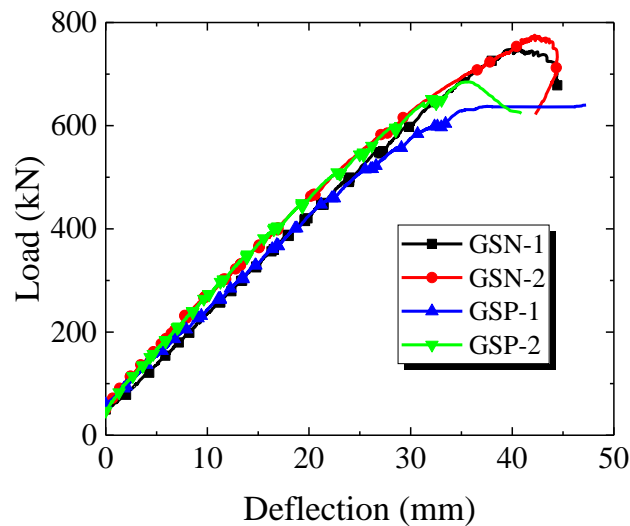


Fig. 11 Load–deflection curves at midspans



Fig. 12 Failure modes of GSP-1

Table 5

Details of the bending stiffness and load-carrying capacity.

Specimen	GSN-1 (a)	GSN-2 (b)	GSP-1 (c)	GSP-2 (d)	(b)/(a)	(c)/(b)	(d)/(b)
k_{200} (kN/mm)	24.1	30.2	26.6	30.1	125%	88%	100%
k_{300} (kN/mm)	22.4	25.8	22.9	26.2	115%	89%	102%
P_u (kN)	750.2	773	643	684.9	103%	83%	89%

Cracking pattern

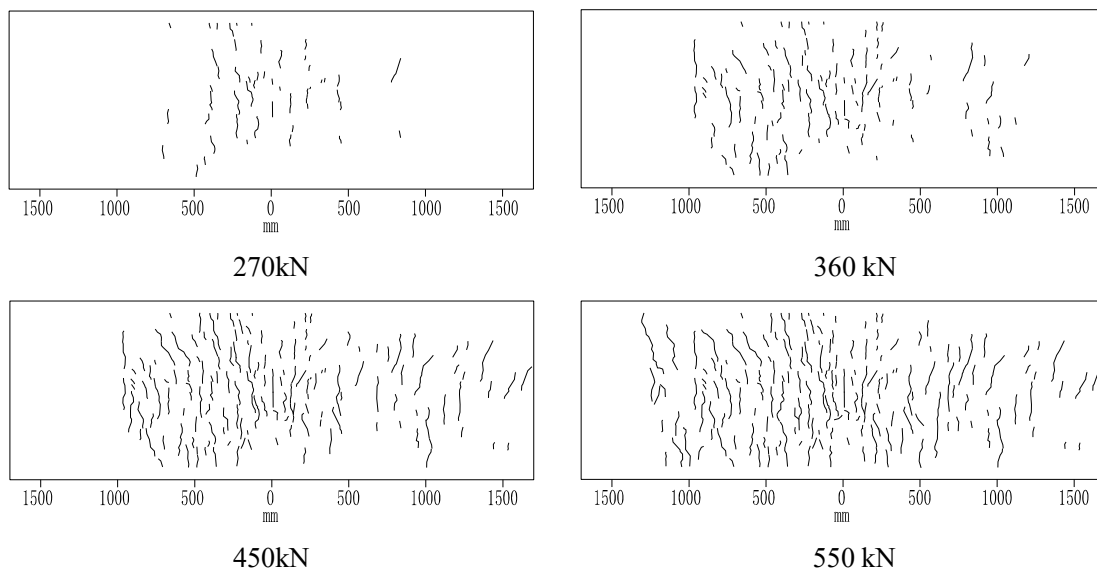
According to visual observations, the initial cracking loads were approximately 110 kN, 200 kN, 200 kN, and 180 kN for GSN-1, GSN-2, GSP-1, and GSP-2, respectively. Table 6 presents the maximum crack widths during the loading process. Accordingly, the RSS connectors contributed to a smaller concrete crack width in GSP-2. However, the influence of increasing the stud spacing on the crack width in GSP-2 was insignificant. Moreover, the prestressing process of the specimen did restrain crack width enlargement.

Fig. 13 illustrates the crack distributions on the concrete deck slab at different load steps. The horizontal scale shows the longitudinal distances from the cracks to the slab centres. All cracks initialised at the slab centres and spread symmetrically in the transverse and longitudinal directions. Based on the comparisons among specimens GSP-1, GSP-2, and GSN-2, the PSC action resulting from the RSS connector configurations mitigated cracks more effectively than that resulting from increasing the stud distance.

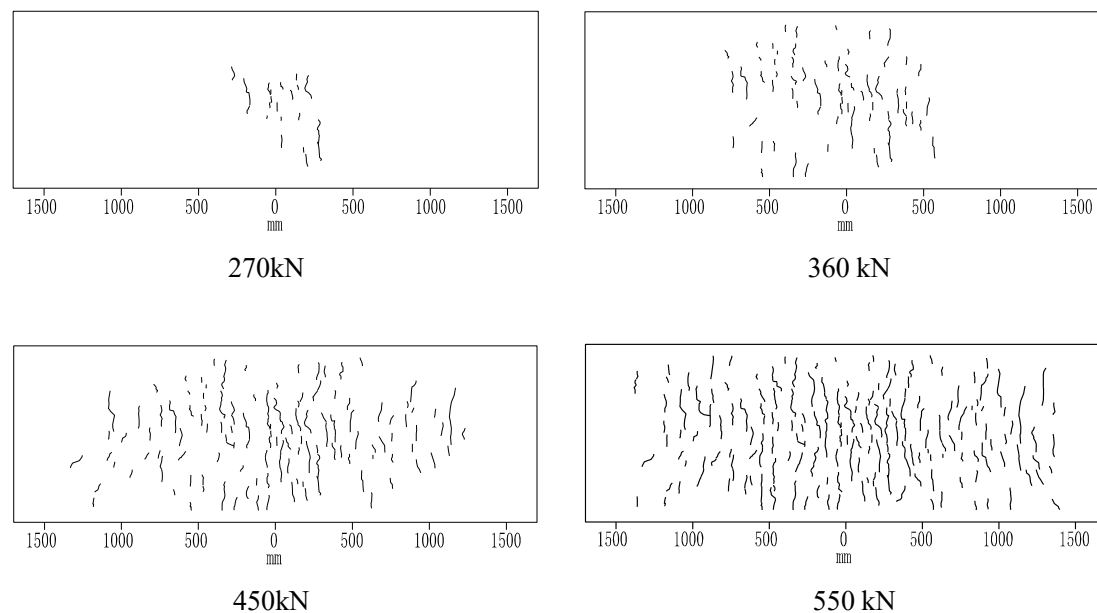
Table 6

Maximum crack widths during the loading process (mm)

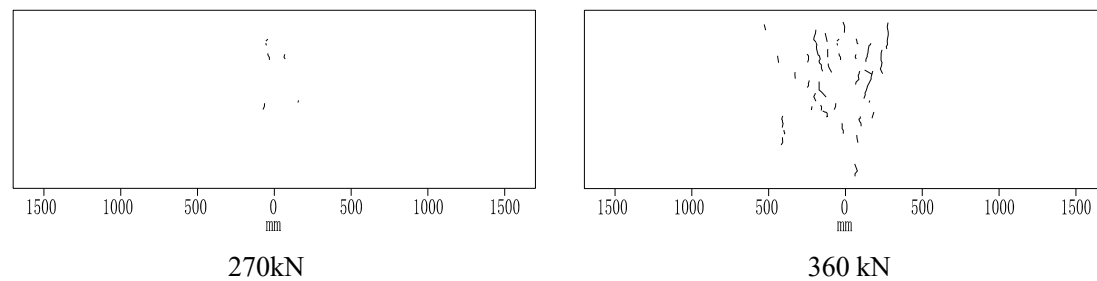
Specimen	Load steps (kN)				
	200	270	360	450	550
GSN-1	0.04	0.07	0.09	0.12	0.13
GSN-2	0.02	0.04	0.06	0.10	0.12
GSP-1	0.02	0.03	0.04	0.08	0.12
GSP-2	0.03	0.05	0.06	0.10	0.11



(a) GSN-1



(b) GSN-2



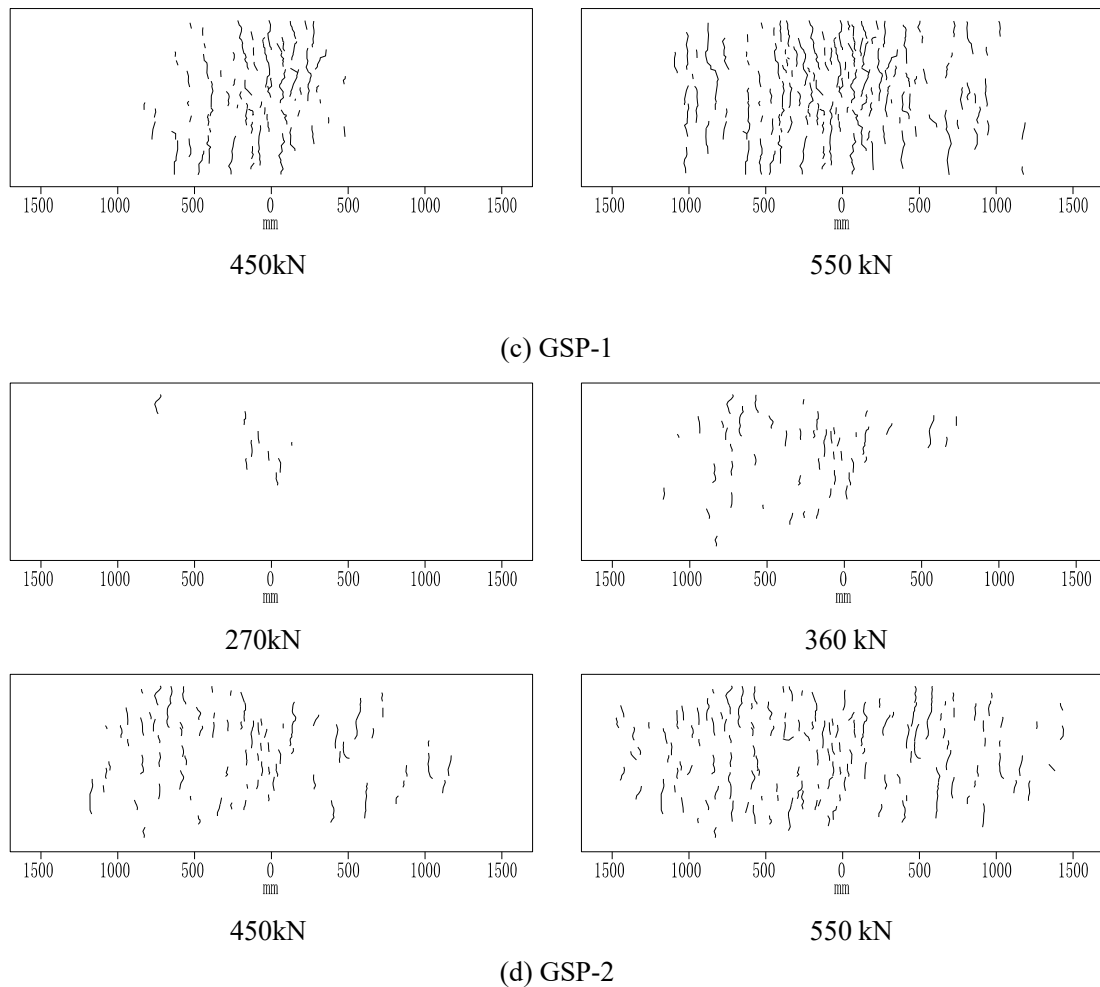


Fig. 13 Tensile concrete crack distributions at different load steps

Strains in concrete and reinforcing steel

Fig. 14 shows the load–strain relationships of the reinforcing steel and concrete slab at the specimen centres up to a load of 200 kN (cracking load of specimen GSP-2), while most of them remained linear during the entire loading process. It can be inferred that the reinforcement and concrete strain in GSP-1 were relatively smaller than those of the other specimens, indicating that the PSC action of the RSS connectors contributed to a decrease in the concrete stress and suppression of crack development. Moreover, the strain in specimen GSN-1 tended to be larger than that in the other specimens owing to the absence of prestress. The load–strain curves of specimens GSP-2 and GSN-2 were similar, which illustrated that the PSC action from increasing the stud distance had a limited effect on the stress decline in the concrete slab.

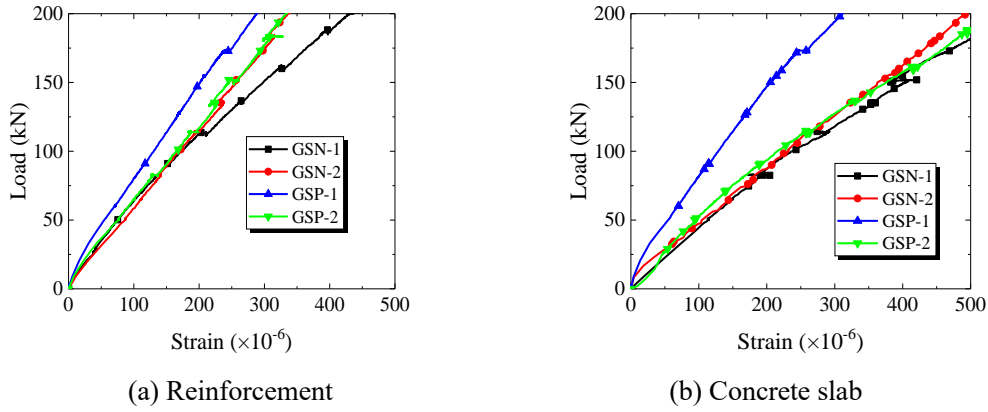


Fig. 14 Load–strain curves of the reinforcement and concrete slab at mid supports

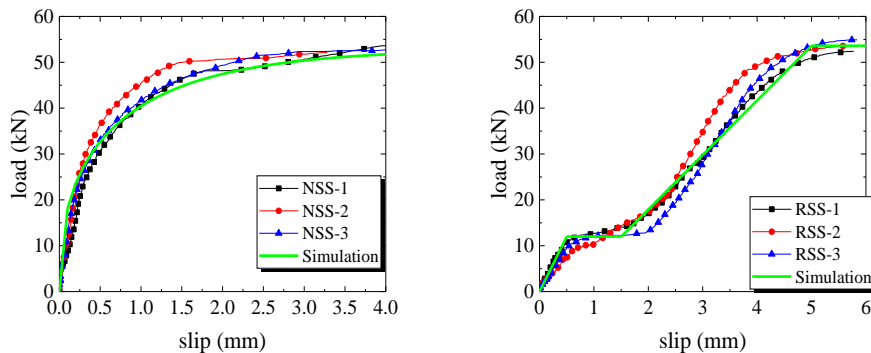
Numerical analysis

Simulation of shear performance

To determine the shear stiffness parameter for the finite element model (FEM), simplified load–slip curves of the stud connectors were simulated according to the push-out tests. For the OHS connectors, the constitutive relation proposed by Ollgaard^[39] (shown in Eq. 1) is widely used, where V and s are the load and slip of a specimen, respectively. In this case, the stud shear strength V_u was 53.0 kN according to the push-out tests. For the RSS connectors, the constitutive relation can be derived based on Nie’s^[40] theory. Eq. 2 presents the modified load–slip relation for the RSS connectors, where s_u is the slip corresponding to V_u . Fig. 15 presents the simulated and measured load–slip curves. It can be inferred that the simulated curves for both the OHS and RSS connectors were in good agreement with the test curves. In both Eq. 1 and Eq. 2 the slip is expressed in millimetres. V is expressed in kN in Eq. 2.

$$V = V_u (1 - e^{-0.71s})^{0.4} \quad (2) \text{ Eq. 1}$$

$$V = \begin{cases} 24s & s \leq 0.5 \\ 12 & 0.5 < s \leq 1.5 \\ 11.9s - 5.9 & 1.5 < s \leq 5 \\ 53.6 & 5 < s \leq s_u \end{cases} \quad (3) \text{ Eq. 2}$$



(a) NSS specimens

(b) RSS specimens

Fig. 15 Comparison between simulated and measured curves

Numerical model setup of composite girders

To further study the effect of PSC action and optimise the structural parameters, FEMs were established using FEM software Abaqus. Fig. 16 shows the element types and meshes of each component in the model. The steel girder was discretised using shell element S4R, the concrete slab was discretised using solid element C3D8R, and the reinforcing bars were discretised using truss element T3D2. The overall mesh size of the model was 50 mm. The prestressed load was simulated by overall cooling of the steel material (using the “Predefined Field” commend in Abaqus). Stud connectors were simulated by the two-node connection element of CONN3DN2. The connection element can simulate the shear stiffness in the longitudinal and transverse directions. The theoretical load–slip curves (Eq. 1 and Eq. 2) of the OHS and RSS connectors calibrated with the experimental results were imported into the “connector section” command (assigned to the connection element) for shear stiffness simulation. “Hard” contact was used to simulate the interaction along the normal direction between the concrete slab and the steel girder. Moreover, the friction coefficient was set as 0.1 [42]. An embedded region was used to constrain the reinforcing bar within the concrete block. In addition, displacement boundary conditions corresponding to the supporting positions were applied, and the loading scheme was uniform loading. The model comprised a total of 33000 elements and 38500 nodes. Considering computational cost and convergence, the analysis procedure adopted Dynamic, Explicit analysis.

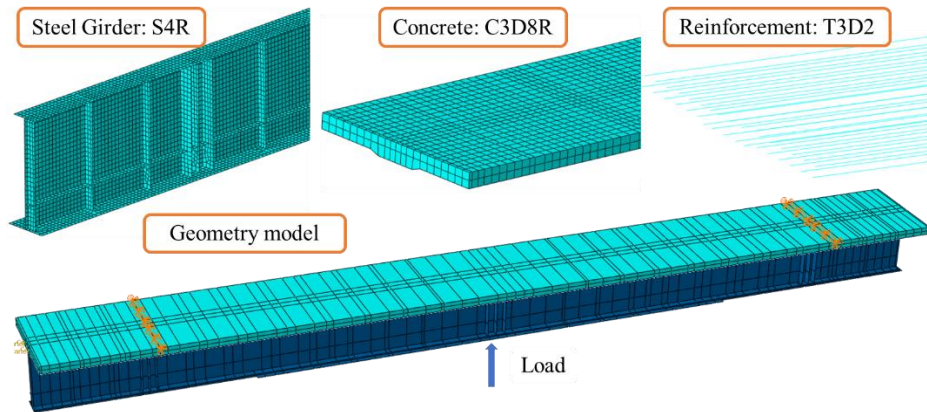


Fig. 16 Element types and meshes of the composite girder model

Sensitivity analyses were carried out to ensure the accuracy of the model as shown in Table 7. The eight models listed were all well converged (A_e/I_e and K_e/I_e were lower than 5%). It can be seen in Table 7 that the dilation angle, the layers of the concrete and the concrete constitutive model have little effect on the accuracy. However, when the mesh size of the steel girder exceeded 100mm, the structural damage pattern changes. To divide the concrete slab into two layers and to simplify the meshing work, mesh size of both concrete and steel took 50mm. The parameters for simulation were determined as the second model in Table 7.

Table 7

Sensitivity analysis results

No.	Dilation angle (°)	Layers of the concrete	Concrete constitutive model	Mesh size(mm)		A_e/I_e (%)	K_e/I_e (%)
				Concrete	Steel		

1	25	2	fib	50	50	3.1%	2.5%
2	37.5	2	fib	50	50	1.2%	0.8%
3	50	2	fib	50	50	1.4%	1.1%
4	37.5	2	fib	50	50	2.9%	1.8%
5	37.5	1	fib	100	100	1.4%	1.2%
6	37.5	2	fib	50	100	1.2%	1.1%
7	37.5	1	fib	75	75	1.3%	1.2%
8	37.5	2	Secant Modulus	50	50	3.3%	1.8%

A_e : Artificial Energy

I_e : Inertia Energy

K_e : Kinetic Energy

Material properties

Concrete

The concrete damage plasticity model [41]-[46] was used for the concrete. The uniaxial stress-strain curve shown in Fig. 17 was derived based on the Chinese Standard GB50010-2010 [47]. Particularly, the tensile and compressive stress-strain curve of concrete could be determined by Eq. 3 and Eq. 6. Eq. 4 and Eq. 7 describes the coefficients of d_t and d_c . Parameter α_t and α_c were the regulation coefficients of the descending part, which were both empirical parameters and provided in GB50010. The plastic strain input into Abaqus equals the total strain minus the elastic strain, where $\varepsilon_{t,r}$ and $0.4f_{c,r}$ were taken as the tensile and compressive elastic strains, respectively [48]. Eq. 9 defines the damage factor d proposed by Sidoroff [49].

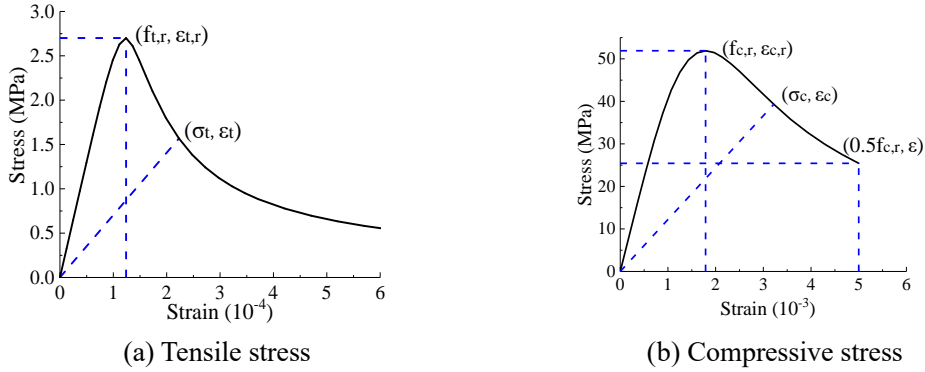


Fig. 17 Stress-strain curve for concrete

$$\sigma = (1 - d_t) E_c \varepsilon, \quad \text{Eq. 3}$$

$$d_t = \begin{cases} 1 - \rho_t [1.2 - 0.2x^5] & x \leq 1 \\ 1 - \frac{\rho_t}{\alpha_t (x-1)^{1.7} + x} & x > 1 \end{cases}, \quad \text{Eq. 4}$$

$$\text{where } x = \frac{\varepsilon}{\varepsilon_{t,r}} \quad \rho_t = \frac{f_{t,r}}{E_c \varepsilon_{t,r}} \quad \text{Eq. 5}$$

$$\sigma = (1 - d_c) E_c \varepsilon, \quad \text{Eq. 6}$$

$$d_c = \begin{cases} 1 - \frac{\rho_c n}{n-1+x^n} & x \leq 1 \\ 1 - \frac{\rho_c}{\alpha_c (x-1)^2 + x} & x > 1 \end{cases}, \quad \text{Eq. 7}$$

where $x = \frac{\varepsilon}{\varepsilon_{c,r}}, \quad \rho_c = \frac{f_{c,r}}{E_c \varepsilon_{c,r}}, \quad n = \frac{E_c \varepsilon_{c,r}}{E_c \varepsilon_{c,r} - f_{c,r}}.$ Eq. 8

$$d = 1 - \sqrt{\frac{\sigma}{E_0 \varepsilon}}. \quad \text{Eq. 9}$$

Steel

Fig. 18(a) presents a trilinear stress–strain curve for simulating steel material characteristics. The specific yielding and ultimate stresses, σ_{ys} and σ_{us} , respectively, of the steel plates with different thicknesses were obtained from the material property tests. The ultimate strain ε_{us} was 0.6%, and the yield strain ε_{ys} was derived using σ_{ys}/E_s , where E_s was 207 GPa. A bilinear stress–strain model was adopted for the reinforcing bar, as shown in Fig. 18(b). The yield stress of the reinforcing bar was taken as 400 MPa with a Young’s modulus of 200 GPa.

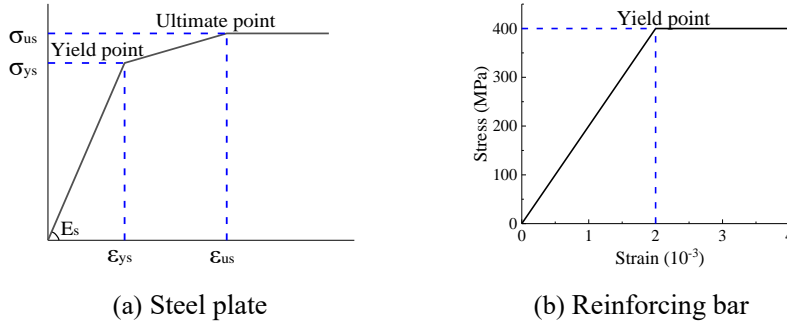


Fig. 18 Stress–strain model for steel

Verification of FEM analysis

Fig. 19 compares the load–deflection curves from the tests and the FEM results for each girder specimen. They are generally well matched with each other. The deviation during the plastic hardening stage was attributed to the accuracy of the material constitutive law and shear connector stiffness distinction. Fig. 20 compares the failure appearances derived from the analysis and test results, both of which show that failure was mainly due to buckling of the bottom steel flange, concrete slab deformation, and web instability.

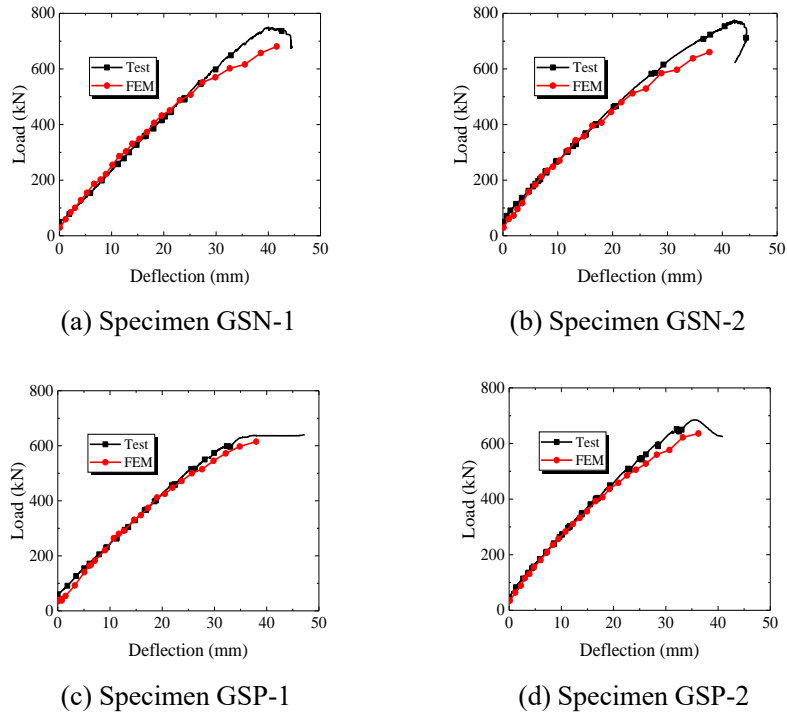


Fig. 19 Comparison of numerical and experimental load–deflection curves at midspan

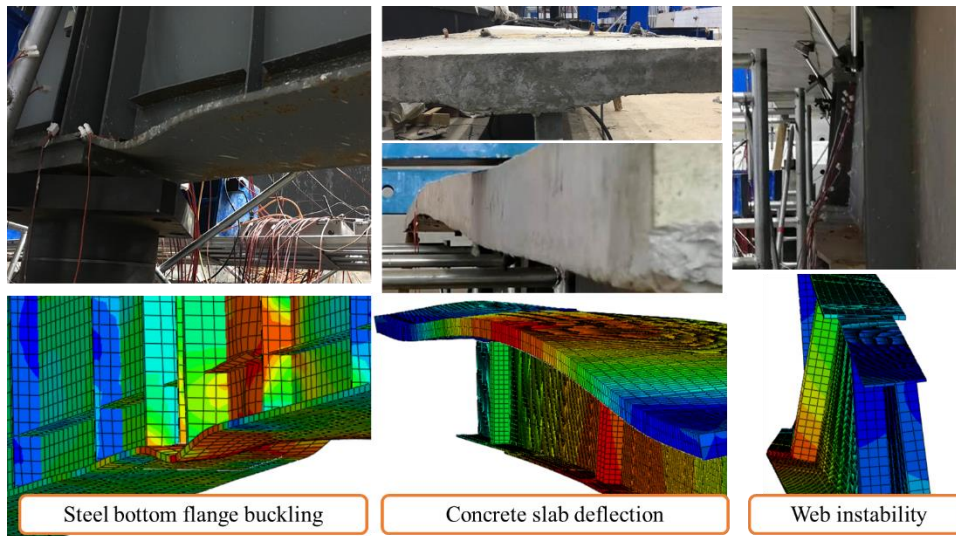


Fig. 20 Comparison of theoretical and experimental failure modes for specimen GSP-1

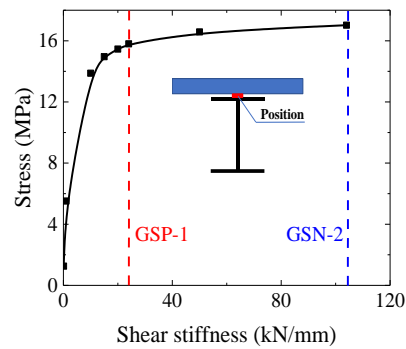
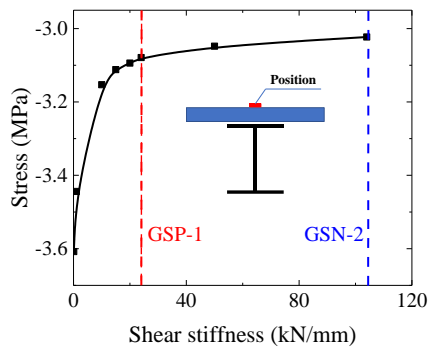
Parametric analysis of composite girders

Effect of PSC action on prestress distribution

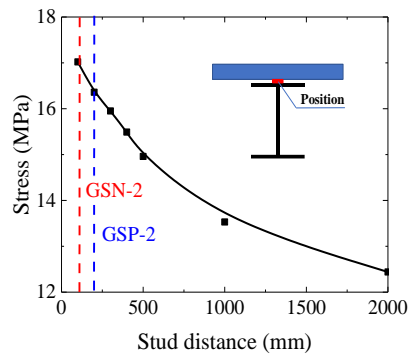
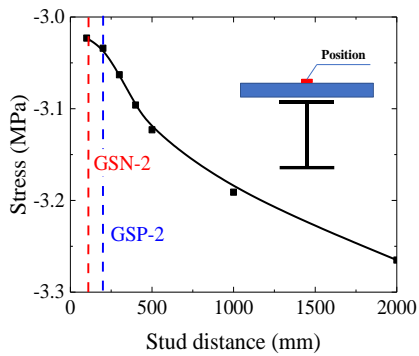
Models with different stud stiffnesses and distances were established for parametric analysis. Fig. 21 and Table 8 reveal the effect of PSC action on the stress state at the midspan due to prestressing. According to the numerical analysis results, the RSS connector and increasing stud distance can both keep the prestress effect from being transferred to the steel girder to increase the prestress level in a concrete slab. In addition, the RSS connector with a shear stiffness less than 20

kN/mm had a larger impact on the prestress distribution. The concrete and steel stresses ranged from -3.09 MPa and 15.46 MPa (for a shear stiffness of 20 kN/mm) to -3.61 MPa and 1.26 MPa (for a shear stiffness of 0.1 kN/mm), respectively. Meanwhile, the stress in the concrete and steel changed uniformly with increasing stud distance.

It can also be inferred that the prestress distribution was more sensitive to the RSS connector than the stud distance, with the concrete stress increasing by 19.4% and the steel stress decreasing by 92.6% when the shear stiffness of the RSS connector was 0.1 kN/mm. However, the stud spacing effect was not significant, with a maximum stress increase in the concrete slab of 8% and a stress decrease in the steel girder of 26.9% (for a stud distance of 2000 mm).



(a) Effect of RSS connectors on concrete slab (b) Effect of RSS connectors on steel girder



(c) Effect of connector distance on the concrete slab (d) Effect of connector distance on the steel girder

Fig. 21 Effect of PSC action on prestress

Table 8

Details of the effect of PSC action on prestress distribution

Models and specimens	Concrete stress (MPa)	Ratio to GSN-2	Steel stress (MPa)	Ratio to GSN-2
GSN-2	-3.02	100.0%	17.02	100.0%
RSS-0.1PS	-3.61	119.4%	1.26	7.4%
RSS-1PS	-3.44	113.9%	5.52	32.4%
RSS-10PS	-3.15	104.3%	13.88	81.6%
RSS-15PS	-3.11	102.9%	14.96	87.9%
RSS-20PS	-3.09	102.3%	15.46	90.8%
RSS-24PS	-3.08	101.9%	15.80	92.8%
RSS-50PS	-3.05	100.8%	16.58	97.4%
DC-200	-3.03	100.4%	16.36	96.1%
DC-300	-3.06	101.3%	15.95	93.7%
DC-400	-3.10	102.4%	15.49	91.0%
DC-500	-3.12	103.3%	14.96	87.9%
DC-1000	-3.19	105.6%	13.53	79.5%
DC-2000	-3.27	108.0%	12.44	73.1%

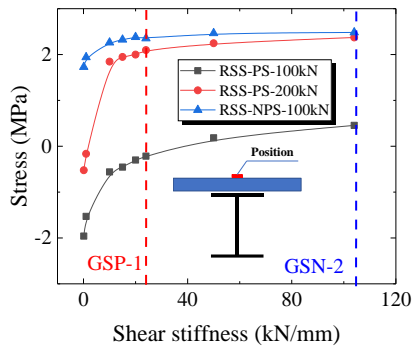
PS: Specimen with prestress. The numbers indicate the shear stiffness (kN/mm).

DC: Distance change. The number indicates the distance between stud connectors in mm

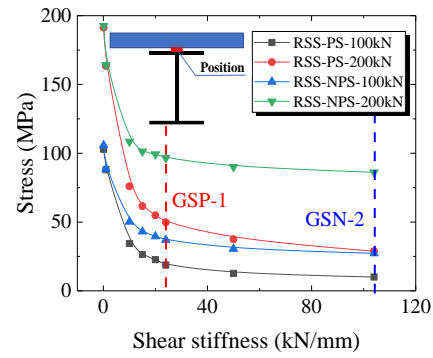
Effect of RSS connector on concrete and steel stress

Fig. 22 shows the stress effect of the connector stiffness and prestressing on the concrete slabs and steel girders at midspan under loads of 100 kN and 200 kN. Concrete stresses for slabs without prestress were not presented under 200 kN because most of the slabs cracked at this load. The RSS connectors with a stiffness lower than 20 kN/mm (approximately 20% of the OHS connector) effectively decreased the stress in the concrete slab, while the steel stress increased accordingly.

Table 9 compares the load-carrying capacities and stress distributions under 100 kN of different specimens with specimen RSS-104NPS corresponding to specimen GSN-1 with an OHS connector and no prestress. It can be inferred that the load-carrying capacity exhibited a maximum decline of 12.3% as the connector stiffness decreased. Meanwhile, the RSS connector contributed to a maximum concrete stress decrease of 30.4% for the NPS group. For the PS group, the concrete stress in specimen RSS-0.1PS exhibited a 530.4% decrease compared with specimen RSS-104PS. It can be concluded that the RSS connector is more effective for prestressed slabs because it prevents the prestress from flowing to the steel girder. In addition, applying an RSS connector could also result in a maximum increase of 288.7% in steel girder stress.



(a) Stress in the concrete slab at midspan



(b) Stress in the steel girder at midspan

Fig. 22 Effect of stiffness of RSS connector

Table 9

Details of the specimens with different connector stiffnesses

Models	Strength		Concrete stress		Steel stress	
	(kN)	Change	(MPa)	Change	(MPa)	Change
RSS-0.1PS	597.3	-12.3%	-1.959	-178.9%	102.9	278.0%
RSS-1PS	610.6	-10.3%	-1.53	-161.6%	88.01	223.3%
RSS-10PS	629.3	-7.6%	-0.5605	-122.6%	34.43	26.5%
RSS-15PS	625.1	-8.2%	-0.4543	-118.3%	26.36	-3.2%
RSS-20PS	648.5	-4.8%	-0.3005	-112.1%	22.64	-16.8%
RSS-24PS	615	-9.7%	-0.215	-108.7%	18.73	-31.2%
RSS-50PS	640.3	-6.0%	0.1827	-92.6%	12.66	-53.5%
RSS-104PS	660.4	-3.0%	0.4552	-81.7%	10	-63.3%
RSS-0.1NPS	607.1	-10.8%	1.729	-30.4%	105.8	288.7%
RSS-1NPS	622.8	-8.5%	1.941	-21.8%	88.58	225.4%
RSS-10NPS	621.3	-8.8%	2.261	-8.9%	50.19	84.4%
RSS-15NPS	635.3	-6.7%	2.325	-6.4%	43.06	58.2%
RSS-20NPS	609	-10.6%	2.38	-4.1%	39.58	45.4%
RSS-24NPS	625.4	-8.2%	2.352	-5.3%	37.04	36.1%
RSS-50NPS	640.8	-5.9%	2.465	-0.7%	30.49	12.0%
RSS-104NPS	680.9	/	2.483	/	27.22	/

PS: Specimen with prestress

NPS: Specimen without prestress

RSS-1024NP: Corresponds to GSN-1

RSS-1024PS: Corresponds to GSN-2

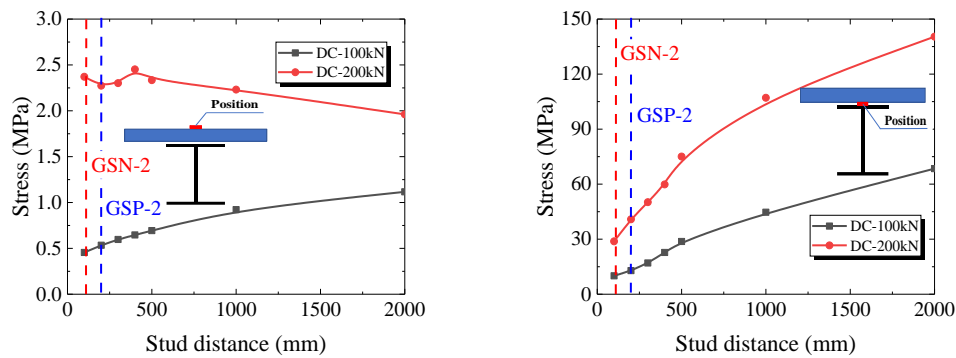
RSS-24PS: Corresponds to GSP-1

Effect of stud distance on concrete and steel stress

Fig. 23 shows the effect of stud spacing on the stresses in the concrete slab and steel girder at midspan under load levels of 100 kN and 200 kN. Table 10 compares the load-carrying capacities and stress distributions under 100 kN for different specimens with specimen DC-100 corresponding

to specimen GSN-2 with 100 mm-stud spacing and prestress. Both the steel girder and concrete slab stresses increased with increasing stud spacing. This can be explained by the stress concentration owing to the larger stud distance, as shown in Fig. 24(a). Because the individual stud shear force increased, the concrete and steel stresses in specimen DC-2000 increased by 145.2% and 584.8%, respectively, compared with specimen DC-100. At a load level of 200 kN, the concrete stress decreased with an increase in the stud distance because the concrete reached its tensile strength, and the stiffness began to decrease. However, the load-carrying capacity hardly changed as the stud distance increased.

In addition, the stud position affected the stress in the concrete slab, particularly when the girder had a large stud distance. As presented in Fig. 24, when the stud distance was fixed at 2000 mm and the stud position at the midspan was avoided (with the maximum bending moment), the concrete stress decreased by 14.4% from 1.1 MPa to 0.95 MPa.



(a) Stress in the concrete slab at midspan (b) Stress in the steel girder at midspan

Fig. 23 Effect of stud distance

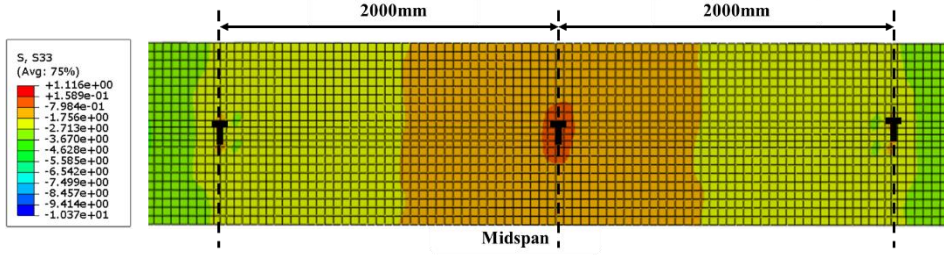
Table 10

Details of the load-carrying capacity and stress distribution of girders with varying stud distances

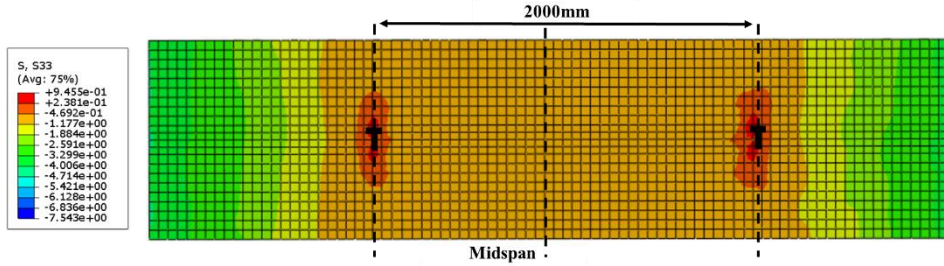
Models	Strength		Concrete stress		Steel stress	
	(kN)	Change	(MPa)	Change	(MPa)	Change
DC-100	660.4	/	0.46	/	10	/
DC-200	636	-3.7%	0.53	17.2%	12.85	28.5%
DC-300	626.5	-5.1%	0.60	31.1%	17.01	70.1%
DC-400	632	-4.3%	0.65	41.9%	22.76	127.6%
DC-500	622.5	-5.7%	0.69	52.4%	28.72	187.2%
DC-1000	639.57	-3.2%	0.92	102.5%	44.68	346.8%
DC-2000	633.22	-4.1%	1.11	145.2%	68.48	584.8%

DC-100: Corresponds to GSN-2

DC-200: Corresponds to GSP-2



(a) Stud in midspan



(a) Stud avoiding midspan

Fig. 24 Concrete stress distribution of specimen with different stud positions (MPa)

Analytical analysis

Analytical model

To further study the influence of stud stiffness on girder stress, an analytical model ^[50] of a girder with PSC action was established. The materials were assumed to be elastic, and the sections of the concrete slab and steel girder were considered plane sections.

Consider a simply supported composite bridge with a span L , concrete slab width w_c , thickness t_c , and steel girder height h_s . When the stud number and stiffness are n_s and k_s , respectively, the shear stiffness per unit length K_s can be derived using Eq. 10.

$$K_s = \frac{n_s k_s}{L} \quad \text{Eq. 10}$$

When a concentrated load P is applied to the midspan, the axial force in the steel girder $N_s(x)$ is equal to the axial force in the concrete slab $N_c(x)$ according to the force balance. The relationship between the bending moment in the steel girder $M_s(x)$ and that in the concrete slab $M_c(x)$ can be deduced using Eq. 11, where h_0 is the distance between the centroidal axes of the steel girder and the concrete slab.

$$M_c(x) + M_s(x) + N_c(x)h_0 = Px / 2 \quad \text{Eq. 11}$$

Considering that the concrete slab has the same curvature as that of the steel girder after deformation, Eq. 12 can be derived.

$$\frac{M_c(x)}{E_c I_c} = \frac{M_s(x)}{E_s I_s} \quad \text{Eq. 12}$$

The axial force can be obtained from the integral of the shear stress per unit length $q(x)$ between

the steel girder and the concrete slab, as shown in Eq. 13.

$$N_c(x) = \int_0^x q(t)dt \quad \text{Eq. 13}$$

The slip strain between the steel girder and concrete slab ε_{slip} (as shown in Fig. 25) can be deduced using Eq. 14, where y_c is the distance between the centroidal axis and bottom edge of the concrete, and y_s is the distance between the centroid axis and top edge of the steel.

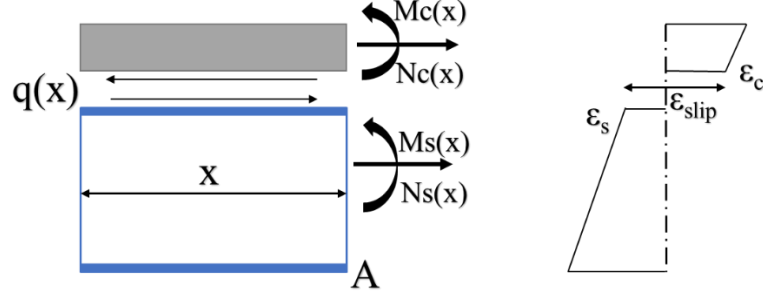


Fig. 25 Illustration of the analytical model

$$\varepsilon_{slip}(x) = \varepsilon_c(x) - \varepsilon_s(x) = \frac{N_c}{E_c A_c} - \frac{M_c y_c}{E_c I_c} - \left(\frac{M_s y_s}{E_s I_s} - \frac{N_s}{E_s A_s} \right) \quad \text{Eq. 14}$$

As $q(x)$ is proportional to K_s and the slip between the steel girder and concrete slab $s(x)$, Eq. 15 can be derived.

$$q(x) = K_s s(x) \quad \text{Eq. 15}$$

As $h_0 = y_c + y_s$, Eq. 16 can be derived by substituting Eq. 14 into Eq. 11.

$$\varepsilon_{slip}(x) = N_c \left(\frac{1}{E_c A_c} + \frac{1}{E_s A_s} + \frac{h_0^2}{EI} \right) - \frac{h_0 P x}{2EI} \quad \text{Eq. 16}$$

Because ε_{slip} can be obtained from the derivative of $s(x)$ (as shown in Eq. 17), Eq. 18 can be

derived by substituting Eq. 17 into Eq. 16, where $\lambda^2 = K_s \left(\frac{1}{E_c A_c} + \frac{1}{E_s A_s} + \frac{h_0^2}{EI} \right)$.

$$\varepsilon_{slip}(x) = \frac{ds(x)}{dx} = \frac{d^2 N_c(x)}{K_s dx^2} \quad \text{Eq. 17}$$

$$N_c''(x) - \lambda^2 N_c(x) = -\frac{h_0 P x K_s}{2EI} \quad \text{Eq. 18}$$

The linear differential equation can be solved as Eq. 19.

$$N_c(x) = \frac{Ph_0 K_s}{2\lambda^3 EI} \left[\lambda x - \frac{\sinh(\lambda x)}{\cosh(\lambda L / 2)} \right] \quad \text{Eq. 19}$$

According to elementary beam theory, the stress at the concrete top edge σ_{ct} and the steel bottom edge σ_{sb} can be derived using Eq. 20. The stress condition can then be obtained by substituting Eq. 19 into Eq. 20.

$$\begin{aligned}\sigma_{ct} &= \frac{N_c}{A_c} + \frac{M_c(w_c - y_c)}{I_c} = \frac{N_c}{A_c} + \frac{(Px/2 - N_c h_0)E_c I_c (w_c - y_c)}{I_c EI} \\ \sigma_{sb} &= \frac{N_s}{A_s} + \frac{M_s(h_s - y_s)}{I_s} = \frac{N_c}{A_s} + \frac{(Px/2 - N_c h_0)E_s I_s (h_s - y_s)}{I_s EI}\end{aligned}\quad \text{Eq. 20}$$

Influence of stud stiffness on stress condition

Focusing on specimen GSN and substituting the section parameters into Eq. 20, the influence of the stud stiffness on the girder stress can be obtained, as shown in Fig. 26. During the parametric analysis, a concentrated load was applied based on the cracking load, and the original stiffness of the stud connector k_{OHS} was selected based on the push-out test. The analysis did not consider the impact of the reinforcing bars.

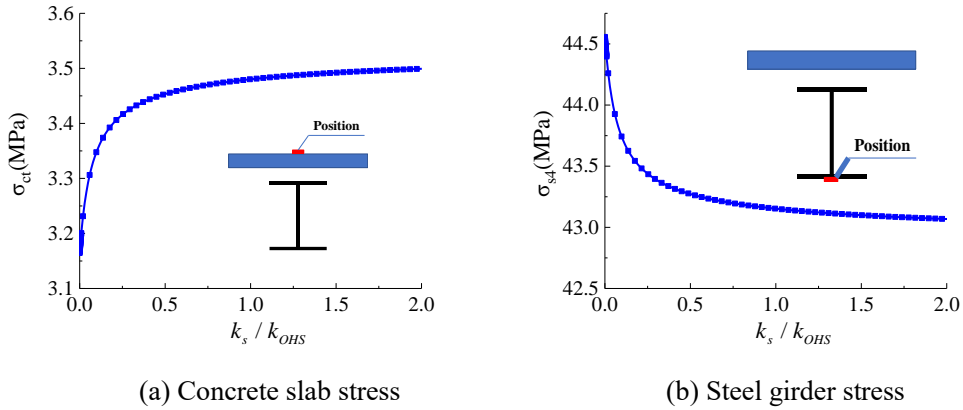


Fig. 26 Influence of stud stiffness on midspan stresses

It can be inferred that the girder stress does not vary linearly with stud stiffness. When the stud stiffness k_s was less than 20% of k_{OHS} , the stress variation in both the concrete slab and the steel girder increased. Taking the concrete stress σ_{ct} as an example, because the flexural stiffness of concrete is negligible ($E_c I_c / EI = 0.0052 \approx 0$), Eq. 20 can be simplified as Eq. 21.

$$\sigma_{ct} = \frac{N_c}{A_c} = \frac{Ph_0 K_s}{2\lambda^3 E I A_c} \left[\lambda x - \frac{\sinh(\lambda x)}{\cosh(\lambda L / 2)} \right] \quad \text{Eq. 21}$$

Because $\sinh(\lambda x) / \cosh(\lambda L / 2) \approx 1$, according to the section parameter, Eq. 22 can be derived by substituting λ into Eq. 21. It can be concluded from Eq. 22 that the concrete stress is exponentially related to the stud stiffness, while the exponential is expected to be 5/3.

$$\sigma_{ct} = \frac{-Ph_0 K_s^{\frac{5}{3}}}{2EI \left(\frac{1}{E_c A_c} + \frac{1}{E_s A_s} + \frac{h_0^2}{EI} \right)^{\frac{3}{2}}} + \frac{Ph_0 L}{4EI \left(\frac{1}{E_c A_c} + \frac{1}{E_s A_s} + \frac{h_0^2}{EI} \right)} \quad \text{Eq. 22}$$

Conclusions

Four simply supported composite girders were fabricated and tested in this study. Six push-out specimens, corresponding to the studs in the girder specimens, were tested. Numerical models of the girder specimens were built for the simulation and parametric analysis. An analytical model of the composite girders with a partial shear connection was also established. Based on the test and simulation results, the following conclusions were drawn:

- (1) According to the push-out tests, wrapping a rubber sleeve (3 mm ×45 mm) around the stud shank (13 mm in diameter) near the stud root achieved stiffness hysteresis characteristics when the steel–concrete interlayer slip was less than 2 mm. Compared with that of an ordinary stud, the shear stiffness of the stud wrapped with the rubber sleeve in this slip range was approximately 90% lower.
- (2) According to the girder tests under negative bending, the failure modes are similar. However, configuring the RSS connectors with a shear stiffness of only 8.1% of the corresponding OHS connectors or setting a 2000 mm OHS spacing caused a reduction in load-carrying capacity of 17% and 11%, respectively. In contrast, the RSS connector decreased the bending stiffness by 12% and reduced concrete crack development, whereas increasing the stud spacing hardly changed the bending stiffness or improved the cracking resistance.
- (3) Based on the parametric analysis of the effect of prestressing the concrete slab, the RSS connector had a greater influence on the prestress distribution between the concrete slab and steel girder than increasing the stud distance. The RSS connector contributed to the prestress increase in the concrete slab by a maximum of 19.4% and to the prestress decline in the steel girder by 92.6%, while the figures were only 8% and 26.9%, respectively, for increasing the stud distance.
- (4) Based on the parametric analysis of the girder under negative bending, the RSS connector with a shear stiffness lower than 20% of the OHS connector effectively decreased the concrete tensile stress, whereas the maximum decrease in load-carrying capacity was only 12.3%. In contrast, when OHS connectors were spaced 2000 mm apart, the concrete and steel stresses increased by 145.2% and 584.8%, respectively. Moreover, avoiding the stud position in the region with a large bending moment decreased the concrete stress by 14.4%.
- (5) According to the analytical results, the stress variation in the composite girder increased when the stud stiffness was less than 20% of the original stiffness. The concrete stress was exponentially related to the stud stiffness, and the exponential was expected to be 5/3.

Acknowledgements

This research was sponsored by the National Natural Science Foundation of China (No. 51978501), Fundamental Research Funds for the Central Universities (No. 22120210437), and China Scholarship Council (No. 202106260050). This support is greatly appreciated.

References

- [1] Ryu H K , Shim C S , Chang S P . Inelastic behaviour of externally prestressed continuous composite box-girder bridge with prefabricated slabs[J]. *Journal of Constructional Steel Research*, 2004, 60(7):989-1005.
- [2] Massaro F M , Malo K A . Stress-laminated timber decks in bridges: Friction between lamellas, butt joints and pre-stressing system[J]. *Engineering Structures*, 2020, 213:110592.
- [3] Steensels R , Vandoren B , Vandewalle L , et al. Evaluation of end-zone detailing of pre-tensioned concrete girders[J]. *Engineering Structures*, 2019, 187(MAY 15):372-383.
- [4] Jiang C , Wu C , Jiang X . Experimental study on fatigue performance of corroded high-strength steel wires used in bridges[J]. *Construction and Building Materials*, 2018, 187(OCT.30):681-690.
- [5] Hamoda A , Hossain K M A , Sennah K , et al. Behaviour of composite high performance concrete slab on steel I-beams subjected to static hogging moment[J]. *Engineering Structures*, 2017, 140:51-65.
- [6] El-Gendy M , El-Salakawy E . Effect of flexural reinforcement type and ratio on the punching behavior of RC slab-column edge connections subjected to reversed-cyclic lateral loads[J]. *Engineering Structures*, 2019, 200:109703-.
- [7] Mohammed A A , Manalo A C , Ferdous W , et al. Experimental and numerical evaluations on the behaviour of structures repaired using prefabricated FRP composites jacket[J]. *Engineering Structures*, 2020, 210.
- [8] Al-Qaralleh M , Toutanji H , Eljufout T . Overloading impact on the flexural behavior of RC beams strengthened with FRP composites under fatigue: Experimental study[J]. *Engineering Structures*, 2020, 221:111045.
- [9] Kim, Choong-Eon, Yun. Structural behavior of a continuous composite truss with a composite bottom chord[J]. *Journal of Constructional Steel Research*, 2015, 10, 1-11.
- [10] Chen X , Su Q , Chong W , et al. Experimental study on double composite action in the negative flexural region of two-span continuous composite box girder[J]. *Journal of Constructional Steel Research*, 2011, 67(10):1636-1648.
- [11] Xu C , Xiao H , Zhang B , et al. Fatigue behavior of steel fiber reinforced concrete composite girder under high cycle negative bending action[J]. *Engineering Structures*, 2021, 241(3):112432.
- [12] Wu T , Sun Y , X Liu, et al. Comparative study of the flexural behavior of steel fiber-reinforced lightweight aggregate concrete beams reinforced and prestressed with CFRP tendons[J]. *Engineering Structures*, 2021, 233(7):111901.
- [13] Hassan R F , Jaber M H , Al-Salim N H , et al. Experimental research on torsional strength of synthetic/steel fiber-reinforced hollow concrete beam[J]. *Engineering Structures*, 2020, 220:110948.
- [14] Ubertini F , Materazzi A L , D'Alessandro A , et al. Natural frequencies identification of a reinforced concrete beam using carbon nanotube cement-based sensors[J]. *Engineering Structures*, 2014, 60(Feb.):265-275.
- [15] D'Alessandro A , Ubertini F , Garcia-Macias E , et al. Static and Dynamic Strain Monitoring of Reinforced Concrete Components through Embedded Carbon Nanotube Cement-Based Sensors[J]. *Shock and Vibration*, 2017, (2017-8-7), 2017, 2017(PT.4):1-11.
- [16] Lin W , Yoda T , Taniguchi N . Application of SFRC in steel-concrete composite

beams subjected to hogging moment[J]. *Journal of Constructional Steel Research*, 2014, 101(oct.):175-183.

[17] Dogu M , Menkulasi F . A flexural design methodology for UHPC beams posttensioned with unbonded tendons[J]. *Engineering Structures*, 2020, 207.

[18] Guo, L., et al. "Seismic evaluation and calculation models of CFDST column blind bolted to composite beam joints with partial shear interaction." *Engineering Structures* 196.OCT.1(2019):109269.1-109269.20.

[19] Al-Sammari, A. T. , P. L. Clouston , and S. F. Brena . "Finite-Element Analysis and Parametric Study of Perforated Steel Plate Shear Connectors for Wood-Concrete Composites." *Journal of structural engineering* 144.10(2018):04018191.1-04018191.10.

[20] Wright H D . The deformation of composite beams with discrete flexible connection[J]. *Journal of Constructional Steel Research*, 1990, 15(1-2):49-64.

[21] Molenstra N , Johnson R P . Partial shear connection in composite beams for buildings[J]. *Proceedings of the Institution of Civil Engineers Part Research & Theory*, 1991.

[22] Loh H Y, Uy B, Bradford M A. The effects of partial shear connection in the hogging moment regions of composite beams: Part I—Experimental study[J]. *Journal of Constructional Steel Research*, 2004, 60(6):897-919

[23] Loh H Y, Uy B, Bradford M A. The effects of partial shear connection in the hogging moment regions of composite beams Part II—Analytical study[J]. *Journal of Constructional Steel Research*, 2004, 60(6):921-962

[24] E. Mirambell, J. Bonilla, L.M. Bezerra, B. Clero, Numerical study on the deflections of steel-concrete composite beams with partial interaction[J]. *Steel Composite Structures* 38 (2021) 67-78.

[25] Bradford MA, Gilbert RI. Composite Beams with Partial Interaction under Sustained Loads[J]. *Journal of Structural Engineering* 1992; 118:1871-83.

[26] El-Sisi, A. A., Hassanin, A. I., Shabaan, H. F., & Elsheikh, A. I.. Effect of external post-tensioning on steel–concrete composite beams with partial connection[J]. *Engineering Structures*, 247, 113130.

[27] Hassanin, A. I., Shabaan, H. F., & Elsheikh, A. I.. The effects of shear stud distribution on the fatigue behavior of steel–concrete composite beams[J]. *Arabian Journal for Science and Engineering*, 45(10), 8403-8426.

[28] Nicoletti, R. S., Rossi, A., de Souza, A. S. C., & Martins, C. H.. Numerical assessment of effective width in steel-concrete composite box girder bridges with partial interaction[J]. *Engineering Structures*, 239, 112333.

[29] Hiragi H, Matsui S, Muto K. Development of favorable stud shear connectors to flexible composite actions[J]. *Struct Eng JSCE* 1998;44A(3):1485–96.

[30] Kitagawa, K. et al. Development of Innovative Composite System-Between Steel and Concrete Members. *International Symposium on connections between Steel and Concrete*, 2001.

[31] Xu X , Liu Y . Analytical and numerical study of the shear stiffness of rubber-sleeved stud[J]. *Journal of Constructional Steel Research*, 2016, 123(aug.):68-78.

[32] Xu X, Liu Y, He J. Study on mechanical behavior of rubber-sleeved studs for steel and concrete composite structures[J]. *Construction and Building Materials* 2014; 53:533-46.

- [33] Zhuang B , Liu Y , Yang F . Experimental and numerical study on deformation performance of Rubber-Sleeved Stud connector under cyclic load[J]. Construction and Building Materials, 2018, 192:179-193.
- [34] Su H , Su Q , Xu C , et al. Shear performance and dimension rationalization study on the rubber sleeved stud connector in continuous composite girder[J]. Engineering Structures, 2021, 240(OCT.30):112371.
- [35] J. Qureshi, D. Lam, Behaviour of Headed Shear Stud in Composite Beams with Profiled Metal Decking[J], Advances in Structural Engineering. 15 (2012) 1547-1558.
- [36] Japanese Society of Steel Construction. Standard on push-out test for headed stud [S]. Japanese Society of Steel Construction, 1996.
- [37] Oehlers DJ, Coughlan CG. The shear stiffness of stud shear connections in composite beams. Journal of Constructional Steel Research 1986; 6:273–84.
- [38] Oehlers DJ, Bradford MA. Elementary behaviour of composite steel & concrete structural members. Butterworth-Heinemann; 1999.
- [39] Ollgaard, J.G.; Slutter, R.G.; Fisher, J.W. Shear strength of stud connectors in lightweight and normal- weight concrete. AISC Eng. J. Am. Inst. Steel Constr. 1971, 8, 55–64.
- [40] Nie J G , Li Y X , Tao M X , et al. Uplift-Restricted and Slip-Permitted T-Shape Connectors[J]. Journal of Bridge Engineering, 2015, 20(4):30-42.
- [41] Li X X L . Parametric Study on Numerical Simulation of Missile Punching Test Using Concrete Damaged Plasticity (CDP) Model[J]. International Journal of Impact Engineering, 2020, 144:103652.
- [42] Rabbat B G , Russell H G . Friction Coefficient of Steel on Concrete or Grout[J]. Journal of Structural Engineering, 1985, 111(3):505-515.
- [43] Choi Y S , Choi S Y , Kim I S , et al. Experimental study on the structural behaviour of calcium-leaching damaged concrete members[J]. Magazine of Concrete Research, 2018, 70(21-22):1102-1117.
- [44] Lubliner, J., Oliver, J., Oller, S. and Oñate, E. . A Plastic Damage Model for Concrete[J]. International Journal of Solids and Structures, 1989, 25(3), 229-326.
- [45] Lee, J. and Fenves, G.L., Plastic-Damage Model for Cyclic Loading of Concrete Structures[J]. Journal of Engineering Mechanics, 1998, 124(8), 892-900.
- [46] Alfarah, B., López-Almansa, F. and Oller, S., New methodology for calculating damage variables evolution in Plastic Damage Model for RC structures[J]. Engineering Structures, 2017, 132, 70-86.
- [47] Chinese Standard GB50010-2010 Code for design of concrete structures, China, 2010
- [48] ENV 1992-1-1. Eurocode-2: design of concrete structures, Part1: general rules and rules for buildings, CEN, 1992.
- [49] Mander J A B , Priestley M J N . Theoretical Stress-Strain Model for Confined Concrete[J]. Journal of Structural Engineering, 1988, 114(8):1804-1826.
- [50] He J , Lin Z , Liu Y , et al. Shear stiffness of headed studs on structural behaviors of steel-concrete composite girders[J]. Steel and Composite Structures, 2020, 36(5):553-568.

6.3 Journal of Bridge Engineering 2023

Tang J, Su Q, Su H, Casas JR, et al. *Experimental and Numerical Study on the Mechanical Behavior of Prestressed Continuous Composite I-Girder Bridges with Partial Connection.*

Journal of Bridge Engineering, 2023, 28: 1084-0702. DOI: 10.1061/JBENF2.BEENG-5955

Note from: Servei de Biblioteques, Publicacions i Arxius de la UPC

This material may be downloaded for personal use only. Any other use requires prior permission of the American Society of Civil Engineers. This material may be found at <https://doi.org/10.1061/JBENF2.BEENG-5955>

Experimental and numerical Study on the Mechanical Behavior of Prestressed Continuous Composite I-Girder bridges with partial connection

Jian Tang ^a, Qingtian Su ^b, Hang Su ^c, Joan Ramon Casas Rius ^d

^a Ph.D. Candidate, Dept. of Bridge Engineering, Tongji Univ. Shanghai 200092, China; Dept. of Civil Engineering, Kyushu Univ., Fukuoka 8190395, Japan. Email: tang.jian.903@s.kyushu-u.ac.jp

^b Professor, Dept. of Bridge Engineering, Tongji Univ. Shanghai 200092, China; Shanghai Engineering Research Center of High Performance Composite Bridge, Shanghai 200092, China (corresponding author). Email: sqt@tongji.edu.cn

^c Ph.D. Candidate, Dept. of Bridge Engineering, Tongji Univ. Shanghai 20092, China; Ph.D. Candidate, Dept. of Civil and Environmental Engineering, Technical Univ. of Catalunya, UPC-BarcelonaTech, Campus Nord, Calle Jordi Girona 1-3, Barcelona 08034, Spain. Email: 2010034@tongji.edu.cn

^d Professor, Dept. of Civil and Environmental Engineering, Technical Univ. of Catalunya, UPC-BarcelonaTech, Campus Nord, Calle Jordi Girona 1-3, Barcelona 08034, Spain. Email: joan.ramon.casas@upc.edu

Abstract

In the prestressed composite girder bridges, the shear connectors will transfer a portion of prestress to the steel girders. However, more prestress is preferred to be remained in the concrete slab to . A Partial Connection-Prestressing (PCP) method is proposed in this paper to decrease the prestress transferred to steel girders. The partial connection is achieved by applying Rubber-Sleeved Studs (RSS) in the prestressed concrete slab in the negative moment region. Since there is no experimental research regarding PCP method in continuous composite girders, two continuous girders specimens were tested under four-point static load to evaluate their mechanical performance. The test results showed that without decreasing ultimate strength and overall stiffness of the steel-concrete composite girders, the PCP method enhanced the cracking load by 3.1 times. Besides, only 12.5% of the prestressing force was transferred into the steel girder at the internal support section with PCP method, while that in girder without PCP reached 25.9%. Thereafter, to elucidate the partial interaction effect and prestress effect on continuous girders' mechanical behavior, numerical models were developed and calibrated with the test results. It was revealed in the numerical analysis

that compared with normal composite girder, applying RSS or prestress alone can improve the cracking load respectively by 11.8% and 157.0 %, while the figure increases to 234.3% when applying RSS and prestressing at the same time. The results indicate that applying RSS in the negative moment region can effectively increase the prestressing efficiency in the concrete slab as well as enhance the bridge serviceability and durability.

Keywords: Steel-concrete composite girders; Static behavior; Experimental study; Rubber - sleeved studs; Numerical study

Nomenclature

NSS: Normal stud
RSS: Rubber-Sleeved Stud
LVDT: Linear Variable Differential Transformer
 σ_p : Concrete stress caused by prestress
 A_p : Area of prestressed tendons
 A_c, A_s : Area of concrete slab and steel girder
 N_c, N_s : Axial force of concrete and steel girder after prestressed
 I_s, I_0 : The inertial moment of steel girder and steel-concrete composite section
 P_{cr}, P_u : Cracking load and ultimate load of specimens
 P_y : Yielding load of bottom steel plate at internal support section
 M_y : Yielding moment of bottom steel plate at the internal support section
 M_u : Ultimate moment at the internal support section
 $\delta_{u-l}, \delta_{u-s}$: Deflection of mid-span at the longer span and shorter span recorded at ultimate load
 f_y, f_u : Yielding stress and ultimate stress of steel plates' coupon test
 $M_{cr,exp}, M_{cr,the}$: Experimental and theoretical cracking moment of concrete slab
 E_c, E_s : Elasticity modulus of concrete slab and steel girder
 h_s : Height of steel girder
 y_0 : Distance between composite neutral axis and steel bottom flange
 y_{comp} : Distance between composite neutral axis and steel top flange (varied with external load)
 Q : Shear force at the steel-concrete interface
 $\sigma_{top}, \sigma_{bot}$: Measured stress of steel top and bottom flange at the section of internal support
 R_m, R_l, R_d : Reactive force of internal support, end support of longer span, end support of shorter span
 $M_{l,test}, M_{s,test}, M_{mid,test}$: The measured bending moments of the mid-span at longer span, mid-span at shorter span, and internal support section
 $M_{l,e}, M_{s,e}, M_{mid,e}$: The elastic calculated bending moments of the mid-span at longer span, mid-span at shorter span, and internal support section
 α : Bending moment modulation factor
 α_t, α_c : The regulation coefficient of the descending part in concrete constitution curve
 $f_{t,r}, f_{c,r}$: Ultimate tensile and compressive strength of the concrete
 $\varepsilon_{t,r}, \varepsilon_{c,r}$: Strain corresponding to the ultimate tensile and compressive strength of the concrete
 k_t : Tensile stiffness of studs
 η : Effective coefficient of prestress application

Introduction

In the negative moment region of medium and long-span continuous composite girders, concrete cracking may facilitate corrosion of connectors and reinforcing steel and have an adverse impact on structures' service and durability performance (Chen et al. 2019; Xu et al. 2021). Prestressing the concrete slab is the most commonly used and effective method to avoid cracking (Tong et al. 2018; Su et al. 2015).

The low prestressing efficiency in the conventional prestressed continuous composite girder can be attributed to the prestress transmission from the concrete slab to the steel girder. Reducing the steel-concrete interaction can decrease the transmission. By far, sparsely arranging connectors and reducing shear connectors' stiffness are commonly adopted to reduce the interaction (Nie et al.

2015; Li et al. 2019; Suwaed et al. 2020; Turmo et al. 2015; Chiorean et al. 2017).

As for the sparse arrangement of shear connectors method, there have been number of experimental and simulation researches in beams. Experimental study conducted for composite beams with different studs spacings verified that applying partial shear connection in negative moment region can increase beam's rotation capacity (Loh et al. 2004). El-Sisi et al. (2021) conducted experimental and finite element studies for strengthened composite beams using externally post-tensioned tendons with partial shear connection under static load. As for analysis method, Hassanin et al. (2020) studied the effects of shear stud distribution on the fatigue behavior of steel-concrete composite beams by nonlinear finite element analysis. Chiorean and Buru (2017) proposed an efficient computer method for non-linear inelastic analysis of composite steel-concrete beams with partial composite action. Lemes et al. (2021) applied a numerical displacement-based formulation with a plastic-hinge approach for the analysis of steel-concrete composite beams with partial shear connection. Furthermore, Nicoletti et al. (2021) studied the interaction degree on the effective width of steel-concrete composite box girder bridges through numerical simulation.

For reducing the stiffness of connectors, a common treatment is wrapping low elastic modulus materials such as foamed plastic, resin mortar, flexible gems, and rubber sleeves (Abe and Hosaka 2002; Mitsunori et al. 2000; Deng et al. 2020; Zeng et al. 2020; Zhuang and Liu 2019; Zhuang et al. 2018, 2020). Abe and Hosaka (2002) applied a new type of flexible connectors to a railway bridge, and verified it could effectively reduce tensile stress generated over the regions at intermediate supports. The research on uplift-restricted and slip-permitted connector showed it had greater slip deformation and could reduce tensile stress of concrete in the negative moment region of composite beams compared with ordinary connectors (Nie et al. 2015; Li et al. 2019). Furthermore, Zhuang et al. (2018, 2019, 2020) and Xu et al. (2020; 2021) investigated the shear mechanism and fatigue performance of rubber-sleeved studs (RSS). Besides, the effects of rubber sleeve height, thickness, stud length, and stud diameter on the shear resistance of rubber-sleeved studs was studied by Xu et al. (2016) and Su et al. (2021). Cao (2017) analysed the effect of connector's shear stiffness on the static performance and deflection of continuous composite girders through linear elastic FE model. The results showed that reducing shear stiffness of the connector in negative moment region can effectively decrease concrete tensile stress, but it cannot prevent concrete slab from cracking.

According to the above review, wrapping low elastic modulus materials around studs can decrease the tensile stress of concrete slabs but can't prevent them from cracking. On the other hand, applying prestress in composite bridges without reducing stud's stiffness will lead to low prestressing efficiency. To date, most of the studies regarding the partial shear interaction of composite structures are based on beams used in building structures. To elucidate the effect of RSS on the overall stiffness and capacity of composite girder bridges, experimental evidences and numerical simulations are needed.

In this paper, Partial Connection-Prestressing (PCP) method was adopted, and the concept of PCP method is illustrated in Fig. 1. The mechanical behavior of prestressed continuous composite I-girder with RSSs in the negative moment region will be studied through the static test of two specimens with large scale ratio of 1:3. A numerical model is also developed and calibrated with the results from the tests.

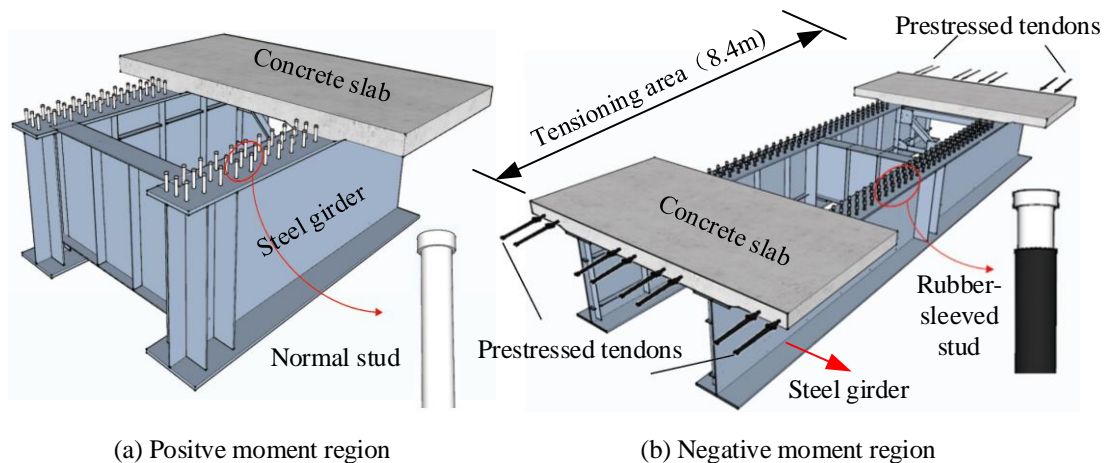


Fig. 1 Three-dimensional illustration of PCP method

Experimental design

Specimen design

The specimens were designed according to 1:3 scaling ratio of a 4×40 m continuous composite girder bridge. The design parameters are shown in Table 1.

Table 1

Structural parameters of continuous girders.

Specimen	span arrangement	Rubber sleeve	Geometrical reinforcement ratio in negative moment region		Geometrical reinforcement ratio in positive moment region
			rebars	prestressing tendon	
GCN	13.14 m + 10.66 m	without	3.77%	0	1.68%
GCRP	13.14 m + 10.66 m	with	3.77%	1.17%	1.68%

The elevation in Fig. 2 shows that the total length of the specimens was 24.18 m. The concrete slab was 2110 mm in width and 85 mm in height with 20 mm thick haunch. The height of the steel girder was 626 mm and the space between the two steel I-girders was 1130 mm.

As for the reinforcement arrangement shown in Fig. 2, there were two layers of longitudinal reinforcements, with diameters in the negative and positive moment region of 12 mm and 8 mm respectively.

For specimen GCRP, the high-strength non-shrink grout was poured in the post-cast region after tensioning. Moreover, 8 prestressed tendons, each tendon containing 2 strands (with the nominal diameter of 15.24 mm), were tensioned in the concrete slab within 4.2 m from the internal support.

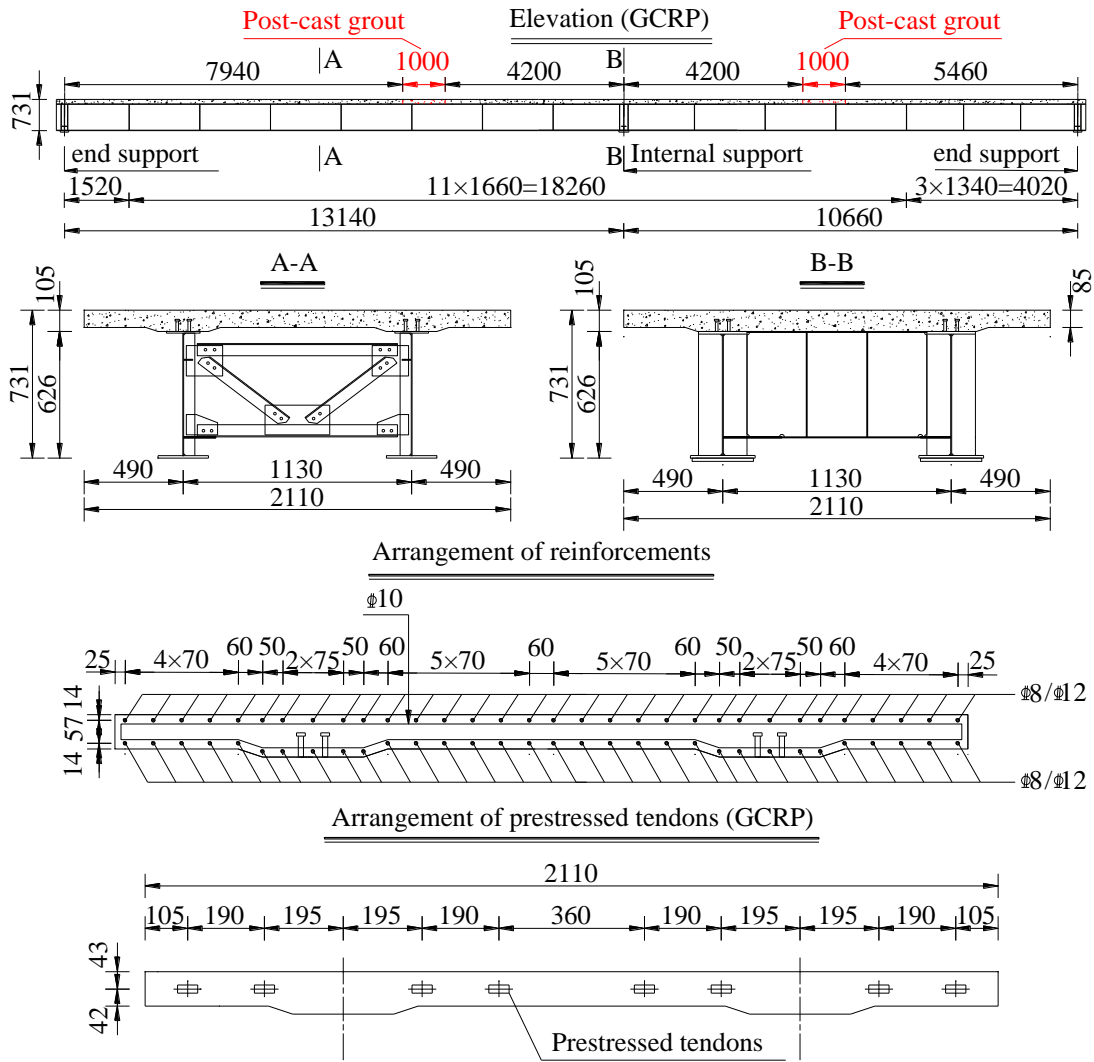


Fig. 2 Overall layout of the specimens (mm)

The studs' layout of the two specimens was the same, with the only difference that RSSs were applied for specimen GCRP within 4.2 m from the internal support. For specimen GCRP as shown in Fig. 3, the longitudinal and transversal spacing of studs was 100 mm and 60 mm respectively and the size of the studs was $\phi 13 \text{ mm} \times 60 \text{ mm}$. In the elevation layout of studs, the red circles are RSSs and black circles are NSSs. According to the research (Xu et al. 2016), the shear stiffness can be significantly reduced when the height of the rubber sleeve reaches 3/4 of the height of the studs and the thickness reaches 1/8 of the diameter of the studs. Thus, the thickness and height of the rubber sleeve were determined as 3 mm and 45 mm respectively.

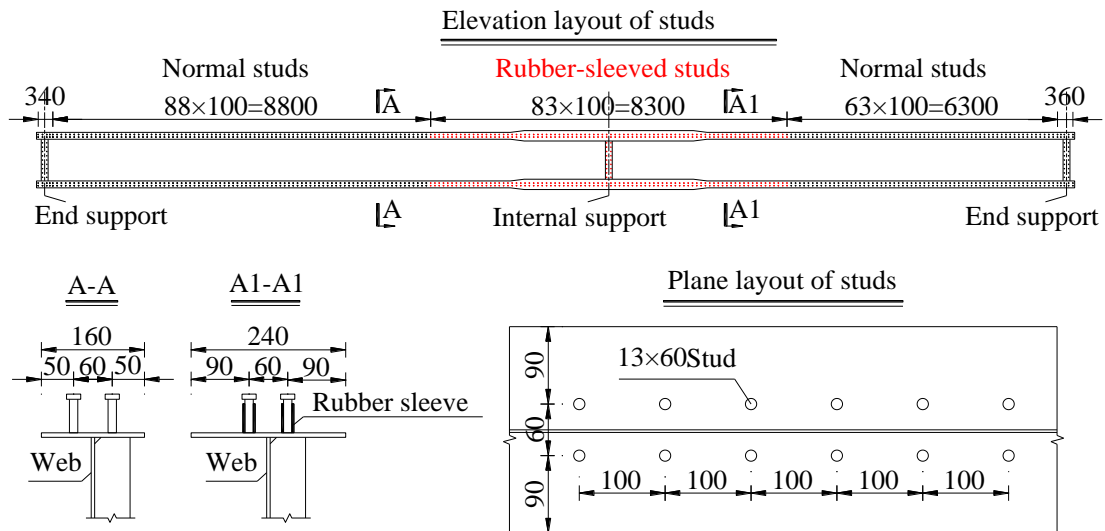


Fig. 3 Studs' layout of GCRP (mm)

Loading program and experimental set-up

Four hydraulic jacks with capacity of 200 tons were used for vertical four-point loading. The loading arrangement is shown in Fig. 4 and Fig. 5. The loading points LP1 and LP4 acted near the mid-span of the longer span and shorter span, respectively. The loading points LP2 and LP3 were determined to get the maximum bending moment value at the internal support section. Six pressure transducers were deployed under each support to monitor the reaction force during loading.

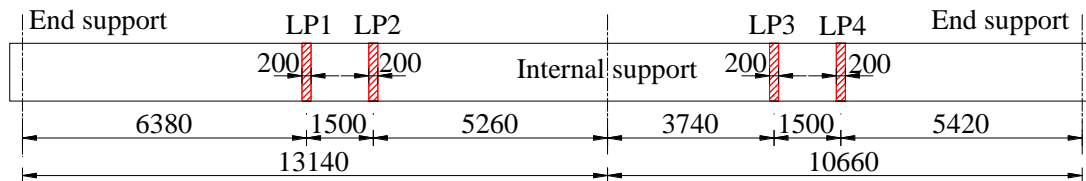


Fig. 4 Loading arrangement

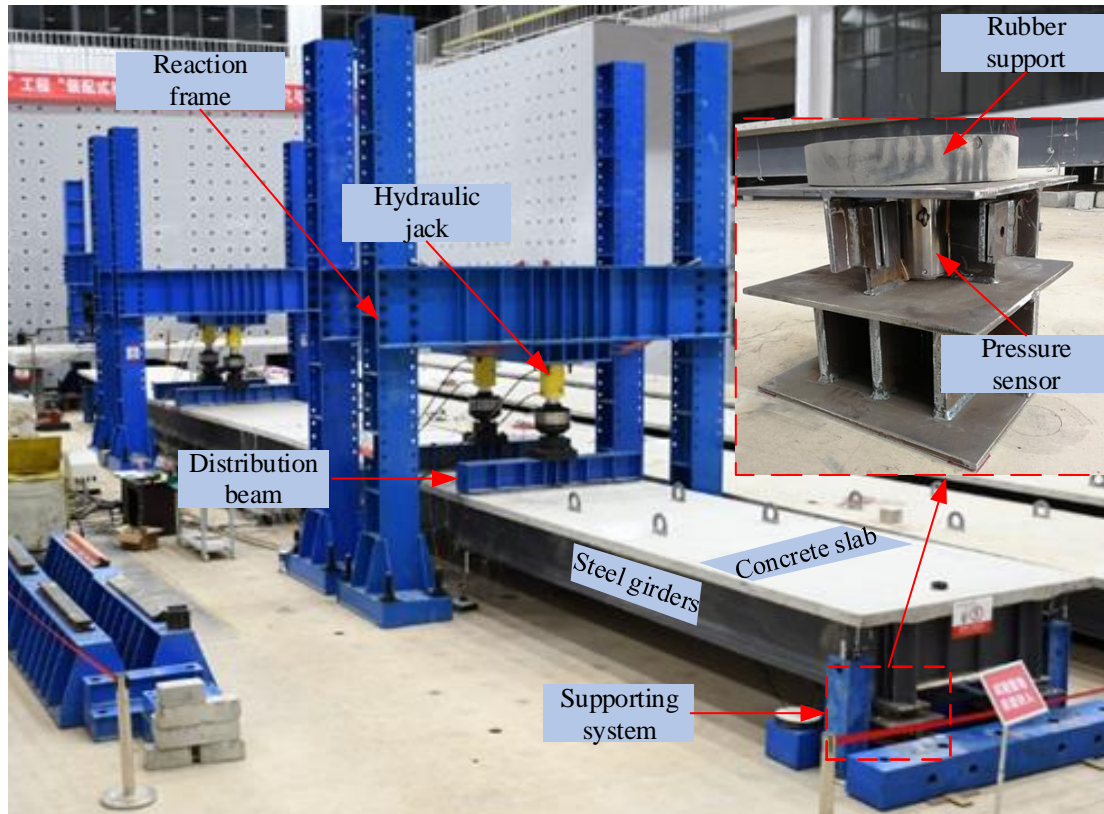


Fig. 5 Loading instrumentation

Fig. 6 shows the layout of displacement sensors and steel-concrete interfacial slip sensors. The displacement was measured at the supports and the sextant positions along the span. The interfacial slip was monitored at the position of support and quartile positions.

Fig. 7 (a) and Fig. 7 (b) show the section number and strain gauges on the webs. The strain gauges were arranged near the internal support and loading points. Besides, the strain was monitored on both steel girders and concrete slab. Fig. 7 (c) illustrates the strain gauges on N5 section. The gauges on the web's inner side were used for checking the out-plane deformations. Also, the strain of reinforcing bars was monitored by strain gauges as shown in Fig. 7 (d).

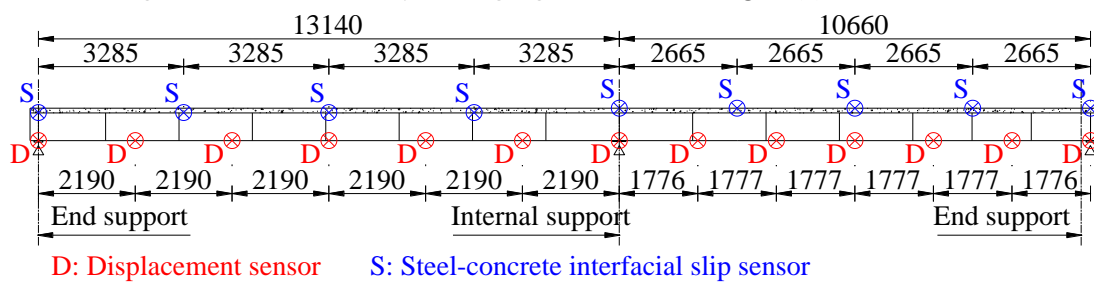
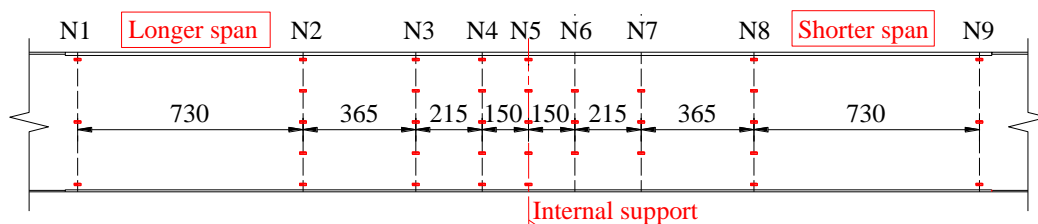
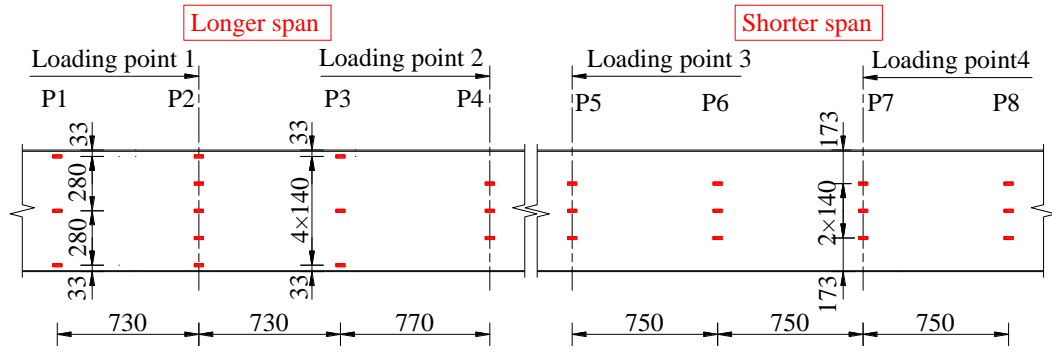


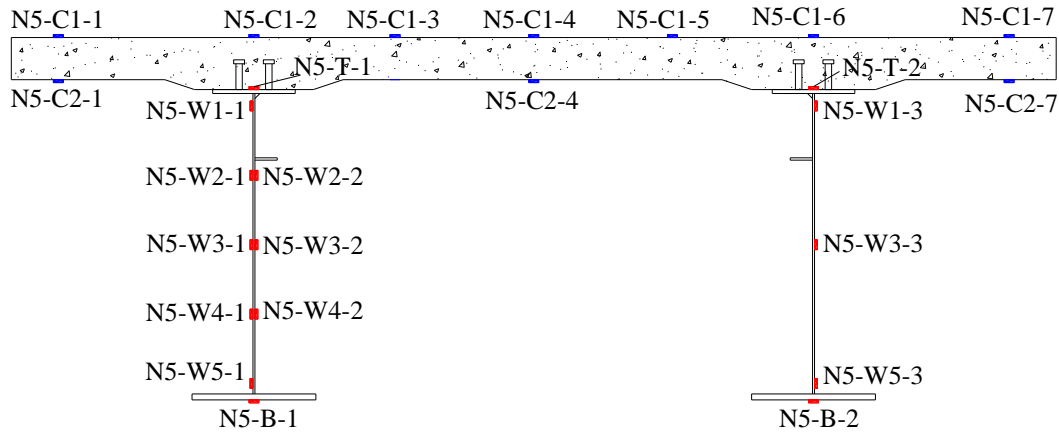
Fig. 6 Position of displacement and slip sensors



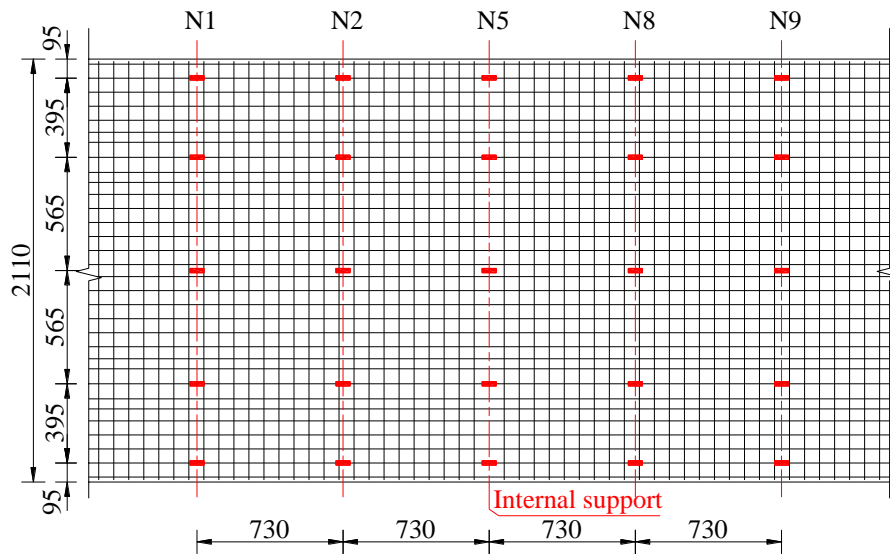
a) Section number and strain gauges in the negative moment region



b) Section number and strain gauges in the positive moment region



c) Strain gauges on N5 section



d) Strain gauges in the reinforcing bars

Fig. 7 Section number and arrangement of strain gauges

Material properties

The compressive strength and Young's modulus of concrete were tested using 150 mm cubic specimens and 150×150×300 mm specimens respectively. The results showed that the 28-day cubic compressive strengths of C50 concrete and high strength non-shrink grout were 51.9 MPa and 65.8 MPa, while the Young's modulus of them were 35300 MPa and 30600 MPa respectively.

Material properties of steel plate and reinforcement were obtained by tensile testing as shown in Table 2. The rubber's properties are listed in Table 3. The prestressing steel was not tested and the standard material properties as provided by the supplier were used.

Table 2
Material properties of steel plate and passive reinforcement.

Thickness /Diameter	4 mm	5 mm	9 mm	8 mm	9 mm	13 mm	Reinforcements	
							8 mm	12 mm
Location	Web	Web	Flange	Flange	Flange	Flange	Positive	Negative
f_y (MPa)	460.7	460.6	334.6	454.5	403.6	441.2	532.0	400.9
f_u (MPa)	515.0	537.3	468.6	530.6	546.6	603.6	636.8	581.1

* “Positive/Negative” indicates the positive/negative moment region.

Table 3
Material properties of NR45 natural rubber

Hardness	Tensile strength (MPa)	Elongation (%)	Brittleness temperature (°C)
45	≥18	≥400	-40

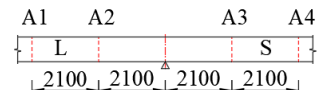
Experimental results

Tensioning of prestressed tendons

The interfacial slip was measured by the dial gauges during the tensioning operation. Four sections were monitored: 2 tensioning ends and 2 quartile positions within the tensioning area. The concrete slab slipping towards the internal support was defined as positive. As shown in Table 4, the prestressed tendons increased the interfacial slip at the anchorage end (A1 section and A4 section).

Table 4
Interface slip after tensioning prestressed tendons (mm).

Section	A1	A2	A3	A4
Slip	0.208	0.072	0.087	0.206



When there is no connection between the concrete slab and the steel girder, the interfacial slip at section A1 can be derived by Eq. (1):

$$\Delta l = \frac{\sigma_p A_p}{A_c E_c} L_0 = \frac{757.5 \times 2240}{208150 \times 3.45 \times 10^4} \times 4.2 \times 10^3 = 0.99 \text{ mm} \quad (1)$$

The above calculated interfacial slip was much larger than the actual value of 0.21 mm. Although the RSS was adopted in the negative moment region, it would still transfer a portion of prestress to the steel girders.

The stress of the concrete slab in the negative moment region after tensioning is shown in Fig. 8. Except for section N5, there were 5 strain gauges in other sections in the negative moment region. The stresses in concrete were not uniformly distributed along the transverse direction, with the smallest compressive stress of -2.2 MPa on section N1 and the largest compressive stress of -4.8 MPa on section N8.

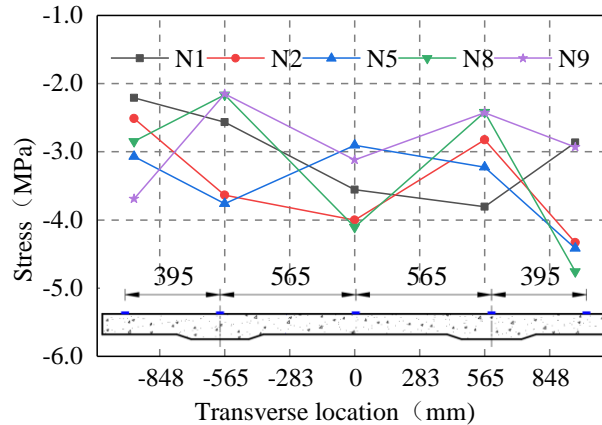


Fig. 8 Concrete stress at negative moment region after prestressing

According to Fig. 8, the mean stress in the concrete slab at section N5 is calculated as 3.5 MPa. Thus, the axial force can be calculated as Eq. (2):

$$N_c = \sigma A_c = 3.5 \times 201850 = 706.5 \text{ kN} \quad (2)$$

Stress diagram of the steel girder after applying prestress can be illustrated in Fig. 9. Since the composite section could not satisfy plane section assumption, the value of y_{comp} is not determined here. Therefore, there are two unknown variables, Q and y_{comp} . Substituting the measured actual stress of the top flange and the bottom flange into Eq. (3) and Eq. (4), the interfacial shear force Q is calculated as 101.4 kN, which means that the axial force transferred to the steel girder is 101.4 kN. Therefore, the ratio of the axial force in the steel girder to the axial force in the concrete slab (Q/N_c) is 1:7.0 for section N5, which means that only 12.5% of the prestress is transferred into the steel girder. It should be noticed that section N5 is the most critical because not only the prestressing force in the concrete is the smallest, but also the ratio (Q/N_c) is the highest.

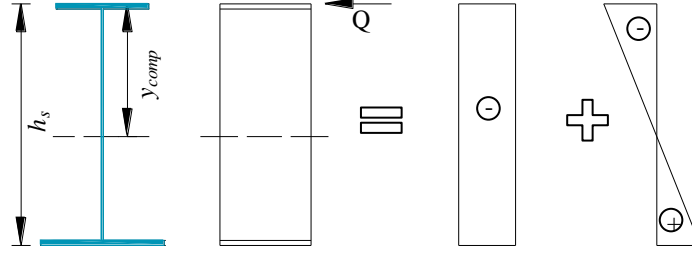


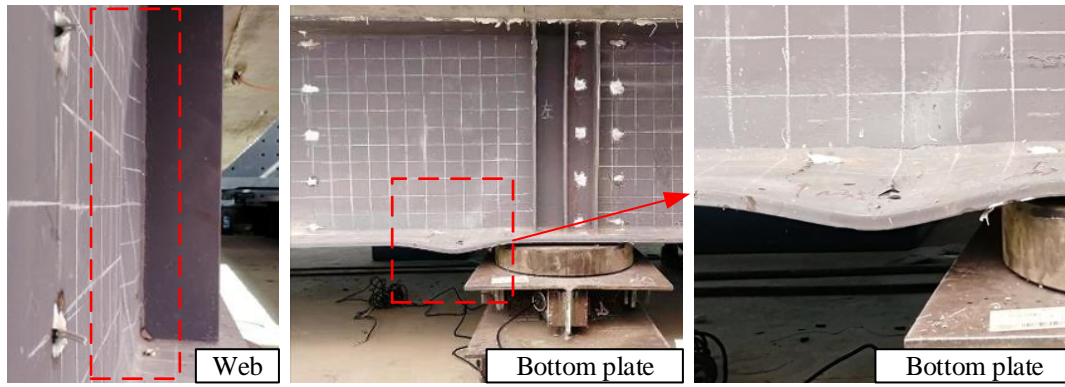
Fig. 9 Stress diagram of steel girder after prestressing

$$\sigma_{top} = \frac{Q}{A_s} + \frac{Q y_{comp}}{I_s} y_{comp} \quad (3)$$

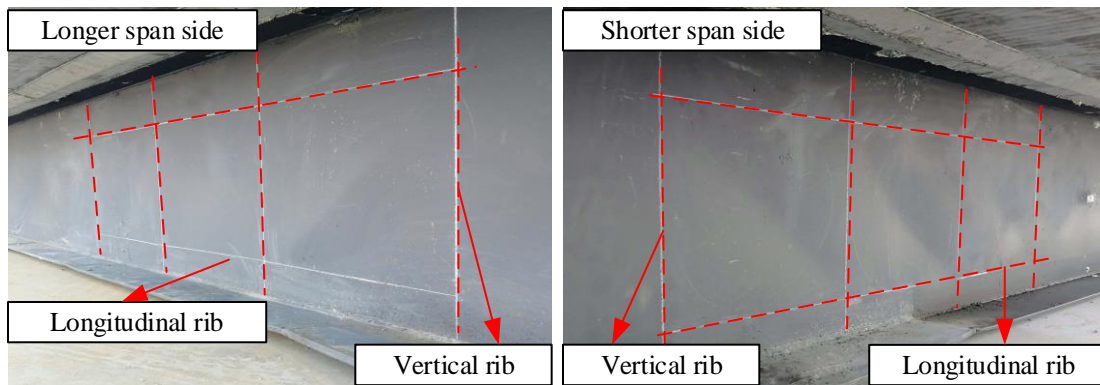
$$\sigma_{bot} = \frac{Q}{A_s} + \frac{Q y_{comp}}{I_s} (h_s - y_{comp}) \quad (4)$$

Failure mode

The failure process of specimen GCN was similar to specimen GCRP. In both cases, the steel bottom plate near the internal support buckled, and the shear buckling of the web occurred in the panel enclosed by the longitudinal stiffening ribs and transverse stiffening ribs. Moreover, the concrete slab was cracked in the negative moment region and the reinforcement yielded near the internal support section. Taking specimen GCRP as an example, the failure pattern of the steel girder is shown in Fig. 10.



a) Buckling of GCRP at middle supporting section



b) Shear buckling of GCRP

Fig. 10 Failure mode of specimen GCRP

Table 5 summarizes the characteristic loads (cracking and ultimate) and ultimate deflection of the two specimens. The reaction force of each support could be obtained by the pressure sensors. Thus, the moment of the two specimens at each section could be calculated according to the static equilibrium equation. The cracking load and cracking moment of specimen GCRP were 3.09 and 3.31 times those of specimen GCN, which means that the cracking performance of the former was significantly improved. The difference between the ratio of load and moment at cracking was because at the beginning of loading, the specimens were not strictly connected with the pressure sensors at the end support. The yielding load and yielding moment of the bottom steel plate at the internal support section in GCRP were 0.81 and 0.86 times those of specimen GCN.

The ultimate load and ultimate bending moment of specimen GCRP were 0.92 and 0.97 times of specimen GCN respectively, which showed that although the ultimate bearing capacity was slightly reduced, the ultimate bending moments were almost unchanged. For specimen GCRP, the ultimate bending moment was 3.0 times of the cracking moment and 1.6 times of the yielding moment, while the figure for specimen GCN was respectively 10.2 and 1.4.

Table 5

Main results for the two specimens.

Specimen	P_{cr} (kN)	M_{cr} (kN·m)	P_y (kN)	M_y (kN·m)	P_u (kN)	M_u (kN·m)	δ_{u-l} (mm)	δ_{u-s} (mm)	M_u/M_{cr}	M_u/M_y
GCRP	170	893.6	350	1664.8	638	2682.7	100.8	49.5	3.0	1.6
GCN	55	270.2	430	1934.9	690	2760.1	117.2	65.7	10.2	1.4
GCRP/GC N	3.0 9	3.31	0.81	0.86	0.92	0.97	0.86	0.75	-	-

*note: P_{cr} , P_u denotes cracking load and ultimate load of specimens; P_y denotes yielding load of bottom steel plate at internal support section; M_y denotes yielding moment of bottom steel plate at the internal support section; M_u denotes ultimate moment at the internal support section; δ_{u-l} , δ_{u-s} denotes deflection of mid-span at the longer

span and shorter span recorded at ultimate load.

Steel-concrete interface slip analysis

The slip between the steel and concrete interfaces during the loading sequence was measured by dial gauges. The positive direction of slip is defined as the concrete slab sliding relative to the steel girder toward the end of the longer span, and the relative slip curves of specimen GCN and specimen GCRP are shown in Fig. 11.

It can be seen that the slip pattern of the two specimens was similar. The slip of them was small near the end support, with the zero point near the internal support and the maximum slip near the quadrant section closer to the internal support in each span. The slip of specimen GCRP was greater than that of specimen GCN at same load level. Moreover, the maximum slip of specimen GCRP was about 10 times that of specimen GCN, which was due to the application of RSS in the negative moment region of specimen GCRP.

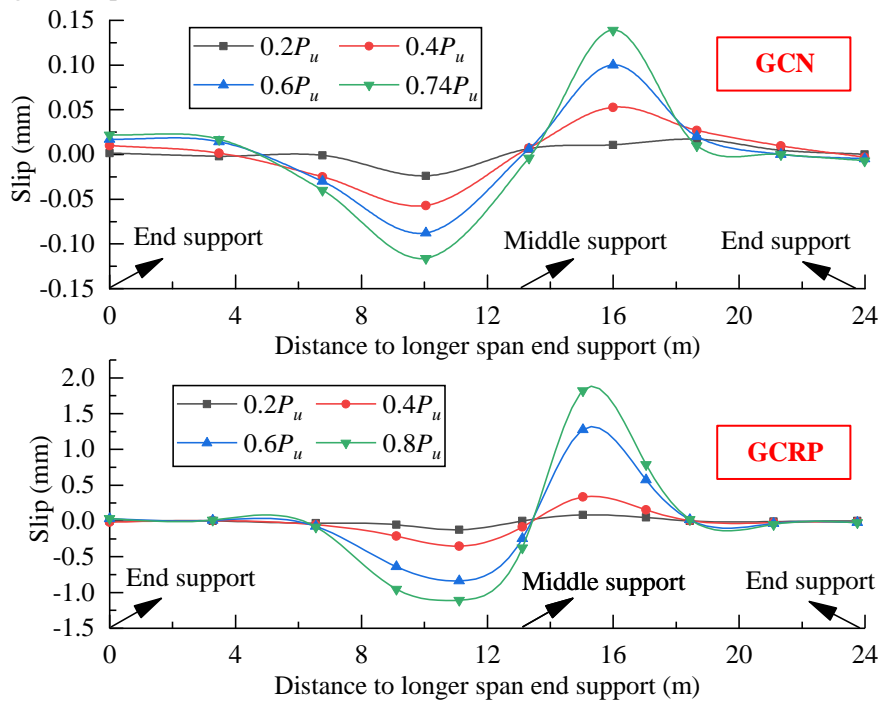


Fig. 11 Interfacial slip between steel and concrete

Load-displacement curve

The deflections at the mid-span in the longer span and the shorter span were measured by LVDTs, and the load-displacement curves of the two specimens are shown in Fig. 12. The load-displacement curves of the two specimens were very close despite of the high interfacial slip of specimen GCRP, which means that RSS has limited effect on the overall stiffness for serviceability loads (below the yielding point). Furthermore, for both specimen GCN and specimen GCRP, the maximum deflection corresponding to the ultimate load was about twice the deflection corresponding to the yielding load of steel plate, indicating that both the two specimens had good ductility.

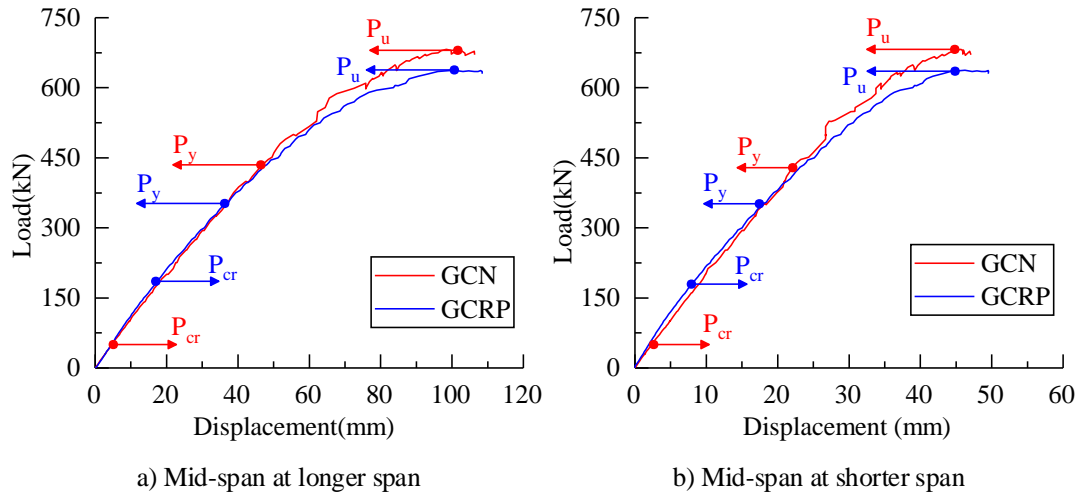


Fig. 12 Load-displacement curve of specimens

Cracking analysis

During the loading process, the crack distribution and crack width in the negative moment region were recorded at each load level as shown in Fig. 13 and Fig. 14. For specimen GCN, when the load was $0.66 P_u$, the cracks were fully developed within twice the section height from the internal support section, and their development was significantly faster than that of specimen GCRP. For specimen GCRP, the cracks were mainly distributed within twice the section height from the internal support section after the load reached $0.8 P_u$.

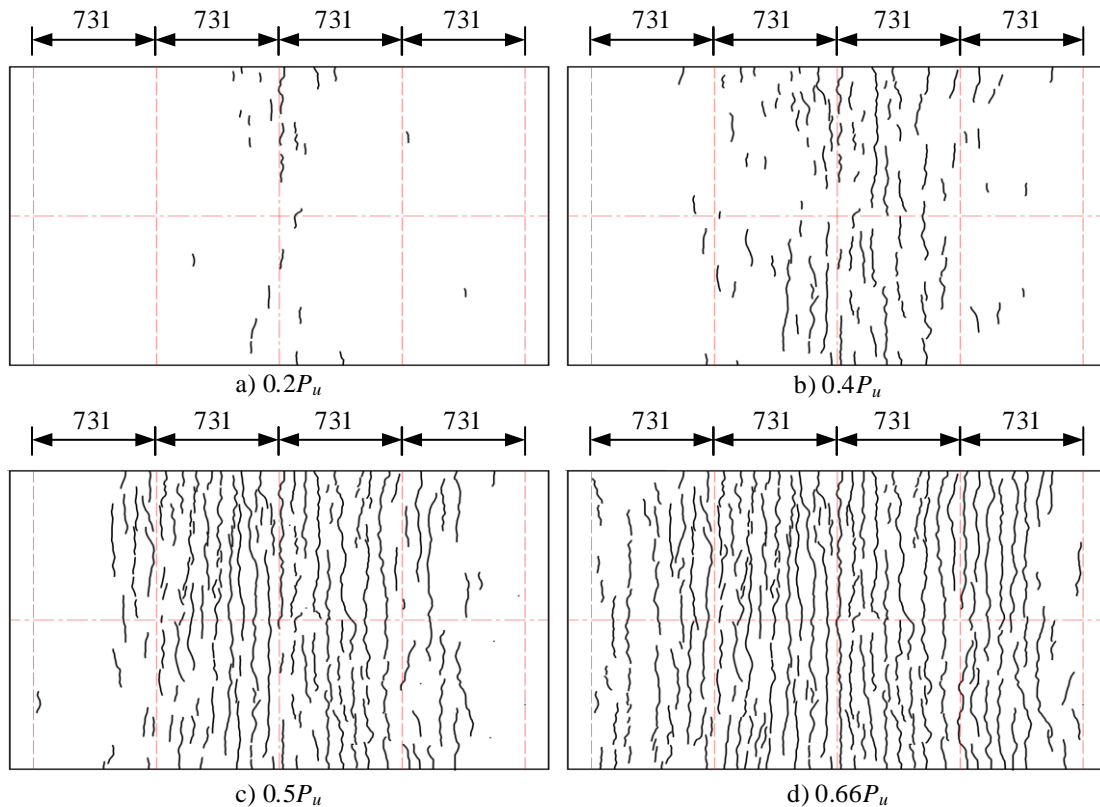


Fig. 13 Cracking development of specimen GCN (Unit: mm)

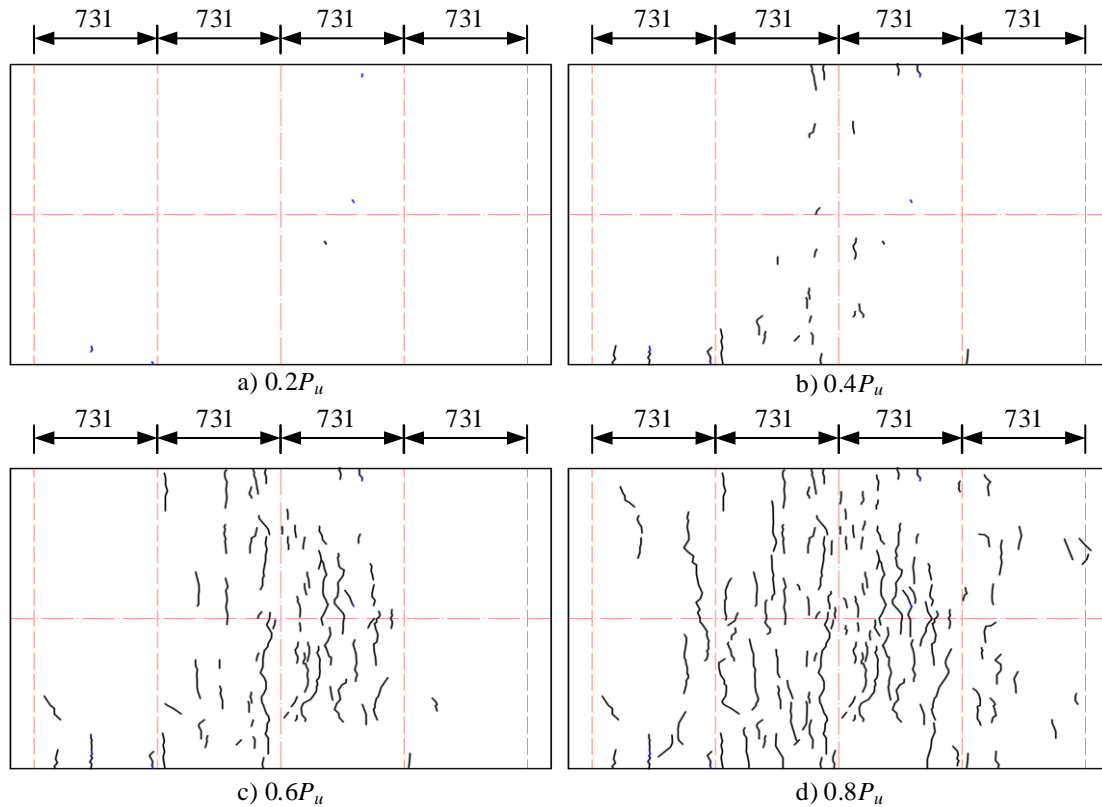


Fig. 14 Cracking development of specimen GCRP (Unit: mm)

The maximum crack width-load curves of the two specimens are shown in Fig. 15(a). It can be seen that for specimen GCRP, the crack development was extremely slow after cracking until the steel bottom flange yielded, and only after 350 kN did the crack start to develop rapidly. The ratio of specimen GCRP's maximum crack width to specimen GCN's maximum crack width versus load is shown in Fig. 15 (b). When the load was in the range of 170~350 kN, the crack width of specimen GCRP was about 50% of that of specimen GCN, and this ratio increased to 81.3 % at load level of 450 kN.

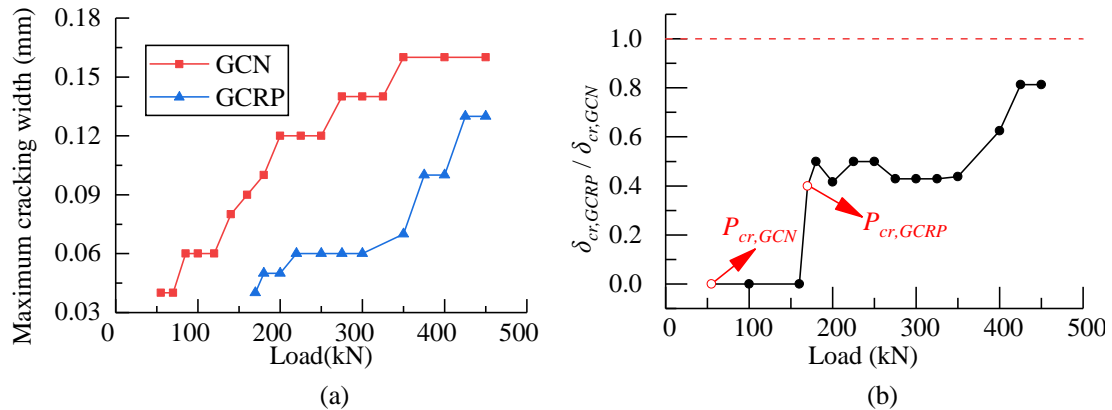


Fig. 15 Maximum cracking with-load curve (Unit: mm)

If the two specimens satisfy plane section assumption and concrete tensile constitutive satisfies the linear relationship as shown in Fig. 16 (a), then the strain distribution under cracking moment can be illustrated in Fig. 16 (b). The cracking bending moment can be calculated as Eq. (5).

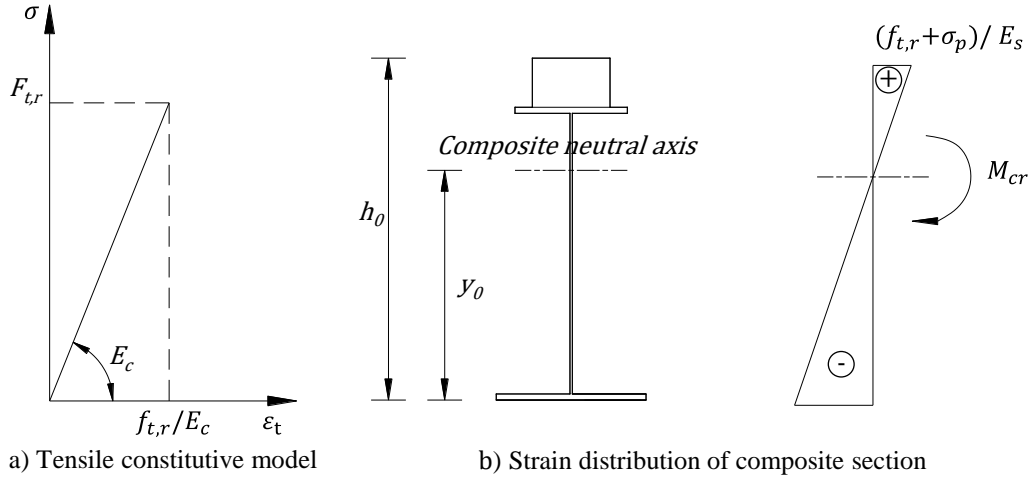


Fig. 16 Strain distribution of composite section under cracking moment

$$M_{cr} = \frac{(f_{t,r} + \sigma_p)I_0 E_s}{(h_0 - y_0)E_c} \quad (5)$$

When prestressing is not present, then $\sigma_p=0$. When structural parameters were substituted into Eq. (5), the theoretical cracking moment, of the two composite I-girders was obtained as presented in Table 6. For specimen GCN, the test value of cracking moment matched well with the theoretical value. However, for specimen GCRP, the test value was significantly higher than the theoretical value, which is due to the partial connection effect on the steel-concrete interface. And because of that, it becomes evident that the assumption of plane section is not valid anymore. For this reason, the theoretical and experimental values do not match well. The studs wrapped with rubber sleeves in the negative moment region helped to decrease the tensile force in the concrete slab under the same load level.

Table 6
Characteristic results of the specimens.

Specimen	$M_{cr,exp}$	$M_{cr,the}$	$M_{cr,exp}/M_{cr,the}$
GCN	270.2	283.8	0.95
GCRP	893.6	660.0	1.35

Load-strain curves

Strain of steel girder

Fig. 17 depicts the load-steel strain responses for the two specimens along the cross-section depth for the intermediate support section. The steel girder exhibited nonlinear behavior at the late loading phase, and the neutral axis was changing during the loading process.

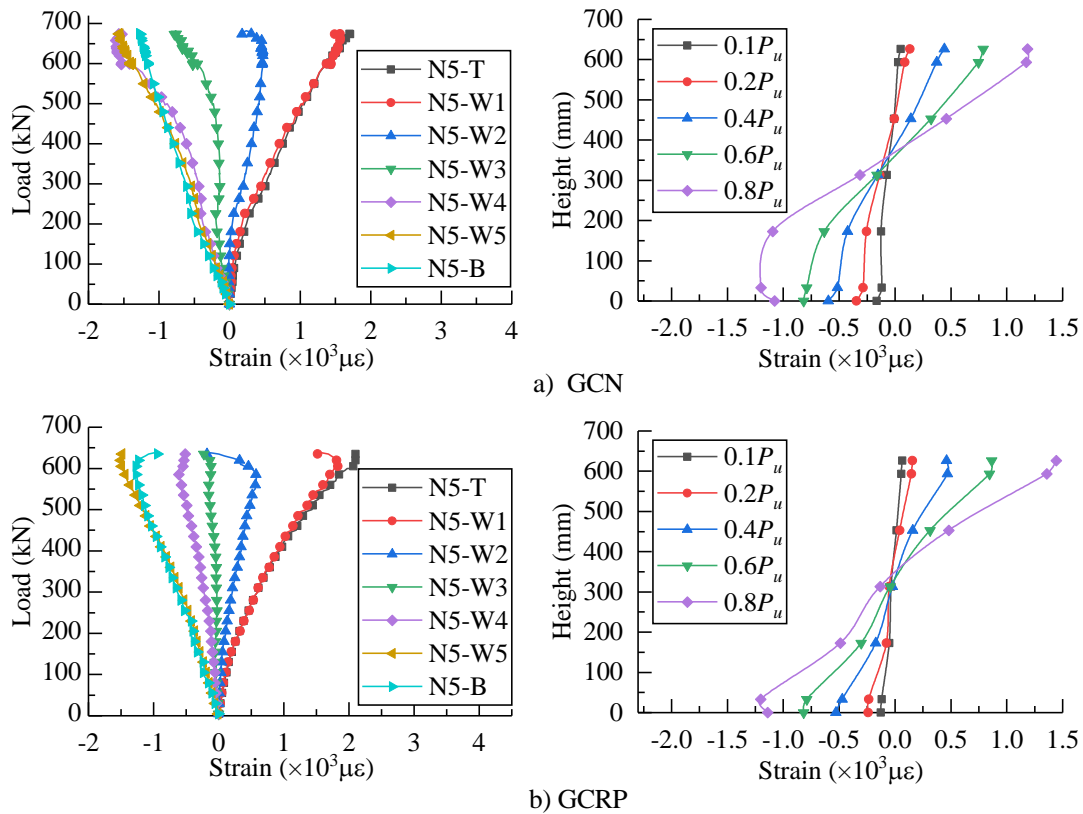


Fig. 17 Strain of steel girder at N5 section

The variation of the neutral axis of the two specimens under different load levels is shown in Fig. 18. The height of the neutral axis of the specimens at section N5 decreased continuously until the load reached 400 kN. For specimen GCRP, the height of its neutral axis was lower than that of GCN due to the partial interaction in the steel-concrete interface. Besides, because of the prestressing in specimen GCRP, its neutral axis decreasing becomes slower than specimen GCN. Combined with the slip data, it can be inferred that after applying RSS in the negative moment region, specimen GCRP was subjected to a large slip in the negative moment region, so the neutral axis shifted down and the composite section no longer met the plane section assumption.

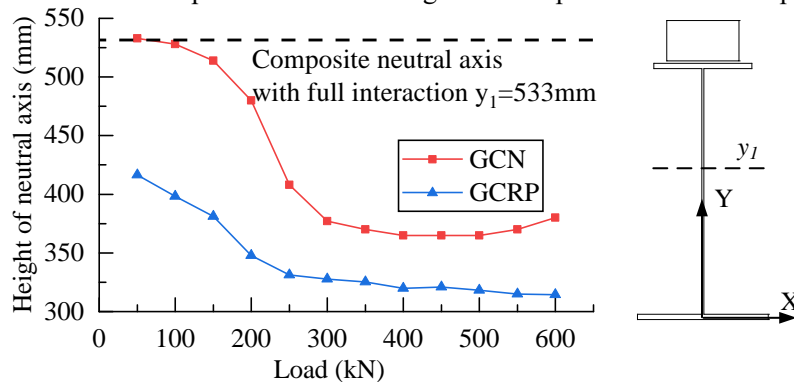


Fig. 18 Neutral axis' position vs load for the two specimens (section N5)

The load-strain curve in the steel upper flange of the two specimens at four sections N5, N4, N3, and N2 were plotted in the same graph for comparison, as shown in Fig. 19. To compare the stress variation under same load level, the stress due to prestressing of specimen GCRP is subtracted. The stresses in the steel upper flange of specimen GCRP were higher than those in specimen GCN under same load level in the negative moment region where the RSS was arranged. The partial shear interaction effect in the steel-concrete interface of GCRP is thus confirmed.

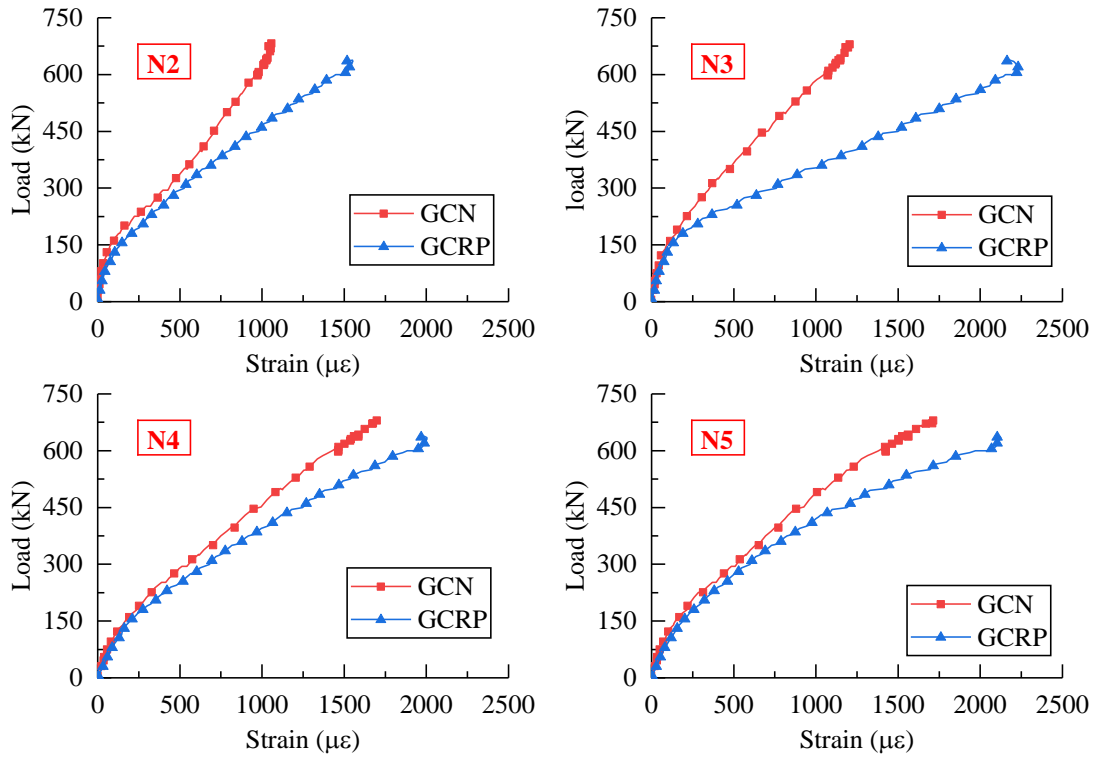
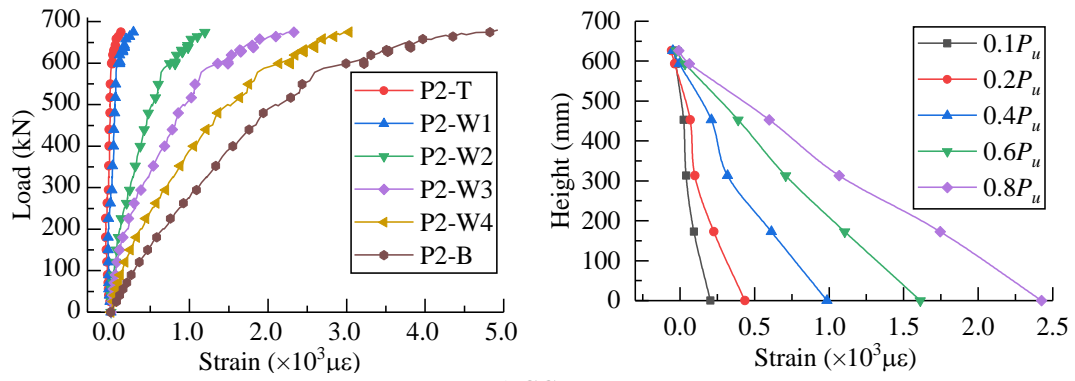
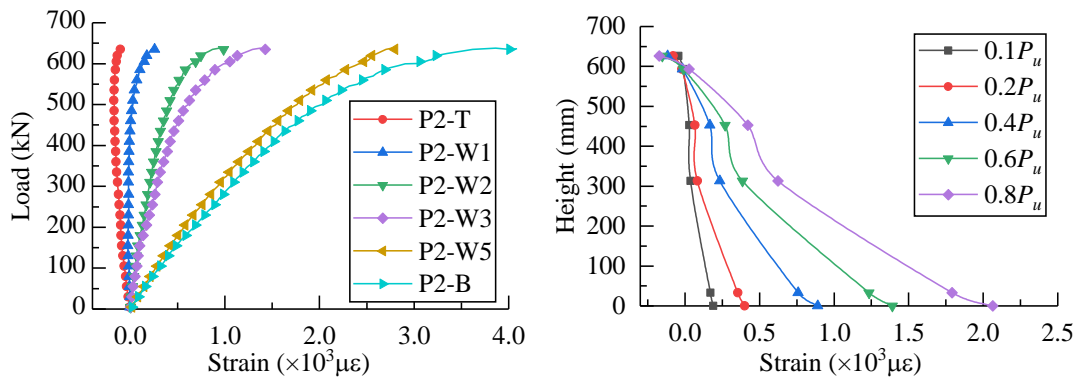


Fig. 19 Strain of steel upper flange at negative moment region

The strain profile at different load levels of section P2 (Loading point 1) and section P7 (Loading point 4) are shown in Fig. 20 and Fig. 21 respectively. The steel bottom flanges of the two specimens had yielded when the structures reached their limit state in both section P2 and section P7. As for section P2, the yielding heights of specimen GCN and specimen GCRP on the web were 313 mm and 173 mm respectively, which means that the specimen GCN had a higher degree of plastic development at the mid-span section in the longer span than specimen GCRP.

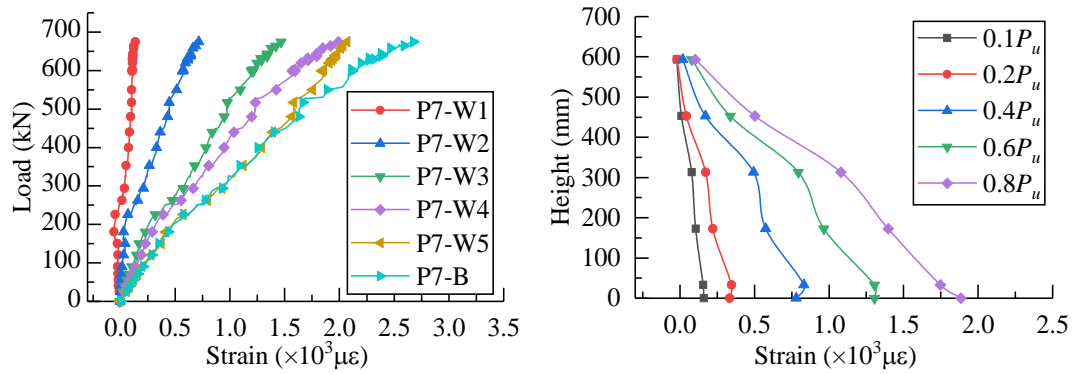


a) GCN

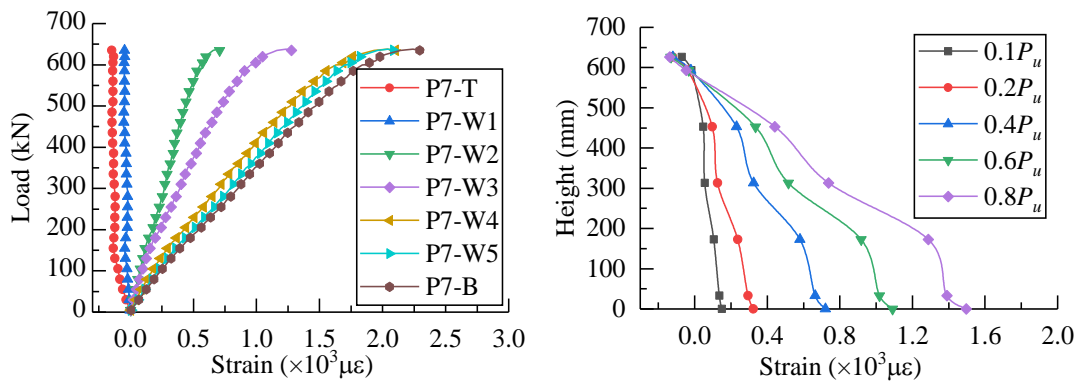


b) GCRP

Fig. 20 Strain profiles at P2 section



a) GCN



b) GCRP

Fig. 21 Strain profiles at P7 section

Strain of reinforcement and concrete

Strain of reinforcement

For the two specimens, only the reinforcement in section N5 went into yield as shown in Fig. 22. Moreover, the strain distribution along the transverse position showed that the strains were not uniformly distributed in the transverse direction. The stress at the position corresponding to the centerline of the steel girder was the largest and the difference between the strains at this location and other locations increased gradually with the increase of loads.

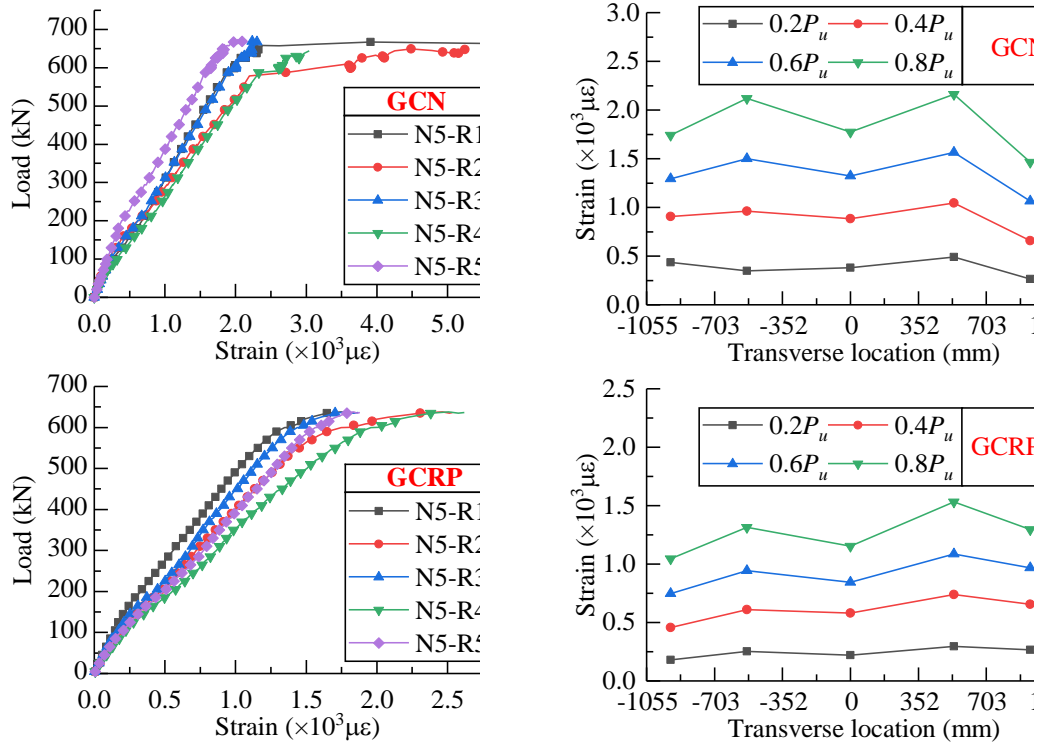
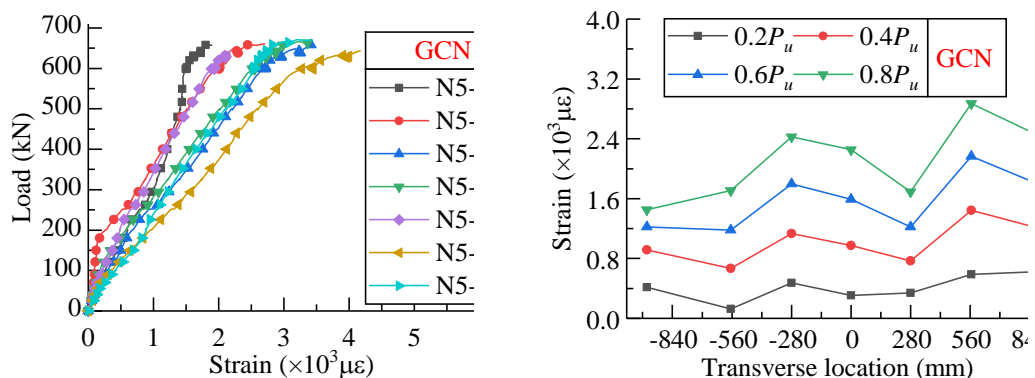


Fig. 22 Strain of reinforcement at N5 section

Strain of concrete slab

The load-strain curves for the concrete slab at N5 section are shown in Fig. 23. There was a sudden increase for both specimens at concrete cracking. Comparing the load-strain curves of the concrete in the two specimens at same load level, the average concrete strain of specimen GCRP at section N5 was less than that in specimen GCN.



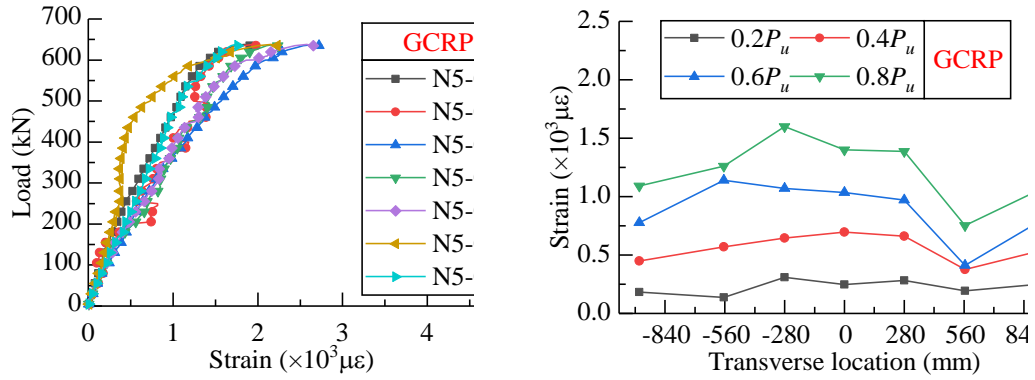


Fig. 23 Strain of concrete slab at N5 section

The distribution of concrete strains along the transverse direction in section P2 is shown in Fig. 24. The strains were roughly symmetrically distributed along the transverse direction. Besides, the strains in the region near the center were higher than in the edges. The specimen GCRP showed a similar pattern to that of specimen GCN. As seen in the figure, the maximum strain in the concrete is always far from the maximum compressive strain. In fact, no crushing of the concrete was detected during the test.

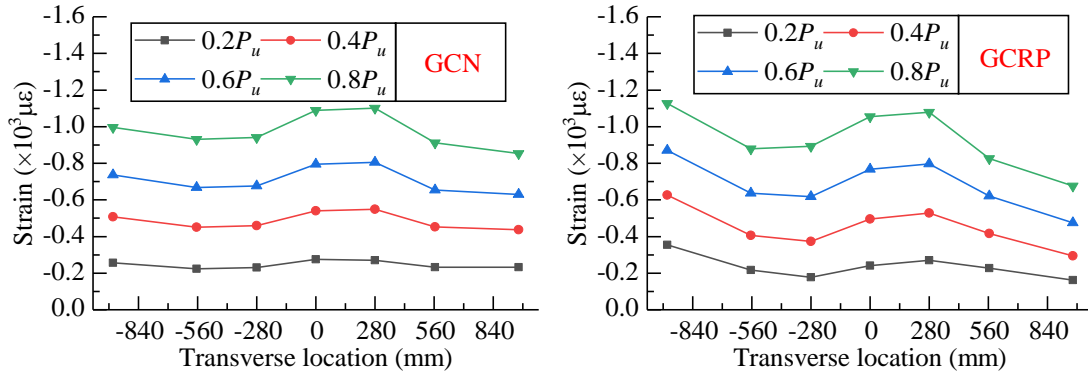


Fig. 24 Strain of concrete slab at P2 section

Internal force redistribution

When the concrete slab in the negative moment region cracks, the structure enters into the non-linear regime. Thereafter, the yielding of the lower flange of the steel in the negative moment region furthers the development of structural plasticity. Since the specimens are statically indeterminate structures, the development of plasticity in the structure results in the redistribution of internal forces, i.e., decrease of bending moment in the negative moment region (where plastic effects are present) while increase of bending moment in the positive moment region.

The reaction force was measured by the pressure transducer under the support. Fig. 25 and Fig. 26 depicts the monitoring results. It can be seen from Fig. 26 that when the response of the structure becomes non-linear, the proportion of the reaction force at the internal support (R_m) continued to decrease, while the proportion of the reaction force at the two end supports (R_l at longer span and R_s at shorter span) kept increasing.

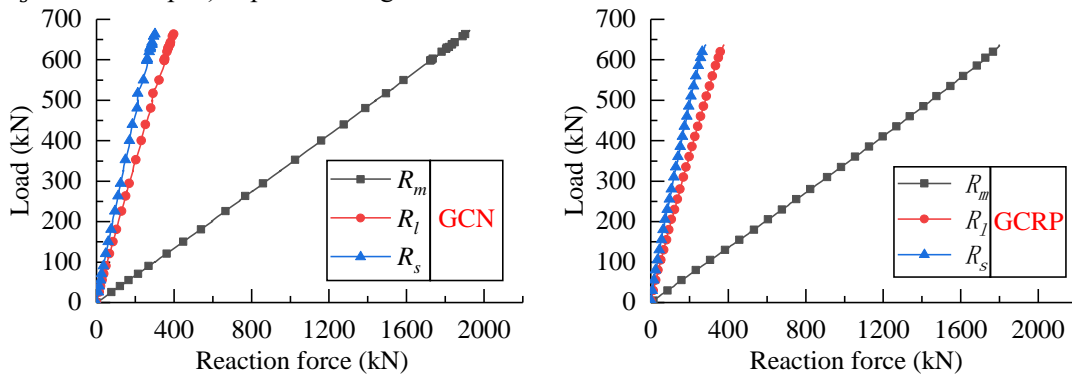


Fig. 25 Load-reaction force curve of the specimens

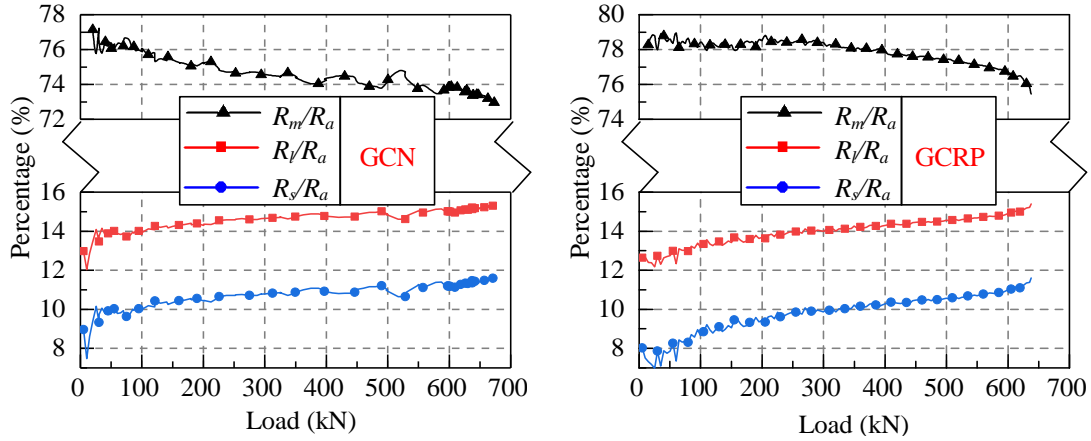


Fig. 26 Reaction force ratio-Load curve

After obtaining the support reaction forces, the bending moment of the specimens was deduced according to the static equilibrium conditions. The elastic bending moment without considering concrete cracking and any redistribution was also calculated with the value of the imposed load and compared with the test results, as shown in Fig. 27.

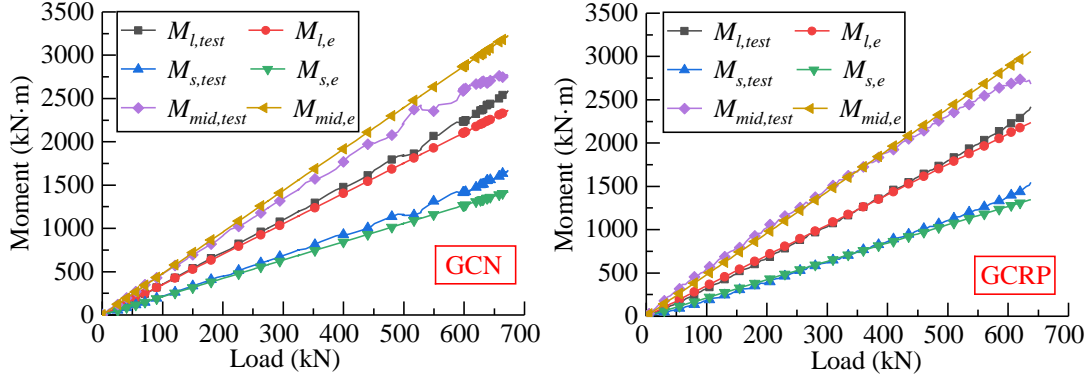


Fig. 27 Moment-load curve for specimens

In Fig. 27, at the plastic phase of both specimens, the measured negative bending moment at the internal support section was smaller than the elastic bending moment, while the positive bending moment at the mid-span section of the longer span and the shorter span were larger than the elastic bending moment. The difference between the measured bending moment and the elastic bending moment increased with the load level, indicating that moment redistribution occurred in both specimens.

The bending moment modulation factor α can be calculated according to Eq. (6). Where M_{test} is the experimental moment of each section when the structure reaches the ultimate carrying capacity and M_e is the elastic bending moment under ultimate load.

$$\alpha = \left| \frac{M_{test} - M_e}{M_e} \right| \times 100\% \quad (6)$$

The moment modulation coefficients for the two specimens are shown in Table 7, which indicates that the difference between the moment modulation coefficients of the two specimens at representative sections P2, N5, and P7 is small and the plastic response of them is similar.

Table 7

Moment modulation coefficients of the specimens.

Specimen	N5	P2	P7	
GCN	14.5%	9.6%	17.4%	
GCRP	15.0%	9.9%	18.0%	

Finite element analysis

General

The experimental results were used to calibrate a numerical model developed that is able to simulate the partial shear connection of the concrete slab and steel girders as well as the prestressing effects. The numerical model is used thereafter to carry out a parametric study of the advantages of the proposed solution.

ABAQUS was used for finite element analysis of the two specimens. Regarding the boundary condition, two longitudinal sliding supports were set at the end supports and the intermediate supports were fixed. The finite element model is shown in Fig. 28.

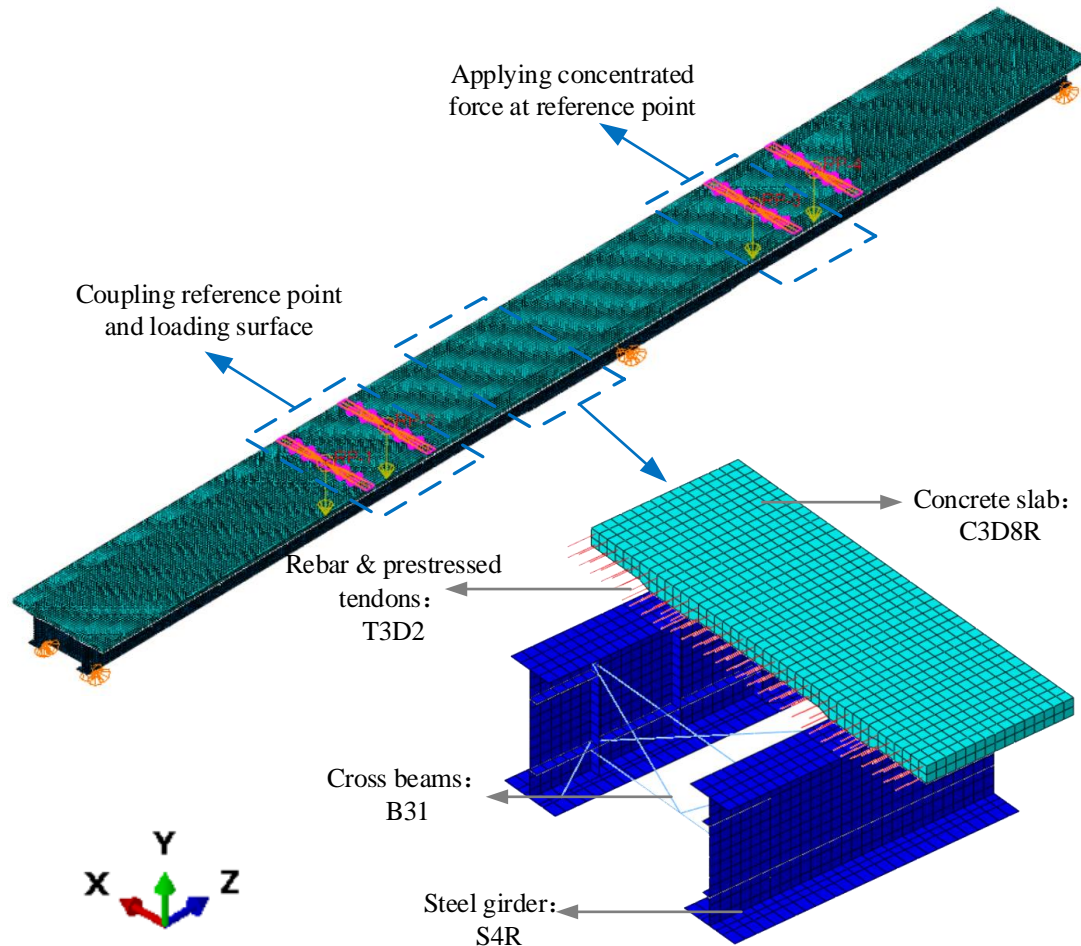


Fig. 28 Illustration of FE model

Constitutive model

(1) Constitutive relation of concrete

Concrete Damage Plasticity (CDP) model was adopted in the concrete slab. The elastic section is referred to Fib model code (fib 2010), and the inelastic section to the Chinese concrete code (GB 50010-2010 2015) as shown in Fig. 29.

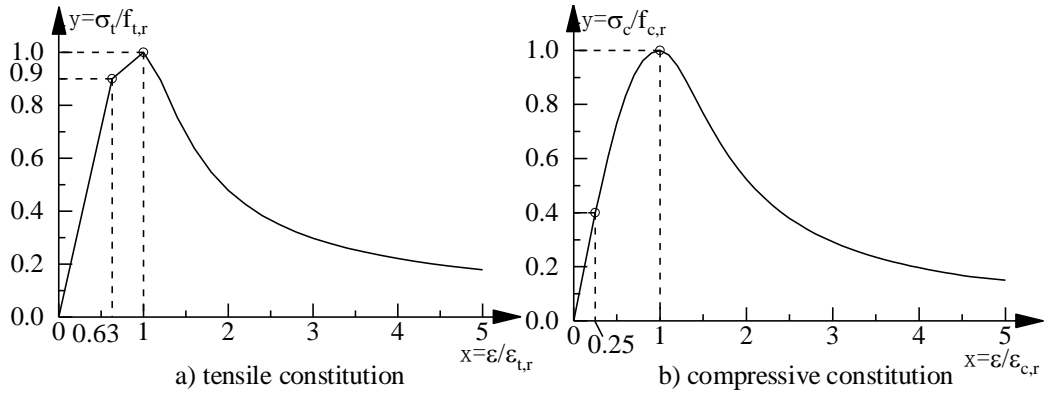


Fig. 29 Constitutive of concrete

The tensile and compressive constitutive relation are expressed in Eq. (7) and Eq (8) respectively. Where $\rho_t = f_{t,r}/(E_c \epsilon_{t,r})$, $\rho_c = f_{c,r}/(E_c \epsilon_{c,r})$.

$$\left\{ \begin{array}{l} y = \frac{1}{\rho_t} x \quad x \leq 0.63 \\ y = \frac{x+9-9\rho_t}{10-9\rho_t} \quad 0.63 < x \leq 1 \\ y = \frac{x}{\alpha_t(x-1)^{1.7} + x} \quad x > 1 \end{array} \right. \quad (7) \quad \left\{ \begin{array}{l} y = \frac{1}{\rho_c} x \quad x \leq 0.25 \\ y = \frac{nx}{n-1+x^n} \quad 0.25 < x \leq 1 \\ y = \frac{x}{\alpha_c(x-1)^2 + x} \quad x > 1 \end{array} \right. \quad (8)$$

(2) Constitutive relation of steel plate and reinforcing steel

The steel type used in this experiment is Q345 (JTG D64, 2015). A trilinear model was applied to simulate the constitutive relationship of steel with reference to the coupon tests and the literature (Zheng et al. 2016). A linear elastic beam model without considering the cracking concrete in the negative moment were analyzed and the results showed that the prestressed tendons kept in elastic range during the test. Therefore, they were considered as elastic material in the FE model. The stress-strain relationship of steel plate and reinforcement are show in Fig. 30.

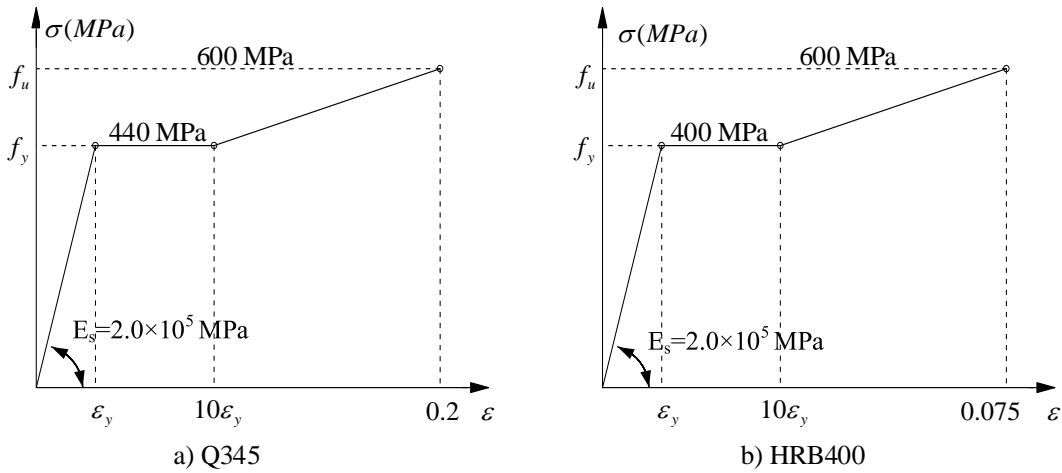


Fig. 30 Mechanical properties of steel plate and reinforcement

(3) Interfacial slip behavior

Connector element CONNED2 was adopted to simulate the shear and tensile performance of studs. In order to get the shear performance of the studs, push-out tests were conducted. The results of shear force versus slip are shown in Fig. 31.

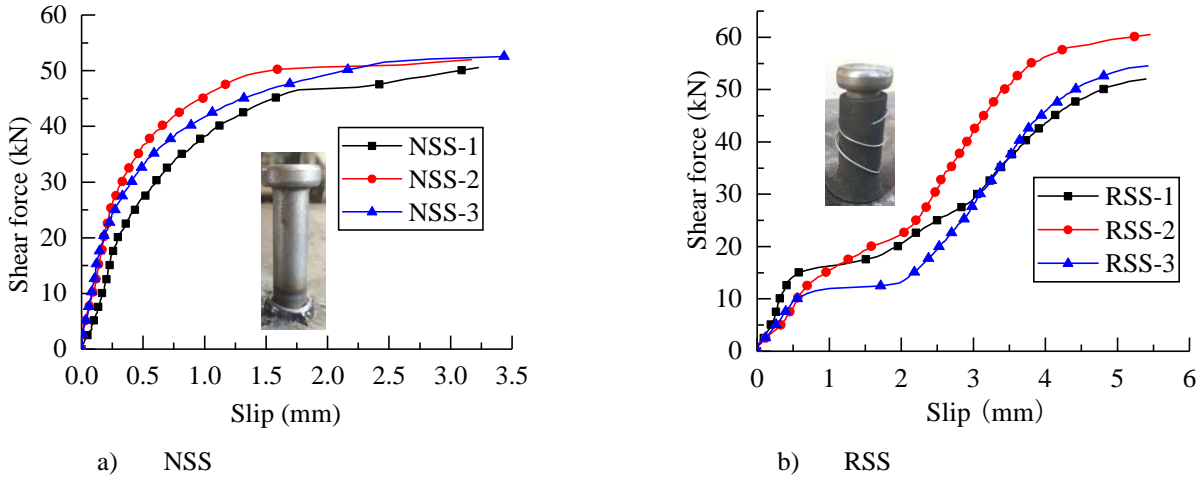


Fig. 31 Shear force-slip curve of push-out tests

The shear stiffness was calculated according to (JSCE 1996). Thus, the shear stiffness of NSS and RSS determined by push-out test were 113.2 kN/mm and 10.6 kN/mm, while the tensile stiffness was calculated referring to the Eq. (9) (Yang et al. 2019).

$$k_t = \frac{E_{stud} A_{stud} h_{ef}}{h_{ef}^2 + 11.5nA_{stud}} \quad (9)$$

Where E_{stud} is the elastic modulus of stud; A_{stud} is the cross-sectional area of studs; h_{ef} is the efficient height of studs; n equals to E_{stud}/E_c . Herein, k_t is calculated as 119 kN/mm by Eq. (9).

Simulation results

Load-displacement & Load slip curve

The numerical results were compared with the experimental results as shown in Fig. 32 and Fig. 33. The simulation results show a satisfactory agreement with test results which confirms the effectiveness and accuracy of the model.

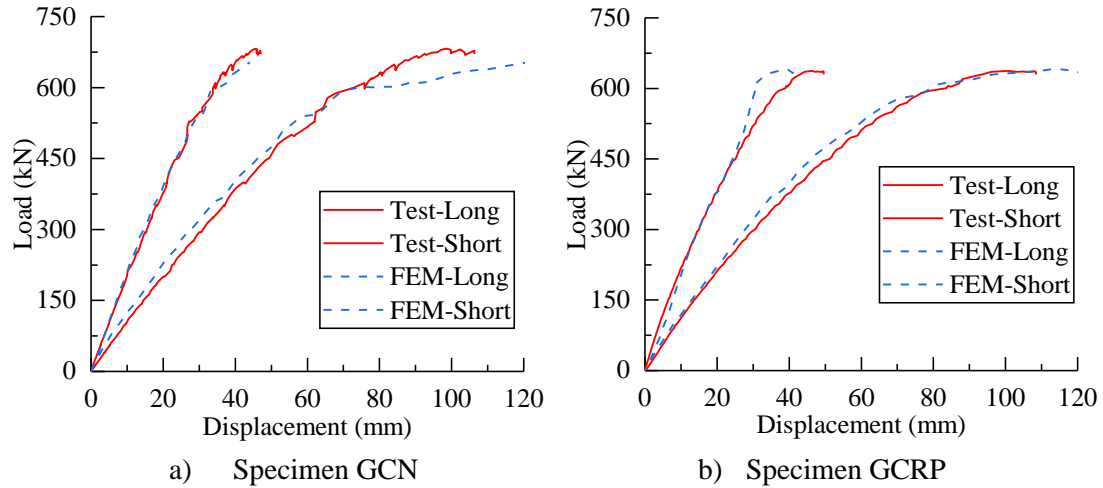


Fig. 32 Comparison of experimental and numerical load-displacement curve

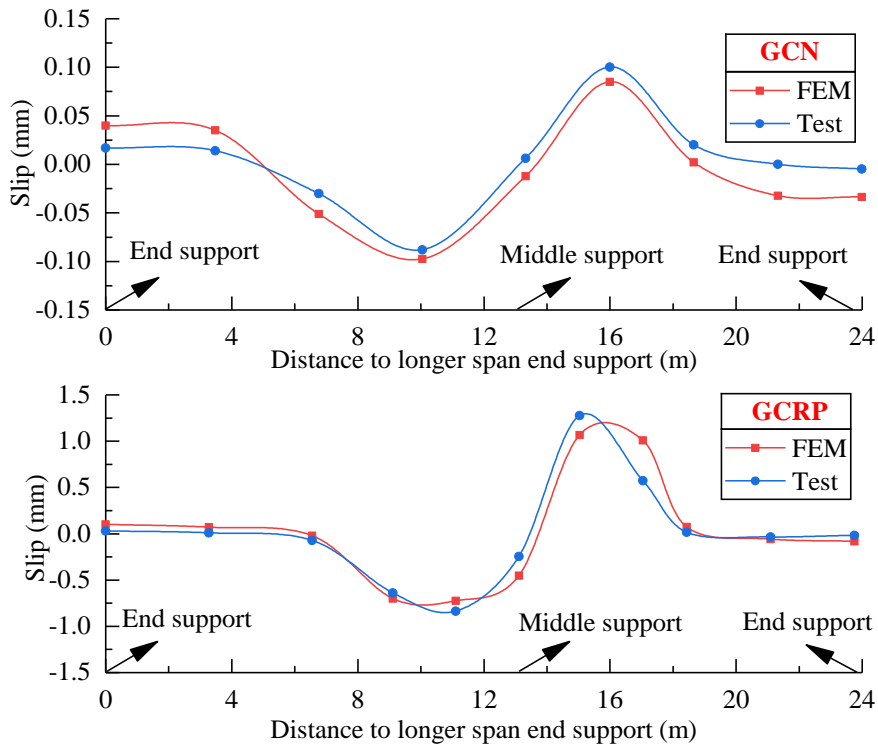
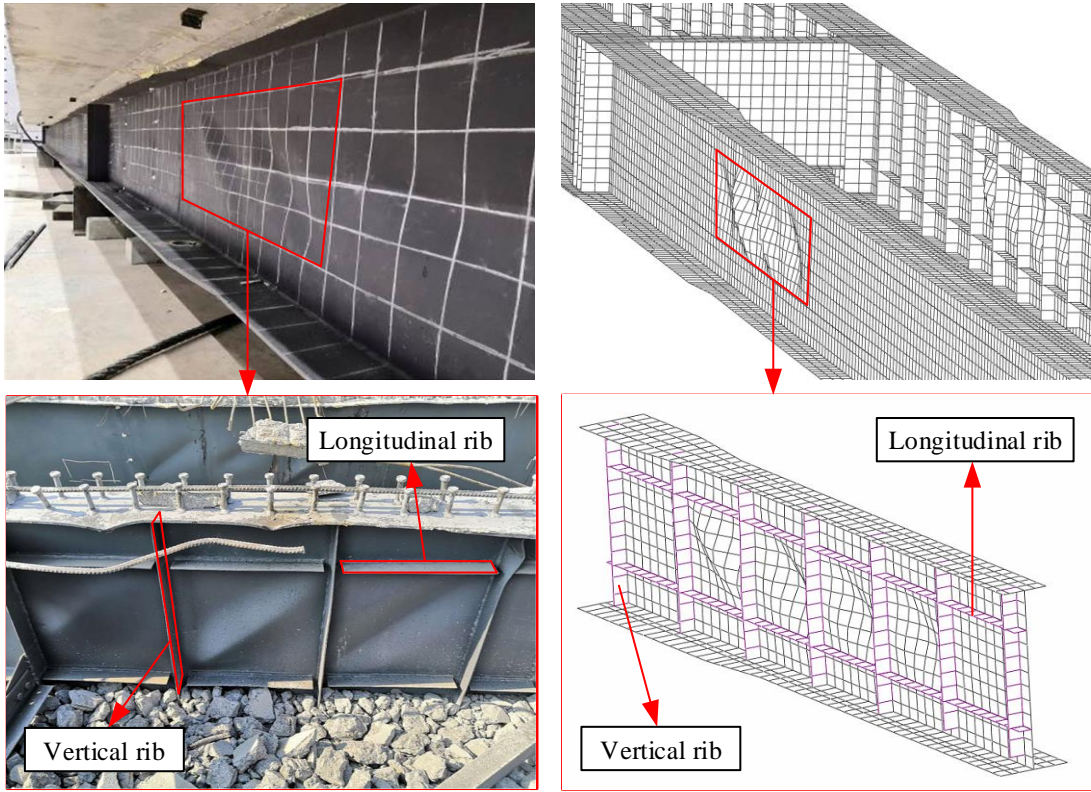


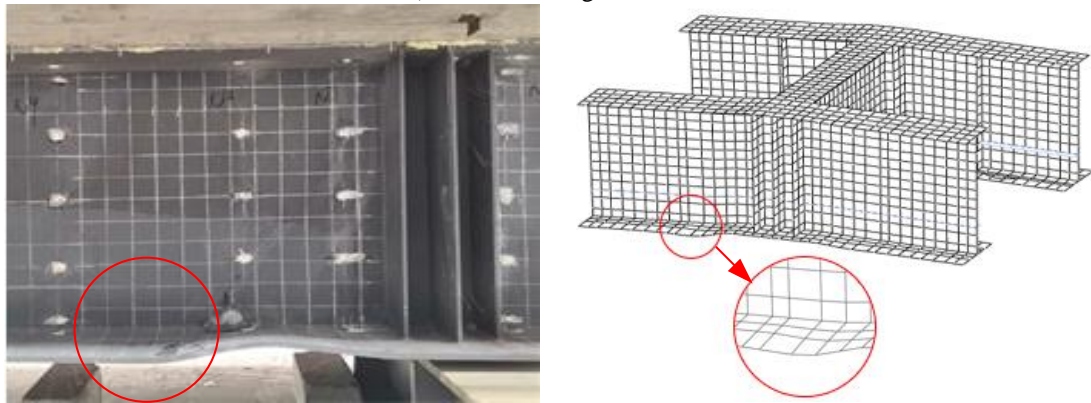
Fig. 33 Comparison of experimental and numerical load-slip curve at load level of $0.6P_u$

Failure mode

As for specimen GCN, the FEM results of steel girder's failure mode met well with that of the experiment as shown in Fig. 34 and so did specimen GCRP. Fig. 35 presents the simulated and tested failure mode of concrete slab in the negative moment region. The simulation results were also consistent with the experimental results, which verified that specimen GCRP has better anti-cracking performance than specimen GCN. Moreover, the simulation results showed that the maximum stress in prestressing steels during loading were 740 MPa (yielding strength 1636 MPa), which means they kept in linear elastic state.

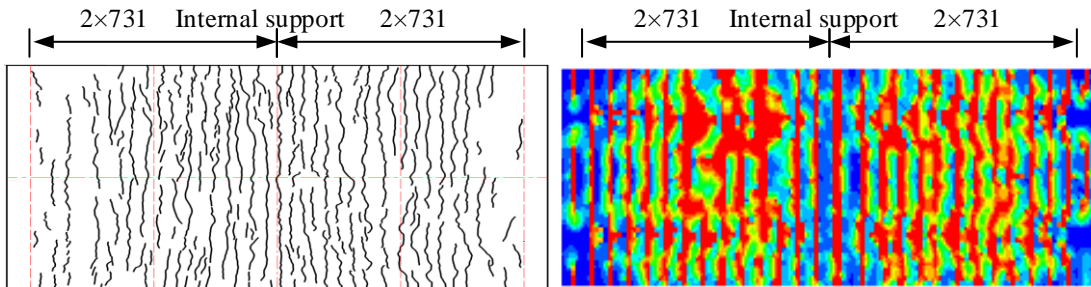


a) Shear buckling of web

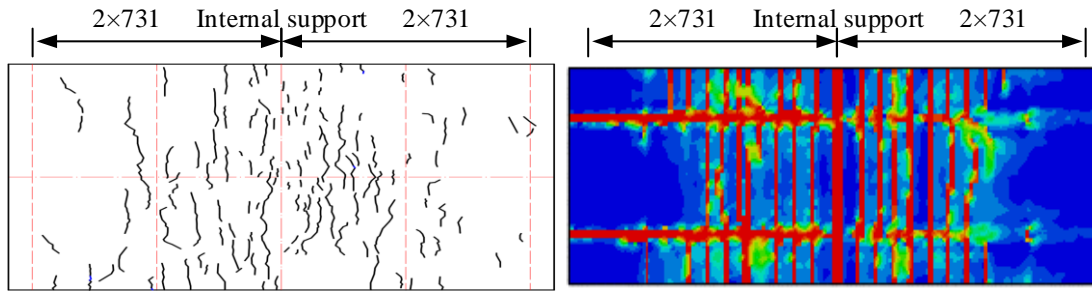


b) Buckling of bottom flange

Fig. 34 Comparison of steel girder's failure mode for specimen GCN



a) Specimen GCN



b) Specimen GCRP

Fig. 35 Comparison of concrete slab's failure mode for specimens (Unit: mm)

Behavior of different composite girders

Since it is time-consuming and expensive to conduct experimental research, only two specimens were tested in this research. However, it is meaningful to study other types of continuous composite girders such as only applying RSS or prestress in the negative moment region. Therefore after checking the good performance of the developed numerical model, another two models (Model GCR & Model GCNP) were simulated here to study the effects of partial interaction and prestressing on continuous girders' mechanical behavior. The detailed model parameters and simulation results are given in Table 8.

The results show that the prestress can obviously enhance concrete slab's cracking behavior. Comparing the results of specimen GCNP and specimen GCRP, it can be inferred that RSS can efficiently improve the anti-cracking effect of the prestressing without affecting the loading capacity.

Table 8

Comparison of Relevant loads as obtained with the numerical model

Model No.	Studs type	Prestress(MPa)	Relevant loads (kN)		
			Cracking	Yielding	Ultimate
GCN	NSS	without	87.5	550.5	658.8
GCR	RSS	without	97.8	549.8	670.5
GCNP	NSS	750	224.9	526.4	649.5
GCRP	RSS	750	292.5	525.1	650.6

Effects of stud's shear stiffness on prestressing efficiency

To study the effect of stud's shear stiffness on prestressing efficiency in the negative moment region, different stiffnesses were adopted based on the tested stiffness of NSS.

The prestress efficiency η is defined according to Eq. (10), where N_c and N_s are the axial forces due to the prestressing force in concrete slab and steel girder respectively. The result is given in Fig. 36. Herein the relative stiffness is defined as K/K_{nss} , where K is the shear stiffness of the studs used in parameter analysis and K_{nss} is the shear stiffness of NSS used in the experimental study. After increasing the relative stiffness to more than 10, the prestressing efficiency keeps stable at about 76%. When the relative stiffness is 0.1, the prestressing efficiency is about 83%.

$$\eta = \frac{N_c}{N_c + N_s} \times 100\% \quad (10)$$

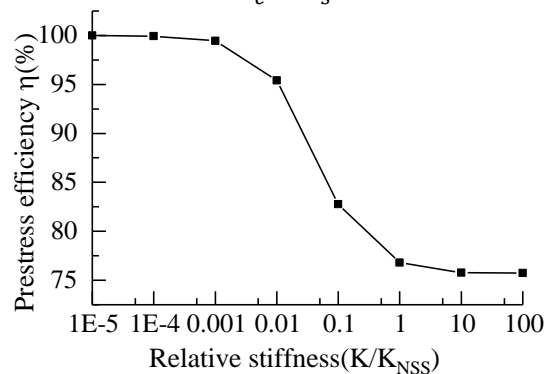


Fig. 36 Prestress efficiency versus relative stiffness of studs

Conclusions

The static performance of two continuous composite girders was tested by four-point static loading in this paper. In addition, the experimental results were used to calibrate a numerical model for a parametric study. Several conclusions can be listed as follows:

- (1) PCP (Partial connecting and prestressing) method can effectively improve the cracking resistance of continuous composite girders. Compared to the specimen GCN, the cracking load of the specimen GCRP was 3.1 times higher. The crack width of specimen GCRP was no more than 81.3 % of that of specimen GCN at same load level.
- (2) Specimen GCRP produced greater interfacial slip (more than 10 times) compared to the specimen GCN, but the overall stiffness of the two specimens were similar, which means that RSS has little effect on the deflection of the composite girders.
- (3) The instability of steel girders occurred in both specimen when they reached limit state and the ultimate load capacity of them were close. The partial shear connection provides a clear increase in the cracking moment without affecting the load capacity.
- (4) The simulation results showed that compared to conventional composite girders, the cracking load increased by 11.8% and 157.0 % when applying RSS and prestress alone, respectively, and by 234.3% when applying RSS and prestressing at the same time.
- (5) In the case of full connection, the shear stiffness of the stud connectors does not have an important influence on the amount of prestressing transferred to the concrete slab. It keeps constant at around 75 % for relative stiffness between 1 and 100.

Acknowledgement

This research is sponsored by the National Natural Science Foundation of China (No. 51978501) & Major research and development project of Jiangxi Province (No. 20165ABC2800).

References

- Abe, H., & Hosaka, T. (2002). *Flexible shear connectors for railway composite girder bridges*. Composite construction in steel and concrete IV (pp. 71-80).
- Cao P. (2017). *Analysis of partial-combination prestressed continuous composite beam*. Tongji University.
- Chen, J., Zhang, H., & Yu, Q. Q. (2019). *Static and fatigue behavior of steel-concrete composite beams with corroded studs*. Journal of Constructional Steel Research, 156, 18-27.
- Chiorean, C. G., & Buru, S. M. (2017). *Practical nonlinear inelastic analysis method of composite steel-concrete beams with partial composite action*. Engineering Structures, 134, 74-106.
- Deng, K., Zeng, X., Kurata, M., Zhao, C., & Onishi, K. (2020). *Damage control of composite steel beams using flexible gel-covered studs*. Journal of Structural Engineering, 146(3), 04019216.
- El-Sisi, A. A., Hassanin, A. I., Shabaan, H. F., & Elsheikh, A. I. (2021). *Effect of external post-tensioning on steel-concrete composite beams with partial connection*. Engineering Structures, 247, 113130.
- Hassanin, A. I., Shabaan, H. F., & Elsheikh, A. I. (2020). *The effects of shear stud distribution on the fatigue behavior of steel-concrete composite beams*. Arabian Journal for Science and Engineering, 45(10), 8403-8426.
- Japanese Society of Steel Construction. (1996). *Standard on push-out test for headed stud*. Japanese Society of Steel Construction.
- Lemes, Í. J., Dias, L. E., Silveira, R. A., Silva, A. R., & Carvalho, T. A. (2021). *Numerical analysis of steel-concrete composite beams with partial interaction: A plastic-hinge approach*. Engineering Structures, 248, 113256.
- Li, Z., Ma, X., Fan, J., & Nie, X. (2019). *Overhanging Tests of Steel-Concrete Composite Girders with Different Connectors*. Journal of Bridge Engineering, 24(11), 04019098.
- Loh, H. Y., Uy, B., & Bradford, M. A. (2004). *The effects of partial shear connection in the hogging moment regions of composite beams: Part I—Experimental study*. Journal of constructional steel research, 60(6), 897-919.
- Ministry of Housing and Urban-Rural Development of China. (2015). *Code for design of concrete structures*. GB 50010-2010. Beijing: China Architecture & Building Press.
- Ministry of Transport of China. (2015). *Specifications for design of highway steel bridge*. JTG D64-

2015. Beijing: China Communication Press.
- Mitsunori S., Hiroshi, W., Yoshihiro, T., Watanabe, H., Kitagawa K., Kurita, A. (2000). *Physical characteristics test of delayed curable resin mortar used for steel-concrete composite structures*. The 55th Annual Scientific Lecture Meeting of the Japan Society of Civil Engineers (I),2000, A255.
- Nicoletti, R. S., Rossi, A., de Souza, A. S. C., & Martins, C. H. (2021). *Numerical assessment of effective width in steel-concrete composite box girder bridges with partial interaction*. Engineering Structures, 239, 112333.
- Nie, J. G., Li, Y. X., Tao, M. X., & Nie, X. (2015). *Uplift-restricted and slip-permitted T-shape connectors*. Journal of Bridge Engineering, 20(4), 04014073.
- Su, H., Su, Q., Xu, C., Zhang, X., & Lei, D. (2021). *Shear performance and dimension rationalization study on the rubber sleeved stud connector in continuous composite girder*. Engineering Structures, 240, 112371.
- Su, Q., Yang, G., & Bradford, M. A. (2015). *Behavior of a continuous composite box girder with a prefabricated prestressed-concrete slab in its hogging-moment region*. Journal of Bridge Engineering, 20(8), B4014004.
- Suwaed, A. S., & Karavasilis, T. L. (2020). *Demountable steel-concrete composite beam with full-interaction and low degree of shear connection*. Journal of Constructional Steel Research, 171, 106152.
- Taerwe, L., & Matthys, S. (2013). *Fib model code for concrete structures 2010*, Ernst & Sohn, Berlin.
- Tong, T., Yu, Q., & Su, Q. (2018). *Coupled effects of concrete shrinkage, creep, and cracking on the performance of postconnected prestressed steel-concrete composite girders*. Journal of Bridge Engineering, 23(3), 04017145.
- Turmo, J., Lozano-Galant, J. A., Mirambell, E., & Xu, D. (2015). *Modeling composite beams with partial interaction*. Journal of Constructional Steel Research, 114, 380-393.
- Xu, X., He, D., Zeng, S., He, W., Tan, H., & Yu, Z. (2021). *Effect of concrete cracks on the corrosion of headed studs in steel and concrete composite structures*. Construction and Building Materials, 293, 123440.
- Xu, X., & Liu, Y. (2016). *Analytical and numerical study of the shear stiffness of rubber-sleeved stud*. Journal of Constructional Steel Research, 123, 68-78.
- Xu, X. Q., Liu, Y. Q., He, J., & Luo, J. (2014). *Numerical simulation on failure process of rubber-sleeved headed stud shear connector*. Key Engineering Materials (Vol. 577, pp. 617-620). Trans Tech Publications Ltd.
- Xu, X., Zhou, X., & Liu, Y. (2020). *Behavior of rubber-sleeved stud shear connectors under fatigue loading*. Construction and Building Materials, 244, 118386.
- Xu, X., Zhou, X., & Liu, Y. (2021). *Fatigue life prediction of rubber-sleeved stud shear connectors under shear load based on finite element simulation*. Engineering Structures, 227, 111449.
- Yang, F., Liu, Y., & Liang, C. (2019). *Analytical study on the tensile stiffness of headed stud connectors*. Advances in Structural Engineering, 22(5), 1149-1160.
- Zeng, X., Deng, K., Kurata, M., Duan, J., & Zhao, C. (2020). *Seismic performance evaluation of damage-controlled composite steel frame with flexible-gel-covered studs*. Engineering Structures, 219, 110855.
- Zhuang, B., & Liu, Y. (2019). *Study on the composite mechanism of large Rubber-Sleeved Stud connector*. Construction and Building Materials, 211, 869-884.
- Zhuang, B., Liu, Y., & Wang, D. (2020). *Shear mechanism of Rubber-Sleeved Stud (RSS) connectors in the steel-concrete interface of cable-pylon composite anchorage*. Engineering Structures, 223, 111183.
- Zhuang, B., Liu, Y., & Yang, F. (2018). *Experimental and numerical study on deformation performance of rubber-sleeved stud connector under cyclic load*. Construction and Building Materials, 192, 179-193.
- Zheng, S., Liu, Y., Yoda, T., & Lin, W. (2016). *Parametric study on shear capacity of circular-hole and long-hole perfobond shear connector*. Journal of Constructional Steel Research, 117, 64-80.

6.4 Journal of Constructional Steel Research 2022

Su H, Su Q, Xu C, Casas JR, et al. Mechanical performance based rationalization research on steel-concrete double composite action. Journal of Constructional Steel Research, 2022, 197:107492. DOI: 10.1016/j.jcsr.2022.107492

Mechanical Performance Based Rationalization Research on Steel-concrete Double Composite Action

Hang Su ^{a,b}, Qingtian Su ^{a,c}, Chen Xu ^{a*}, Joan R. Casas ^b, Guandong Zhou ^d

^a *Department of Bridge Engineering, Tongji University, 1239 Siping Road, Shanghai, China 200092*

^b *School of Civil Engineering. Department of Civil and Environmental Engineering, Technical University of Catalunya, c/Jordi Girona 1-3. Campus Nord. Modulo C-1, Barcelona (Spain) 08034*

^c *Shanghai Engineering Research Center of High Performance Composite Bridge, 901 Zhongshanbeier Road, Shanghai, China 200092*

^d *Guangdong Communication Planning & Design Institute Group Co., Ltd, No.22 Xinghua Road, Guangzhou, China 510507*

Abstract

Casting an extra concrete bottom layer to a steel-concrete composite box girder in a hogging moment region can increase sectional stiffness and prevent steel buckling. However, a lower sectional neutral axis may not be favorable to concrete slab cracking and steel flange stress control. To this end, a double composite girder segment was proposed and investigated. Particularly, a static loading test on a large-scaled two-span continuous girder specimen with the double composite action in hogging moment region was conducted for mechanical investigation. Meanwhile, parametric analysis was carried out as well for a rational design scheme of the double composite section. The test results revealed that the load-carrying capacity of double composite section could be increased due to the contribution of extra bottom concrete layer. The transverse deformation of steel parts was favorably constraint. The parametric analysis results indicated that slab thickness that was 15 % of steel girder height could provide most obvious contributions to the improvements of both sectional load-carrying capacity and cracking moment. Due to the additional reinforcement, the steel web thickness of double composite girder can be saved 16.7% and the steel bottom flange thickness only needs to meet the constructing requirement compared with common composite girder. Besides, the analysis also showed replacing the tub section with steel box section in the hogging moment region can reduce the stress on top flange by 24.4%. These results are an important basis for establishing a rational design scheme for the novel double composite section.

Keywords: Steel-concrete composite structure; Double composite; Numerical study; Large-

scaled experiment; Hogging moment region

Nomenclature

f_y : Tensile yield strength of the steel material
 f_u : Ultimate strength of the steel material
 V_u : Stud shear strength
 K_{s1}, K_{s2} : Secant modulus corresponding to $1/3 V_u, 1/2 V_u$
LVDT: Linear Variable Differential Transducer
 D : deflection sensor
 S : steel-concrete interlayer slip sensor
 LS : longitudinal stiffening rib
 TS : transverse stiffening rib
FEM: finite element method
 E_c, E_s : Elasticity modulus of concrete and steel
 E'_c : Reduced elasticity modulus
 A_e : Artificial Energy
 I_e : Inertia Energy
 K_e : Kinetic Energy
 ε_c : Strain in concrete slab
 α_t, α_c : Regulation coefficient of the descending part of the concrete
 d_c, d_t : Compressive and tensile damage factor of the concrete
 $f_{t,r}, f_{c,r}$: Ultimate tensile and compressive strength of the concrete
 $\varepsilon_{t,r}, \varepsilon_{c,r}$: Strain corresponding to the ultimate tensile and compressive strength of the concrete
 E_0 : Initial elasticity modulus of concrete
 σ_{yS} : Stress at yield point
 σ_{uS} : Stress at ultimate point
 ε_{yS} : Strain at yield point
 ε_{uS} : Strain at ultimate point
 M_i : Bending moment under different construction stages
 $2LS$: Specimen of web with upper and lower longitudinal stiffening ribs
 $1LS$: Specimen of web with upper longitudinal stiffening rib
 $\sigma_{st}^i, \sigma_{sb}^i, \sigma_r^i$: Steel top flange, steel bottom flange and reinforcement stress under different construction stages
 σ_c^i : Concrete top edge stress under different construction stages
 I_i : Sectional bending moment of inertia under different construction stages
 y_i : Vertical distance from the sectional neutral axis to the upper fiber under different construction stages
 h_s, h_{cs}, h_{bc} : Height of the steel girder, the concrete deck slab and the concrete bottom slab
 n : Modulus ratio of concrete to steel
 A_c, A_s, A_{bc}, A_r : Section area of the concrete deck slab, the steel girder, the concrete bottom slab and the reinforcement
 I_c, I_s, I_{bc} : Sectional bending moment of inertia of the concrete deck slab, the steel girder and the concrete bottom slab
 f_{ct} : Concrete tensile strength
 M_{cr} : Bending moment corresponding to cracking stage
 R_{cr} : Cracking moment ratio between specimen with different h_{bc} and specimen without concrete bottom slab

Introduction

Compared with steel and prestressed concrete structures, a continuous steel-concrete composite girder has merits in concrete compression and steel tension in sagging moment regions. However, steel compression and concrete tension confronted in hogging moment regions can easily result in steel buckling and concrete cracking. In order to improve mechanical responses of hogging moment regions in steel-concrete composite girders, a number of methods have been proposed.

Applying initial prestress in the concrete slab of composite girder is one of the common techniques to prevent the concrete tension in hogging moment region. Ryu^[1] conducted static test on a continuous composite box-girder and revealed the inelastic behaviour of externally prestressed continuous composite box-girder bridge with prefabricated slabs. Moscoso^[2] analyzed the mechanical behavior of pre-stressed steel concrete composite beams through numerical simulation and revealed its stress distribution and cracking pattern. Lu^[3] optimized the pre-stress operation on the composite girder with corrugated webs for global deflection reduction and steel local buckling prevention.

Partial shear connection achieved by adopting connector with an initial lower stiffness or reducing connector number could decrease the level of composite action and make a reduction of stresses on the concrete slab. Zhuang^[4] conducted push-out tests on studs wrapped with rubber sleeves and revealed an obviously lower stiffness and larger bending deformation of rubber-sleeved stud as compared with a normal stud, while the strength varied little. Su^[5] conducted 15 push-out tests and analyzed the connector stiffness effect on a continuous composite girder, showing a 39% reduction of concrete slab stress in the hogging moment region. Xu^[6] and He^[7] respectively conducted analytical study and presented the calculation methods of rubber-sleeved stud connector and composite girder with partial shear connection.

Moreover, fiber reinforced concrete has also been applied for improving the material cracking stiffening performance. Lin^[8] conducted four girder tests and revealed the contribution of steel fiber reinforced concrete (SFRC) to the composite girders subjected to hogging moment. Zhu^[9] investigated the cracking behavior of curved composite girder with steel fiber reinforced concrete and engineered cementitious composites (ECC) under a hogging moment. Xu^[10] studied the fatigue behavior of steel fiber reinforced concrete composite girder under high cycle negative bending action and revealed the crack restrain effect of SFRC during fatigue loading. Zhang^[11] replaced the normal strength concrete in composite girder with ultra-high performance concrete (UHPC) in the hogging moment regions and presented its cracking and flexural improvement. Cheng^[12] investigated the flexural improvement of composite bridge decks with corrugated steel deck and ultra-high-performance concrete slab through six composite bridge deck specimens.

Besides the cracking issue in a hogging moment region, out-plane deformation of the steel bottom flange in the region is another challenging issue. Increasing steel bottom flange thickness is a normal alternative for strength and stability needs. However, a steel plate with a large thickness has lower strength and is difficult to weld, while the additional steel can markedly increase the cost. German engineers firstly proposed a double composite girder^{[15][16]} including an additional layer of concrete to the bottom flange of a steel girder. It could prevent steel buckling, increase sectional

stiffness and limiting concrete crack propagations in hogging moment regions. The pioneer application was reported in Ciervana bridge in Spain in 1978. Kim^[18] proposed a railway bridge with a double composite section and investigated the behavior of the shear connection in the double composite section. In addition, Kim^[19] proposed a study on a double composite bridge and analyzed the mechanical behavior of the double composite girder with high strength steel. Shim^[20] conducted tests on double composite girder with high strength steel, showing the steel high strength can be better utilized due to the prevention of the local buckling. Jiang^[21] proposed a study on a composite girder with the web encased in the concrete for steel buckling prevention. Xu^[22] tested two continuous composite girders and studied the mechanical behavior of double composite action in hogging moment region.

In addition to the cracking performance, there is another problem which is the large stress on steel top flanges in the hogging moment region of a steel tub girder. This is because the steel top flanges have much smaller section area compared with bottom flanges, while steel top flange with large thickness also has a lower quality of fabrication and welding. This paper proposes a replacement of a steel tub in a double composite section by a steel box in hogging moment region to address the large stress issue. Compared with steel tub double composite section, the proposed steel box double composite section has larger section area of steel top flange. And it can further strengthen the sectional flexure resistance. In addition, the steel top flange can work as a formwork for concrete casting, which is favorable for construction.

Though applications of double composite actions have been reported in particular bridge practices, there have been few particular design criteria in the design codes so far. The global mechanical behavior of composite girder with double composite action was concerned by some previous researches. However, large-scaled experimental study focused on its detailed mechanical behavior is rare.

In this paper, an experimental study on a large scaled composite girder was conducted for detailed mechanical investigation on double composite action, and a parametric study was executed as well for rational design criteria of the additional slab thickness in a double composite section.

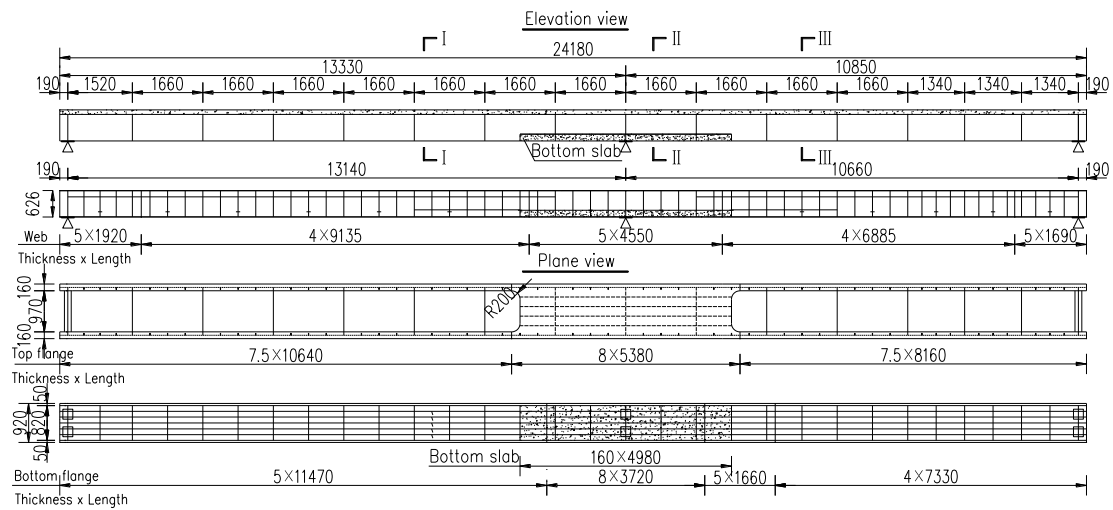
Experimental set-up

Specimen design

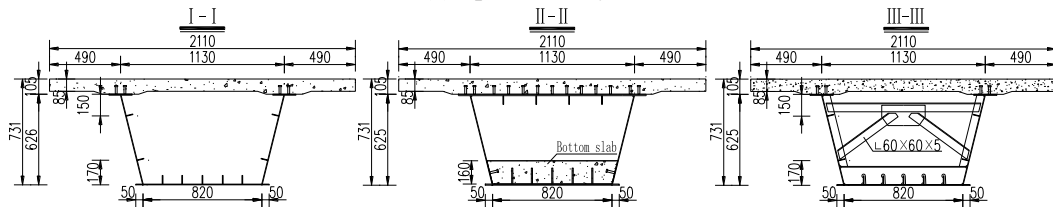
A two-span continuous composite girder specimen with double composite action in the hogging moment region was prepared and tested. Fig. 1 shows the specimen dimensional details, which obeyed one third shrunk scale to an actual 5×40m continuous composite bridge. Considering the limitation of the laboratory space and loading equipment, the longitudinal dimension of the specimen and length of each span was decided based on the intercepted segment between the two reverse bending points under dead load.

Fig. 1 (a) shows the two spans, with span-lengths of 13.33m and 10.85m, including a 0.19 m free extension at each end. A 4.55m long and 160mm thick extra concrete slab was cast on the steel bottom flange in the hogging moment region. A steel box section in the hogging moment region was adopted while a steel tub section was used in the rest. The angle-bar braces were installed to strengthen lateral stiffness and stability.

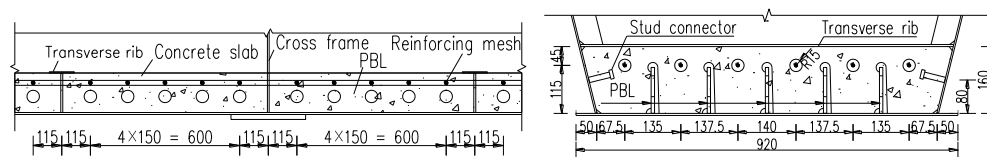
Fig. 1 (b) shows that the composite girder height was 731 mm and the steel girder height was 626 mm. The concrete slab and haunch underneath were respectively 105 mm and 20 mm. The width of concrete slab was 2110 mm. Fig. 1 (c) and Fig. 1 (d) respectively show the reinforcement configuration and connection details in the bottom and top side concrete slab. There were two layers of longitudinal reinforcement. The diameter of the longitudinal reinforcement is 12 mm within the region with the double composite action and 8mm in the rest of the specimen. The stud height and shank diameter were 60 mm and 13 mm, respectively. The longitudinal and transverse stud spacing in sagging moment region were 60 mm and 100 mm, while in hogging moment region were both 100mm. Fig. 2 shows the real specimen components (Fig. 2(a), Fig. 2 (c) and Fig. 2 (d)) and casting situation (Fig. 2 (b)).



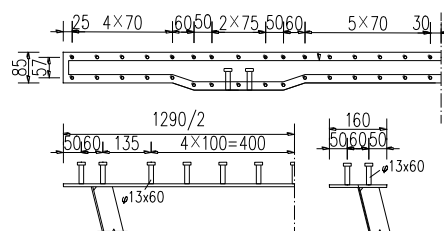
(a) Specimen layout



(b) Composite sections

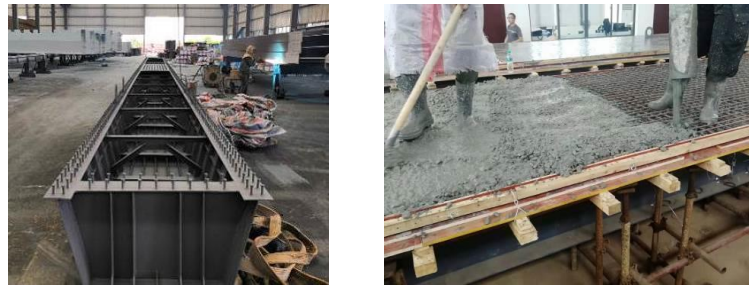


(c) Concrete bottom slab



(d) Reinforcement configuration and stud arrangement

Fig. 1 Description of test specimen (mm)



(a) Steel girder

(b) Pouring concrete



(c) Shear connector of concrete bottom slab



(d) Reinforcement of concrete bottom slab

Fig. 2 Execution of the test specimen

Material properties

The material properties of concrete were tested according to GB/T 50081-2019^[23] at the 28th curing day. The uniaxial compressive strength test used 150 mm cubic test specimens. The tensile strength and Young's modulus tests used 40×40×160 mm specimens and 100×100×300 mm specimens, respectively. The compressive strength, tensile flexural strength and elastic modulus results were 56.8MPa, 5.76 MPa and 34300MPa respectively.

Table 1 summarizes the yielding and ultimate strength of steel plates. The data is the average value of three specimens calculated according to GB/T 228-2002^[24]. Tensile properties of reinforcement are also listed in Table 1. During the tensile tests on the reinforcement with diameter of 8mm and 10 mm, the material yielding points were not obvious.

Push-out tests with 3 specimens were conducted to assess the shear stiffness of the stud connector in the girder test. The obtained shear strength and stiffness are summarized in Table 2.

Table 1

Steel and reinforcement properties (MPa)

Plate thickness or rebar diameter(mm)	4	5	7.5	8	R8	R10	R12
f_y	489.3	460.6	337.9	447.4	-	-	400.9
f_u	550.4	537.3	476	499.7	636.8	645.4	581.1

* f_y is the yielding strength; f_u is the ultimate tensile strength

Table 2

Groups of test specimens.

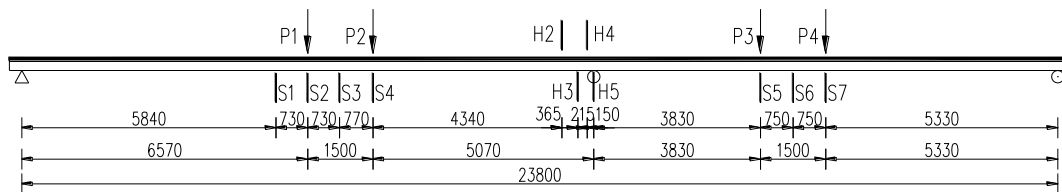
Specimen	V_u (kN)	K_{s1} (kN/mm)	K_{s2} (kN/mm)
----------	------------	---------------------	---------------------

1	53.7		91.4		81.1	
2	52.1	53.0	109.6	102.4	102.8	89.1
3	53.3		106.1		83.5	

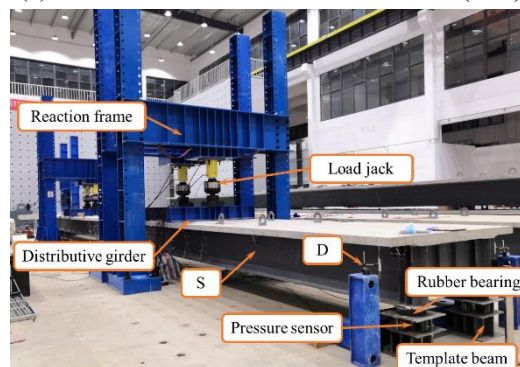
* V_u is the stud shear strength; K_{s1} , K_{s2} is the secant modulus corresponding to $1/3 V_u^{[25]}$, $1/2 V_u^{[26][27]}$

Load and monitoring setup

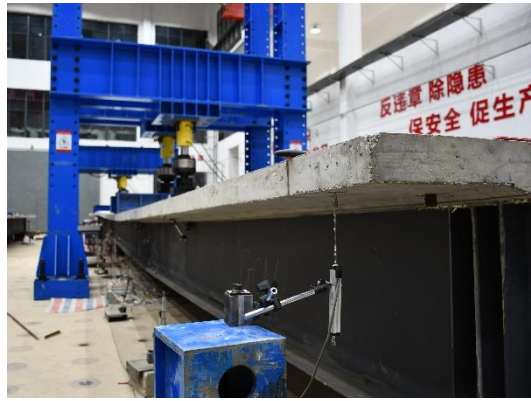
Fig. 3 (a) shows the bending test setup on the specimen. Four hydraulic jacks(P1~P4) were deployed. To maximize the bending moment at the mid support, P1 and P4 jacks were placed at the mid-span, while P2 and P3 jacks were respectively 1500mm away from P1 and P4 according to calculation. Critical sections of S1-S7 and H2-H5 were installed with longitudinal strain gauges. The loading program included a 50kN preload and a monotonic load increased up to ultimate states. Fig. 3 (a) also shows the positions of sections under investigation in the test. Fig. 3 (b) shows the loading arrangement on site. Deflection of each specified position was measured by 18 linear variable differential transducers (LVDTs), while the steel-concrete interlayer slip was measured by 18 dial indicators. The installation method of the LVDTs and the dial indicators are shown in Fig. 3 (c) and Fig. 3 (d). A thin glass was pasted onto the concrete slab where the LVDT was installed to decrease the friction and prevent the LVDT from tilting. The sensor positions are shown in Fig. 4. In particular, there were two symmetrically mounted transducers in transverse direction to check possible load eccentricity. There were 27 strain gauges installed onto each typical section. Fig. 4(b) shows the typical strain gauge distribution in a cross section of each specimen, including the steel girder and the concrete slab. Moreover, the crack width and crack pattern in concrete were also monitored.



(a) Identification of sections of interest (mm)



(b) View of the loading set up



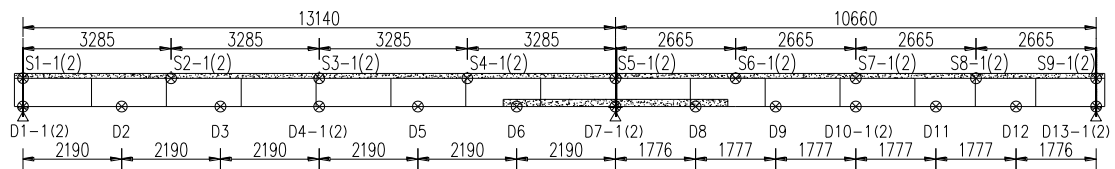
(c) Installation of LVDT



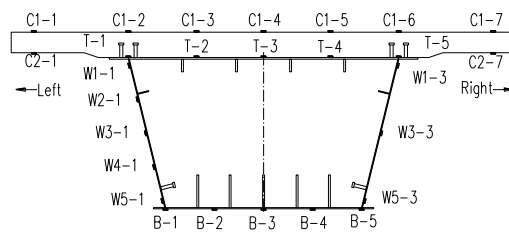
(d) Installation of dial indicators

Fig. 3 View of the loading set up

D: deflection sensor; S: steel-concrete interlayer slip sensor



(a) Deflection sensor and steel-concrete interlayer slip sensor



(b) Arrangement of the strain gauge on steel girder and concrete slab

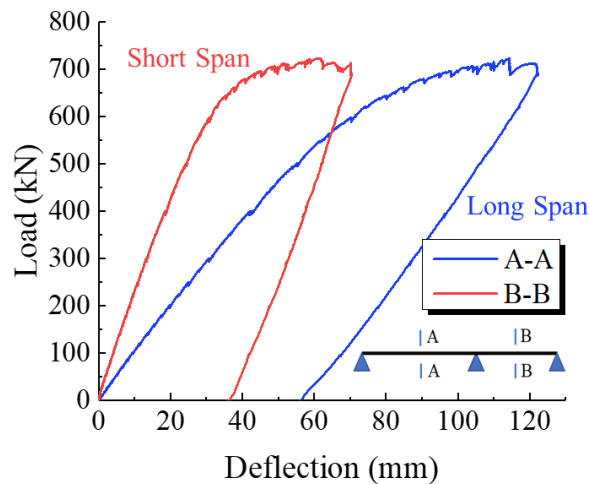
Fig. 4 Sensor positions

Experimental results

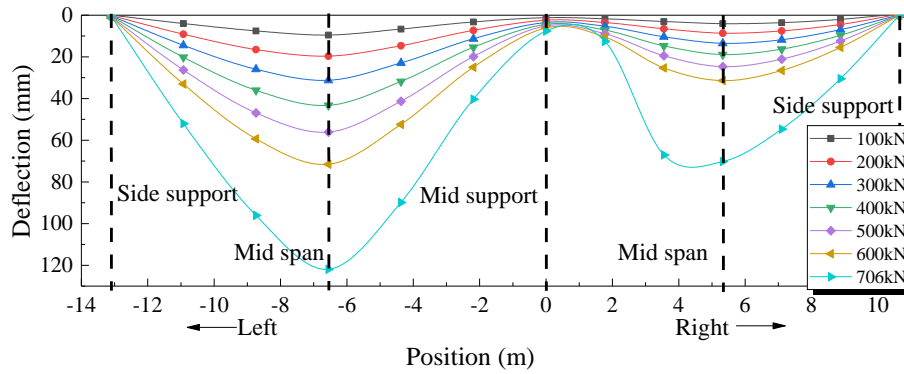
Load–deflection relationship and failure mode

Fig. 5 presents load-deflection curves at mid-spans and longitudinal deflection profile at different load stage. The depicted load and deflection values in Fig. 5(a) were both averages of the twin jacks which were parallel in one hydraulic system. The curves included an elastic, a plastic hardening and an unloading stage. The derived initial bending stiffness of short span (24.6kN/mm) at the load stage of 100kN was significantly larger than that of the long span(10.5kN/mm) in the elastic stage. As load kept increasing, steel yielding and web buckling happened in the hogging moment region without concrete bottom slab and led to nonlinear deflection development. The load maximum was 706kN in the test, at which severe steel web buckling at short span and concrete fracture nearby can be observed in the hogging moment region. Afterwards, specimen deflections grew drastically with a slowly increasing load until failure.

Fig. 6 provides the failure mode of specimen, which consisted of cracking in concrete slab and shear buckling in steel girder. During the loading progress, there was an obvious steel-concrete interlayer bond-breaking noise at the load of 275kN. The development of cracks in the hogging moment region had fully developed at 350kN. At the load stage of 550kN, slight diagonal shear deformation appeared in the web between the two loading points, while the steel web buckling was observed out of the region with concrete bottom slab, indicating that the concrete bottom slab could restrain the lateral deformation of steel webs. The shear deformation of the web at the short span kept developing until reaching the load carrying capacity at 620kN, resulting in a rapid increase in the strain of the steel bottom flange at mid span. When it came to 706kN, the steel web in the hogging moment region without concrete bottom slab lost its load bearing capacity and the shear force transferred to the concrete, resulting in obvious shear diagonal cracks in the concrete slab near mid support (as shown in Fig. 6(b)). Meanwhile, steel web and steel bottom flange within the range of the double composite section remained undeformed.



(a) Load–deflection curves at mid-spans



(b) Deflection distribution at different load stage

Fig. 5 Load-deflection relationship



(a) Web buckling in short span



(b) Concrete diagonal crack in short span

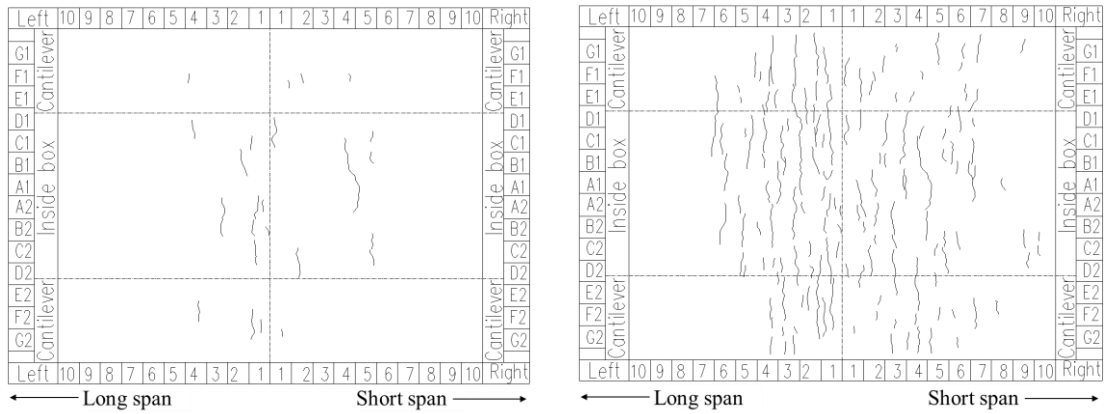
Fig. 6 Failure modes

LS: longitudinal stiffening rib, TS: transverse stiffening rib

Cracking feature and concrete stress in the hogging moment region

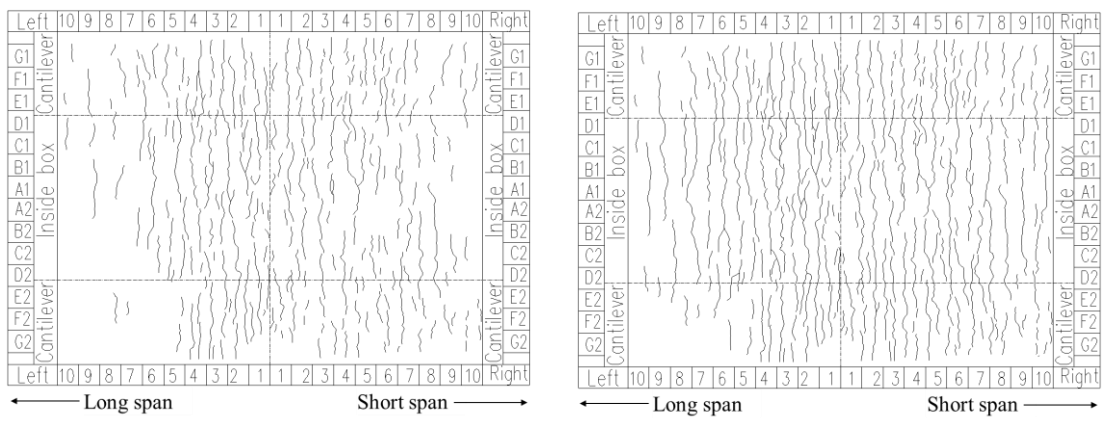
The crack development was detected by visual inspection and manually labeled during the loading, while the maximum crack width was measured by DJCK-2 fracture width gauges during each load step. Fig. 7 illustrates the crack distributions on the concrete deck slab at several load steps. The horizontal scale shows longitudinal distances from cracks to the slab center. And a grid unit represents a 150 mm distance. It shows that all cracks initialized from the slab center and spread symmetrically along the transverse direction, and the cracks developed a little faster in short span than in long span. Besides, the stirrup spacing and the observed crack spacing were approximately equal to each other.

Fig. 8 shows the maximum concrete crack width development. Since a crack may stop developing at a certain load stage, the presented crack width may correspond to a different crack at different load stage. A crack was initially detected at 55kN, whose width was 0.04mm. Many cracks over the entire range of slab width could be observed in the hogging moment region at load stage of 200kN and developed over the entire range of slab width at 300kN. And the maximum crack width among them was nearly 0.17mm when the load was around 450kN.



(a) Cracking at 100kN

(b) Cracking at 200kN



(c) Cracking at 300kN

(d) Cracking at 450kN

Fig. 7 Crack pattern development in hogging moment region(mm)

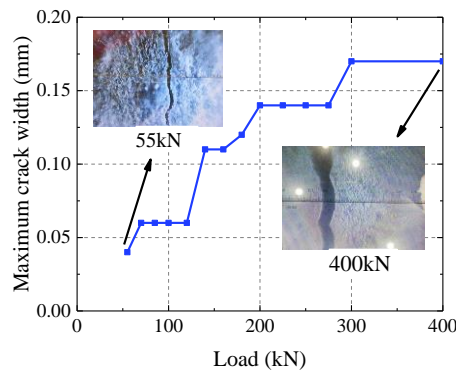


Fig. 8 Maximum crack width observation

Fig. 9 reflects the load-strain curves of concrete slab at mid support position of the specimen before 200kN. An obvious stress mutation at load step of around 60kN can be observed due to concrete cracking.

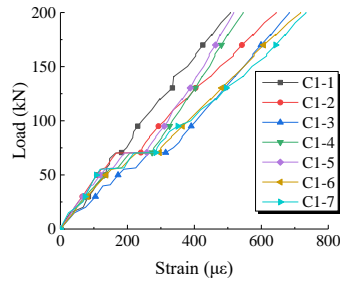


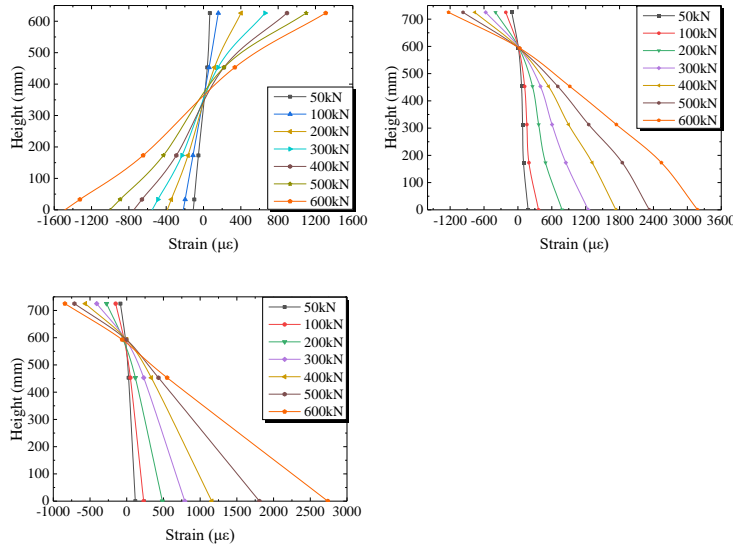
Fig. 9 Load–strain curves of concrete slab at mid support (see figures 4 for location of strain gauges)

Sectional strain profiles

The sectional strain distributions at internal support and mid spans are shown in Fig. 10. The distributions generally matched with the plane section assumption. When the load level was beyond 500kN, the section at internal support began to yield. Meanwhile, sections at mid spans were in elastic stage when the load level was below 600kN. Table 3 lists the neutral axis position translation feature in terms of Fig. 10 (a), showing it became lower due to concrete cracking.

In the case of constant bending moment and sectional bending moment of inertia, the neutral axis position and the elasticity modulus are the main parameters affecting the concrete stress (as shown in Eq. 1). Therefore, a reduced elasticity modulus ratio E'_c/E_c could be calculated according to the decreasing neutral axis position for reflecting the decreasing mechanical contribution of the concrete slab due to cracking (as shown in Table 3). Consider the concrete slab reaches the ultimate state when the reinforcement yields, the relationship between the reduced elasticity modulus ratio and the reinforcement stress is presented in Fig. 11. As the increasing of the reinforcement stress, variation trend of the reduced elasticity modulus ratio was stable at about 0.2 before the reinforcement yielding. It can be concluded that the load-carrying capacity of the concrete slab remained about 20% of the original after the full development of cracking.

$$\sigma_{st}^i = E'_c \varepsilon_c = \frac{M_i}{I_i} y_i \quad \text{Eq. 1}$$



(a) Mid support (b) Mid-span of the long span (c) Mid-span of the short span

Fig. 10 Sectional strain distributions

Table 3

Neutral axis position (from the bottom) and corresponding reduced elasticity modulus ratio at several load steps at mid support

	Load level (kN)				
	50	100	200	300	400
Neutral axis position(mm)	382	374	317	293	271
Reduced elasticity modulus ratio	1	0.77	0.4	0.22	0.19

Neutral axis position: the distance from the bottom of the girder to the neutral axis

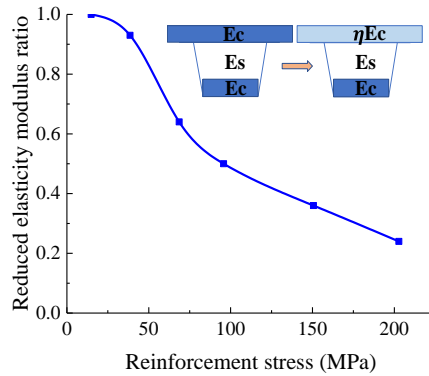


Fig. 11 Relationship between reduced elasticity modulus ratio and reinforcement stress

Load-slip results

Load-slip distribution under several load stages is presented in Fig. 12, where the positive value indicates the slip of the concrete slab from the steel girder at the side support of the long-span. It can be inferred that there is no slip at the mid support and mid-span. The maximum slip was attained at the quarter-span position from the mid support, with a maximum value of 0.26mm at load level of 600kN.

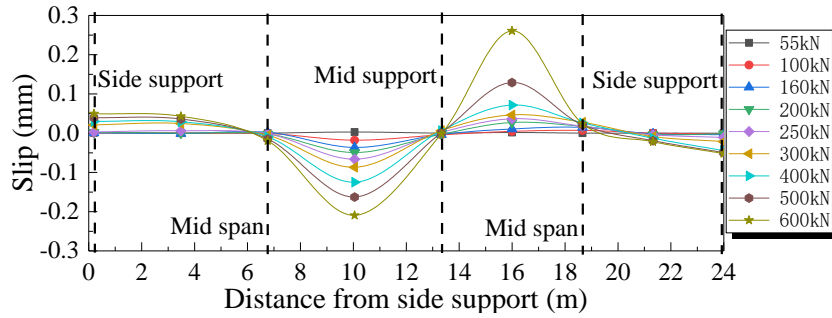


Fig. 12 Load-slip distribution

Numerical and analytical analysis

Numerical model

It has been proved that the double composite action conduces to prevent steel buckling and increase integral rigidity. However, the additional concrete slab may also increase the dead load and lower the neutral axis height. To further study the effect of the concrete bottom slab, finite element models (FEM) were established through Abaqus for parametric analysis.

Fig.13 shows the element type and mesh of each component in the model. The concrete deck slab and concrete bottom slab were discretized with solid element C3D8R, the steel girder with shell element S4R, the open diaphragm with beam element B31, and the reinforcements with truss element T3D2. The overall mesh size of the model was 50mm. Tie commend was introduced to simulate the steel-concrete interlayer interactions^[5]. Embedded region was set to constrain the reinforcement with the concrete block. Besides, displacement boundary condition was applied corresponding to the supporting positions, while the mid support restrained both longitudinal and transversal displacement and the side supports only restrained the longitudinal displacement. The model adopted the explicit dynamic solver, and the analysis step adopted 2s. The loading process was monitored by the ratio of Kinetic energy to Internal energy, while the loading can be considered as quasi-static when the ratio is less than 5%. In addition, the thickness of the steel plates in the tested specimen was measured and a 0.2mm deviation in the steel plates with a thickness of 5mm and 8mm was detected. This geometric imperfection of the steel plate thickness was also considered in the model.

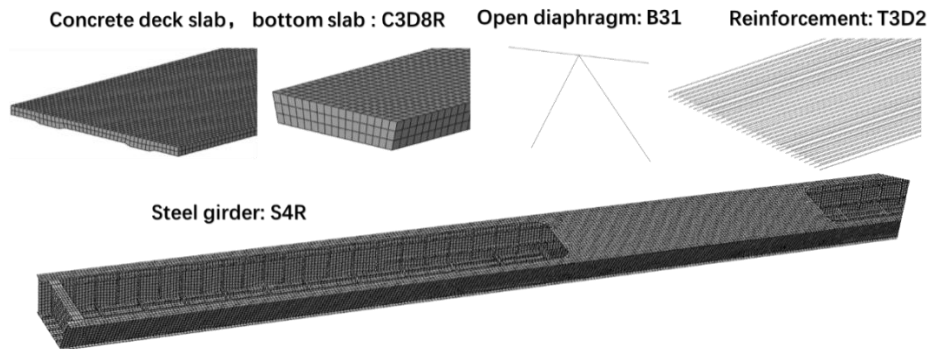


Fig. 13 Element type and mesh of the model

To ensure the accuracy of the model, sensitivity analyses were carried out as shown in Table 4.

The listed nine models were all well converged since A_e/I_e and K_e/I_e were lower than 5%. It can be seen that the dilation angle, the layers of the concrete and the concrete constitutive model have little effect on the accuracy. However, the structural damage pattern changes when the mesh size of the steel girder exceeds 100mm. To divide the concrete slab into two layers and simplify the meshing work, mesh size of both concrete and steel took 50mm. The parameters for simulation were determined as the second model in Table 4.

Table 4

Sensitivity analysis results

No.	Dilation angle (°)	Layers of the concrete	Concrete constitutive model	Mesh size(mm)		A_e/I_e (%)	K_e/I_e (%)
				Concrete	Steel		
1	25	2	fib	50	50	3.4%	1.9%
2	37.5	2	fib	50	50	0.8%	0.4%
3	50	2	fib	50	50	0.4%	0.3%
4	37.5	3	fib	50	50	2.2%	0.8%
5	37.5	4	fib	50	50	2.8%	1.1%
6	37.5	2	fib	100	100	0.4%	0.2%
7	37.5	2	fib	50	100	0.4%	0.4%
8	37.5	2	fib	75	75	0.5%	0.4%
9	37.5	2	Secant Modulus	50	50	2.8%	1.3%

A_e : Artificial Energy

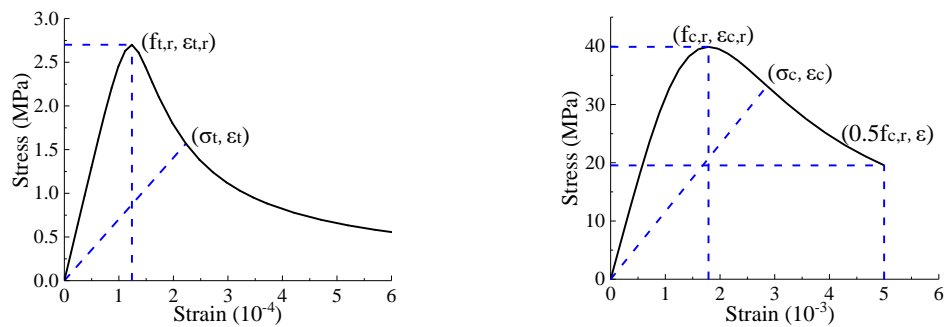
I_e : Inertia Energy

K_e : Kinetic Energy

Material properties

Concrete

Concrete damaged plasticity model^{[28][29]} was introduced for concrete. Fig. 14 presents the uniaxial stress-strain curve determined by Eq.2~Eq.7^[30]. The plastic strain inputting into Abaqus equals to the total strain minus the elastic strain, where $\epsilon_{t,r}$ and $0.4f_{c,r}$ were respectively taken as the tensile and compressive elastic strain^[31]. Eq. 8 defines the damage factor d proposed by Sidoroff^[32].



(a) Tensile stress

(b) Compressive stress

Fig. 14 The stress–strain curve of concrete

$$\sigma = (1 - d_t) E_c \varepsilon \quad \text{Eq. 2}$$

$$d_t = \begin{cases} 1 - \rho_t [1.2 - 0.2x^5] & x \leq 1 \\ 1 - \frac{\rho_t}{\alpha_t (x-1)^{1.7} + x} & x > 1 \end{cases} \quad \text{Eq. 3}$$

$$x = \frac{\varepsilon}{\varepsilon_{t,r}} \quad \rho_t = \frac{f_{t,r}}{E_c \varepsilon_{t,r}} \quad \text{Eq. 4}$$

Where

$$\sigma = (1 - d_c) E_c \varepsilon \quad \text{Eq. 5}$$

$$d_c = \begin{cases} 1 - \frac{\rho_c n}{n-1+x^n} & x \leq 1 \\ 1 - \frac{\rho_c}{\alpha_c (x-1)^2 + x} & x > 1 \end{cases} \quad \text{Eq. 6}$$

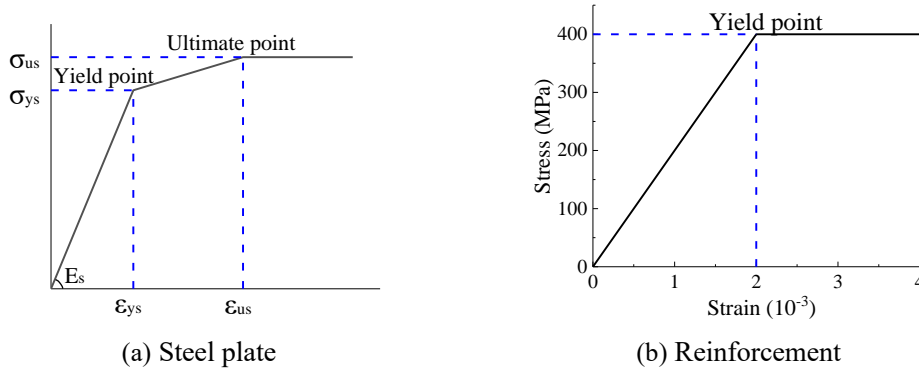
$$x = \frac{\varepsilon}{\varepsilon_{c,r}}, \quad \rho_c = \frac{f_{c,r}}{E_c \varepsilon_{c,r}}, \quad n = \frac{E_c \varepsilon_{c,r}}{E_c \varepsilon_{c,r} - f_{c,r}} \quad \text{Eq. 7}$$

Where

$$d = 1 - \sqrt{\frac{\sigma}{E_0 \varepsilon}} \quad \text{Eq. 8}$$

Steel

Fig. 15(a) presents a trilinear stress–strain curve used to model the material of the steel plate. Stress at yield point σ_{ys} and ultimate point σ_{us} of the steel plates with different thickness took reference from the material property test. The ultimate strain ε_{us} was 0.6% and yield strain ε_{ys} was derived by σ_{ys}/E_s , where E_s was 207GPa. Fig. 15(b) shows a bilinear stress–strain model for the reinforcement. Yield stress of the reinforcement was taken as 400 MPa, with Young's modulus of 200 GPa.

**Fig. 15 The stress-strain model for steel material**

Validation of FEM analysis

Fig. 16 and Fig. 17 compares the load-deflection curves and load-strain curves between the analysis and the test results. They matched with each other in general. The difference was believed mainly due to the material constitution accuracy and full interlayer interaction assumption.

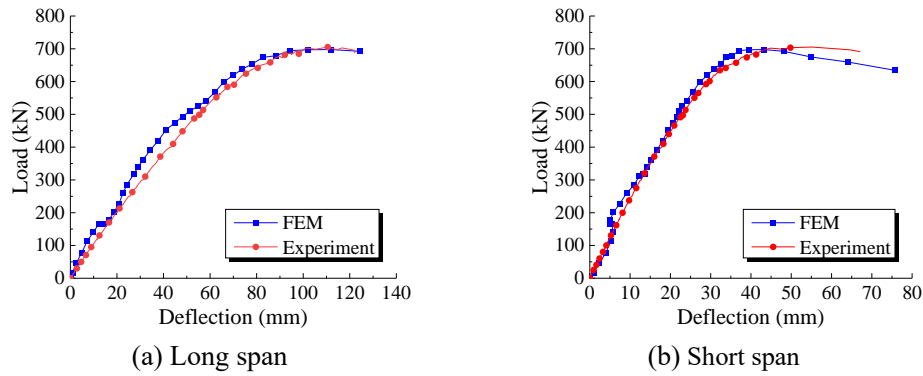


Fig. 16 Comparison of load-deflection curves at mid-spans

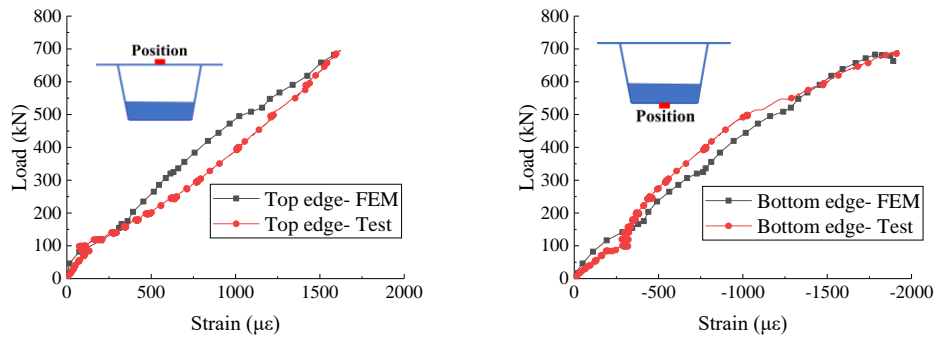


Fig. 17 Comparison of load-strain curves of steel flange at mid support

Fig. 18 shows shear stress distribution on the steel web in the FEM model. The shear stress was particularly large in the hogging moment regions. Meanwhile, the shear stress of the steel web within the range of concrete bottom slab was relatively smaller, indicating that the double composite action helped to reduce the web stress level in the hogging moment region. Fig. 18 compares the failure appearance derived from analysis and test results. It was in consistency that the shear buckling appeared on the steel web adjacent to the additional concrete bottom slab.

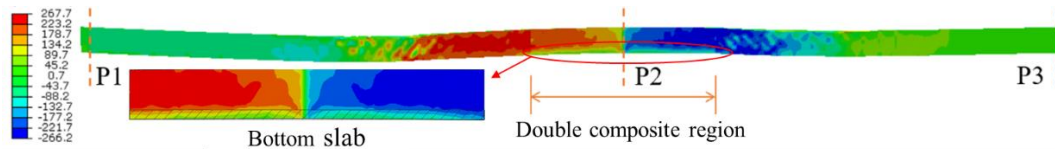
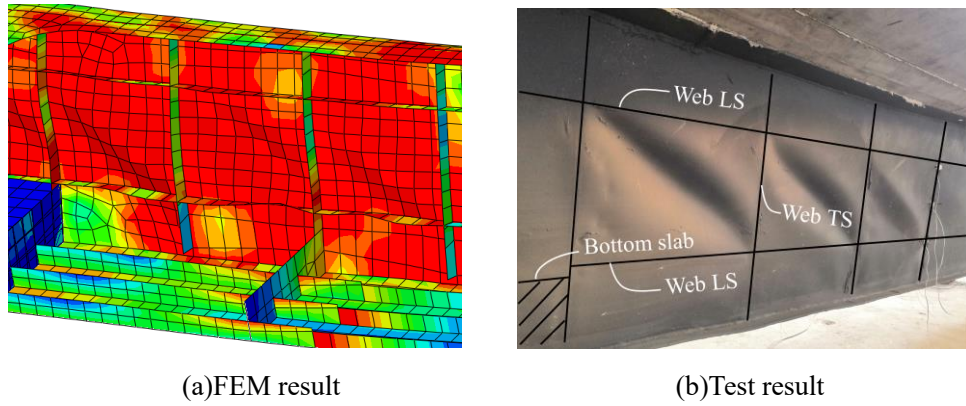


Fig. 18 Shear stress distribution of the steel web at failure



(a)FEM result (b)Test result
(4) Fig. 19 Failure mode comparison

Parametric analysis

According to the test and analysis results, web and bottom stress around the internal support was reduced obviously by the double composite action. Therefore, the thicknesses of steel web and bottom concrete slab can be optimized. Besides, the effect of the steel box section in hogging moment region was also analysed.

Concrete bottom slab thickness

FEM models of specimens with and without double composite action were firstly established and compared as shown in Table 5. The model with double composite action was established corresponding to the test specimen, while the model without double composite action removed the concrete bottom slab. It can be concluded that the additional concrete slab helps to increase the cracking load and ultimate strength by 12% and 4%. Besides, the concrete bottom slab also helps to prevent the steel web from buckling (as shown in Fig. 20).

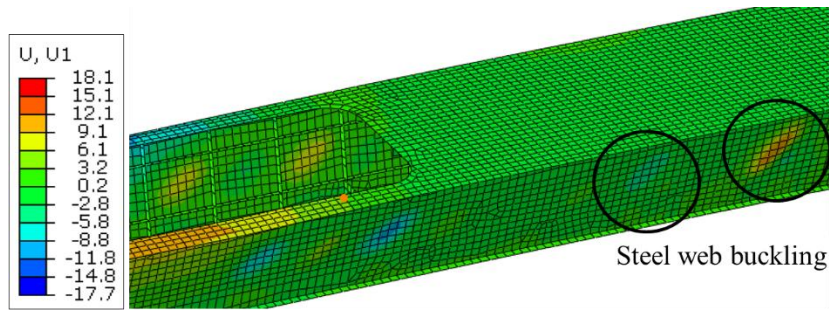
However, the additional concrete slab is not conducive to inhibiting crack development. As shown in Fig. 21, the plastic damage distance of two specimens remains the same during load stage of 70kN. However, when it comes to 100kN, the plastic damage distance of specimen with double composite action is 14% more than specimen without double composite action. This can be attributed to the additional gravity load. Therefore, although the double composite action reinforces the cross section and improves the cracking load and ultimate strength, its additional gravity load can accelerate the crack development.

Table 5

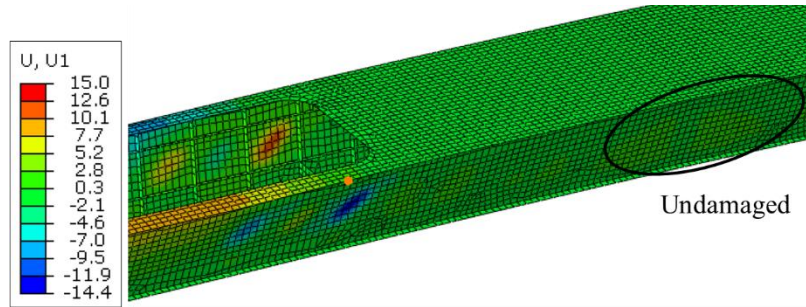
Comparison of specimens with and without double composite action

	Cracking Load (kN)	Ultimate strength (kN)	Crack extension at 70kN (m)	Crack extension at 100kN (m)
With DC (a)	45.625	699	2.1	4
Without DC (b)	40.75	674	2.1	3.5
Ratio (a)/ (b)	112%	104%	100%	114%

DC: Double composite

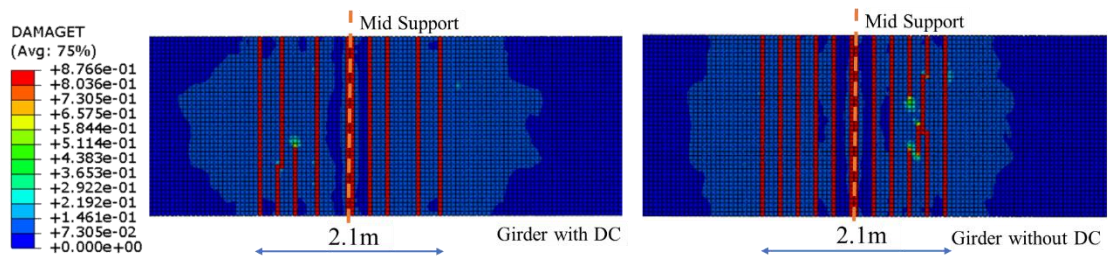


(a) Specimen without double composite

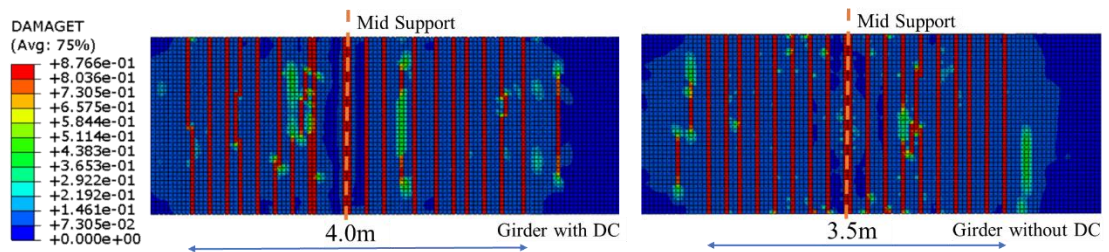


(b) Specimen with double composite

Fig. 20 Failure mode of steel web at the mid support



(a) Load Stage of 100kN



(b) Load Stage of 200kN

Fig. 21 Plastic damage at different load stage

In addition, FEM models with different concrete bottom slab thickness and different forms of longitudinal stiffening ribs were established. Table 4 shows the analyzed ultimate strength of each specimen, in which 2LS indicates the specimen web has both upper and lower longitudinal stiffening ribs, while 1LS indicates the specimen web only has upper longitudinal stiffening rib.

It can be seen that the load-carrying capacity can be increased by a bottom concrete with a thickness lower than 100mm. When the thickness became larger, the load-carrying capacity turned to reduce due to a downward translation of sectional neutral axis. The optimal concrete slab

thickness (100 mm) was found around 15 % of the height of the steel girder (625 mm).

Referring to the effect of longitudinal stiffener, its influence on load-carrying capacity was less remarkable when the concrete bottom slab thickness was larger than 100mm. The contribution of concrete bottom slab to web buckling restraint and sectional strength improvement were the main reason. In other words, the concrete bottom slab can replace the function of the lower longitudinal stiffening ribs.

Table 6

Details of the load-carrying capacity of specimens with different bottom slab thickness

Bottom slab thickness	0mm	50mm	100mm	150mm	200mm
2LS Ultimate strength (kN)	674	687	689	687	686
Ratio to 0mm	100%	101.9%	102.2%	101.9%	101.8%
1LS Ultimate strength (kN)	658	676	689	687	683
Ratio to 0mm	100%	102.7%	104.7%	104.4%	103.8%

2LS: Specimen of web with upper and lower longitudinal stiffening ribs

1LS: Specimen of web with upper longitudinal stiffening rib

Steel web and steel bottom flange thickness

It has been revealed from the previous analysis that the concrete bottom slab helps to restrain the lateral deformation of steel webs. Besides, it also reinforces the steel bottom flange. Thus, models with different steel web and steel bottom flange thickness are established to reveal how much steel can be saved after using the double composite action. Table 7 and Table 8 lists the ultimate strength derived from each model. It can be inferred from Table 7 that the variation of the load-carrying capacity is within 5% with the web thickness larger than 4mm, which means the steel web thickness can be saved 16.7% when using the double composite action. Table 8 also revealed that the steel bottom flange no longer affects the load carrying capacity after using the double composite action. Therefore, the steel bottom flange thickness no longer contributes to the stress condition in the whole girder, whereas needs to meet the constructing requirements present in the design codes.

Table 7

Details of the load-carrying capacity of specimens with different web thickness

Web thickness	4.8mm (1)	4.6mm (2)	4.4mm (3)	4.2mm (4)	4mm (5)	3.8mm (6)
Ultimate strength (kN)	699	694	689	686	675	657
(n)/(1)	100%	99.3%	98.6%	98.1%	96.6%	94.0%

Table 8

Details of the load-carrying capacity of specimens with different steel bottom flange thickness (MPa)

Steel bottom flange thickness	8mm (1)	7mm (2)	6mm (3)	5mm (4)	4mm (5)	3mm (6)	2mm (7)	1mm (8)
Ultimate strength	699	696	695	695	694	693	693	693
(n)/(1)	100.0%	99.6%	99.4%	99.4%	99.3%	99.1%	99.1%	99.1%

Effect of box section

Fig. 22 compares the stress distribution between specimens with or without box section under load stage of 55kN (load according to the initial crack in the test) and 600kN (load according to the yielding point in the test). Stress in the steel girder adopted Mises stress, and stress in concrete slab adopted axial stress in longitudinal direction. Compared with tub section, the box section contributed to a 24.4% and 14.0% stress decline in steel top flange respectively under load stage of 55kN and 600kN. The box section also relieved the stress concentration in concrete slab. The inconspicuous stress decline in concrete slab may be attributed to the increasing coupling stiffness between the concrete slab and the steel girder.

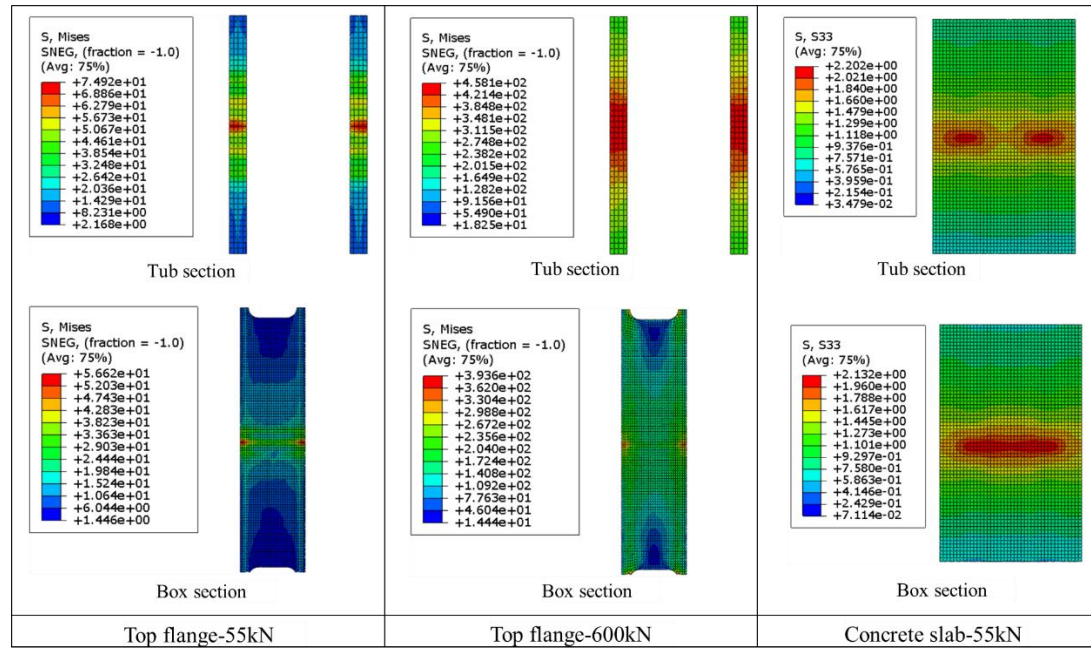


Fig. 22 Comparison between specimens with or without box section

Models with different steel top flange thickness were established and analyzed as shown in Table 9. It can be seen that the steel top flange stress decreases with the growth of the flange thickness, while the concrete stress varies little. Besides, compared with tub section, the box section can decrease the steel top flange stress by 30.5% and 16.5% at the load stage of 55kN and 600kN when the flange thickness is 12mm. It can be inferred that the reduction rate tends to be larger with a thicker top flange.

Table 9

Details of the stress condition of specimens with different steel top flange thickness (MPa)

Top flange thickness (mm)		2	4	6	8	10	12
Box section	Steel stress at 55kN (a)	88.3	73.6	63.8	56.6	51.2	48.5
	Steel stress at 600kN (b)	457.9	447.9	442.4	393.6	386.5	382.4
	Concrete stress at 55kN (c)	2.1	2.1	2.1	2.1	2.1	2.1
Tub section	Steel stress at 55kN (d)	109.4	88.1	79.7	74.9	71.9	69.9
	Steel stress at 600kN (e)	457.8	459.0	459.9	458.1	458.4	458.2
	Concrete stress at 55kN (f)	2.2	2.2	2.2	2.2	2.2	2.2
	(a)/(d)	80.7%	83.6%	80.1%	75.6%	71.3%	69.4%
	(b)/(e)	100.0%	97.6%	96.2%	85.9%	84.3%	83.5%

Evaluation of the double composite section at service stage

The numerical study presented above only concerned the effect of concrete bottom slab on ultimate limit capacity. The serviceability limit state had not been investigated. It was also necessary for proposing a well-established design criteria of double composite section. Therefore, the sectional cracking moment and stress level in the service state were evaluated as well in this study.

Uncracked state

The uncracked sectional stress distribution can be evaluated by transformed section method. Moreover, the stress evaluation takes several construction stages into account, which is shown in Fig. 23. At first, the self-weight of steel and concrete bottom slab was supported by steel girder. Then, the weight of concrete deck slab was supported by steel girder with bottom concrete slab. Afterwards, the additional external dead and live loads were supported by the entire composite section.

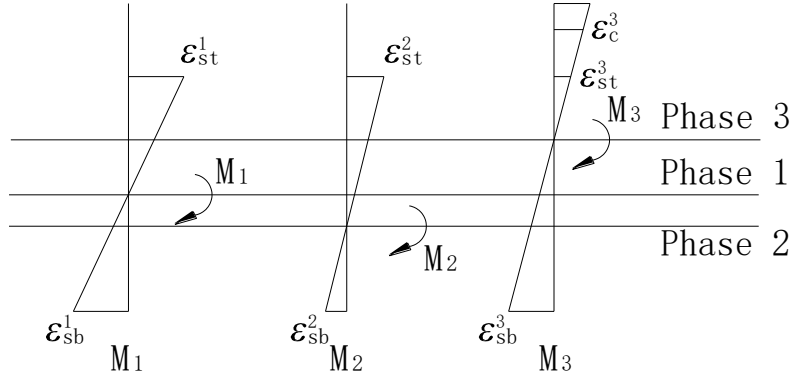


Fig. 23 Sectional strain distribution under different construction phases

The steel top flange stress σ_{st} , the steel bottom flange stress σ_{sb} and the concrete top edge stress σ_c can be derived by Eqs.9-11.

$$\sigma_{st}^i = -\frac{M_i}{I_i} y_i \quad i = 1, 2, 3 \quad \text{Eq. 9}$$

$$\sigma_{sb}^i = \frac{M_i}{I_i} (h_s - y_i) \quad i = 1, 2, 3 \quad \text{Eq. 10}$$

$$\sigma_c^i = \frac{M_i}{n_i I_i} (y_i + h_c) \quad i = 3 \quad \text{Eq. 11}$$

The cross-section area, vertical distance from the neutral axis to the upper fiber of the steel girder and moment of inertia under different construction phases can be derived by Eqs.12-15. Fig. 24 illustrates the geometrical parameters for the calculations in Eqs.12-15.

$$A_2 = A_s + \frac{A_{bc}}{n} \quad \text{Eq. 12}$$

$$y_2 = \frac{1}{A_2} \left(A_s y_s + \frac{A_{bc} y_{bc}}{n} \right) \quad \text{Eq. 13}$$

$$A_3 = A_s + \frac{A_{bc}}{n} + \frac{A_c}{n} \quad \text{Eq. 14}$$

$$y_3 = \frac{1}{A_3} \left(A_s y_s + \frac{A_{bc} y_{bc}}{n} - \frac{A_c y_c}{n} \right) \quad \text{Eq. 15}$$

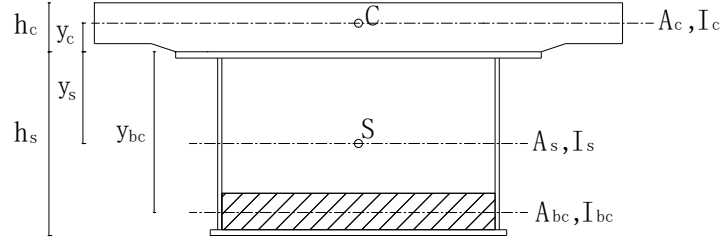


Fig. 24 Definition of cross-sectional parameters of double composite section before concrete cracking

Considering cracking begins when σ_c^3 reaches the concrete tensile strength f_{ct} , the bending moment corresponding to cracking stage M_{cr} can be derived by Eq. 16.

$$M_{cr} = -\frac{f_{ct}}{h_c + y_3} n I_3 \quad \text{Eq. 16}$$

Cracked state

The contribution of cracked concrete deck slab can be ignored, while the steel girder, concrete bottom slab and the reinforcements in concrete deck slab are still in elastic stage. Section parameters during this stage can be derived by Eqs.17-18, and Fig. 25 illustrates the geometrical parameters for the calculations.

$$A_4 = A_s + \frac{A_{bc}}{n_c} + A_r \quad \text{Eq. 17}$$

$$y_4 = \frac{1}{A_4} \left(A_s y_s + \frac{A_{bc} y_{bc}}{n_c} - A_r y_r \right) \quad \text{Eq. 18}$$

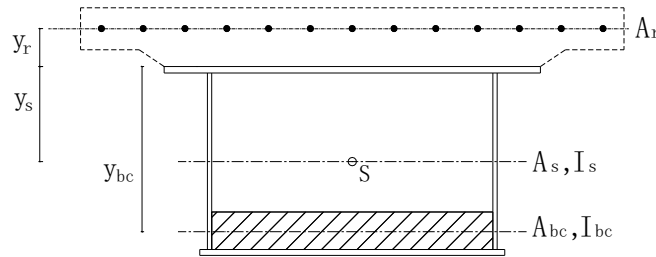


Fig. 25 Definition of cross-sectional parameters of double composite section after concrete cracking

After concrete cracking, σ_{st} , σ_{sb} and reinforcements stress σ_r can be derived by Eq.19-21 using linear superposition method.

$$\sigma_{st}^4 = -\frac{M_1}{I_s} y_s - \frac{M_2}{I_2} y_2 - \frac{M_4}{I_4} y_4 \quad \text{Eq. 19}$$

$$\sigma_{sb}^4 = \frac{M_1}{I_s} (h_s - y_s) + \frac{M_2}{I_2} (h_s - y_2) + \frac{M_4}{I_4} (h_s - y_4) \quad \text{Eq. 20}$$

$$\sigma_r^4 = -\frac{M_4}{I_4} (y_r + y_4) \quad \text{Eq. 21}$$

Case study and parameter optimization

A three span (35+60+35) m continuous composite girder bridge was taken as an example to evaluate the double composite performance and rationalize the critical component dimensions. Fig. 26 and Table 5 provide the sectional details.

The sectional cracking moment M_{cr} can be derived by substituting necessary parameters into Eq. 17. And the variation feature of M_{cr} indicated by R_{cr} with concrete bottom slab thickness was depicted in Fig. 27. R_{cr} is the cracking moment ratio of a double composite section to a conventional composite section. The development of it experiences increase and decrease stages with an increasing h_{bc} . During the increasing stage, the sectional moment of inertia growth was greater than the decline of the neutral axis. When h_{bc} reached beyond 250mm, the sectional cracking moment decreased because of an obvious downward translation of sectional neutral axis. It meant that the optimal h_{bc} for cracking moment improvement was around 250mm. Besides, it can also be concluded that with the decrease of steel bottom flange thickness, the cracking moment improvement became obvious.

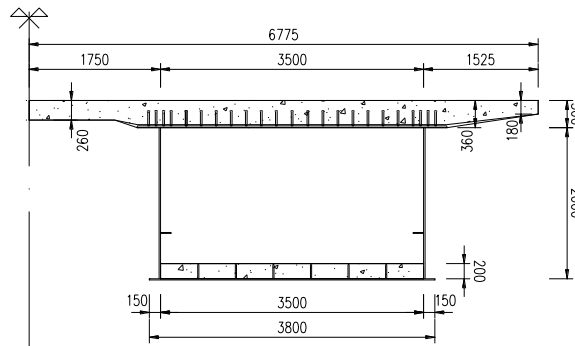


Fig. 26 Definition of the example bridge (mm)

Table 10

Section detail of the (35+60+35) m continuous composite girder (mm)

Steel top flange		Steel bottom flange		Web		Reinforcements	
Width	Thickness	Width	Thickness	Height	Thickness	Diameter	quantity
4100	24	3800	26	2000	20	22	138

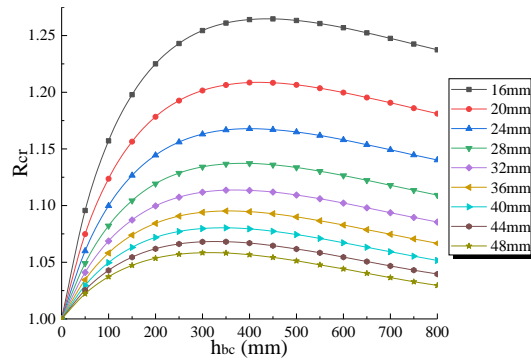


Fig. 27 Relationship between cracking moment ratio and concrete bottom slab thickness for different steel bottom flange thickness

A numerical analysis of continuous composite girder, which included construction process^[34], was established as shown in Fig. 28. It was for extracting the bending moments during three construction or loading phases. Particularly, $M_1=21813\text{kN}\cdot\text{m}$, $M_2=3630\text{kN}\cdot\text{m}$, $M_3=26049\text{kN}\cdot\text{m}$. In terms of Eq. 21-23, the steel top flange stress σ_{st}^4 , the steel bottom flange stress σ_{sb}^4 and reinforcements stress σ_r^4 can be derived. And the relationship between σ_{st}^4 , σ_{sb}^4 , σ_r^4 and h_{bc} is shown in Fig. 29. It can be deduced from Fig. 29 (a) and Fig. 29 (c) that the concrete bottom slab thickness has little influence on σ_{st}^4 and σ_{sb}^4 , as the stress change was within 5%. However, the steel bottom flange stress decreased up to 20% with the growth of h_{bc} , and the rapid descent stage was before h_{bc} reached 300mm.

Based on the results obtained for the cracking moment and stress state of different representative points of the cross-section in the mid support, the conclusion is that the optimal concrete bottom slab thickness is 300mm, which represents around $0.15h_s$. The result also coincides with the parametric analysis.

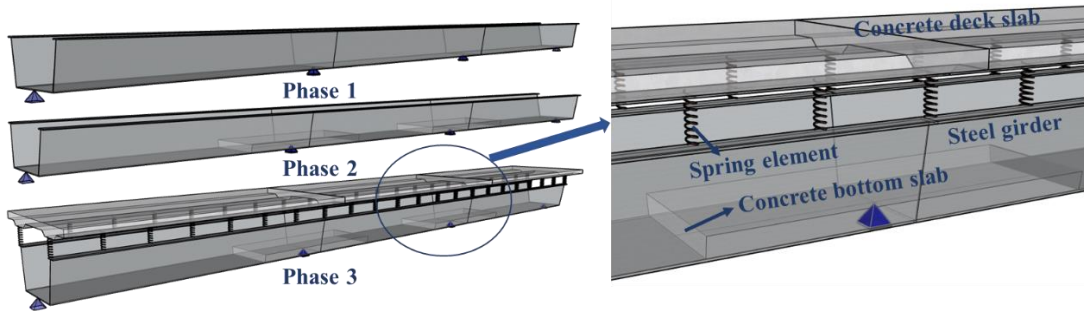
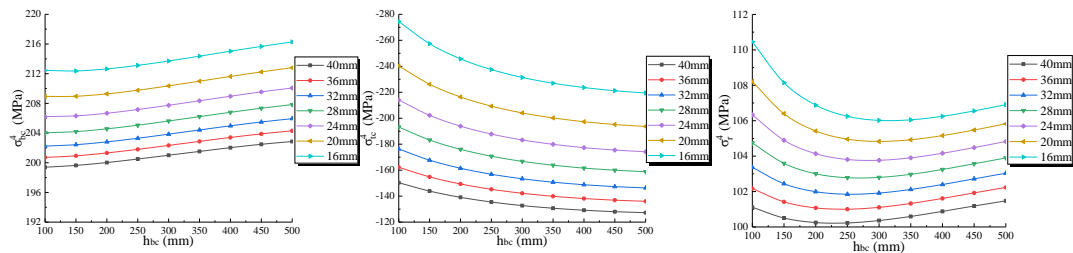


Fig. 28 Linkage FEM model



(a) Steel top flange stress (b) Steel bottom flange stress (c) Reinforcements stress

Fig. 29 Relationship between stress value and concrete bottom slab thickness

Conclusions

A large scaled (1:3) two-span continuous girder specimen with double composite action in the hogging moment region was fabricated and tested. A numerical analysis was also conducted. Based on the experimental and analytical results, the following conclusions can be drawn.

- (1) According to the test observations, the concrete bottom slab helps to restrain lateral deformation of steel web and steel bottom flange. It can effectively improve the anti-buckling ability of the continuous girder.
- (2) Based on the parametric analysis, the additional concrete slab helps to increase the cracking load and ultimate strength by 12% and 4%. However, the additional gravity load can accelerate the crack development. Besides, the optimal concrete slab thickness was found around 15 % of the height of the steel girder. The ultimate strength decreases afterwards mainly due to a continuing downward translation of the sectional neutral axis. In addition, the concrete bottom slab can also replace the function of the lower longitudinal stiffening ribs.
- (3) Based on the parametric analysis, the steel web thickness can be saved 16.7%, while the steel bottom flange thickness only needs to meet the constructing requirement after using the double composite action. Besides, the box section could contribute to a 24.4% and 3.2% stress decline respectively in steel top flange and concrete slab compared with tub section.
- (4) According to the concrete bottom slab optimization, the cracking moment was increasing to a maximum and after that decreasing with the increase of the concrete bottom slab thickness, while the steel bottom flange stress can be decreased up to 20%. Taking into account both the cracking moment and stress state at the service stage, the optimal concrete bottom slab thickness was 15% of steel girder height. This is also in agreement with the optimal thickness obtained according to conclusion 2.
- (5) Due to its advantage of steel flange stress reduction and buckling prevention, the novel double composite system is particular economical for long-span continuous composite bridge which bears high stress level in the hogging moment region. Furthermore, the double composite action can be applied together with high strength steel. Since the local buckling is prevented, the high strength of the steel material can be better utilized.

Acknowledgement

This research is sponsored by the National Natural Science Foundation of China (No. 51978501) and the China Scholarship Council (No. 202106260050). The supports are gratefully appreciated.

References

- [1] Ryu H K , Shim C S , Chang S P . Inelastic behaviour of externally prestressed continuous composite box-girder bridge with prefabricated slabs[J]. Journal of Constructional Steel Research, 2004, 60(7):989-1005.
- [2] Morsch, Inacio, B, et al. Numerical simulation of external pre-stressed steel-concrete composite beams[J]. Computers & Concrete, 2017, 19(2):191-201.
- [3] Lu Y , Ji L . Behavior of optimized prestressed concrete composite box-girders with

corrugated steel webs[J]. *Steel and Composite Structures*, 2018, 26(2):183-196.

[4] Zhuang B, Liu Y, Yang F. Experimental and numerical study on deformation performance of Rubber-Sleeved Stud connector under cyclic load[J]. *Construction and Building Materials*, 2018, 192:179-193.

[5] Su H, Su Q, Xu C, et al. Shear performance and dimension rationalization study on the rubber sleeved stud connector in continuous composite girder[J]. *Engineering Structures*, 2021, 240(OCT.30):112371.

[6] Xu X, Liu Y. Analytical and numerical study of the shear stiffness of rubber-sleeved stud[J]. *Journal of Constructional Steel Research*, 2016, 123(aug.):68-78.

[7] He J, Lin Z, Liu Y, et al. Shear stiffness of headed studs on structural behaviors of steel-concrete composite girders[J]. *Steel and Composite Structures*, 2020, 36(5):553-568.

[8] Lin W, Yoda T, Taniguchi N. Application of SFRC in steel-concrete composite beams subjected to hogging moment[J]. *Journal of Constructional Steel Research*, 2014, 101(oct.):175-183.

[9] Zhu L, Wang J J, Li X, et al. Experimental and Numerical Study of Curved SFRC and ECC composite beams with Various Connectors[J]. *Thin-Walled Structures*, 2020, 155:106938.

[10] Xu C, Xiao H, Zhang B, et al. Fatigue behavior of steel fiber reinforced concrete composite girder under high cycle negative bending action[J]. *Engineering Structures*, 2021, 241(3):112432.

[11] Zhang Y, Cai S, Zhu Y, et al. Flexural responses of steel-UHPC composite beams under hogging moment[J]. *Engineering Structures*, 2020, 206(2020):1-15.

[12] Cheng Z, Zhang Q, Bao Y, et al. Flexural behavior of corrugated steel-UHPC composite bridge decks[J]. *Engineering Structures*, 2021, 246(3):113066.

[13] Mohammed A A, Manalo A C, Ferdous W, et al. Experimental and numerical evaluations on the behaviour of structures repaired using prefabricated FRP composites jacket[J]. *Engineering Structures*, 2020, 210.

[14] Al-Qaralleh M, Toutanji H, Eljufout T. Overloading impact on the flexural behavior of RC beams strengthened with FRP composites under fatigue: Experimental study[J]. *Engineering Structures*, 2020, 221:111045.

[15] Saul, Reiner. Bridges with Double Composite Action[J]. *Structural Engineering International*, 1996, 6(1):-.

[16] Stroh S, Sen R. STEEL BRIDGES WITH DOUBLE-COMPOSITE ACTION: INNOVATIVE DESIGN[J]. *Transportation Research Record Journal of the Transportation Research Board*, 2000, 1696:299-309.

[17] Martinez-Calzon, J. Strict Box Composite Bridges. A New Design of the Optimum Use of Composite Topology. Proc., 12th Annual International Bridge Conference and Exhibition, June 19–21, 1995, Pittsburgh, Pa., Engineers' Society of Western Pennsylvania, pp. 258–264.

[18] Kim H H, Shim C S. Experimental investigation of double composite twin-girder railway bridges[J]. *Journal of Constructional Steel Research*, 2009, 65(6):1355-1365.

[19] Kim, Choong-Eon, Yun. Structural behavior of a continuous composite truss with a composite bottom chord[J]. *Journal of Constructional Steel Research*, 2015, 10, 1-11.

- [20] Shim C S , Whang J W , Chung C H , et al. Design of Double Composite Bridges using High Strength Steel[J]. Procedia Engineering, 2011, 14(12):1825-1829.
- [21] Jiang, Yuchen, Xiamin, et al. Experimental study and theoretical analysis of partially encased continuous composite beams[J]. Journal of Constructional Steel Research, 2016, 117, 152-160.
- [22] Chen Xu, Qingtian Su, Chong Wu, Kunitomo Sugiura. Experimental study on double composite action in the negative flexural region of two-span continuous composite box girder[J]. Journal of Constructional Steel Research, 2011, 67(10):1636-1648.
- [23] Chinese Standard GB/T 50081-2019 Standard for test methods of concrete physical and mechanical properties, China, 2019
- [24] Chinese Standard GB/T 228-2002 Metallic materials- Tensile testing at ambient temperature, China, 2002
- [25] Japanese Society of Steel Construction. Standard on push-out test for headed stud [S]. Japanese Society of Steel Construction, 1996.
- [26] Oehlers DJ, Coughlan CG. The shear stiffness of stud shear connections in composite beams. Journal of Constructional Steel Research 1986; 6:273–84.
- [27] Oehlers DJ, Bradford MA. Elementary behaviour of composite steel & concrete structural members. Butterworth-Heinemann; 1999.
- [28] Li X X L . Parametric Study on Numerical Simulation of Missile Punching Test Using Concrete Damaged Plasticity (CDP) Model[J]. International Journal of Impact Engineering, 2020, 144:103652.
- [29] Choi Y S , Choi S Y , Kim I S , et al. Experimental study on the structural behaviour of calcium-leaching damaged concrete members[J]. Magazine of Concrete Research, 2018, 70(21-22):1102-1117.
- [30] Chinese Standard GB50010-2010 Code for design of concrete structures, China, 2010
- [31] ENV 1992-1-1. Eurocode-2: design of concrete structures, Part1: general rules and rules for buildings, CEN, 1992.
- [32] Mander J A B , Priestley M J N . Theoretical Stress-Strain Model for Confined Concrete[J]. Journal of Structural Engineering, 1988, 114(8):1804-1826.
- [33] Nguyen H T , Kim S E . Finite element modeling of push-out tests for large stud shear connectors[J]. Journal of Constructional Steel Research, 2009, 65(10-11):1909-1920.
- [34] Chinese Standard JTG D60-2004 General Code for Design of Highway Bridges and Culverts, China, 2004

6.5 Structural Engineering International 2022

Su H, Su Q, Casas JR, et al. Application of Partial Shear Connection in Steel–Concrete Semi-Continuous Composite Girder Bridges. Structural Engineering International, 2022, 32: 411-420. DOI: 10.1080/10168664.2022.2048436

Application of Partial Shear Connection in Steel-concrete Semi-continuous Composite Girder Bridges

Hang Su ^{a,b}, Qingtian Su ^{a,c}, Joan R. Casas ^b, Xu Jiang ^{a*}, Guandong Zhou ^d

^a *Department of Bridge Engineering, Tongji University, 1239 Siping Road, Shanghai, China 200092*

^b *School of Civil Engineering. Department of Civil and Environmental Engineering, Technical University of Catalunya, c/Jordi Girona 1-3. Campus Nord. Modulo C-1, Barcelona (Spain) 08034*

^c *Shanghai Engineering Research Center of High Performance Composite Bridge, 901 Zhongshanbeier Road, Shanghai, China 200092*

^d *Guangdong Communication Planning & Design Institute Group Co., Ltd, No.22 Xinghua Road, Guangzhou, China 510507*

Abstract

In the hogging moment regions of steel-concrete composite continuous girder bridges, detrimental condition appears that concrete slab bears tensile stress and steel girder bears compressive stress. Decreasing the shear connection in the hogging moment regions helps to improve the mechanical performance for steel-concrete continuous composite girder bridges. In this paper, analytical models for the calculation of composite girder considering PSC action are discussed. A project case of Qiwu bridge in Jiangxi Province using partial shear connection action was introduced. Nonlinear finite element model of Qiwu Bridge was established through ABAQUS to simulate and predict the mechanical properties and structural performance. Based on the FEM results, the influence of partial shear connection on various parameters were analysed by performing a parametric analysis. Numerical results showed that arranging partial shear connection region can effectively reduce the crack region and disperse the area with high stress concentration, but the shear stiffness mutation can magnificently increase the stress level at the edge of the partial shear connection region.

Keywords: Partial Shear Connection; Steel-concrete Composite Girder; Hogging Moment Region; Parametric Analysis

Introduction

Steel-concrete composite structure is a reasonable configuration for simply supported bridges because sagging bending moment is present in the whole span. That is, the upper concrete slab bears compressive stress, and the steel girder at lower edge bears tensile stress. However, for continuous girder bridges, stress distribution is more complicated due to hogging moment regions^{[1]-[3]}, where concrete slab bears tensile stress and steel girder bears compressive stress. In response to this issue, many different solutions were proposed^{[4]-[12]}, where decreasing the stiffness of shear connectors in the hogging moment regions is one of the most effective ones. Normal steel and concrete composite structures often adopt full shear connection (FSC) due to clear mechanical properties and convenient construction. However, under the effects of temperature and external load, large tensile stress will be generated at the joint between concrete slab and steel girder in the hogging moment regions due to non-compatibility of strains. Partial shear connection (PSC) helps to decrease the binding extent between concrete slab and steel girder in hogging moment regions, simultaneously maintaining the ultimate bearing capacity and overall stiffness of the structure^{[13][14]}. Loh et.al^{[15][16]} carried out experimental and analytical studies on partial shear connection of composite girders in hogging moment regions and found that as the degree of connection decreases, the ultimate bearing capacity of the composite girders remains basically unchanged. For designing of PSC, Hiragi et al.^[17] wrapped urethane at the root of the ordinary headed stud (OHS) and carried out push-out and bending tests. Results reflected that the proposed shear connector showed remarkable flexible behavior. J. Nie et al.^[18] proposed a concept of uplift-restricted and slip-permitted (URSP) connection, including screw-type, sliding-type and T-shape connectors.

In this paper, a case study, the Qiwu bridge in Jiangxi Province using PSC action is introduced. A non-linear finite element model of Qiwu Bridge was established through ABAQUS to simulate the mechanical properties and the predict the bridge performance. Based on the FEM results, the influence of PSC action on various parameters were analysed by performing parametric analysis. The results reported herein supplement the numerical data of PSC component and to shed further light into practical application of PSC in bridge engineering.

Analytical Models of composite girders with PSC action

Calculation of deflection

In practice, the composite action may exist somewhere between FSC and no shear connection. Unlike composite girders with FSC, girders with PSC action don't satisfy the assumption of plane section, which is often overlooked during the design because of the complexity in the analysis. This will underestimate the deflection prediction. Computing methods of the maximum deflection of composite girder considering PSC action has been discussed in many literatures. Bradford^[19] deduced the maximum deflection of simply supported composite girder with PSC action as Eq.1.

$$\Delta_p = \Delta_f + CF_{sh} \quad \text{Eq. 1}$$

Where

$$C = \frac{L_s}{K_s} (h_c + h_s) \frac{\overline{EA}}{EI}; \sum EI = E_c I_c + E_s I_s; \frac{1}{EA} = \frac{1}{E_c A_c} + \frac{1}{E_s A_s}; \overline{EI} = \sum EI + \overline{EA} (h_c + h_s)^2$$

$$F_{sh} = \frac{\overline{EA} (h_c + h_s)}{EI} w L^2 \left\{ \frac{x(L-x)}{2L^2} + \frac{C_1^2}{\pi^2} \left[\frac{1 - \cosh \frac{\pi}{C_1}}{\sinh \frac{\pi}{C_1}} \sinh \left(\frac{\pi x}{C_1 L} \right) + \cosh \frac{\pi x}{C_1 L} - 1 \right] \right\}$$

$$C_1 = \frac{\pi}{L} \sqrt{\frac{L_s \overline{EA} \sum EI}{K_s EI}}$$

Δ_p, Δ_f : Deflection due to partial composite action and full composite action

L_s, K_s, F_{sh} : Spacing, initial modulus and total shear force of the shear connector

L : Length of the girder; x : distance from the support

The equation of the maximum deflection of simply supported composite girder with PSC action under uniformly distributed load w proposed by Girhammar ^[20] is as Eq.2.

$$\Delta_{\max} = \frac{5wL^4}{384EI_f} + \frac{w}{\alpha^4 EI_f} \left(\frac{EI_f}{\sum EI} - 1 \right) \left[\frac{1}{\cosh \left(\frac{\alpha L}{2} \right)} + \frac{1}{8} \alpha^2 L^2 - 1 \right] \quad \text{Eq. 2}$$

Where

$$\alpha^2 = K \left[\frac{1}{E_c A_c} + \frac{1}{E_s A_s} + \frac{(h_c + h_s)^2}{\sum EI} \right]$$

EI_f : is the bending stiffness of the composite cross section with complete interaction

The computing method of the maximum deflection introduced by Nie ^[21] is as Eq.3.

$$\Delta_{\max} = \frac{5wL^4}{384EI_f} + \beta w \left(\frac{L^2}{8h} + \frac{2e^{\frac{\mu L}{2}} - 1 - e^{-\frac{\mu L}{2}}}{\mu^2 h (1 + e^{\mu L})} \right) \quad \text{Eq. 3}$$

Where

$$\mu^2 = \frac{K}{A_1 E_s I_0 L_s}; \beta = \frac{A_1 (h_c + h_s) P}{K}; A_1 = \frac{A_0}{I_0 + A_0 (h_c + h_s)^2}; A_0 = \frac{A_s A_c}{n A_s + A_c}; I_0 = \frac{I_c}{n} + I_s; n = \frac{E_s}{E_c}$$

Considering specimens designed according to IRC:22-2008 ^[22], and the design parameters as shown in Table 1, with a width of the concrete slab equal to 2500mm for all spans, the mid-span deflection according to the abovementioned models was calculated. FEM models of girders considering various design parameters have also been established using Abaqus (as shown in Fig 1a). The geometrical and material modeling method is similar to the simulation above, except that the shear connectors are modelled as spring elements. The numerical results are compared with the analytical models discussed above.

Considering the degree of interaction as 1 when the shear stiffness of the spring element satisfies the full shear connection ^[9], the midspan deflections of girders with different degrees

of interactions are shown in Fig 1(b). It can be inferred that the deflection drops nearly linearly with the increase of the interaction degree. Fixing the interaction as 0.8, the midspan deflection increase of girders with different span-lengths can be obtained as Fig 1(c), which shows a smaller deflection increment with the increase of the span. Besides, it can be inferred that the numerical result matches up with the Nie's model, while that of the Bradford's model and Girhammar's model are relatively conservative. Thus, Nie's model is recommended for deflection.

It is worth noting that all the analytical models for deflection were studied by using a simple beam. When applying the analytical models to continuous bridges or semi-continuous composite bridges as Qiwu Bridge, the calculation model should be simplified accordingly. For continuous girder, there is an inflection point between the hogging moment region and the sagging moment region, while the region between the two points of inflection can be simplified as a simply supported beam [23]. Thus, when calculating continuous bridges, we can use Nie's model and replace the calculated span with the distance between the two points of inflection. As for semi-continuous composite bridges as Qiwu Bridge (3×60m), the calculation model can be simplified to a 60m simply supported bridge. The limited deflection increase due to the simplification is small (around 5 %) and on the safe side for structural checks.

Table 1. Design parameters

Span (m)	Top flange		Bottom flange		Web		Concrete slab	Load (kN/m)
	width (mm)	thickness (mm)	width (mm)	thickness (mm)	width (mm)	thickness (mm)	thickness (mm)	
10	200	20	200	20	600	8	150	36
15	250	25	250	25	850	8	175	36.5
20	300	30	300	30	1000	10	200	37
25	350	35	350	35	1200	10	225	38
30	400	40	400	40	1300	12	250	39

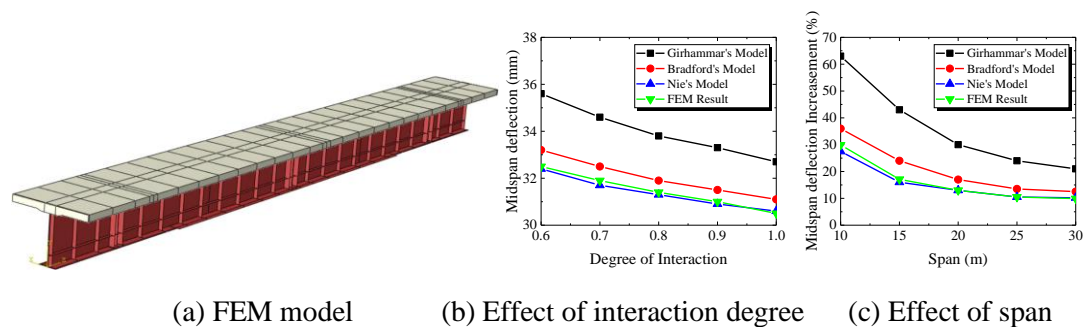


Fig. 1 Parametric analysis on the midspan deflection

Calculation of stress

Stress condition is an important parameter for construction design. He [24] deduced the concrete and steel stress with PSC action under uniform load p as Eq.4 and Eq.5, where shear stiffness of the stud connectors along the whole girders were considered as the same.

$$\sigma_c = \frac{N_c}{A_c} + \frac{M_c y_c}{I_c} = \frac{N_c}{A_c} + \frac{(pLx/2 - px^2/2 - N_c h_0) E_c I_c y_c}{I_c EI} \quad \text{Eq. 4}$$

$$\sigma_s = \frac{N_c}{A_c} - \frac{M_s y_s}{I_s} = \frac{N_c}{A_c} - \frac{(pLx/2 - px^2/2 - N_c h_0) E_s I_s y_s}{I_s EI} \quad \text{Eq. 5}$$

Where

$$N_c(x) = C_1 \sinh(\lambda x) + C_2 \cosh(\lambda x) + \frac{h_0 p K_s (Lx - x^2 - 2/\lambda^2)}{2\lambda^2 EI}$$

$$\lambda^2 = K_s \left(\frac{1}{E_c A_c} + \frac{1}{E_s A_s} + \frac{h_0^2}{EI} \right), \quad C_1 = \frac{h_0 p K_s \tanh(\lambda L/2)}{\lambda^4 EI}, \quad C_2 = \frac{h_0 p K_s}{\lambda^4 EI}$$

N_c, M_c, M_s : Axial force and bending moment in concrete and steel girder

h_0 : Distance between the centroid of concrete slab and steel girder

y_c, y_s : Distance from the centroid of the beam to the concrete slab and steel girder

K_s : Shear stiffness of the stud connector

As for composite girders using stud connectors with different shear stiffness, Su [25] conducted numerical analysis on the effect of stud stiffness on girder stress and summarized a series of empirical equations. The numerical analysis considers the whole hogging moment region as PSC region and decrease the shear stiffness of the stud connectors within the area.

Calculation of stud stiffness

To calculate the stress and deflection of composite girders with PSC action, stud stiffness should also be determined. Xu [26] conducted push-out tests and deduced the shear stiffness of ordinary headed stud (OHS) connector and rubber-sleeved stud (RSS) connector through method of elastic foundation beam (as shown in Eq.6 and Eq.7). It can be inferred that the stud stiffness can be controlled by the rubber sleeve height H_r .

$$K_{OHS} = 0.374 d_s^3 E_c^4 E_s \quad \text{Eq. 6}$$

$$K_{RSS} = \exp(-0.648 \frac{H_r}{d_s}) K_{OHS} \geq 12 E_s I_s / H_s^3 \quad \text{Eq. 7}$$

K_{OHS}, K_{RSS} : Shear stiffness of OHS connector and RSS connector

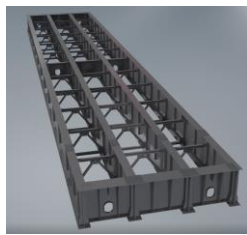
d_s, H_s : Diameter and height of the stud connector

H_r : Height of the rubber sleeve

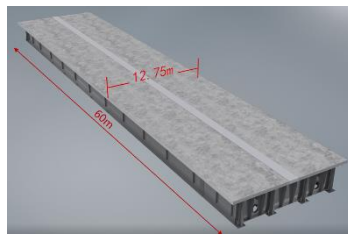
Case study of Qiwu Bridge

Overall design

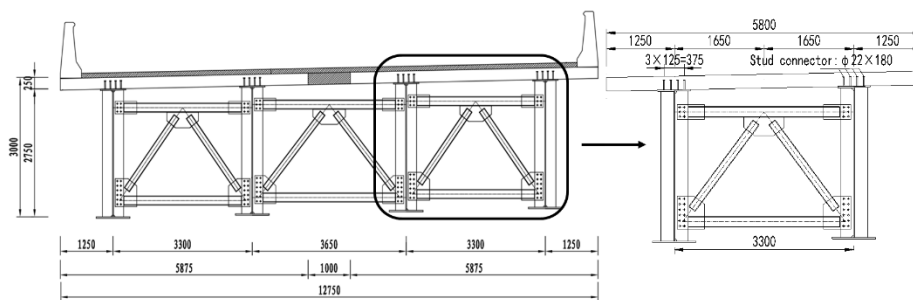
Qiwu Bridge is a three-span steel-concrete continuous composite girder bridge being built in Jiangxi Province, China. The span length is 60m for all spans. Layout of half of a standard span is shown in Fig. 2. The total width of the concrete slab is 26m, with a 0.5m space between the two halves. At the mid support of Qiwu Bridge, the concrete slab is continuous and the steel girder remains disconnected. The steel girder quality of Qiwu Bridge is Q420, and the slab concrete strength is C50. Height of the I-shaped steel girder and the concrete slab are 2.75m and 0.25 respectively. Thickness of the top flange and the web adopts 25mm and 20mm respectively, and the thickness of the bottom flange is variational, which is shown in Fig. 2(d). Solid diaphragms are applied to the mid-span and beam-end of the steel girder, while the other diaphragms adopt K-shape open diaphragms. Stud connector in Qiwu Bridge adopts $\phi 22 \times 180$, and the longitudinal and transverse spacing are 150mm and 125mm respectively. Reinforcement bars in the concrete slab adopts HRB400, of which the diameter is 20mm and the separation distance is 150mm. The layout of reinforcement bars in quarter cross section is shown in Fig. 2(e). Within the range of stiffness mutation, reinforcement diameter is increased and separation distance is decreased to control the crack width. The construction of Qiwu Bridge has just begun. Some pictures during the construction process are shown in Fig. 3.



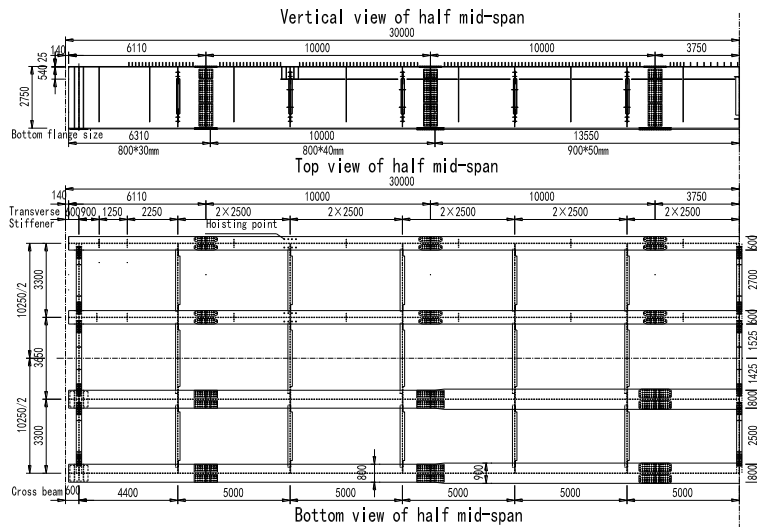
(a) Steel girder



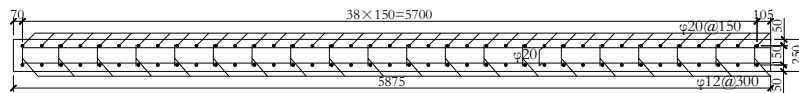
(b) Composite girder



(c) Layout of half cross section (mm)



(d) Layout of half steel girder (mm)



(e) Layout of reinforcement bars in quarter cross section (mm)

Fig. 2 Half span of Qiwu Bridge



(a) Component fabrication

(b) Assembling

(c) Coating

Fig. 3 Pictures during construction process

Construction sequence

Qiwu Bridge adopts simply supported-continuous system. Different parts of the 60m-steel girder are assembled on a pedestal with camber in the prefabrication factory, where the cross beam is bolted to the steel girder segment and different steel girder segments are welded to each other. The concrete slab of each span is then prefabricated in the same factory, and afterwards the composite girders are hoisted onto the piers as simply-supported spans. The concrete wet joint between spans is finally poured, transforming the simply-supported system into a semi-continuous system where the concrete slab is continuous and the steel girders remain separate. The construction method avoids the concrete slab over the piers bearing the permanent load and helps to relieve the tensile stress in the hogging moment region. Fig. 4 illustrates the construction method of Qiwu Bridge.

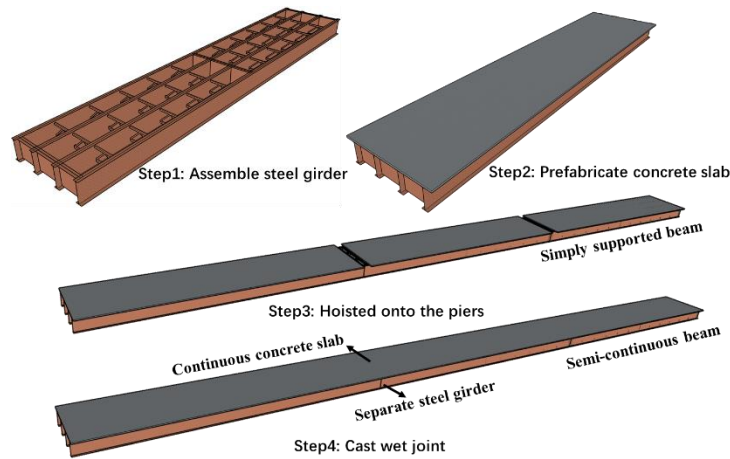


Fig. 4 Construction sequence of Qiwu Bridge

Design of partial shear connection

The hogging moment regions of Qiwu Bridge adopts PSC action to decrease the tensile stress in concrete slab. PSC is generally achieved by reducing connector number or adopting connectors with initial lower stiffness. Qiwu Bridge radically removes all the shear connectors within the range of 5.6 m near the mid support and thoroughly separates the concrete slab from the steel girder, which means most existing formulas considering PSC action may not be applicable to Qiwu bridge. To prevent stress concentration, reinforcement ratio is increased at the stiffness mutation area. The effect of PSC action on Qiwu Bridge is illustrated in the following section.

Design of link slab

Simply supported bridge is a statically determinate structure, which has the characteristics of simple structural behaviour, convenient construction and easy maintenance. However, the presence of expansion joints at each support reduces the durability of the bridge components and has adverse impact on the safety and comfort of the driving condition. Continuous bridge is one of the common types of highway seamless structure without expansion joints, but its construction process is more complicated.

The structural system of Qiwu Bridge applies continuous concrete slab and disconnected steel girder at the mid support, which has both advantages of smooth driving condition of continuous bridge and clear mechanical behaviour of simply supported bridge at the same time. Wet joint of the continuous concrete slab is called link slab, which is illustrated in Fig. 5. In order to increase the tensile bearing capacity, steel fiber reinforced concrete is applied to the link slab. The reinforcement ratio at the link slab is also increased for cracking prevention.

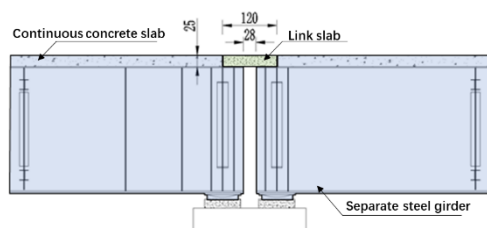


Fig. 5 Configuration of link slab (cm)

Numerical simulation

General

Finite element models were established for numerical simulation and parametric analysis, which was an important step for the further mechanism understanding. Fig. 6 shows the geometrical model for the FEM analysis, which included concrete slab, steel girder, reinforcement bars, open diaphragms and solid diaphragms. The concrete slab was meshed with solid element C3D8R, the steel girder was meshed with shell element S4R, the open diaphragm was meshed with beam element B31, and the reinforcement bar was meshed with truss element T3D2. Considering the convergence condition, calculation accuracy and computational efficiency, the overall mesh size of the model was determined as 150mm. To simplify the FEM model, Tie command was introduced to simulate the steel-concrete interlayer interactions with stud connectors^[9] which prevented the relative sliding of the steel girder and the concrete slab. Embedded region was set to constrain the reinforcement bar with the concrete block. Displacement boundary condition was applied corresponding to the supporting position. Construction process was simulated by Model Change order in Abaqus. Load of gravity, pavement, handrail, traffic, temperature (including integral temperature and thermal gradient), shrinkage and creep were considered according to JTG D60-2004^[27]. Besides, “Elcopy” order was added to the INP files to make the model easier to converge.

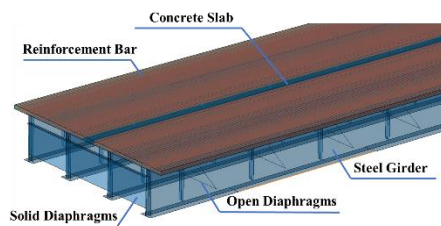


Fig. 6 Geometrical model

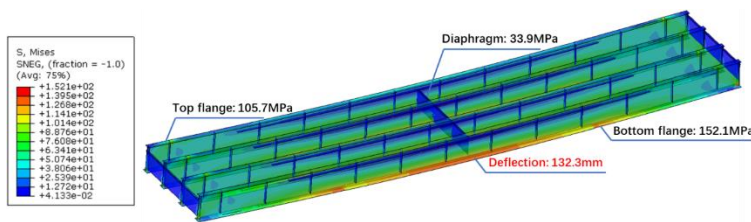
Material modelling

During the numerical simulation, the concrete damaged plasticity model^{[28][29]} was introduced for concrete material modeling. The material modeling refers to the Chinese Standard GB50010-2010^[30]. The value of compressive strain $\varepsilon_{t,r}$ and tensile strain corresponding to $0.4f_{c,r}$ were taken as the elastic strain when inputting the stress–strain data into the concrete damaged plasticity model in Abaqus, and the plastic strain equaled to the total strain minus the elastic strain. The damage factor d was calculated by principle of energy equivalence as proposed by Sidoroff^[31]. A trilinear stress–strain curve was used to model the mechanical behaviour of the steel plate. Stress at yield point σ_{ys} took 420MPa, and the ultimate stress σ_{us} took $1.36\sigma_{ys}$. The ultimate strain ε_{us} was 0.6% and yield strain ε_{ys} was derived by σ_{ys}/E_s , where E_s was 207GPa^[30]. Bilinear stress–strain model is used for the reinforcement bar. Yield stress of the reinforcement bar was taken as 400 MPa, with initial Young’s modulus of 200 GPa.

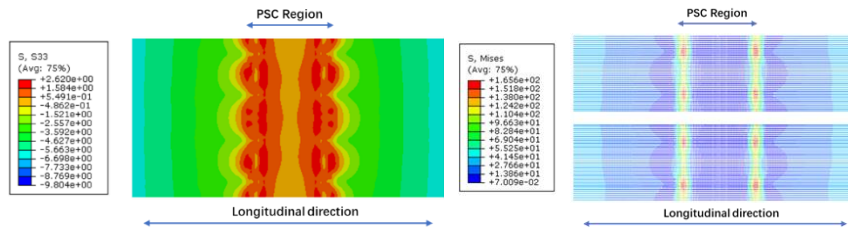
Mechanical performance analysis using numerical result

Mechanical performance of Qiwu Bridge

Stress distribution of the steel girder (central span) under dead load and traffic action is shown in Fig. 7(a), which is also labelled with the maximum stress in different parts and the maximum deflection. Stress in the steel girder adopted Mises stress, and stress in concrete slab adopted axial stress from longitudinal direction. The maximum stress in steel top flange and steel bottom flange respectively appeared at the shear stiffness mutation area and the mid-span. Under dead load and traffic action, the maximum stress in steel top flange was within 110MPa, while that in steel bottom flange was around 150MPa. The stress level in diaphragm is relatively smaller, which was below 35MPa. Deflection of the central span was 132.3mm, which was 11.5mm smaller than side span.



(a) Steel girder



(b) Concrete slab

(c) Reinforcement

Fig. 7 Stress distribution of Qiwu Bridge

Stress distribution of the concrete slab and the reinforcement is shown in Fig. 7(b) and Fig. 7(c). It can be found that the maximum stress of both components appeared at the edge of the PSC Region, with the figure reached 2.62MPa in concrete slab and 165.6MPa in reinforcement. The phenomenon of stress concentration inferred that the shear stiffness mutation magnificently increased the stress level at the edge of PSC region and made it easier to crack. Taking actions of increasing the reinforcement ratio or adopting high-performance concrete at this position is essential for crack control.

Parametric analysis

PSC region

In addition to the simulation on Qiwu Bridge, additional FEM models were established for the parametric analysis on range of PSC action. In order to control variables, arrangement of the reinforcement was set as the same in different models. Fig. 8(a) to Fig. 8(c) present the stress distribution of the concrete slab with different PSC region, and illustration of the parameter is shown in Fig. 8(d). Considering the design tensile strength of C50 concrete as 1.89MPa [27],

elements with stress above 1.89MPa were presented as grey. Compared with bridge without PSC region (PR), PSC region effectively reduce the crack region (CR), with the figure decreasing from 1.9m (PR=0) to 0.5m (PR=5.6m) and 0.15m (PR=10m) under dead load. Besides, PSC action helps to disperse the stress concentrate region, while the crack region of the bridge without PSC action tends to be wider and continuous with the increase of the load. Hence, it is easier for bridges with PSC action to control cracks.

It is worth noting that although the PSC action helps to reduce the maximum concrete stress and crack region, the stress level at the edge of the PSC region remains at a relatively high level due to stress concentration. For this problem, steel fiber reinforced concrete is applied and reinforcement ratio is increased at the edge of the PSC region in Qiwu Bridge to control the crack condition. To further decrease the concrete stress, setting a transition area using RSS connectors at the edge of the PSC region is also effective. In this area, RSS connectors with lower shear stiffness are arranged. Stiffness of the RSS connector can be optimized and adjusted by changing the height of the rubber sleeve. It is revealed that setting a transition area of 2m at the edge of the PSC region can reduce the stress concentration by more than 30% [25].

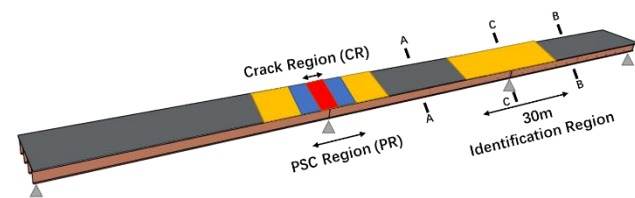
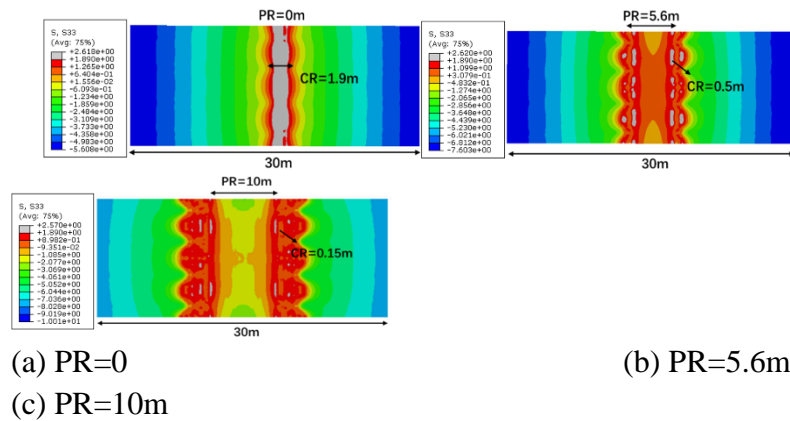


Fig. 8 Stress distribution of the concrete slab under dead load and vehicle load

Table 2 summarized the analysed deflection and stress information of models with different PR values. It can be inferred that PSC action had limit influence on the stress in mid-span section and the deflection of the whole structure. With PR increasing from 0 to 10m, the growth rate of deflection and steel bottom flange stress at midspan was respectively below 4% and 2%. Meanwhile, the steel top flange stress at mid-support declined rapidly (up to 62.4%) with the increase of PR, indicating the stress reduction in concrete slab around the mid-support.

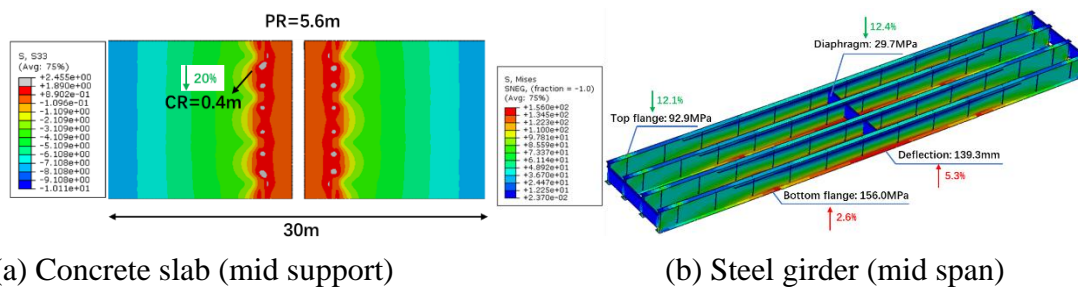
Table 2. Influence of PSC action on steel girder

Position	A-A	B-B	C-C
----------	-----	-----	-----

PR	Deflection	Stress at steel	Deflection	Stress at steel	Stress at steel
(m)	(mm)	bottom flange (MPa)	(mm)	bottom flange (MPa)	top flange (MPa)
0 (a)	130.8	132.1	143	144	23.7
2 (b)	131	132.2	143.2	144.2	13.4
5.6 (c)	132.3	132.8	143.8	144.4	9.2
10 (d)	135.8	134.2	145.1	145.2	8.9
[(b)-(a)]/(a)	0.2%	0.1%	0.1%	0.1%	-43.5%
[(c)-(a)]/(a)	1.1%	0.5%	0.6%	0.3%	-61.2%
[(d)-(a)]/(a)	3.8%	1.6%	1.5%	0.8%	-62.4%

Structural form

A three-span simply supported model was established to study the effect of link slab on the mechanical behaviour of Qiwu Bridge. Fig. 9 shows the stress distribution of Qiwu bridge without link slab under dead load and vehicle load. Comparison of different parameters between the two structural forms is also labelled. It can be seen that compared with structural form of continuous concrete slab and separate steel girder, the steel top flange stress and diaphragm stress of simply supported beam decrease by 12.1% and 12.4%, while the steel bottom flange stress and bridge deflection increase by 2.6% and 5.3% respectively. Tensile stress in concrete slab at mid support also declines because of the vanishing of the hogging moment region. It can be inferred that the link slab can improve the driving comfort with limited influence on the stress distribution.



(a) Concrete slab (mid support)

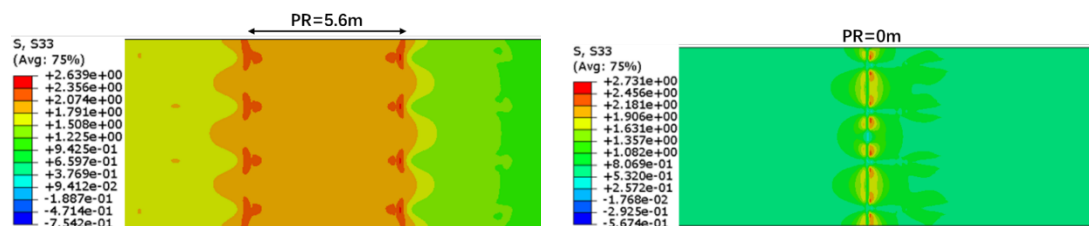
(b) Steel girder (mid span)

Fig. 9 Stress distribution of Qiwu bridge without link slab

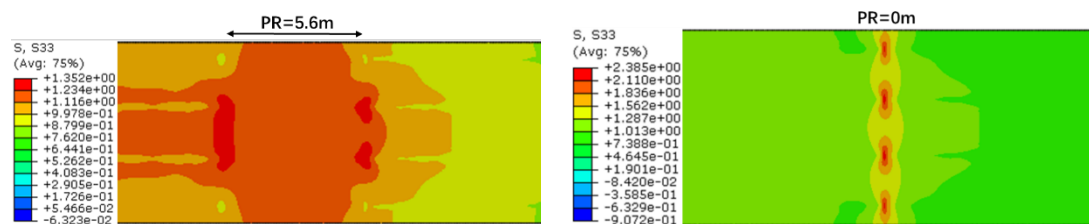
Effect of indirect actions

Effect of indirect actions including temperature, shrinkage and creep on models with different PR is calculated. During the calculation, shrinkage is converted to concrete temperature reduction, and creep is considered by conversion of modulus of elasticity. The influence of integral temperature reduction, gradient cooling and shrinkage on the stress distribution of the concrete slab at mid support is presented in Fig. 10. It can be inferred that integral temperature reduction and shrinkage have an obvious effect on the concrete slab with or without PSC region, and the tensile stress increasing by about 2.7MPa respectively in both structures. Meanwhile, gradient cooling has a larger impact when PR=0, with the tensile stress increasing by 2.4MPa, while there is only a 1.4MPa increasement when PR=5.6MPa. The influence of concrete creep is

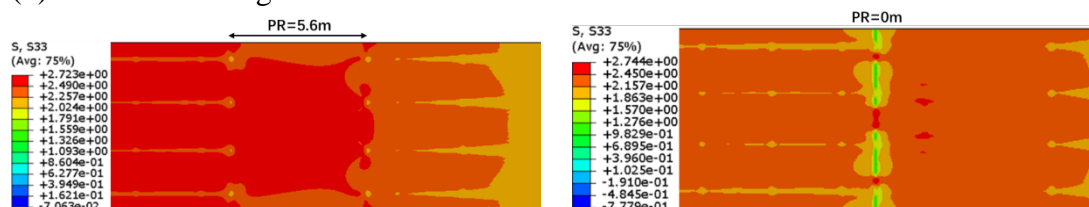
subtle, with the stress variation (stress increasement after the deduction of concrete modulus of elasticity) limiting in 0.2MPa in both structures.



(a) Integral temperature reduction



(b) Gradient cooling



(c) Shrinkage

Fig. 10 Effect of indirect actions on Qiwu bridge

Conclusions

Structural design of Qiwu Bridge with PSC action was illustrated and analysed. Nonlinear finite element model corresponding to Qiwu Bridge was established through ABAQUS for mechanical characterization. Based on the numerical results, the following conclusions can be drawn:

- (1) The midspan deflection of composite girder drops linearly with the increase of the interaction degree, and the deflection increase rate decreases with the span-length. The numerical result matches up with the Nie's model, which is recommended for simply-supported and semi-continuous bridge design. In the case of continuous composite-bridges, the model can be also adopted based on the considerations presented in the paper
- (2) Arranging PSC region can effectively reduce the crack region. Compared with bridge without PSC region, CR decreases from 1.6m (PR=0) to 0.5m (PR=5.6m) and 0.3m (PR=10m) under dead load. The decline becomes even larger under load combination of dead load and vehicle load. In addition, while the crack region tends to be wider and continuous with the increase of the load, PSC action helps to disperse the concentrated stress in the zone.
- (3) The shear stiffness mutation can magnificently increase the stress level at the edge of PSC region in concrete slab and made it easier to crack. Actions of increasing the reinforcement ratio or adopting high-performance concrete at this position is essential for crack control.

- (4) Except for the hogging moment region, PSC action had limit influence on the whole structure. With PR increasing from 0 to 10m, the growth rate of deflection and steel bottom flange stress at midspan was respectively below 4% and 2%. Meanwhile, the steel top flange stress at mid-support declined rapidly with the increase of PR, which also hints the stress reduction in concrete slab around the mid-support.
- (5) Integral temperature reduction and shrinkage can obviously increase the tensile stress in concrete slab with or without PSC region, and gradient cooling has a larger impact on structures without PSC region. The influence of concrete creep is subtle in both kinds of structures.
- (6) Influence of the link slab on the stress variation of the whole structure is within 15%, which infers that the link slab can improve the driving comfort with limited influence on the mechanical behaviour.

References

- [1] Hamoda, A., et al. "Behaviour of composite high performance concrete slab on steel I-beams subjected to static hogging moment." *Engineering Structures* 140(2017):51-65.
- [2] Y Zhang, et al. "Flexural responses of steel-UHPC composite beams under hogging moment." *Engineering Structures* 206.2020(2020):1-15.
- [3] Alkhalil, J. , and T. El-Maaddawy . "Nonlinear Flexural Response of Continuous Concrete Slab Strips Strengthened with Near Surface-Mounted Composites." *Journal of Composites for Construction* 21.1(2017):04016071.1-04016071.11.
- [4] El-Gendy, M. , and E. El-Salakawy . "Effect of flexural reinforcement type and ratio on the punching behavior of RC slab-column edge connections subjected to reversed-cyclic lateral loads." *Engineering Structures* 200(2019):109703-.
- [5] Chin, C. L. , et al. "Confining stress path dependent stress-strain model for pre-tensioned steel-confined concrete." *Engineering Structures* 201(2019):109769-.
- [6] Massaro, F. M. , and K. A. Malo . "Stress-laminated timber decks in bridges: Friction between lamellas, butt joints and pre-stressing system." *Engineering Structures* 213(2020):110592.
- [7] Steensels, R. , et al. "Evaluation of end-zone detailing of pre-tensioned concrete girders." *Engineering Structures* 187.MAY 15(2019):372-383.
- [8] Jiang, Chao , C. Wu , and X. Jiang . "Experimental study on fatigue performance of corroded high-strength steel wires used in bridges." *Construction and Building Materials* 187.OCT.30(2018):681-690.
- [9] Su, H., et al. " Shear Performance and Dimension Rationalization Study on the Rubber Sleeved Stud Connector in Continuous Composite Girder." *Engineering Structures* 240(2021):112371.
- [10] Kim, C. E. , et al. "Structural behavior of a continuous composite truss with a composite bottom chord." *Journal of Constructional Steel Research* 105.feb.(2015):1-11.
- [11] Chen, X. , et al. "Experimental study on double composite action in the negative flexural region of two-span continuous composite box girder." *Journal of Constructional Steel Research* 67.10(2011):1636-1648.
- [12] Wan-Wendner, L. , R. Wan-Wendner , and G. Cusatis . "Age-dependent size effect and fracture characteristics of ultra-high performance concrete." *Cement and Concrete Composites* (2018):S0958946516305297.

- [13] Guo, L., et al. "Seismic evaluation and calculation models of CFDST column blind bolted to composite beam joints with partial shear interaction." *Engineering Structures* 196.OCT.1(2019):109269.1-109269.20.
- [14] Al-Sammari, A. T. , P. L. Clouston , and S. F. Brena . "Finite-Element Analysis and Parametric Study of Perforated Steel Plate Shear Connectors for Wood-Concrete Composites." *Journal of structural engineering* 144.10(2018):04018191.1-04018191.10.
- [15] Loh, H. Y. , B. Uy , and M. A. Bradford . "The effects of partial shear connection in the hogging moment regions of composite beams: Part I—Experimental study." *Journal of Constructional Steel Research* 60.6(2004):897-919.
- [16] Loh, H. Y. , B. Uy , and M. A. Bradford . "The effects of partial shear connection in the hogging moment regions of composite beams Part II—Analytical study." *Journal of Constructional Steel Research* 60. 6(2004):921-962.
- [17] Hiragi, H. , S. Matsui , and K. Muto . "Development of favorable stud shear connectors to flexible composite actions." (1998).
- [18] Nie, J. , et al. "New technique and application of uplift-restricted and slip-permitted connection." *China Civil Engineering Journal* (2015).
- [19] Oehlers, D.J., Bradford, M.A., " *Steel and Concrete Composite Structural Members: Fundamental Behaviour*". Pergamon Press, Oxford, 1995.
- [20] Girhammar, U. A., and Gopu, V. K. A. "Composite beam-column switch interlayer slip exact analysis." *Journal of Structural Engineering*, vol. 119(4), pp.1265-1282, 1993.
- [21] Nie, J. G., and Cai, C. S., "Steel-concrete composite beams considering shear slip effects." *Journal of Structural Engineering*, vol.129(4), pp. 495-506, 2003.
- [22] M. G. Kalibhat and A. Upadhyay, "Effect of partial shear interaction in steel concrete composite girders," *IOP Conf. Ser.: Mater. Sci. Eng.*, 245 022044, 2017.
- [23] Cao P. "Analysis of Partial-Combination Prestressed Continuous Composite Beam". Master's thesis, Tongji University, 2017.
- [24] He J , Lin Z , Y Liu, et al. "Shear stiffness of headed studs on structural behaviors of steel-concrete composite girders". *Steel and Composite Structures*, 2020, 36(5):553-568.
- [25] Su, Q, Su H, Wu, F. "Mechanical Analysis on the Influence of Rubber-sleeved stud connector on the steel-concrete composite girder". *Journal of Tongji University (Natural Science)*, 2021, 49(8):9.
- [26] Xu X , Liu Y . "Analytical and numerical study of the shear stiffness of rubber-sleeved stud". *Journal of Constructional Steel Research*, 2016, 123(Aug.):68-78.
- [27] Chinese Standard JTGD60-2004 General code for design of highway bridges and culverts, China, 2004
- [28] Li, Xxl . "Parametric Study on Numerical Simulation of Missile Punching Test Using Concrete Damaged Plasticity (CDP) Model." *International Journal of Impact Engineering* 144(2020):103652.
- [29] Choi, et al. "Experimental study on the structural behaviour of calcium-leaching damaged concrete members." *Magazine of Concrete Research* (2018).
- [30] Chinese Standard GB50010-2010 Code for design of concrete structures, China, 2010
- [31] Mander, Jab , and M. Priestley . "Theoretical Stress-Strain Model for Confined Concrete." *Journal of Structural Engineering* 114.8(1988):1804-1826.

6.6 Structure and Infrastructure Engineering 2023

Su H, Su Q, Casas JR, et al. Structural performance and on-site monitoring of steel-concrete composite bridge with link slab. Structure and Infrastructure Engineering. Submitted.

Structural performance and on-site monitoring of steel-concrete composite bridge with link slab

Hang Su ^a, Qingtian Su ^b, Joan R. Casas ^{c*}, Huayong Wu ^d, An Liu ^e, Zhiquan Chen ^f

^a Department of Bridge Engineering, Tongji University, Shanghai, China; School of Civil Engineering, Department of Civil and Environmental Engineering, Technical University of Catalunya, Barcelona, Spain; Shanghai Research Institute of Building Sciences Co, Ltd, Shanghai, China.

^b Department of Bridge Engineering, Tongji University, Shanghai, China; Shanghai Engineering Research Center of High Performance Composite Bridge, Shanghai, China.

^c School of Civil Engineering, Department of Civil and Environmental Engineering, Technical University of Catalunya, Barcelona, Spain. *Corresponding author

^d Shanghai Research Institute of Building Sciences Co, Ltd, Shanghai, China.

^e Jiangxi Transportation Consulting Company Limited, Jiangxi, China.

^f China Railway 21st Bureau Group The 3rd Engineering Co., Ltd. Shannxi, China.

Abstract

The project case of Qiwu bridge using link slab action between simply supported composite spans is introduced. The 60m-span girder of Qiwu bridge is the longest and heaviest among the composite girders erected by bridge-erecting machine in China. Qiwu Bridge consists of a series of 3 simply supported spans built with composite girders and connected at the pier supports by a link slab. This solution has both advantages of: 1) smooth driving condition and enhancement of durability by removing expansion joints and 2) clear structural behavior as simply supported spans. A finite element model was established to simulate and predict the mechanical response of this semi-continuous solution. Numerical results showed that the removal of the shear connection around the link slab decreased the stress level but also caused a stress mutation. Qiwu Bridge was also monitored by vibrating strain meters to follow its actual structural response. From preliminary monitoring data and numerical results, it can be concluded that the proposed construction method and the static scheme is safe for the 60-span composite girder with a large safety margin. Further experimental results will be obtained during the service stage of the bridge to validate the in-service performance of the proposed steel-concrete composite bridge with link slab.

Keywords: Steel–concrete composite bridge; Link slab; Partial shear connection; Numerical

study; Bridge monitoring; Construction load; Vibrating strain meter; Bridge-erecting machine

Nomenclature

E_c : Elasticity modulus of concrete

α_t and α_c : Regulation coefficients of the descending part of concrete

d_c and d_t : Compressive and tensile damage factor of the concrete

$f_{t,r}$ and $f_{c,r}$: Ultimate tensile and compressive strengths, respectively, of concrete

$\varepsilon_{t,r}$ and $\varepsilon_{c,r}$: Strains corresponding to the ultimate tensile and compressive strengths of concrete, respectively

E_0 : Initial elasticity modulus of concrete

σ_{yS} : Stress at yield point

σ_{uS} : Stress at ultimate point

ε_{yS} : Strain at yield point

ε_{uS} : Strain at ultimate point

FEM: finite element model

t : Current concrete age

t_s : Age of concrete at the onset of shrinkage

$\varepsilon_{sc}(t, t_s)$: Shrinkage strain during t_s to t

ε_{sco} : Nominal shrinkage factor

β_s : Contraction development factor over time

f_{cm} : Compressive strength of concrete blocks

β_{RH} : Annual average relative humidity factor

RH : Annual average relative humidity

h : Theoretical thickness of components

t_0 : Age of concrete at load application

$\phi(t, t_0)$: Creep coefficient during t_0 to t

ϕ_0 : Nominal creep factor

β_c : Coefficient of creep over time

E_{cl} : Converted elastic modulus

GTV: Girder transport vehicle

PSC: Partial shear connection

PR: Partial shear connection region

CR: Crack region

Introduction

Simply supported bridge is a statically determinate structure, which has the characteristics of simple structural behavior, convenient construction and easy maintenance (Deng et al., 2015; Han et al., 2013; X. Li et al., 2018; Ye et al., 2012). However, the presence of expansion joints at each support reduces the durability of the bridge components and has adverse impact on the safety and comfort of the driving condition (Au et al., 2013; Gan et al., 2013; Yang & DesRoches, 2015). Continuous bridge is one of the common types of highway seamless structure without expansion joints. However, its construction process is more complicated and the response to imposed deformations, as temperature and foundation settlements (An et al., 2021; Chen et al., 2021), is less efficient. A link slab in steel-concrete composite bridges joins the concrete slab of two spans together but keeps the steel beams disconnected, in a so-called “semi-continuous” solution. This kind of structural form has both advantages of smooth driving condition and durability enhancement as for a continuous bridge, but still a clear mechanical behavior as simply supported spans at the same time (Kim et al., 2004; Ulku et al., 2009).

In the case of precast concrete bridges, for designing of link slab, Alampalli et al. (1998) improved the bridge deck without expansion joints built in New York in the early stage to improve its mechanical behavior. Caner (1998) carried out experimental research on the mechanical behavior of the specimens with link slabs that supported different conditions and proposed the idea of designing the link slab by using the three-moment equation. El-Safty and Okeil (2008) derived the calculation expression of the link slab under static action, which was verified by tests and finite element analysis. At the same time, they also studied the influence of the stiffness of the pavement layer on the mechanical behavior of the link slab. With the application of new materials in bridge engineering, Chu et al. (2021) did numerical investigation on static behavior of steel and GFRP-reinforced link slabs and found that GFRP-reinforced link slab shows higher load, deflection and ductility capacity compared to their steel-reinforced counterparts. Karim and Shafei (2021) carried out an experimental study on fiber-reinforced concrete link slabs with embedded steel and GFRP rebars and highlighted how a proper choice of construction materials can lead to delivering the expected ductility and crack resistance, while meeting the other structural performance requirements. Based on the good corrosion resistance of carbon fiber reinforced polymer (CFRP) and high ductility of engineered cementitious composites (ECC), the CFRP reinforced ECC link slabs were proposed by Xia et al. (2019). The behavior of this novel link slab was investigated through a series of experimental tests.

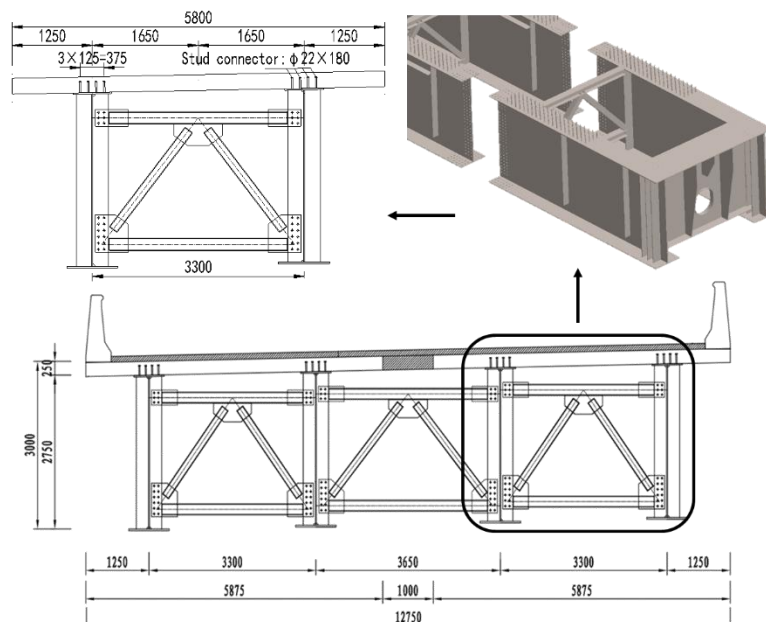
Although link slab in concrete bridges has been widely studied (Chu et al., 2022; Qian et al., 2009; Wang et al., 2016), there are few researches specifically on the link slab in steel-concrete composite bridges (Wang et al., 2019; Wang et al., 2022). In this case, the composite solution of Qiwu bridge adopting link slab is introduced in the present work to study the structural performance of this semi-continuous solution. A non-linear finite element model of Qiwu Bridge was established to simulate the mechanical behaviour and to predict the bridge response. Qiwu Bridge was also monitored by vibrating strain meters to study the long-term behavior as well as the evolution of

stresses during the construction sequence and to check the validity of the proposed numerical model. The numerical and experimental results are expected to push ahead with the practical application of the link slab solution in steel-concrete composite bridges.

Description of the bridge

Qiwu Bridge (Su, Su, Casas, Jiang, et al., 2022) consists of a series of 60m simply supported spans made of composite girders. Each 3 spans are connected at the pier supports by a link slab. Configuration of half a span is shown in Figure 1. The composite girder of Qiwu Bridge was prefabricated in the factory, including the steel beam and the concrete slab. After the concrete curing, and transport to the construction site, the prefabricated girders are then erected onto the piers by a bridge-erecting machine, remaining as a simply supported structure. After casting the transversal wet joint (link slab), the structural form is turned from simply supported to semi-continuous structure. The structural response in the vertical direction is still similar to a simply-supported structure, but the expansion joint is removed in the link slab location. Figure 2 and Figure 3 respectively present the construction sequence and some pictures during the construction process.

Link slabs (transversal wet joints of the continuous concrete slab) are constructed between the adjacent girders where expansion joints are not installed to ensure continuity only through the concrete slab, but preserving the separation between the steel beams. Configuration of link slab is illustrated in Figure 4 (a). Construction method of the link slab is shown in Figure 4 (b). The bottom mold is fixed by the suspender which is supported by the distributive girder. Within the range of 5.6 m around the link slab, all the shear connectors are removed (stiffness mutation) to decrease the stress level of the link slab. The reinforcement ratio is increased in relation to the normal zone for crack prevention.



(a) Configuration of half standard section

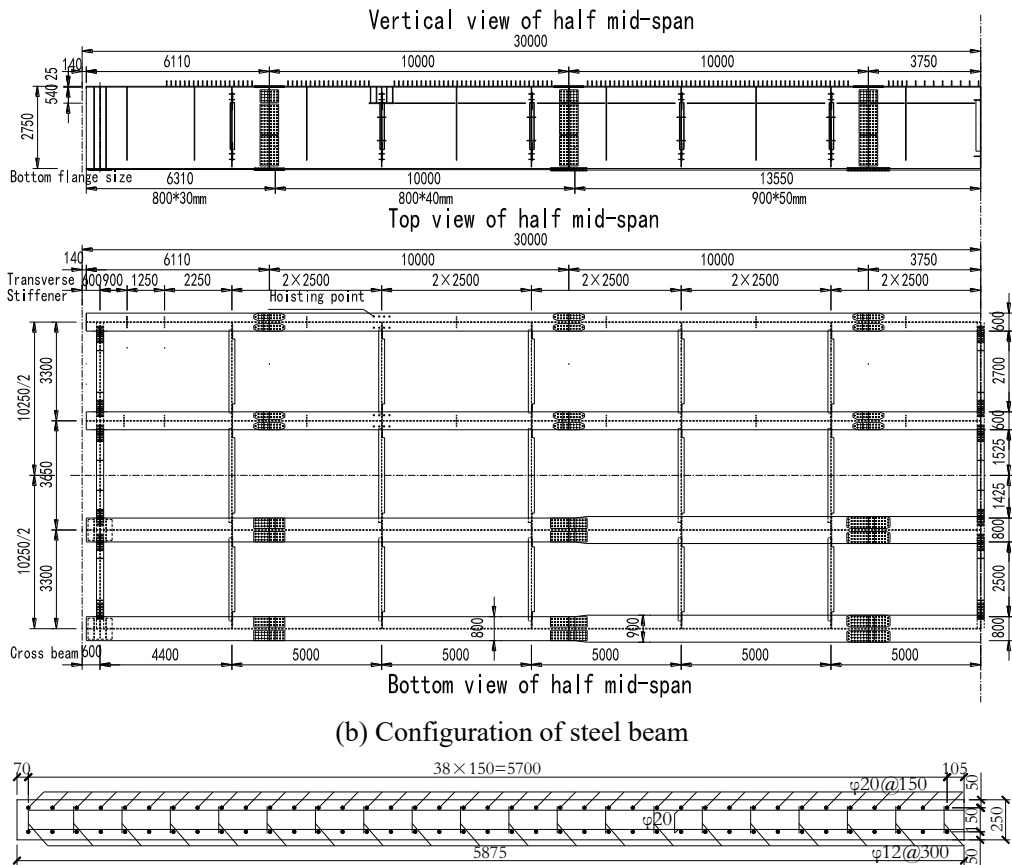


Figure 1. Half span of Qiwu Bridge (mm)

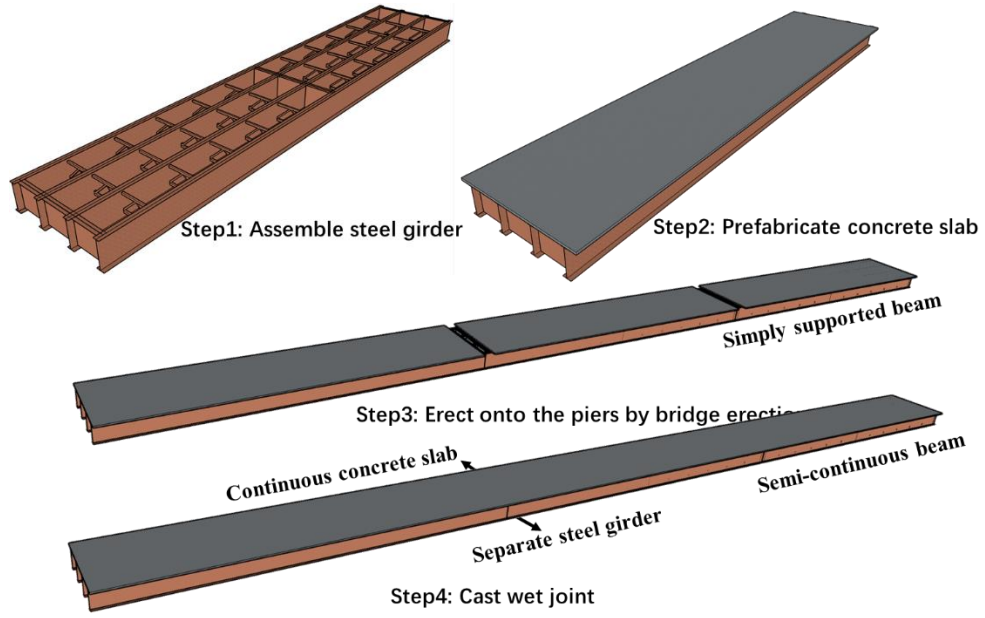


Figure 2. Construction sequence of Qiwu Bridge



Figure 3. Pictures during the construction process

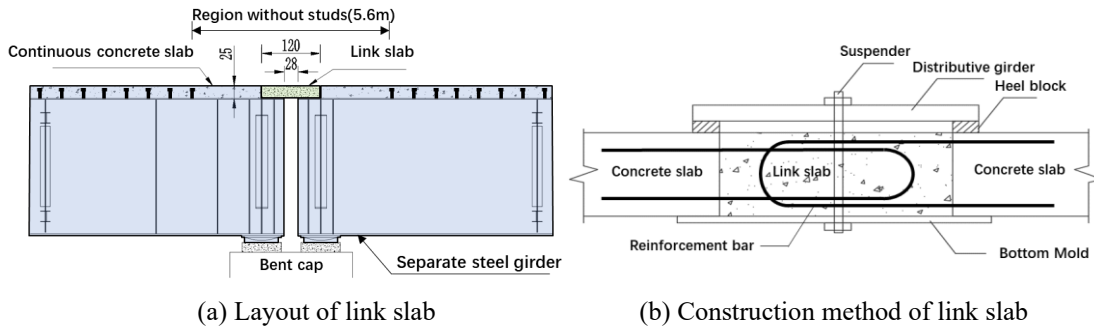


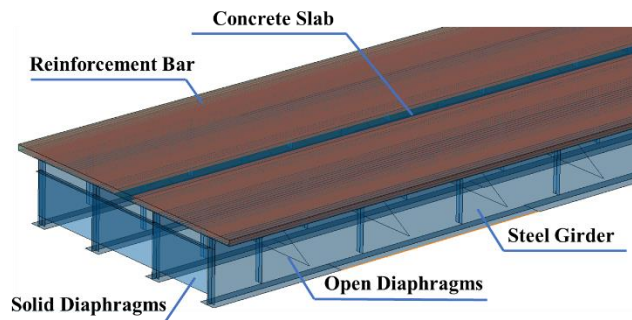
Figure 4. Configuration of link slab

Numerical analysis under serviceability limit states

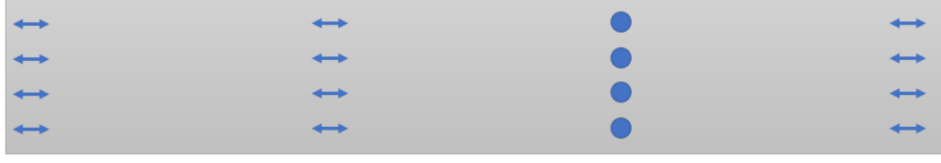
General

A finite element model of the complete bridge (3 spans) was established for numerical simulation. Figure 5 (a) shows the geometrical model for the FEM analysis (Su, Su, Xu, et al., 2022), which included concrete slab (meshed with C3D8R), steel beam (meshed with S4R), reinforcement bars (meshed with T3D2), open diaphragms (meshed with B31) and solid diaphragms (meshed with S4R). The steel-concrete and concrete-reinforcement interaction is respectively simulated by Tie and Embedded region commend. Displacement boundary condition is shown in Figure 5 (b), where the circle means the displacement in all directions are restrained and the arrow means only the longitudinal or the transversal displacement is not restrained.

Since the steel beams between the two spans are disconnected, there are two bearing devices on each pier as shown in Figure 4 (a). Besides, rotations along all directions are not restrained. Model Change in Abaqus was used to simulate the construction steps. Actions due to dead load, live load and indirect load were considered (JTG3362-2018, 2018). Besides, “Elcopy” order was added to the INP files to make the model easier to converge.



(a) geometrical model



(b) Displacement boundary condition

Figure 5. Finite element model

Material modelling

The concrete damaged plasticity model (Choi et al., 2018; X.-X. Li, 2020) was introduced for concrete material modeling. The constitutive relation of the concrete refers to the Chinese Standard GB50010-2010 (as shown in Figure 6), which can be determined by Equation (1) and Equation (3). Equations (2) and (4) describe the coefficients of d_t and d_c . The value of $\varepsilon_{t,r}$ and strain corresponding to $0.4f_{c,r}$ was respectively taken as the tensile and compressive elastic strain. The damage factor d was calculated by principle of energy equivalence (determined by Equation (5)) as proposed by Sidoroff (Mander et al., 1988).

Figure 6 (c) presents the stress–strain curve of the steel plate, which adopts a trilinear curve. Stress at yield point σ_{ys} took 420MPa, and the ultimate stress σ_{us} took $1.36\sigma_{ys}$. The ultimate strain ε_{us} was 0.6% and yield strain ε_{ys} was derived by σ_{ys}/E_s , where E_s was 207GPa (GB50010-2010, 2015). Figure 6 (d) shows the stress–strain curve of the reinforcement bar, in which the initial Young's modulus and yield stress of the reinforcement bar was respectively taken as 200 GPa and 400 MPa.

$$\sigma = (1 - d_t) E_c \varepsilon, \quad (1)$$

$$d_t = \begin{cases} 1 - \rho_t [1.2 - 0.2x^5] & x \leq 1 \\ 1 - \frac{\rho_t}{\alpha_t (x-1)^{1.7} + x} & x > 1 \end{cases}, \quad (2)$$

$$x = \frac{\varepsilon}{\varepsilon_{t,r}} \quad \rho_t = \frac{f_{t,r}}{E_c \varepsilon_{t,r}}$$

where

$$\sigma = (1 - d_c) E_c \varepsilon, \quad (3)$$

$$d_c = \begin{cases} 1 - \frac{\rho_c n}{n-1+x^n} & x \leq 1 \\ 1 - \frac{\rho_c}{\alpha_c (x-1)^2 + x} & x > 1 \end{cases}, \quad (4)$$

$$x = \frac{\varepsilon}{\varepsilon_{c,r}}, \quad \rho_c = \frac{f_{c,r}}{E_c \varepsilon_{c,r}}, \quad n = \frac{E_c \varepsilon_{c,r}}{E_c \varepsilon_{c,r} - f_{c,r}}$$

where

$$d = 1 - \sqrt{\frac{\sigma}{E_0 \varepsilon}} \quad (5)$$

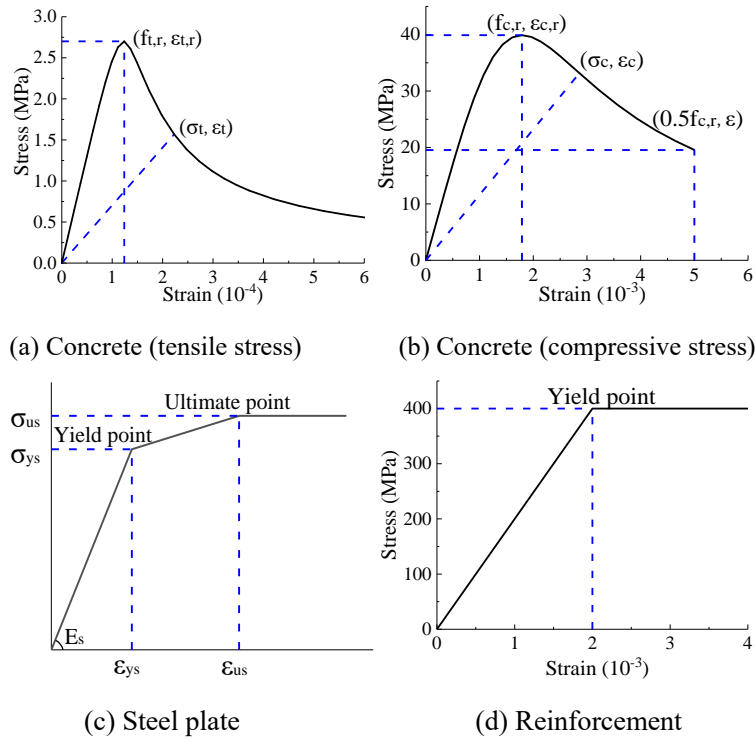


Figure 6. Stress–strain curve of materials

Structural performance under serviceability limit states

The stress condition of Qiwu Bridge under the action of dead and live load (JTG3362-2018, 2018) is presented in Figure 7. It can be seen that the maximum stress in steel top and bottom flange was 106MPa and 152MPa. The stress state in the diaphragm remains at a low level (below 35MPa). Deflection of the central and side span was respectively 132.3mm and 143.8mm. Figure 7 also shows the stress distribution of the concrete slab and the reinforcement around the link slab. The maximum tensile stress of concrete and reinforcement appeared at the region without studs, respectively reaching 2.6MPa and 165.6MPa.

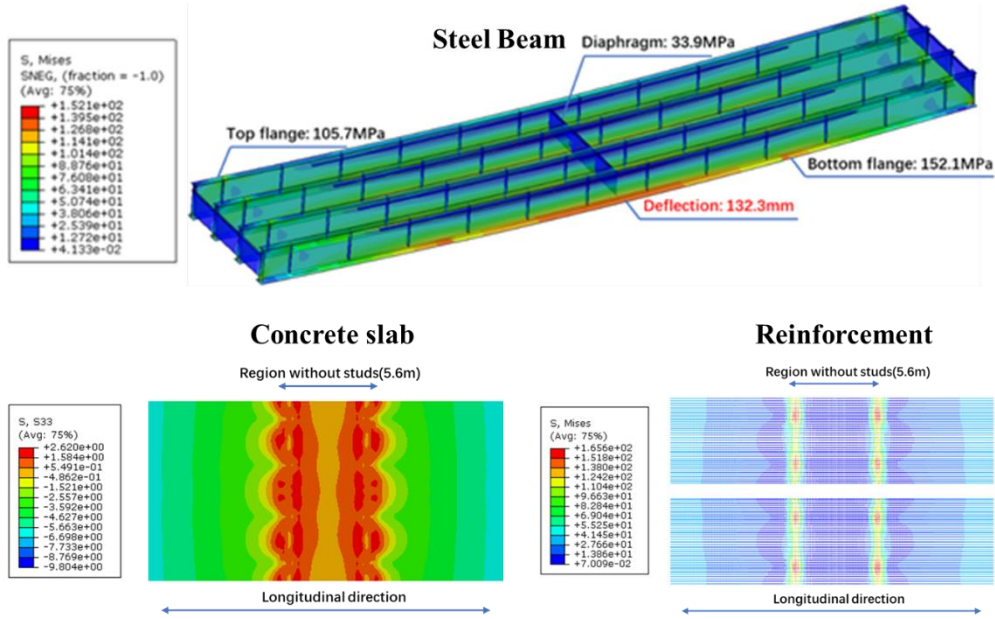


Figure 7. Stress condition in different components of the bridge (MPa)

The reinforcement ratio around the link slab was increased to account for the stress concentration in this area. In addition, as the stress concentration was caused by the stiffness mutation of the shear connector, adopting rubber-sleeved stud connectors instead of removing all the shear connectors also helped to solve the problem (Q. Su et al., 2021). Wrapping rubber sleeve on a stud connector can markedly decrease its shear stiffness (Su, Su, Casas, Xu, et al., 2022; H. Su et al., 2021; Tang et al., 2023), while gradually decreasing the sleeve thickness contributed to a gently overshoot of the stress mutation. As the stress condition is complex around the shear stiffness mutation region, it should be closely monitored.

Effects of temperature, shrinkage, and creep (JTGD60-2015, 2015) are also calculated. Shrinkage strain $\varepsilon_{sc}(t, t_s)$ can be determined from the nominal shrinkage factor ε_{sco} multiply by contraction development factor over time β_s (as presented in Equation (6)), where t and t_s respectively represents the current concrete age and age of concrete at the onset of shrinkage. ε_{sco} and β_s can be derived by Equation (7) and Equation (8). The shrinkage strain $\varepsilon_{sc}(t, t_s)$ is converted to concrete temperature reduction during numerical simulation.

$$\varepsilon_{sc}(t, t_s) = \varepsilon_{sco} \cdot \beta_s (t - t_s) \quad (6)$$

$$\varepsilon_{sco} = \varepsilon_s(f_{cm}) \cdot \beta_{RH} \quad (7)$$

Where $\varepsilon_s(f_{cm}) = [160 + 50(9 - f_{cm}/10)] \cdot 10^{-6}$, $\beta_{RH} = 1.55(1 - RH^3)$

$$\beta_s(t-t_s) = \left[\frac{(t-t_s)}{350(h/100)^2 + (t-t_s)} \right]^{0.5} \quad (8)$$

Creep coefficient $\phi(t, t_0)$ can be derived by Equation (9), where ϕ_0 and β_c is respectively the nominal creep factor and coefficient of creep over time, which can be described by Equation (10) and Equation (11). Creep is calculated by the elasticity conversion in the numerical model. During the creep period, the elastic modulus of the concrete material is considered gradually changed to the converted elastic modulus E_{cl} (described as Equation (12)).

$$\phi(t, t_0) = \phi_0 \cdot \beta_c(t-t_0) \quad (9)$$

$$\phi_0 = \phi_{RH} \cdot \beta(f_{cm}) \cdot \beta(t_0) \quad (10)$$

Where $\phi_{RH} = 1 + \frac{1-RH/RH_0}{0.46(h/h_0)^{\frac{1}{3}}}$, $\beta(f_{cm}) = \frac{5.3}{(f_{cm}/f_{cm0})^{0.5}}$, $\beta(t_0) = \frac{1}{0.1+(t_0/t_1)^{0.2}}$

$$\beta_c(t-t_0) = \left[\frac{(t-t_0)/t_1}{\beta_H + (t-t_0)/t_1} \right]^{0.3} \quad (11)$$

Where $\beta_H = 150 \left[1 + \left(1.2 \frac{RH}{RH_0} \right)^{18} \right] \frac{h}{h_0} + 250 \leq 1500$

$$E_{cl} = \frac{E_c}{1 + 0.55\phi(t, t_0)}, \quad (12)$$

Figure 8 shows the stress condition of the concrete slab around the link slab under indirect load. The identification length in Figure 8 takes 15m. The creep stress is obtained by the difference value of two load steps. The first load step adds the dead and live load, and the second load step changes the modulus of elasticity of the concrete by the “Inp” file in Abaqus. The numerical results shows that the creep action only increases the concrete stress by 0.2MPa, while the influence of temperature and shrinkage action is obvious. Tensile stress due to yearly temperature reduction, gradient cooling and shrinkage is respectively 2.6MPa, 1.4MPa and 2.7MPa, which is similar to those produced by dead and live load.

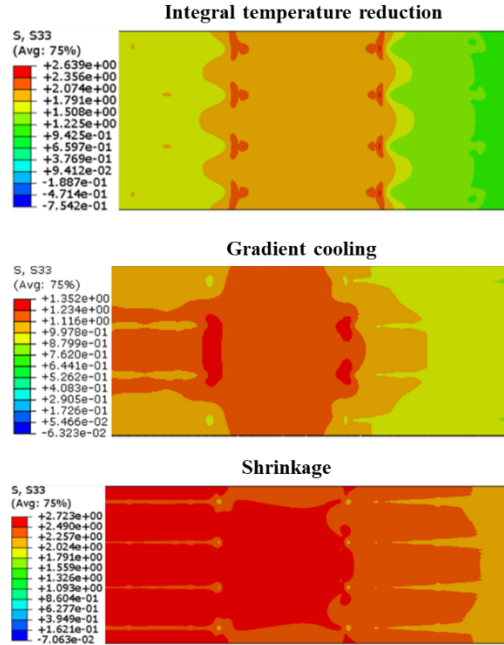


Figure 8. Stress condition of the concrete slab under indirect load (MPa)

Structural performance during construction stage

During the construction stage of Qiwu bridge, the whole girder was prefabricated in the factory and installed onto the piers through bridge-erecting machine. During the erection process of the composite girder, the bridge-erecting machine and the girder transport vehicle were both loaded onto the monitored girder (as shown in Figure 9). The 60m-span girder was the longest and heaviest among the composite girders erected by bridge-erecting machine in China up to now, thus challenging the construction process. Therefore, the critical key steps during construction should be focused during monitoring.

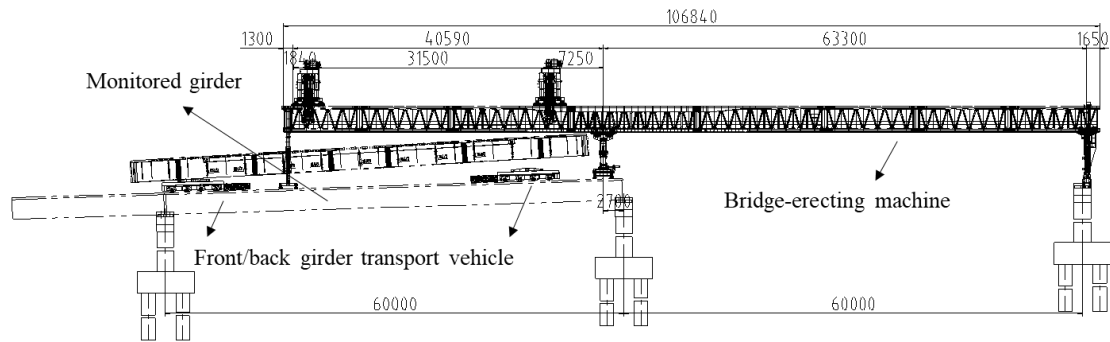


Figure 9. Installation of the composite girder through bridge-erecting machine (mm)

In the numerical analysis, four construction stages of hoisting, girder erected onto the piers, front girder transport vehicle reaching mid-span and back girder transport vehicle reaching hoisting position were emphatically analyzed and compared with the monitored results. Weight of the girder transport vehicle and composite girder was respectively 28t and 190t, and the bearing conditions of the latter two construction stages are shown in Figure 10. In Figure 10 (a), the front girder transport vehicle reached mid-span, and the monitored girder bore the load of the bridge-erecting machine and the front girder transport vehicle (with the erecting girder). As for Figure 10 (b), part of the

erecting girder has been hoisted on to the bridge-erecting machine, while the back girder transport vehicle reached the back hoisting position. The monitored girder bore the load of the bridge-erecting machine, the front girder transport vehicle (without the erecting girder) and the back girder transport vehicle (with the erecting girder).

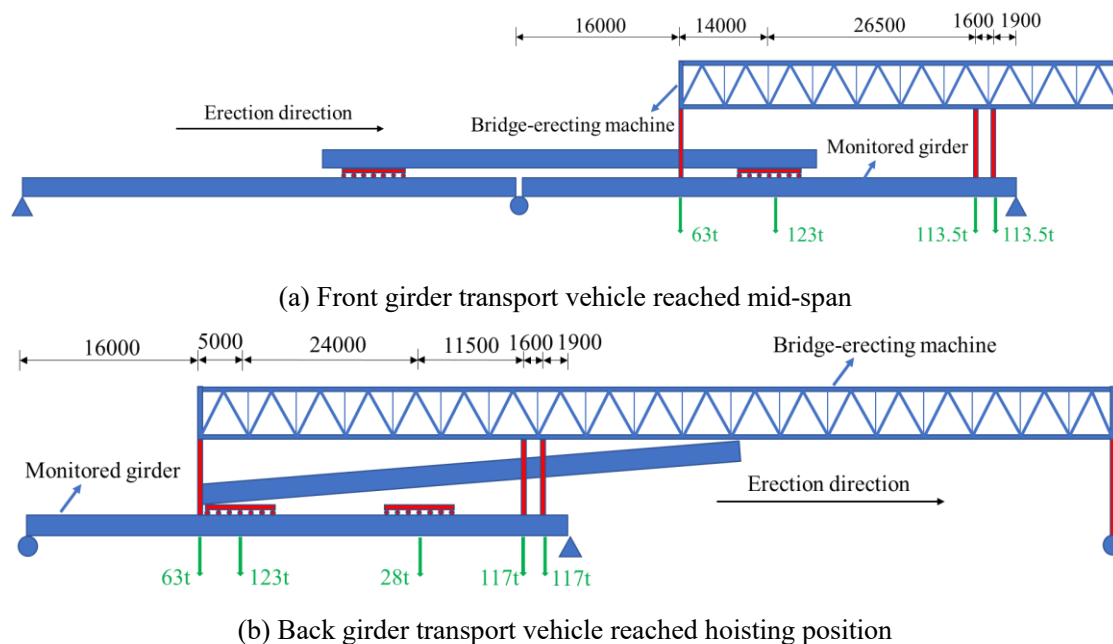


Figure 10. Bearing conditions during construction (mm)

Table 1 shows the structural response during the four key construction stages at mid-span. It can be found that the largest stress condition and deflection appears when the back girder transport vehicle reached hoisting position. The largest tensile and compressive steel stress is respectively 162.9MPa and -72.0MPa, illustrating that the steel beam remained in elastic stage during construction. Tensile stress didn't appear in the concrete slab during construction, while the largest compressive stress came to -19.4MPa, far away from the maximum allowable compressive stress.

Therefore, the numerical analysis shows that the 60m-span girder can be safely deployed using bridge-erecting machine, and bridge-erecting machine can be the priority construction method for long-span composite girders.

Table 1

Structural response during four construction stages at mid-span

	Steel stress (MPa)		Concrete stress (MPa)		Deflection (mm)
	Tensile	Compressive	Top flange	Bottom flange	Mid-span
Hoisting	68	-36	-7.1	-4.4	33.6
Erected onto the piers	85.1	-45	-10.8	-5.2	75.6
Front GTV reached mid-span	146.3	-63	-12.6	-9.7	126
Back GTV reached hoisting position	162.9	-72	-19.4	-11.8	154

GTV: Girder transport vehicle

Parametric analysis on the area without shear connectors

In order to decrease the stresses of the link slab, the stud connectors near the mid support (in a length of 5.6 m) are removed. The region without shear connectors can be defined as partial shear connection (PSC) region (Su, Su, Xu, et al., 2022). Parametric analysis of the PSC region length was conducted to reveal its influence on the stress redistribution in the concrete slab.

Figure 11 presents the concrete stress versus different length of the PSC region (PR). Elements with stress above 1.89MPa (according to GB50010-2010) were considered reaching the tensile stress and presented as grey. It can be inferred that the increase of the PSC region contributed to a decrease of the cracked region. The cracked region decreased from 1.9m to 0.5m and 0.15m when PSC region increased from 0m to 5.6m and 10m respectively. In addition, the stress concentration area was relieved by PSC region. It can be inferred that the stress varied rapidly in the PSC region, and the stress condition around this area should be monitored intensively.

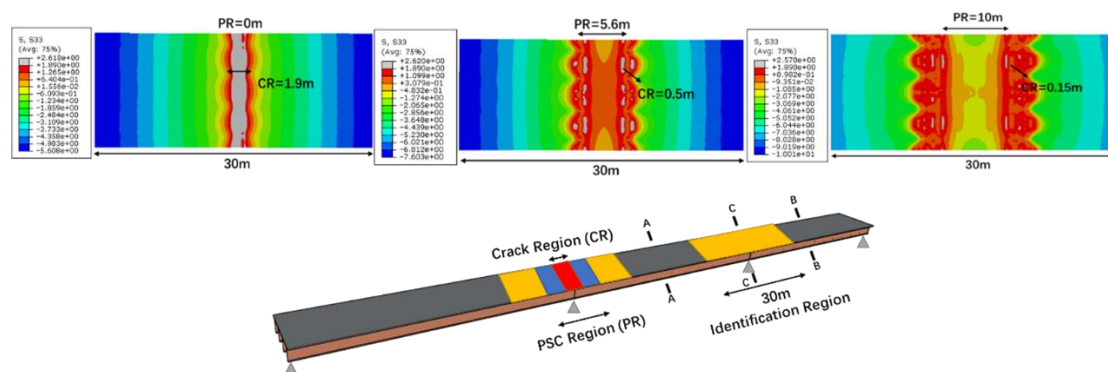


Figure 11. Concrete stress (MPa) with different length of the PSC region (PR)

On-site monitoring of Qiwu bridge

Monitoring method

Vibrating strain meters were installed onto Qiwu bridge to measure the full service-life strain distribution. The measurement system adopts JM-2100 automatic network measurement system, where all channels can be collected and transmitted in real-time with the minimum interval of 2 seconds. The collected data can be gathered and updated to the internet by the system to be monitored online. The on-site monitoring of Qiwu bridge will be conducted in three different time-spans respectively in summer, autumn, and winter to study the influence of the yearly temperature on the stress distribution.

According to the results from the numerical calculation, the major monitored cross sections include mid-span section (M-M), shear stiffness mutation section (P-P) and pier support section (S-S). Vibrating strain meters installed in the concrete slab at section S-S were located at the middle of the link slab. The installation method of the vibrating strain meters and position of the monitoring cross sections are shown in Figure 12 and Figure 13.



Figure 12. Installation of the vibrating strain meters in the steel and reinforcing bars

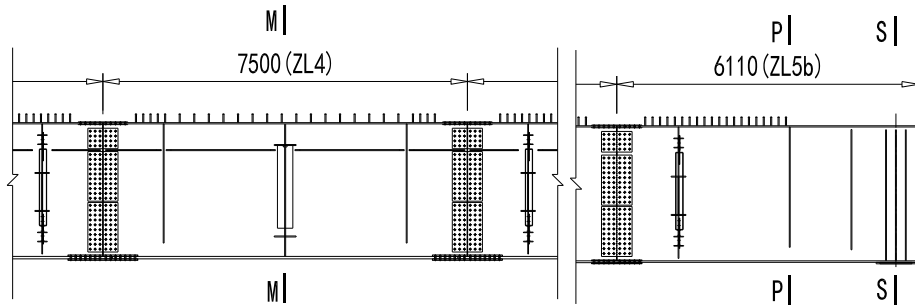
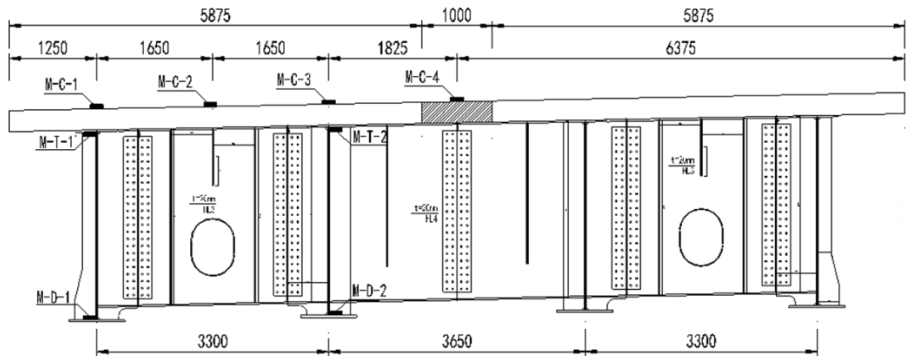
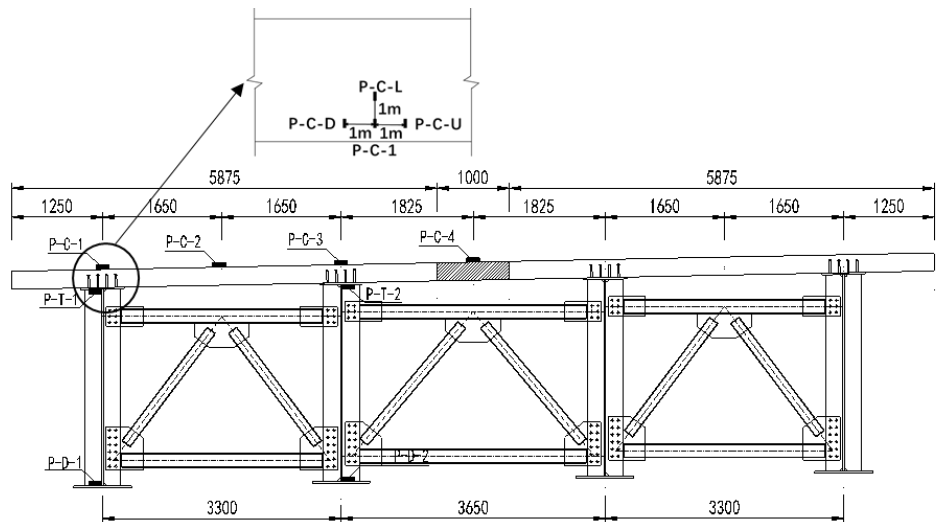


Figure 13. Monitoring cross sections (mm)

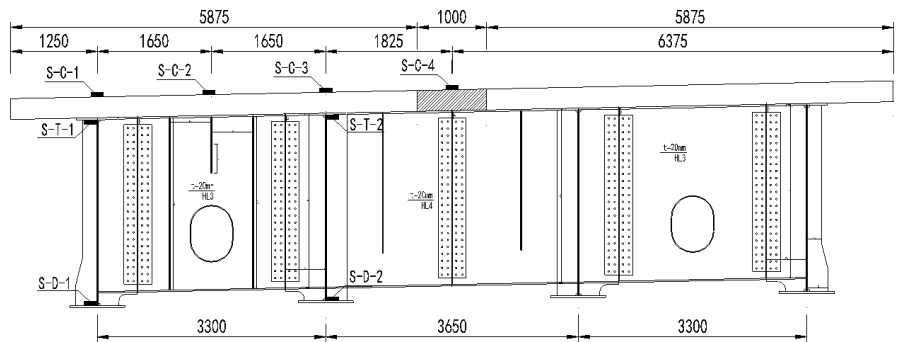
At each monitored cross section, vibrating strain meters are welded onto the steel flanges and lashed into the reinforcing mesh to monitor the stress distribution of the steel beam and the concrete slab. The installed positions of the strain meters on each section are presented in Figure 14. As the largest stress condition is located at the shear stiffness mutation section, three additional vibrating strain meters were installed (as shown in Figure 14 (b)) to study the stress mutation around this area.



(a) Mid-span section (M-M)



(b) Shear stiffness mutation section (P-P)



(c) Support section (S-S)

Figure 14. Positions of the strain meters on critical sections (mm)

Monitoring results

By now, it has been about 400 days since the vibrating strain meters were installed onto the girder. Figure 15 shows the strain data obtained in the upper and bottom flanges of the steel beam and in the concrete slab (see Figure 14 for the monitored positions). Qiwu bridge has not been open to traffic yet. Thus, there hasn't been any live load onto the bridge yet and concrete stress at the support section still stays at a low level and therefore the results are not presented. To smooth the curve, the fetch interval in Figure 15 takes 24h. As the action load of the girder transport vehicle only lasted about an hour, the stress variation corresponding to the construction stage of the front girder transport vehicle reaching mid-span and back girder transport vehicle reaching hoisting position was recorded separately and is not reflected in Figure 15.

Within the monitoring period, the concrete slab was casted on day 2, and the girder was hoisted to the pier on day 60. It can be seen that the strain in both the concrete slab and the steel beam has a sudden increase when casting the concrete slab because of the heavy construction equipment and the large turnover. When the concrete slab began curing and the equipment were removed, the strain level started to decrease. There was also a strain boost while hoisting the girder on day 60, because both the steel beam and the concrete slab start to bear the dead load. The longitudinal wet joint and the transversal wet joint (link slab) was respectively built on day 120 and 133. As the concrete

casting was quick and within hours, the strain variation due to the construction load was not reflected in the figures. Railings of the monitored girder were built on day 152, which contributed to a strain increase, especially in the steel top flange at mid span and shear stiffness mutation section.

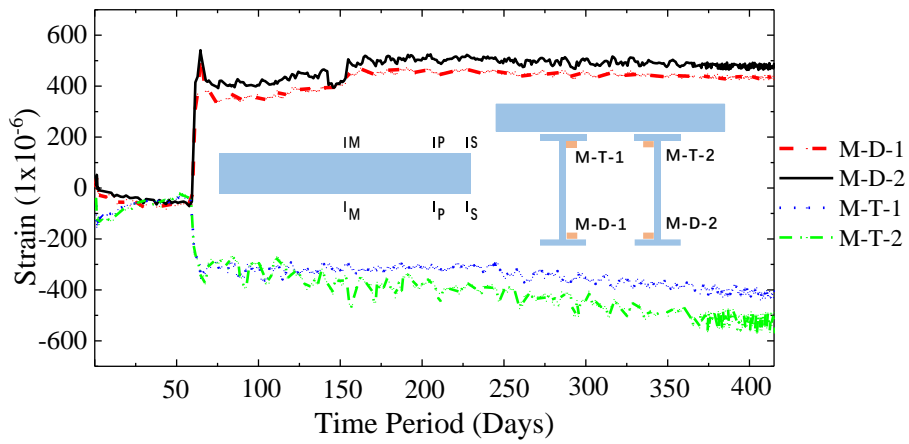
Compared with the shear stiffness mutation and the side support sections, strain of the steel beam at the mid-span section was obviously larger, with the figure reaching the maximum of $541\mu\epsilon$ after the girder was hoisted onto the pier. However, the maximum strain at the shear stiffness mutation section and the side support section was only $229\mu\epsilon$ and $90\mu\epsilon$ respectively. Compressive strain in the concrete slab shares the same phenomenon, with the strain boosted up to $501\mu\epsilon$ at the mid-span section but remained below $207\mu\epsilon$ at the shear stiffness mutation section.

Besides the dead load and construction load, indirect actions also have influence on the structure. Although the strain in the bottom flange remains quite constant along time, there is an increasing trend of the compression strain in the steel top flange over time due to the shrinkage and creep of the concrete slab, especially at the mid span and shear stiffness mutation section. The concrete shrinkage lasted over a year, which gradually increased the compressive stress both in the concrete slab and the steel top flange. Creep effects will still act in the next years.

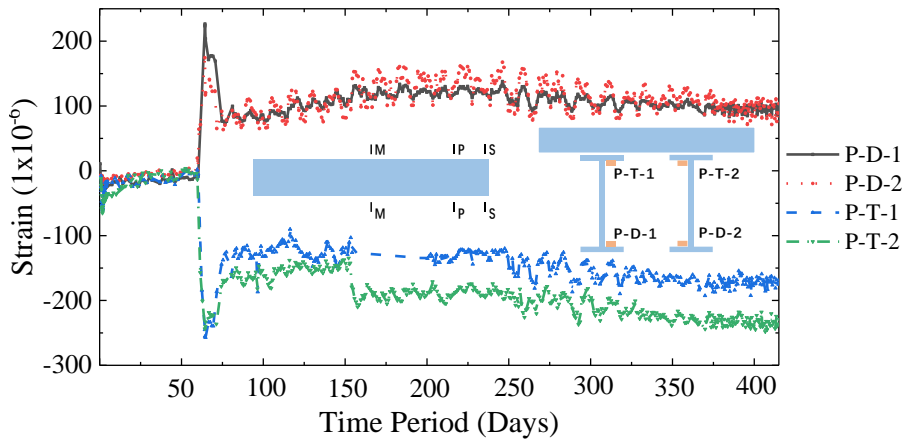
There is a daily strain fluctuation both in the concrete slab and the steel beam because of the temperature variation, being relatively larger in the concrete slab than that in the steel beam. The fluctuation frequency was fast, indicating the fluctuation was due to the daily temperature variation but not the shrinkage or creep. The daily strain variation in the steel girder can be up to $117\mu\epsilon$, $76\mu\epsilon$, and $65\mu\epsilon$ respectively at the mid-span, shear stiffness mutation and support sections, while that of the concrete slab is $175\mu\epsilon$ and $101\mu\epsilon$ respectively at the mid-span and shear stiffness mutation sections. Strain variation became larger at the edge of the concrete slab than at the middle.

The seasonal strain variation due to the seasonal temperature change (with a superposition of shrinkage and creep) is also larger in the concrete slab than in the steel beam. The local temperature at the Qiwu Bridge location is 30°C in summer and 6°C in winter in average. Under the integral temperature reduction of 24°C from summer to winter (with a superposition of shrinkage and creep), the seasonal strain variation in the concrete slab and steel beam is respectively $114\mu\epsilon$, $101\mu\epsilon$ at mid-span section, and $163\mu\epsilon$, $46\mu\epsilon$ at shear stiffness mutation section.

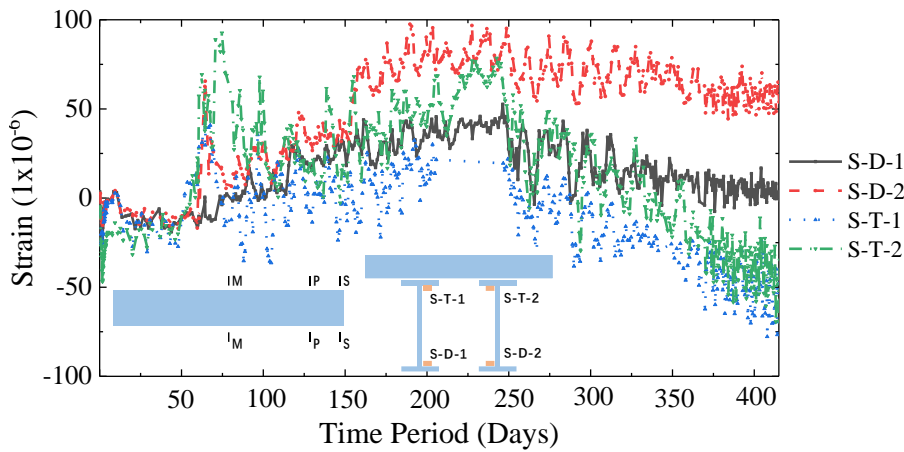
Stress changes around the shear stiffness mutation area are also observed. As shown in Figure 15 (e), stress profile around this area has an obvious gradient. The closer to the side support, the larger the stress appeared. The strain variation within the 2m zone (between P-C-U and P-C-D) can be up to $59\mu\epsilon$, while the strain variation at the same section (between P-C-1 and P-C-L) is not obvious. Thus, the shear stiffness mutation section should be strengthened by high reinforcement ratio and high-strength concrete.



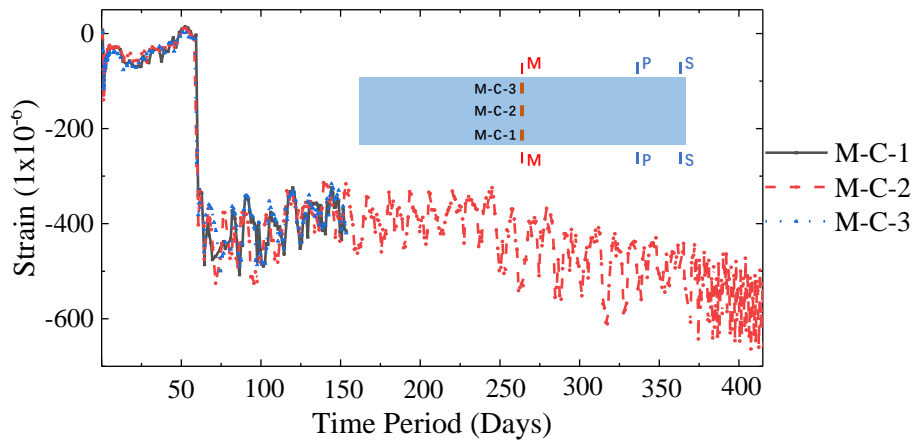
(a) Strain of steel beam at mid-span section



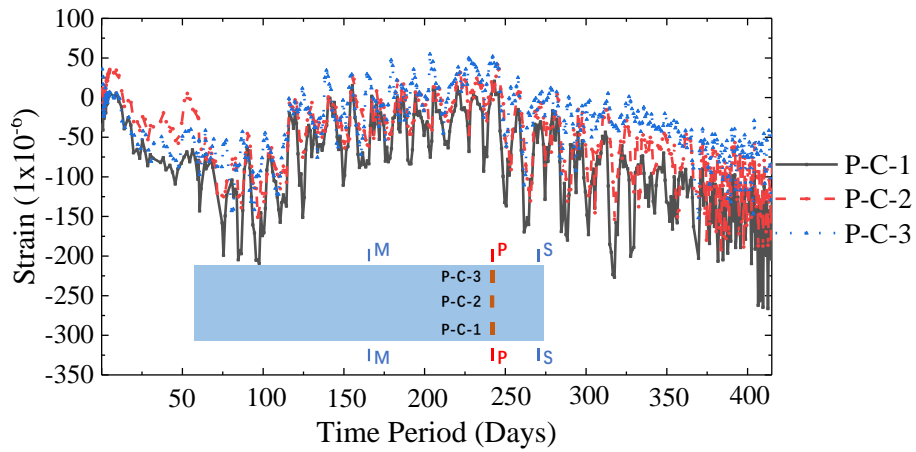
(b) Strain of steel beam at shear stiffness mutation section



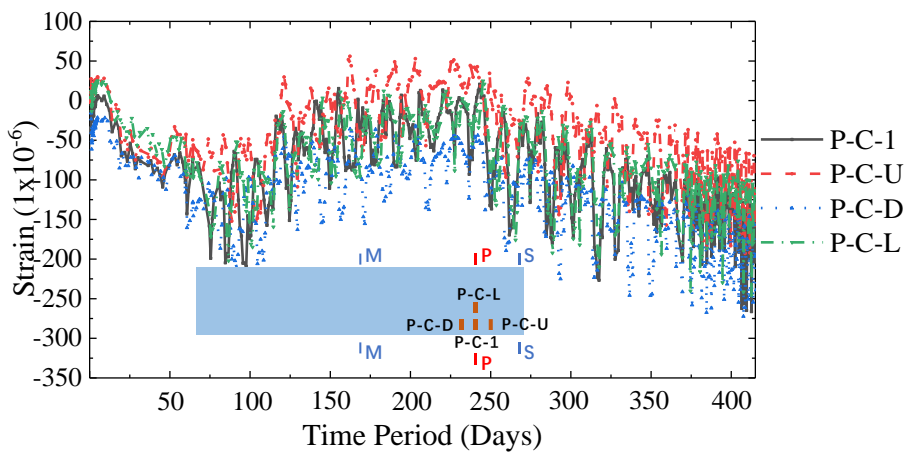
(c) Strain of steel beam at support section



(d) Strain of concrete slab at mid-span section
 (Vibrating strain meters M-C-1 and M-C-3 went out of work after 150 days)



(e) Strain of concrete slab at shear stiffness mutation section



(e) Strain of concrete slab around shear stiffness mutation section

Figure 15. Strain results of the monitored positions

Comparison between monitoring results and numerical results

Monitoring and numerical stresses at mid-span are compared in Table 2. They matched well with each other in general. As the steel beam and the concrete slab both worked in elastic stage, the experimental stress is calculated by strain times elastic modulus. It can be inferred that the monitored stress is generally larger than that of numerical result, which can be explained by the additional actual strain that is not accurately considered in the numerical model due to the temperature, shrinkage and creep.

The largest tensile and compressive stress appeared respectively at the steel bottom flange and the steel top flange during the construction stage when the back girder transport vehicle reached the hoisting position. The largest tensile and compressive stress were both less than the steel yield stress. Tensile stress was not detected in the concrete slab during the construction, and the largest compressive stress appeared during the construction stage when the back girder transport vehicle reached the hoisting position. The largest compressive stress was also quite below the compressive strength.

Based on the monitoring and numerical results, the adopted construction method is safe for the 60-span composite girder with a large safety factor. Thus, longer and heavier composite girder spans can still be built by a bridge-erecting machine.

Table 2

Comparison between monitoring and numerical results at mid-span (construction stage)

		Hoisting	Erected onto the piers	Front GTV reached mid-span	Back GTV reached hoisting position
Steel top flange (MPa)	Monitoring result	-37.1	-58.8	-84.2	-93.3
	Numerical Result	-36	-45	-63	-72
	Deviation	3.1%	30.7%	33.7%	29.6%
Steel bottom flange (MPa)	Monitoring result	71	88.6	168.7	186.4
	Numerical Result	68	85.1	146.3	162.9
	Deviation	4.4%	4.1%	15.3%	14.4%
Concrete top flange (MPa)	Monitoring result	-8.8	-13.8	-16.9	-25.3
	Numerical Result	-7.1	-10.8	-12.6	-19.4
	Deviation	23.9%	27.8%	34.1%	30.4%

GTV: Girder transport vehicle

Conclusions

In this paper, the case study of Qiwu Bridge using link slab between simply supported spans and partial shear connection (shear connectors between concrete and steel are removed in an area of 5.6 meters around the support) is introduced. The design concepts of Qiwu bridge were illustrated and analyzed by numerical calculation to investigate the effect of the link slab on the construction process and posterior life cycle performance of steel-concrete composite bridge. The numerical results show a correct performance of the bridge during both construction and service. Qiwu Bridge is also monitored by vibrating strain meters to experimentally check the results from the numerical model to study the mechanical behavior of this structural solution both during the construction and operating stages. As the bridge is not yet in operation, up to now, only experimental results during

construction are available and presented here. The following conclusions can be drawn from the numerical and monitoring results up to the actual construction stage:

(1) Numerical results from the dead load and traffic action showed that the removal of the shear connectors closes to the hogging section (shear stiffness mutation) contributed to a stress decrease around this area. The increase of the PSC region contributed to a decrease of the cracked region in the slab. The cracked region decreased from 1.9m to 0.5m and 0.15m when PSC region increased from 0m to 5.6m and 10m. The shear stiffness mutation section should be closely monitored due to the stress concentration as detected in the numerical analysis

(2) Numerical results show the obvious effect of the global temperature reduction (from summer to winter) and shrinkage on the concrete slab, with the tensile stress increasing by 2.6MPa and 2.7MPa respectively. These increments are of the same order of magnitude as the maximum stresses due to dead load and traffic action. Daily gradient cooling has an impact of 1.4MPa on stress increment, while concrete creep only increases the stress by 0.2MPa. Therefore, the effects of temperature and concrete shrinkage have to be fully considered when designing the concrete slab and reinforcement in this critical zone in order to avoid cracking or even rupture of the slab.

(3) From the monitoring results, it is observed that during construction, the strain of the steel beam at the mid-span section was obviously larger than at the shear stiffness mutation section and the support section as will be during service. There is a daily strain fluctuation both in the concrete slab and the steel beam because of the temperature variation. The fluctuation in the concrete slab is relatively larger than that in the steel beam.

(4) Monitored and numerical stresses matched well in general. The best comparison is observed in the bottom flange of the steel beam. The largest tensile and compressive stress appeared during the construction stage when the back girder transport vehicle reached the hoisting position. Based on the monitoring and numerical results, the construction method is safe for the 60-span composite girder with an important safety margin. Thus, larger spans with the same solution can be considered for construction by a bridge-erecting machine technique in the future.

Conflict of interest

All authors declare that no support, financial or otherwise, has been received from any organization that may have an interest in the submitted work; and there are no other relationships or activities that could appear to have influenced the submitted work.

Acknowledgements

The first author acknowledges the support provided by the China Scholarship Council (No. 202106260050). The third author acknowledges the support provided by the Spanish Ministry of Science and Innovation through the research project PID2021-126405OB-C31 and AGAUR for support to consolidated research groups.

References

- Alampalli, S., Yannotti, A. P., & Natl Res, C. (1998). In-service performance of integral bridges and jointless decks (*Structural Analysis and Design: Bridges, Culverts, and Pipes* (pp. 1-7). <https://doi.org/10.3141/1624-01>
- An, W., Song, G., & Chen, S. (2021). Near-Fault Seismic Response Analysis of Bridges Considering Girder Impact and Pier Size [Article]. *Mathematics*, 9(7), Article 704. <https://doi.org/10.3390/math9070704>
- Au, A., Lam, C., Au, J., & Tharmabala, B. (2013). Eliminating Deck Joints Using Debonded Link Slabs: Research and Field Tests in Ontario [Article]. *Journal of Bridge Engineering*, 18(8), 768-778. [https://doi.org/10.1061/\(ASCE\)BE.1943-5592.0000417](https://doi.org/10.1061/(ASCE)BE.1943-5592.0000417)
- Caner, A. (1998). Behavior and design of link slabs for jointless bridge decks [Article]. *PCI Journal*, 43(3), 68+. <https://doi.org/10.15554/pcij.05011998.68.80>
- Chen, S., Xia, H., An, W., & Wen, Y. (2021). Theoretical Investigation on Multiple Separation of Bridge under Near-Fault Vertical Ground Motion [Article]. *Mathematical Problems in Engineering*, 2021, Article 6634917. <https://doi.org/10.1155/2021/6634917>
- Choi, Y. S., Choi, S. Y., Kim, I. S., & Yang, E. I. (2018). Experimental Study on the Structural Behaviour of Calcium-Leaching Damaged Concrete Members [Article]. *Magazine of Concrete Research*, 70(21), 1102-1117. <https://doi.org/10.1680/jmacr.17.00297>
- Chu, K., Hossain, K. M. A., & Lachemi, M. (2021). Numerical Investigation on Static Behaviour of Steel- and GFRP-Reinforced ECC Link Slabs [Article]. *Arabian Journal for Science and Engineering*, 46(11), 11027-11045. <https://doi.org/10.1007/s13369-021-05644-1>
- Chu, K., Hossain, K. M. A., & Lachemi, M. (2022). Static and Fatigue Behaviour of ECC Link Slabs in Reinforced Concrete Girder Joint-Free Bridges [Article]. *Structures*, 41, 1301-1310. <https://doi.org/10.1016/j.istruc.2022.05.080>
- Deng, L., He, W., & Shao, Y. (2015). Dynamic Impact Factors for Shear and Bending Moment of Simply Supported and Continuous Concrete Girder Bridges [Article]. *Journal of Bridge Engineering*, 20(11), Article 04015005. [https://doi.org/10.1061/\(ASCE\)BE.1943-5592.0000744](https://doi.org/10.1061/(ASCE)BE.1943-5592.0000744)
- El-Safty, A., & Okeil, A. M. (2008). Extending the Service Life of Bridges Using Continuous Decks [Article]. *PCI Journal*, 53(6), 96-111. <https://doi.org/10.15554/pcij.11012008.96.111>
- Gan, Y., Liu, D., Ning, W., & Xia, Z. (2013). Model Test Study of a New Type of Seamless Bridge Deck Expansion Joint [Article]. *Bridge Construction*, 43(6), 71-75, Article 1003-4722(2013)43:6<71:XXwfm>2.0.Tx;2-6. (in Chinese).
- GB50010-2010. (2015). Code for design of concrete structures. Ministry of Construction People's Republic of China. (in Chinese).
- Han, Y., Wang, X., & Li, C. (2013, 2013). *Influence of Moving Vehicles on Vertical Vibration of Simply Supported Bridge* [Proceedings Paper]. Progress in Industrial and Civil Engineering II, PTS 1-4.
- JTG3362-2018. (2018). Code for design of highway reinforced concrete and prestressed concrete bridges and culverts. China Communication Press Co.,Ltd. (in Chinese).
- JTG60-2015. (2015). General code for design of highway bridges and culverts. China Communication Press Co.,Ltd. (in Chinese).
- Karim, R., & Shafei, B. (2021). Performance of fiber-reinforced concrete link slabs with embedded steel

- and GFRP rebars [Article]. *Engineering Structures*, 229, Article 111590. <https://doi.org/10.1016/j.engstruct.2020.111590>
- Kim, Y. Y., Fischer, G., & Li, V. C. (2004). Performance of bridge deck link slabs designed with ductile engineered cementitious composite [Article]. *ACI Structural Journal*, 101(6), 792-801.
- Li, X.-X. (2020). Parametric study on numerical simulation of missile punching test using concrete damaged plasticity (CDP) model [Article]. *International Journal of Impact Engineering*, 144, Article 103652. <https://doi.org/10.1016/j.ijimpeng.2020.103652>
- Li, X., Zhong, J., Jiang, L., Yuan, W., & Ieee. (2018, 2018). *Analysis of the Seismic Vulnerability of Simply-supported Girder Bridge under Two Level Seismic Hazard* [Proceedings Paper]. 2018 3rd International Conference on Smart City and Systems Engineering (ICSCSE).
- Mander, J. B., Priestley, M. J. N., & Park, R. (1988). Theoretical Stress-Strain Model for Confined Concrete [Article]. *Journal of Structural Engineering-ASCE*, 114(8), 1804-1826. [https://doi.org/10.1061/\(ASCE\)0733-9445\(1988\)114:8\(1804\)](https://doi.org/10.1061/(ASCE)0733-9445(1988)114:8(1804))
- Qian, S., Lepech, M. D., Kim, Y. Y., & Li, V. C. (2009). Introduction of Transition Zone Design for Bridge Deck Link Slabs Using Ductile Concrete [Article]. *ACI Structural Journal*, 106(1), 96-105.
- Su, H., Su, Q., Casas, J. R., Jiang, X., & Zhou, G. (2022). Application of Partial Shear Connection in Steel-Concrete Semi-Continuous Composite Girder Bridges [Article]. *Structural Engineering International*, 32(3), 411-420. <https://doi.org/10.1080/10168664.2022.2048436>
- Su, H., Su, Q., Casas, J. R., Xu, C., Tang, J., & Jiang, C. (2022). Influence mechanism of Steel-concrete interlayer partial shear connections on mechanical properties of composite girders [Article]. *Structures*, 46, 503-520. <https://doi.org/10.1016/j.istruc.2022.10.082>
- Su, H., Su, Q., Xu, C., Casas, J. R., & Zhou, G. (2022). Mechanical performance based rationalization research on steel-concrete double composite action [Article]. *Journal of Constructional Steel Research*, 197, Article 107492. <https://doi.org/10.1016/j.jcsr.2022.107492>
- Su, H., Su, Q., Xu, C., Zhang, X., & Lei, D. (2021). Shear performance and dimension rationalization study on the rubber sleeved stud connector in continuous composite girder [Article]. *Engineering Structures*, 240, Article 112371. <https://doi.org/10.1016/j.engstruct.2021.112371>
- Su, Q., Su, H., & Wu, F. (2021). Mechanical Analysis of the Influence of Rubber-Sleeved Stud Connector on the Steel-Concrete Composite Girder [Article]. *Journal of Tongji University. Natural Science*, 49(8), 1079-1087, Article 0253-374x(2021)49:8<1079:Xjhdzh>2.0.Tx;2-5. (in Chinese).
- Tang, J., Su, Q., Su, H., & Casas, J. R. R. (2023). Experimental and Numerical Study on the Mechanical Behavior of Prestressed Continuous Composite I-Girder Bridges with Partial Connection [Article]. *Journal of Bridge Engineering*, 28(3), Article 04022154. <https://doi.org/10.1061/JBENF2.BEENG-5955>
- Ulku, E., Attanayake, U., & Aktan, H. (2009). Jointless Bridge Deck with Link Slabs Design for Durability [Article]. *Transportation Research Record*(2131), 68-78. <https://doi.org/10.3141/2131-07>
- Wang, C., Shen, Y., Wang, G., & Xie, X. (2016). Field tests on mechanical characteristic of link slab on hollow-cored slab beam bridge [Article]. *Journal of Zhejiang University. Engineering Science*, 50(8), 1438-1445, Article 1008-973x(2016)50:8<1438:Kxblqq>2.0.Tx;2-e. (in Chinese).
- Wang, C., Shen, Y., Zou, Y., Zhuang, Y., & Li, T. (2019). Analysis of Mechanical Characteristics of Steel-

- Concrete Composite Flat Link Slab on Simply-Supported Beam Bridge [Article]. *KSCCE Journal of Civil Engineering*, 23(8), 3571-3580. <https://doi.org/10.1007/s12205-019-1921-1>
- Wang, C., Xie, J., Shen, Y., & Jiang, J. (2022). Research on the Mechanical Behavior of a Steel-Concrete Composite Link Slab on a Simply Supported Girder Bridge [Article]. *Metals*, 12(9), Article 1410. <https://doi.org/10.3390/met12091410>
- Xia, L., Zhang, L., & Zheng, Y. (2019). Structural performance of CFRP reinforced ECC link slabs in jointless bridge decks [Article]. *Acta Materialiae Compositae Sinica*, 36(4), 848-859, Article 1000-3851(2019)36:4<848:Czqgcs>2.0.Tx;2-f. (in Chinese).
- Yang, C.-S. W., & DesRoches, R. (2015, 2015). *Bridges with Innovative Buckling Restrained SMA Expansion Joints Having a High Symmetrical Tension/Compression Capacity* [Proceedings Paper]. Structures Congress 2015.
- Ye, W., Li, X., Duan, H., Shan, C., & Liu, X. (2012, 2012). *Analytical solution for Vertical Dynamic Response of Railway Simply Supported Beam Bridge under Bidirectional Moving Loads* [Proceedings Paper]. Advances In Industrial And Civil Engineering, PTS 1-4.

Chapter 7 Conclusions and Future Research

7.1 Conclusions

This thesis has the main focus in the research of the structural performance of different solutions proposed to solve the problem of high tensile stress and cracking in the upper concrete slab in the hogging moment zone of continuous composite steel-concrete bridges. According to the different proposed solutions, the following conclusions could be obtained:

1.- Partial shear connection

(1) Wrapping rubber sleeve around the stud shank near stud root could enhance the slip capacity and reduce the stiffness of the connector in the push-out tests, while it could hardly affect the shear strength of the connector. In terms of the effect on stud stiffness reduction, the rational rubber sleeve thickness and height were 4mm and 50mm for a 22mm-diameter and 220mm-high stud. The parametric analysis results showed that the RSS stiffness began to decrease obviously when the elastic modulus of the wrapped material was 10% lower than that of concrete.

(2) Configuring the RSS connectors with a shear stiffness only 8.1% of corresponding OHS connectors or setting a 2000mm OHS spacing could respectively cause 17% and 11% reductions of the load-carrying capacity. On the other hand, the RSS connector could also lead to a 12% decrease of bending stiffness and relieve the concrete crack development, while increasing stud spacing could hardly change the bending stiffness or improve the cracking resistance.

(3) Based on the parametric analysis on the effect of prestressing the concrete slab, RSS connector had a larger influence on the prestress distribution between concrete slab and steel girder than increasing the stud distance. RSS connector could contribute to a maximum pre-stress increase in concrete slab by 19.4% and decline in steel girder by 92.6%, while the figures were only 8% and 26.9% for increasing the stud distance.

(4) Based on the parametric analysis on girder under negative bending, RSS connector with shear stiffness lower than 20% of the OHS connector could efficiently decrease the concrete tensile stress, while the load-carrying capacity could have a maximum decline of only 12.3%. On the other hand, when setting OHS connectors with

a 2000mm spacing, the concrete and steel stress could increase by 145.2% and 584.8%. Besides, avoiding stud position at region with large bending moment could decrease the concrete stress by 14.4%.

(5) The stress variation in composite girder became larger when the stud stiffness was less than 20% of the origin stiffness. The concrete stress was exponentially related to the stud stiffness, while the exponential was supposed to be $5/3$.

(6) Partial shear connection can effectively improve the cracking resistance of continuous composite girders. Compared to the normal composite girder specimen, the cracking load of the partial connection-prestressing girder specimen was 3.1 times higher. The crack width of the partial connection-prestressing girder specimen was no more than 81.3 % of that of the normal composite girder specimen at same load level. Compared to conventional composite girders, the cracking load increased by 11.8% and 157.0 % when applying RSS and prestress alone, respectively, and by 234.3% when applying RSS and prestressing at the same time.

2.- Double composite action

(1) Casting an extra concrete bottom layer to a steel-concrete composite box girder in a hogging moment region can increase sectional stiffness and prevent steel buckling. The concrete bottom slab helps to restrain lateral deformation of steel web and steel bottom flange. It can effectively improve the anti-buckling ability of the continuous girder

(2) The additional concrete slab helps to increase the cracking load and ultimate strength by 12% and 4%. However, the additional gravity load can accelerate the crack development. Besides, the optimal concrete slab thickness was found around 15 % of the height of the steel girder. The ultimate strength decreases afterwards mainly due to a continuing downward translation of the sectional neutral axis. In addition, the concrete bottom slab can also replace the function of the lower longitudinal stiffening ribs.

(3) The steel web thickness can be saved 16.7% when adopting double composite action, while the steel bottom flange thickness only needs to meet the constructing requirement. Besides, the box section could contribute to a 24.4% and 3.2% stress decline respectively in steel top flange and concrete slab compared with tub section.

(4) The cracking moment was increasing to a maximum and after that decreasing with the increase of the concrete bottom slab thickness, while the steel bottom flange

stress can be decreased up to 20%. Taking into account both the cracking moment and stress state at the service stage, the optimal concrete bottom slab thickness was 15% of steel girder height.

3.- Semi-continuous bridge with link slab

(1) Arranging PSC region can effectively reduce the crack region. Compared with bridge without PSC region, crack region decreases from 1.6m (when the length of the PSC region is 0m) to 0.5m (when the length of the PSC region is 5.6m) and 0.3m (when the length of the PSC region is 10m) under dead load. The decline becomes even larger under load combination of dead load and vehicle load. In addition, while the crack region tends to be wider and continuous with the increase of the load, PSC action helps to disperse the concentrated stress in the zone.

(2) The shear stiffness mutation can magnificently increase the stress level at the edge of PSC region in concrete slab and made it easier to crack. Actions of increasing the reinforcement ratio or adopting high-performance concrete at this position is essential for crack control.

(3) Except for the hogging moment region, PSC action had limit influence on the whole structure. With the length of PSC region increasing from 0 to 10m, the growth rate of deflection and steel bottom flange stress at midspan was respectively below 4% and 2%. Meanwhile, the steel top flange stress at mid-support declined rapidly with the increase of the length of PSC region, which also hints the stress reduction in concrete slab around the mid-support.

(4) Integral temperature reduction and shrinkage can obviously increase the tensile stress in concrete slab with or without PSC region, and gradient cooling has a larger impact on structures without PSC region. The influence of concrete creep is subtle in both kinds of structures.

(5) Influence of the link slab on the stress variation of the whole structure is within 15%, which infers that the link slab can improve the driving comfort with limited influence on the mechanical behaviour.

(6) From the monitoring results, it is observed that during construction, the strain of the steel beam at the mid-span section was obviously larger than at the shear stiffness mutation section and the support section as will be during service. There is a daily strain fluctuation both in the concrete slab and the steel beam because of the temperature variation. The fluctuation in the concrete slab is relatively larger than that in the steel

beam.

7.2 Future Research

(1) In this thesis, the study of the Rubber Sleeved Stud (RSS) mainly focuses on the mechanical performance under static load, while the rubber sleeve wrapped around the stud connector may gradually deteriorate over time to affect the long-term performance of the structure. It is hoped that more in-depth long-term performance studies can be carried out in the future.

(2) The tests and finite element models analyzed in this thesis are based on static loads, while the fatigue loads or earthquake loads are not analyzed. It is hoped that in the future more in-depth study related on beams under fatigue loads and earthquake loads can be carried out.

References

- [1] El-Gendy M , El-Salakawy E . Effect of flexural reinforcement type and ratio on the punching behavior of RC slab-column edge connections subjected to reversed-cyclic lateral loads[J]. *Engineering Structures*, 2019, 200:109703-.
- [2] Chin C L , Khun M C , Awang A Z , et al. Confining stress path dependent stress-strain model for pre-tensioned steel-confined concrete[J]. *Engineering Structures*, 2019, 201:109769-.
- [3] Massaro F M , Malo K A . Stress-laminated timber decks in bridges: Friction between lamellas, butt joints and pre-stressing system[J]. *Engineering Structures*, 2020, 213:110592.
- [4] Steensels R , Vandoren B , Vandewalle L , et al. Evaluation of end-zone detailing of pre-tensioned concrete girders[J]. *Engineering Structures*, 2019, 187(MAY 15):372-383.
- [5] Jiang C , Wu C , Jiang X . Experimental study on fatigue performance of corroded high-strength steel wires used in bridges[J]. *Construction and Building Materials*, 2018, 187(OCT.30):681-690.
- [6] Kim H H , Shim C S . Experimental investigation of double composite twin-girder railway bridges[J]. *Journal of Constructional Steel Research*, 2009, 65(6):1355-1365.
- [7] Kim C , Kim J , Yun N , et al. Structural behavior of a continuous composite truss with a composite bottom chord[J]. *Journal of Constructional Steel Research*, 2015, 105:1-11.
- [8] Xu C , Su Q , Wu C , et al. Experimental study on double composite action in the negative flexural region of two-span continuous composite box girder[J]. *Journal of Constructional Steel Research*, 2011, 67(10):1636-1648.
- [9] Meszoely T , Randl N . Shear behavior of fiber-reinforced ultra-high performance concrete beams[J]. *Engineering Structures*, 2018, 168(AUG.1):119-127.
- [10] Wan-Wendner L , Wan-Wendner R , Cusatis G . Age-dependent size effect and fracture characteristics of ultra-high performance concrete[J]. *Cement and Concrete Composites*, 2018:S0958946516305297.

[11] Poon C S , Kou S C , Lam L . Compressive strength, chloride diffusivity and pore structure of high performance metakaolin and silica fume concrete[J]. *Construction and Building Materials*, 2006, 20(10):858-865.

[12] Ribeiro F , Sena-Cruz J , Branco F G , et al. 3D finite element model for hybrid FRP-confined concrete in compression using modified CDPM[J]. *Engineering Structures*, 2019, 190(JUL.1):459-479.

[13] Abdullah A , Bailey C G . Punching behaviour of column-slab connection strengthened with non-prestressed or prestressed FRP plates[J]. *Engineering Structures*, 2018, 160:229-242.

[14] Oehlers D, Coughlan C, The shear stiffness of stud shear connections in composite beams. *Journal of Constructional Steel Research*, 1986, 6(4):273-284.

[15] Oehlers D , Bradford M A , Elementary behaviour of composite steel and concrete structural members. Butterworth-Heinemann, 1999

[16] Uddin M , Sheikh A , Bennett T , et al. Large deformation analysis of two layered composite beams with partial shear interaction using a higher order beam theory[J]. *International Journal of Mechanical Sciences*, 2017, 122:331-340.

[17] Keo P , Nguyen Q H , Somja H , et al. Exact finite element formulation for an elastic hybrid beam-column in partial interaction with shear-deformable encasing component[J]. *Engineering Structures*, 2016, 125(oct.15):494-503.

[18] Loh H Y, Uy B, Bradford M A. The effects of partial shear connection in the hogging moment regions of composite beams: Part I—Experimental study[J]. *Journal of Constructional Steel Research*, 2004, 60(6):897-919

[19] Loh H Y, Uy B, Bradford M A. The effects of partial shear connection in the hogging moment regions of composite beams Part II—Analytical study[J]. *Journal of Constructional Steel Research*, 2004, 60(6):921-962

[20] Mackay H.M., Gillespie P. & Lelua C. Report on the strength of steel I-beams haunched with concrete. *Engineering Journal*, Canada, 1923,6(8):365–369

[21] Viest IM. Investigation of stud shear connectors for composite concrete and steel T-beams. *Journal of the American Concrete Institute*, 1956,27(8): 875-891

[22] Davies C. Steel concrete composite beams with flexible connectors: a survey of research. *Concrete*, 1967(12):425-430

[23] Batho C, Lash SD & Kirkham RHH. The properties of composite beams, consisting of steel joints encased in concrete, under direct and sustained

- loading. *Journal of the Institution of Civil Engineers*,1939,11(4):61-114
- [24]D. Lam. Composite steel beams with precast hollow core slabs: behavior and design. *Composite structures*,2002,11(4):179-185
- [25]Chapman J C . Composite construction in steel and concrete: The behavior of composite beams. *The Structure Engineer*,1964,42(4):115-125
- [26]Chapman J C , Balakrishnan S. Experiments on composite beams. *The Structural Engineer* 1964,42(11):369-383
- [27]Slutter RG, Driscoll GC. Flexural strength of steel-concrete composite beams. *Journal of the Structural Division (ASCE)*,1965,91(ST2):71-99
- [28]Ollgaard JG, Slutter RG & Fisher JW. Shear strength of stud connectors in lightweight and normal weight concrete. *Engineering Journal(AISC)*,1971, 8(2):55-64
- [29]Johnson R P , May I M. Partial-interaction design of composite beams. *The Structural Engineer*. 1975, 53(8):305-311
- [30]Joint Committee IABSE/CEB/FIP/ECCS. *Composite Structures (Model Code)*. London: Construction Press,1981
- [31]EC Commission. Eurocode 4: Common unified rules for composite steel and concrete structures. Report EUR 9886 EN, Commission of the European Communities, Luxembourg,1985
- [32]Eurocode 4. Design of composite steel and concrete structures, Part1.1: General rules and rules for buildings. European Committee for Standardization(CEN), Brussels, Belgium,1994
- [33]László P K , George S. *Mechanics of Composite Structures*. Cambridge University Press, 2003
- [34]Wang Y C . *Steel and Composite Structures: Analysis and Design for Fire Safety*. Taylor & Francis, 2002
- [35]David C . *Steel Concrete Composite Bridges*. Thomas Telford Services Ltd, 2005
- [36]Andrews E S . *Elementary principles of reinforced concrete construction*. Scott, Greenwood and Sons, 1912
- [37]Newmark N M , Siess C P , Viest, I.M. Test and analysis of composite beams with incomplete interaction. *Experimental Stress Analysis*, 1951,9(6):896-901
- [38]Viest I M , Investigation of stud shear connector for composite concrete

and steel T-beams, Journal of ACI, 1956, 27(8): 875-891

[39] Viest I M . Review of research on composite steel-concrete beams. J. Structural Division, 1960, 86(6):1-21

[40] Barnard P R , Johnson R P , Ultimate strength of composite beams. Proc. Instn. Civ. Engrs., Part2,1965,32(10),161-179

[41] Mallick S K , Chattopadhyay S K Ultimate strength of continuous composite beams. Building Science,1975,10(3): 189-198

[42] Mallick S K , Chattopadhyay S K . Behaviour of continuous steel-concrete composite beams. Indian Concrete Journal, 1975,49(6):173-178

[43] Hamada S , Longworth J . ultimate strength of continuous composite beams. J. structural division, 1976,102(7):1463-1478

[44] Ansourian P . Experiments on continuous composite beams. Proc. Instn. Civ. Engrs., Part 2,1981, 71(2):25-71

[45] Rotter J M , Ansourian P . Cross-section behavior and ductility in composite beams. Proc. Instn. Civ. Engrs, Part2,1979(6),453-474

[46] Bradford M A , Gilbert R I . Composite beams with partial interaction under sustained loads. Journal of Structural Engineering. 1992, 118(7): 1871-1883

[47] Richard Y , Lin Y , Lai M T . Composite beams subjected to static and fatigue loads. Journal of Structural Engineering. 1997,123(6):765-771

[48] Brain U y . Application behavior and design of composite steel-concrete beams subjected to combined actions. Proceedings of the 9th international conference on steel concrete composite and hybrid structures (ASCCS2009), Leeds, UK, July 2009

[49] Zhang Q, Jia D, Bao Y, et al. Flexural Behavior of Steel-Concrete Composite Beam Considering Interlayer Slip[J]. Journal of Structural Engineering, 2019, 145(9):04019084.1-04019084.14.

[50] Guo Z W, Chen H L, Li L J , et al. Stress distribution characteristics of concrete slabs of steel-concrete composite girder bridges[J]. Journal of Shenyang University (Natural science) ,2019, 35(4):586-593

[51] Hou Z M , Xia H, Li Y S. Vehicle-bridge dynamic response analysis of a steel-concrete continuous composite bridge under high-speed train loading[J]. Steel Construction,2019,34(12):82-87.

[52] Jin L, Yang Y W, Deng L. FEM analysis on mechanical behavior of steel-concrete joint section of hybrid girder cable-stayed bridge[J]. Journal of China &

Foreign Highway,2019,39(2):70-75

[53]Luo J, Shao X, Fan W, et al. Flexural cracking behavior and crack width predictions of composite (steel + UHPC) lightweight deck system[J]. Engineering Structures, 2019, 194(SEP.1):120-137.

[54]Zhang Q H, Han S H, Jia D L, et al. Mechanical performance of novel prefabricated composite girder with top flange of ultra-high performance concrete waffle deck panel [J]. Journal of Southwest Jiaotong University,2019,54(3):445-452

[55]Liu Y, Zhang Q, Meng W, et al. Transverse fatigue behavior of steel-UHPC composite deck with large-size U-ribs[J]. Engineering Structures, 2019, 180(FEB.1):388-399.

[56]Newmark N M , Siess C , Viest M . Tests and analysis of composite beams with incomplete interaction. Society for Experimental Stress Analysis, 1951, 9(1):75-92

[57]Viest I M . Review of research on composite steel-concrete beams. Journal of the Structural Division ASCE, 1960, 86(ST6): 1-21

[58]Ollgaard J G , Slutter R G , Fisher J W , Shear strength of stud connectors in lightweight and normal-weight concrete. AISC Engineering Journal, 1971, 8(2):55-64

[59]An L, Cederwall K. Push-out tests on studs in high strength and normal strength concrete. Journal of Constructional Steel Research, 1996, 36(1):15-29

[60]Wang Y C . Deflection of steel-concrete composite beams with partial shear interaction. Journal of Structural Engineering, 1998, 124(10): 1159-1165

[61]Kim H H , Shim C S , Experimental investigation of double composite twin-girder railway bridges. Journal of Constructional Steel Research. 2009, 65(6):1355-1365

[62]Shim C , Lee P , Yang T. Static behavior of large stud shear connectors. Engineering structures, 2004,26(12):1853-1860

[63]Pallares L , Hajar J F . Headed steel stud anchors in composite structures, Part I:Shear. Journal of Constructional Steel Research, 2010, 66(2):198-212

[64]Xue D, Liu Y, Yu Z, et al. Static behavior of multi-stud shear connectors for steel-concrete composite bridge. Journal of Constructional Steel Research,2012; 74:1-7

[65]Zhai C , Lu B , Wen W , et al. Experimental study on shear behavior of

studs under monotonic and cyclic loadings. *Journal of Constructional Steel Research*, 2018, 151:1-11

[66] Wang J , Xu Q , Yao Y , et al. Static behavior of grouped large headed stud-UHPC shear connectors in composite structures. *Composite Structures*,2018, 206: 202-214

[67] Kumar P , Chaudhary S . Effect of reinforcement detailing on performance of composite connections with headed studs. *Engineering Structures*, 2019, 179: 476-492

[68] Chin C L , Khun M C , Awang A Z , et al. Confining stress path dependent stress-strain model for pre-tensioned steel-confined concrete[J]. *Engineering Structures*, 2019, 201:109769

[69] Massaro F M , Malo K A . Stress-laminated timber decks in bridges: Friction between lamellas, butt joints and pre-stressing system[J]. *Engineering Structures*, 2020, 213:110592

[70] Steensels R , Vandoren B , Vandewalle L , et al. Evaluation of end-zone detailing of pre-tensioned concrete girders[J]. *Engineering Structures*, 2019, 187(MAY 15):372-383

[71] Jiang C , Wu C , Jiang X . Experimental study on fatigue performance of corroded high-strength steel wires used in bridges[J]. *Construction and Building Materials*, 2018, 187(OCT.30):681-690

[72] Hamoda A , Hossain K M A , Sennah K , et al. Behaviour of composite high performance concrete slab on steel I-beams subjected to static hogging moment[J]. *Engineering Structures*, 2017, 140:51-65

[73] El-Gendy M , El-Salakawy E . Effect of flexural reinforcement type and ratio on the punching behavior of RC slab-column edge connections subjected to reversed-cyclic lateral loads[J]. *Engineering Structures*, 2019, 200:109703

[74] Ubertini F , Materazzi A L , D'Alessandro A , et al. Natural frequencies identification of a reinforced concrete beam using carbon nanotube cement-based sensors[J]. *Engineering Structures*, 2014, 60(Feb.):265-275

[75] D'Alessandro A , Ubertini F , Garcia-Macias E , et al. Static and Dynamic Strain Monitoring of Reinforced Concrete Components through Embedded Carbon Nanotube Cement-Based Sensors[J]. *Shock and Vibration*,2017,(2017-8-7), 2017, 2017(PT.4):1-11.

[76] Shaheen E , Shrive N G . Optimization of Mechanical Properties and

Durability of Reactive Powder Concrete[J]. ACI Materials Journal, 2006, 103(6):444-451.

[77]Li M , Li H . Study on the Mechanical Properties of Minorexpansion Fiber Concrete[J]. Building Structures, 2005, 35(10):32-34.

[78]Guo R , Su Q , Li C , et al. Experimental studies on cracking behavior of post-combined prestressed concrete slab in hogging zone of composite girder[J]. Journal of Tongji University, 2015, 43(3):352-356.

[79]He Y , Qiu M , Zhao X , et al. Negative moment cracking control method of continuous Steel-Concrete composite girder bridge based on UHPFRC thin layers[J]. Structural Concrete, 2023, Early Access

[80]Mohammed A A , Manalo A C , Ferdous W , et al. Experimental and numerical evaluations on the behaviour of structures repaired using prefabricated FRP composites jacket[J]. Engineering Structures, 2020, 210: 110358

[81]Al-Qaralleh M , Toutanji H , Eljufout T . Overloading impact on the flexural behavior of RC beams strengthened with FRP composites under fatigue: Experimental study[J]. Engineering Structures, 2020, 221: 111045

[82]Keo P , Nguyen Q H , Somja H , et al. Exact finite element formulation for an elastic hybrid beam-column in partial interaction with shear-deformable encasing component[J]. Engineering Structures, 2016, 125(oct.15):494-503

[83]Wright H D . The deformation of composite beams with discrete flexible connection[J]. Journal of Constructional Steel Research, 1990, 15(1-2):49-64

[84]Molenstra N , Johnson R P . Partial shear connection in composite beams for buildings[J]. Proceedings of the Institution of Civil Engineers Part Research & Theory, 1991

[85]Keo P , Nguyen Q H , Somja H , et al. Exact finite element formulation for an elastic hybrid beam-column in partial interaction with shear-deformable encasing component[J]. Engineering Structures, 2016, 125(OCT.15):494-503

[86]Guo, L. , Wang J , Wang W , et al. Seismic evaluation and calculation models of CFDST column blind bolted to composite beam joints with partial shear interaction. Engineering Structures, 2019, 196(OCT.1):109269.1-109269.20

[87]Al-Sammari A T , Clouston P L , Brena S F . Finite-Element Analysis and Parametric Study of Perforated Steel Plate Shear Connectors for Wood-Concrete Composites. Journal of structural engineering, 2018, 144(10): 04018191.1-04018191.10.